USING ULTRAFAST VIBRATIONAL SPECTROSCOPY FOR A COMPREHENSIVE UNDERSTANDING OF STRUCTURAL AND ROTATIONAL MOTIONS FOR WATER TO PROTIC IONIC LIQUIDS

by

Clinton Alan Johnson

B.S. Chemistry, Frostburg State University, 2013

Submitted to the Graduate Faculty of

the Kenneth P. Dietrich School of Arts and Sciences in partial fulfillment

of the requirements for the degree of

Doctor of Philosophy

University of Pittsburgh

2020

UNIVERSITY OF PITTSBURGH

KENNETH P. DIETRICH SCHOOL OF ARTS AND SCIENCES

This dissertation was presented

by

Clinton Alan Johnson

It was defended on

July 6th, 2020

and approved by

Sean Garrett-Roe, Associate Professor, Department of Chemistry

David W. Waldek, Professor, Department of Chemistry

Jennifer Laaser, Assistant Professor, Department of Chemistry

Daniel S. Lambrecht, Assistant Professor, Department of Chemistry and Physics, Florida Gulf Coast University

Dissertation Director: Sean Garrett-Roe, Associate Professor, Department of Chemistry

USING ULTRAFAST VIBRATIONAL SPECTROSCOPY FOR A COMPREHENSIVE UNDERSTANDING OF STRUCTURAL AND ROTATIONAL MOTIONS FOR WATER TO PROTIC IONIC LIQUIDS

Clinton Alan Johnson, PhD

University of Pittsburgh, 2020

In this work, two-dimensional infrared (2D-IR) spectroscopy investigates the timescale of solvent fluctuations for proton and hydride transfers. To elucidate hydride transfer dynamics, the BH stretch of BH_4^- is probed in various solvents from H_2O to ionic liquids (ILs). For proton transfer dynamics, a vibrational probe (SCN^-) explores the three-dimensional hydrogen bonding environment of a protic ionic liquid (PIL).

BH_4^- is first investigated in increasing NaOH concentrations to develop a molecular understanding of suppressing the hydrogen evolution reaction. As the concentration increases, the timescale of frequency fluctuations decrease. Born Oppenheimer molecular dynamics (BOMD) simulations suggest that a crowding effect of ions around BH_4^- inhibits the rearrangement of dihydrogen bonds between BH_4^- and H_2O. To completely suppress the hydrogen evolution reaction, ILs with BH_4^- as the anion are investigated. The linear and 2D-IR spectra of the antisymmetric BH stretch of BH_4^- are complicated due to Fermi resonances. The narrow linear and 2D-IR linewidths of BH_4^- in an IL allow a comprehensive assignment of all diagonal peaks and crosspeaks. Confirmed with a model Hamiltonian, two anharmonicities for the antisymmetric BH stretch of BH_4^- are characterized.

Polarization- and temperature-dependent 2D-IR is employed to investigate the hydrogen bonding network of the PIL ethyl-ammonium nitrate (EAN). SCN^- experiences two hydrogen bonding subensembles in EAN as two separate vibrational relaxation times are resolved. Furthermore, the polarization-weighted frequency fluctuation correlation function can be sep-

arated into two components: structural spectral diffusion (SSD) and reorientation-induced spectral diffusion (RISD). For SCN^- in EAN, the timescales of frequency fluctuations are in the rotational limit as the SSD is unresolved. Temperature-dependent 2D-IR extracts the enthalpy and entropy of activation for frequency fluctuations. For SCN^- in EAN, the enthalpy of activation for rotational motions are similar as to SCN^- in H_2O, and this suggests that the breaking and forming of hydrogen bonds around SCN^- undergoes a similar mechanism in EAN as in H_2O.

TABLE OF CONTENTS

LIST OF TABLES

LIST OF FIGURES

PREFACE

"This is the worst thing that I've read in twenty plus years!" These words are not meant to give you pause in reading my thesis for it's not a warning, and I do not consider myself to be a poor, novice writer. The comment and manuscript, however, are related. There may not be one without the other. As much as we build up our self-confidence as we develop into an independent scientist, a brutal negative comment will have a lasting impression. We do have a choice though. The comment can be allowed to be a crutch, an excuse. 'I'm not cut out for graduate school and this proves it.' Is there a way out, *i.e.* a chance to ignore significant damage to one's self-confidence? Another option includes perseverance and a refusal to run away from inadequate and inappropriate advising comments. While the comment is an ineffective mentoring technique, somehow it resulted in a much larger revelation.

I joined a lab in the Spring of 2014. By the Summer of 2014, I have passed my two semesters of classes and was now ready to throw on my lab coat and goggles to begin the journey of my doctoral degree. In my undergraduate career at Frostburg State University, I excelled in every aspect and received only two course grades lower than an A. Now, here I am, a graduate student ready for research and a PhD, please sign here _____. I was ready to go there and back again with multiple passes through the so-believed treacherous woods of Mirkwood. I would not deviate from the path. In retrospect, no one is ever ready at the beginning, but like Bilbo Baggins, everyone has a 'Tookish' side.

The research I was performing in the lab was not a strength of mine, yet I felt like I needed to produce rapidly. I came to graduate school with the expectation of performing ultrafast spectroscopy. My research, however, focused solely around synthesis. In all honesty, I lacked the skills to be successful, and did not have the support needed to make progress.

I was encouraged by other group members to write a report to sum up the pitfalls I was encountering. The 'finished' manuscript was met with little enthusiasm.

I didn't realize that scientific writing is a from of storytelling. As in fiction, an effective journal article needs to be able to convey a complete and interesting story. King writes in his book On Writing, "It's best to have your tools with you. If you don't, you're apt to find something you didn't expect and get discouraged." [1] I was unaware that my tools were not developed or at least packed in an efficient, logical manner. I became discouraged to the point of feeling inadequate. My saboteur took over.

In the Fall of 2014, I joined a new lab led by Prof.Sean Garrett-Roe. The new research project reinvigorated my drive and gave me a sense of purpose. Also, I spent a tremendous amount of time invested in developing technical scientific writing skills. What story structure is the most effective based on your audience? How do I funnel from a broad opening into my claims? How can I decrease the amount of 'lard' in my sentence to improve clarity? I organized and filled up my writing toolbox.

While teaching physical chemistry labs at Pitt, I realized that students were facing similar inadequacies in their writing. Without sounding self-righteous, I didn't want others to experience the emotional rollercoaster of being unprepared in graduate school. With the help of Dr. Eugene Wagner, I developed a guided-inquiry based approach to help students develop their own understanding of how to write an effective scientific story. While my career goal was to be a professor after I received my PhD, it wasn't until this experience until I had a grasp of the important role I can make in someone's career. I began to realize that I had a profound interest in chemical education.

I would first like to thank my advisor Prof. Sean Garrett-Roe for setting me up to succeed at Pitt and my future endeavor into academia. Not only did he provide me with encouragement and support with my research, but he introduced me to the ideology of process-oriented guided inquiry learning (POGIL) and connected me to its large community of educators. I would also like to thank Dr. Paul Donaldson who acted as an unofficial second advisor. Thanks to Paul, my three visits to the Central Laser Facility (CLF) at the Rutherford Appleton Laboratory were rich with experience and produced an insurmountable amount of data. I am looking forward to continuing these collaborations while allowing

undergraduates to gain an exposure to a state-of-the art research facility. Also, I want to thank Prof. Tony Parker who supported our initial CLF experiments. More importantly, he always made sure we had a tea break at 3 pm, just as long as we supplied the cream. Another unofficial advisor would be Dr. Eugene Wagner who, with an outstanding amount of enthusiasm, encouraged me to help change the physical chemistry lab curriculum at Pitt.

We are no one without our family and friends. From a young age, my parents instilled the importance of education and that belief assisted my path into academia. My sister, Dr. Katie Gares, has had a huge influence on my life and my career in chemistry. She has always been there to support me every step of the way, and I'm grateful to have her to lean on. Unfortunately, she performs the 'wrong' kind of vibrational spectroscopy that doesn't even show up on a FTIR spectrum. Shane Steckman, my best friend for the last decade or so, has been there to help me decompress with really bad horror movies and buffalo chicken pizza. May my thesis be dedicated to your white Nike shorts that were lost due to grease leaking from the box of an XL buffalo chicken pizza. May their sacrifice not be in vain. Also, I would like to thank Katelin Omecinski and Emily Sample for teaching me the importance of being yourself.

Finally, I wouldn't be here, or at least be partially sane, without my partner in crime Casey Hansen. We met at Pitt and were able to bond over the annoyances of being a graduate student in STEM. Without her, I'm not sure I would have grown as a person and developed a level of acceptance of who I am. I'm glad to have her, especially since she puts up with my excessive buying of books and Funko Pops. Here's to our future together and our new adventures.

Of course I would never forget to mention my two cats, Turtle and Tiger. Their unwavering love not only lowered my blood pressure but gave me the emotional support needed to manage graduate school life. Tiger is a ham if there ever was a ham who was good at hamming it up. Turtle is the true Queen of the Seven Kingdoms, and I pledge my loyalty to her forever and always.

Figure 1: Turtle (left), who is not actually a turtle, and Tiger (right), whose personality resembles that of Garfield.

1.0 INTRODUCTION AND BACKGROUND

In this research investigation, the solvent dynamics of hydrides in aqueous solutions, hydride molten salts, and protonated molten salts are investigated to shed light on how they transfer hydrides and protons. Two-dimensional infrared (2D-IR) spectroscopy provides information that can elucidate solvent rearrangement of various hydrogen bonded environments. 2D-IR has been used broadly in investigations into amides,[2–5] H_2O,[6–10] and ionic liquids (ILs).[11–14] There is also a need to explore solvents that are candidates for hydride reduction reactions and proton conducting electrolytes.

The world energy economy is based mostly on burning fossil fuels. The emitted CO_2 threatens the climate at a global scale. This urgent problem can be addressed by efficiently converting the emitted CO_2 to liquid fuel or finding an alternative to current conventional energy production. One solution is carbon capture and utilization, in which emitted CO_2 will be captured and converted back to fuels using solar energy. This process would be carbon neutral. Another solution is to develop a hydrogen economy, where solar energy is used to make H_2 (water splitting), and the H_2 is utilized in fuel cells. Understanding the facilitation of hydrides and protons is crucial in optimizing the mediums and ultimately the efficiency of the process for both solutions.

On one hand, driving hydride transfers remains a key hurdle in reducing CO_2 to produce liquid fuels. There is currently a lack of efficiency in reducing CO_2 past formate into methanol. The poor CO_2 reduction efforts are plagued by high over-potentials, poor selectivities, and no strategic method on how to tune solvent compositions. On the other hand, hydrogen fuel cells are limited by the electrolyte that facilitates proton transfer to O_2, thus making chemical energy. The electrolyte is commonly an aqueous-based polymer with a low operation temperature, and the conductivity is proportional to the water content.

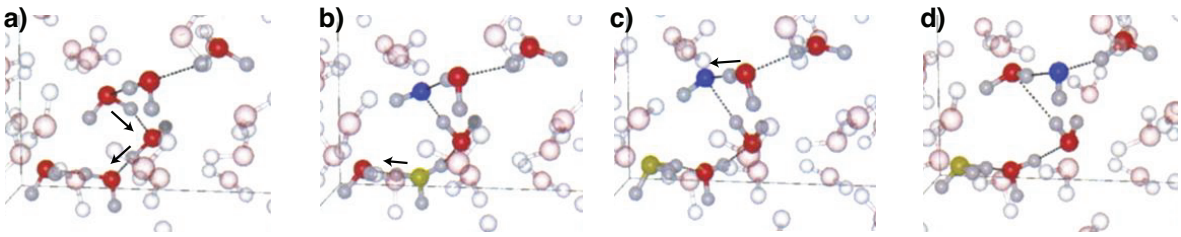

Figure 2: The autoionization of H_2O (oxygen $\rightarrow$ red) by solvent fluctuations activates proton transfer by surrounding H_2O molecules as the hydronium (oxygen $\rightarrow$ yellow) and hydroxide (oxygen $\rightarrow$ blue) ions move away each other. Hydrogen bonds are represented by dotted lines and the movement of protons are shown by arrows. The figure is taken and adapted from the work by Geissler *et al.* using Car-Parrinello *ab initio* molecular dynamics.[15]

The lack of a clear mechanistic picture that incorporates solvation dynamics for hydride and proton transport hinders the further development of chemical synthesis, industrial processing, CO_2 reduction, and proton conducting electrolytes.

Hydrogen bond fluctuations are critical to the autoionization of H_2O determined from Car-Parrinello *ab initio* molecular dynamics (Figure 2).[15] During the autoionization of H_2O, a proton is transferred to a nearby H_2O molecule forming a pair of hydronium (H_3O^+) and hydroxide (OH^-) ions. A series of proton transfers occurs as the H_3O^+ and OH^- move away from each other. The series of proton transfers along neighboring H_2O molecules is like a proton wire where proton transport occurs via a Grotthus mechanism.

Solvent fluctuations also play a crucial role in hydride transfer. Groenenboom *et al.*[16] show that the solvent plays a critical role in stabilizing an unstable intermediate in the reduction of CO_2 by BH_4^- in an aqueous solution (Figure 3). An unstable BH_3 intermediate is formed as a hydride is transferred to CO_2, forming formate. The intermediate is immediately stabilized by the addition of a single H_2O molecule. Upon forming $BH_3(H_2O)^-$, a proton from the bound H_2O transfers through a rearrangement of neighboring H_2O molecules, a proton wire.

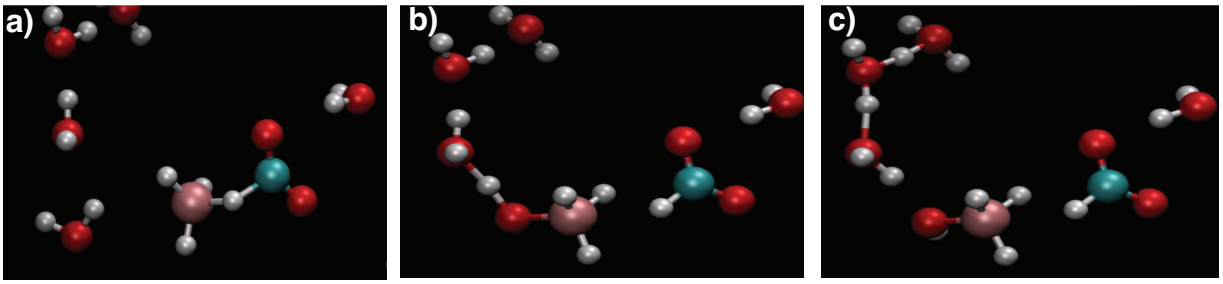

Figure 3: A H_2O molecule stabilizes the hydride donor as CO_2 is reduced to formate. a) The reduction reaction begins with BH_4^- forming a complex with CO_2. b) A hydride is then transferred to CO_2 and a neighboring H_2O forms a complex with an unstable BH_3 intermediate. c) A proton from the bound H_2O is transferred to neighboring water molecules through a proton wire. Using Car-Parrinello *ab initio* molecular dynamics, the snapshots are courtesy of Prof. Keith from a personal communication.[16]

Reorganization of the hydrogen bonding network is part of the transition state for both hydride and proton transfers. If the rearrangement does not occur, the reactant does not cross the reaction barrier. The proton or hydride retreats back to its initial position, *i.e.* the reactant well. The reorganization of hydrogen bonds is a necessary component for proton and hydride transfer.

Furthermore, a jump model is an influential picture for hydrogen bond rearrangement. From classical molecular dynamics simulations, H_2O undergoes large angle jumps (Figure 4).[17] During the switching process, there is a lengthening of the hydrogen bond followed by a rotation. During the rotation, the initial hydrogen bond breaks and a new hydrogen bond is formed with a neighboring/approaching H_2O molecule. While this model is useful, it should be noted that this picture captures only $\sim$ 60 % of the trajectories, and there are other trajectories and motions that contribute to the breaking and forming of hydrogen bonds.

Hydride and proton transfers are coupled to the local reorganization of surrounding H_2O molecules. Therefore, hydrogen bond breaking and forming dynamics are crucial to understand.[6–8,12,18,19] In this work, polarization and temperature-dependent 2D-IR are utilized for

a comprehensive picture of the solvent dynamics of hydrogen bonded environments through the coupling of vibrational modes, solvation dynamics, and separating structural and rotational motions. For hydrides, the antisymmetric stretch of BH_4^- will directly probe the rearrangement of dihydrogen bonds. First, the spectrum of BH_4^- needs to be assigned due to vibrational coupling of modes with vibrational energy states of mixed character. Following the peak assignments, the timescale of rearrangement of dihydrogen bonds between BH_4^- and H_2O will shed light on the decrease of the hydrolysis rate at high NaOH solutions. The solvation of BH_4^- will be further investigated in a non-aqueous environment where the hydrolysis is completely suppressed. For protonated molten salts, SCN^- will indirectly probe the hydrogen bonding network of protic ionic liquids. The rotational component of the solvation dynamics that SCN^- experiences in a protic ionic liquid (PIL) will be explored and compared with SCN^- in H_2O.

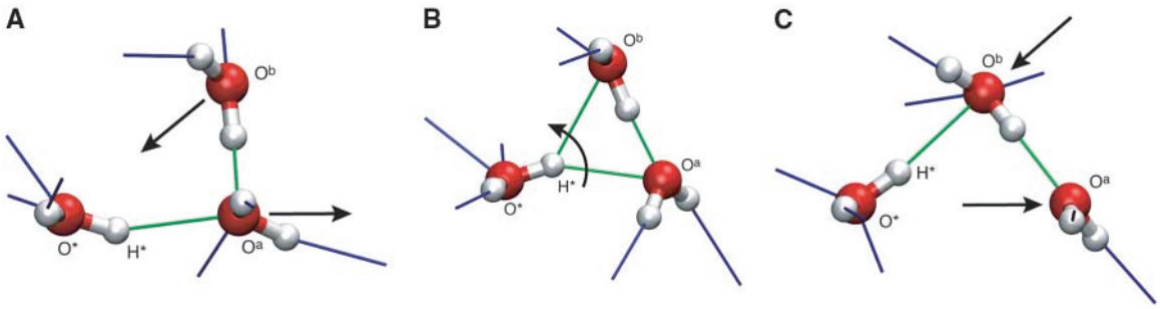

Figure 4: The hydrogen bond switching event occurs by a jump reorientation of one H_2O molecule to an incoming neighbor H_2O. a) First, there is a concerted lengthening of the hydrogen bond as a neighboring H_2O approaches. b) The H_2O undergoes a large angle jump breaking one hydrogen bond and c) forming another hydrogen bond as the previous hydrogen bonding partner moves away. Hydrogen bonds are represented by green lines and the blue lines are used to represent 3D-space, i.e.the x, y, and z coordinates. The black arrows indicate motions of the H_2O molecules. The figure is taken and adapted from the work by Laage and Hynes using classical molecular dynamic simulations.[17]

1.1 INTRODUCTION TO 2D-IR

1.1.1 2D-IR Spectra

2D-IR spectroscopy reveals frequency fluctuations that relate to fluctuations of the solvent around a vibrational probe. A 2D-IR spectrum consists of an initial vibrational frequency correlated to a final vibrational frequency after some time delay (Figure 5). The initial (ω_1) and final (ω_3) vibrational frequencies are plotted as the x and y components of a 2D-IR plot, respectively. A typical 2D-IR spectrum consists of 2 peaks. The ground state bleach, GSB, and stimulated emission, SE, peak stretches along the diagonal; and the excited state absorbance, ESA, peak shifts anharmonically from the diagonal peak.

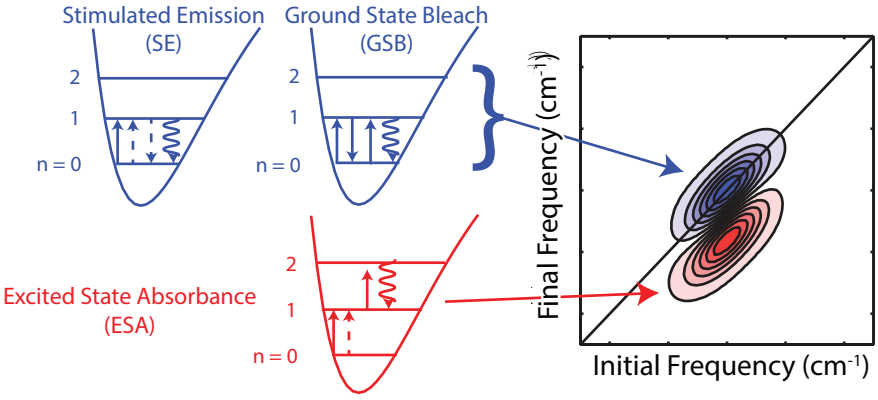

Figure 5: A typical 2D-IR spectrum consists of a negative, diagonal peak (blue) and a positive, off-diagonal peak (red). The diagonal peak corresponds to the ground state bleach (GSB) and stimulated emission (SE), and the off-diagonal peak corresponds to the excited state absorbance (ESA).

2D-IR is a 3rd order nonlinear spectroscopic technique that uses a 3 pulse sequence with an emitted photon echo response (Figure 6). The first pump pulse generates a coherence state, i.e. a linear superposition between the ground state and the first excited state. The second pump pulse generates a population state, either in the ground or first excited state. The third pulse, the probe, generates another coherence state in the first or second excited state. There is then a detected emitted field, known as the vibrational photon echo, that

heterodyne mixes with a local oscillator. In a pump-probe geometry, the probe is the local oscillator. The measured signal can be described as

$$S(t_{LO};t_1;t_2) \propto \int_0^\infty |E_{LO}(t_3 - t_{LO}) + E^{(3)}_{\text{sig}}(t_3;t_2;t_1)|^2 dt_3 \tag{1.1}$$

where $E_{\text{sig}}(t_3;t_2;t_1)$ is the emitted field signal, i.e. the vibrational photon echo, and $E_{LO}(t_3 - t_{LO})$ is the local oscillator, i.e. the probe. Since $E_{\text{sig}}(t_3;t_2;t_1)$ is small, we are only interested in the cross term, $2(E_{LO}(t_3 - t_{LO}) \times E^{(3)}_{\text{sig}}(t_3;t_2;t_1))$.

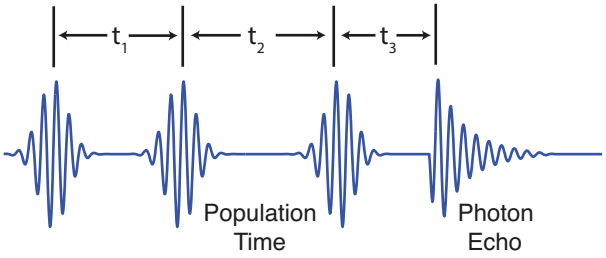

Figure 6: 2D-IR consists of a three pulse sequence that emits a photon echo response. The first coherence time, t_1 occurs between the two pump pulses, a population time, t_2, occurs between the second pump and the probe, and a second coherence time, t_3, occurs between the probe and emitted response.

1.1.2 Solvent Dynamics

By varying t_2, timescales of frequency fluctuations can be determined for a 2D-IR experiment. Molecules have different vibrational frequencies in different local environments, and a vibrational band is made up of many Lorentzians, where each Lorentzian has a 'natural linewidth.' (Figure 7 a). As t_2 increases, the solvent reorganizes around the molecule. At early t_2 times, the initial vibrational frequency of the molecule will be highly correlated to its final frequency, and the diagonal peak will be stretched along the diagonal (Figure 7 b). The initial solvent conditions will change very little around the molecule. As t_2 increases, the molecule will experience different solvent environments and lose the correlation between the initial and final frequencies (Figure 7 c). The loss in correlation causes the diagonal

peak to be more round as it loses its memory of its initial conditions (Figure 7 d). The random motions of molecules cause a random walk in frequency space, called spectral diffusion. From the change in shape of the spectra, a frequency fluctuation correlation function (FFCF) can be extracted by various methods, such as center line slope (CLS),[20–22] ellipticities,[23,24] nodal-slope,[25] and phase-slope,[24] to name a few.

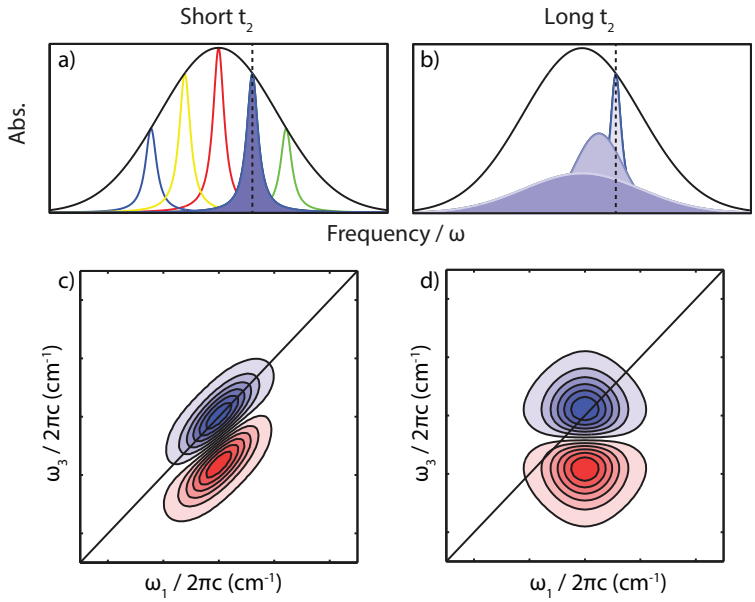

Figure 7: a) A linear vibrational band is composed of several Lorentzian bands. Each Lorentzian corresponds to the vibrational probe experiencing a different solvent environment. b) In a 2D-IR spectrum at an early t_2, the peak is stretched along the diagonal as the initial solvent conditions are highly correlated to the final conditions. c) As t_2 increases, the solvent around a vibrational probe will reorganize and the probe will experience different frequencies in the linear vibrational band. d) In a 2D-IR spectrum at a long t_2, the initial frequency is no longer correlated to the final frequency and the system is spectrally diffused.

Typically, spectral diffusion is treated as though spectral fluctuations in the vibrational frequency are independent of orientational motions. Therefore, the third order nonlinear response ($R^{(3)}(t_3, t_2, t_1)$ can be separated into two components

$$R^{(3)}(t_3, t_2, t_1) = R_{\mathrm{v}}(t_3, t_2, t_1) R_{\eta\gamma\beta\alpha}(t_3, t_2, t_1) \tag{1.2}$$

correlating to orientational motions, $R_{\eta\gamma\beta\alpha}(t_3, t_2, t_1)$ and structural fluctuations, $R_{\mathrm{v}}(t_3, t_2, t_1)$. The $R_{\mathrm{v}}(t_3, t_2, t_1)$ component captures spectral diffusion and is isotropic, i.e. all orientations of the transition dipole moment (μ) of the vibrational probe are weighted equally. The $R_{\eta\gamma\beta\alpha}(t_3, t_2, t_1)$ component affects the amplitude of the signal where η, γ, β, and α are the relative μ directions at each respective pulse, and the vibrational frequency is sensitive to the orientation of the transition dipole moment of the molecule, μ. In some cases, orientational motions may contribute to the overall spectral diffusion.

Based on the work by Kramer et al.,[26,27] the FFCF correlates to a product of structural and rotational motions. Therefore, there are two contributions to spectra diffusion: local structural changes of the solvent (structural spectral diffusion, SSD) and rotational motions of the molecule (reorientation-induced spectral diffusion, RISD). This theoretical framework was first developed to explain vibrational sum-frequency-generation spectroscopy.[28] In Chapter 6 and 7, the effect of RISD on the FFCF will be explored by probing SCN^- in a PIL.

1.2 2D-IR OF H_2O

Solvent reorganization timescales in H_2O relate to fluctuations of the hydrogen bonding networks, such as the breaking and forming of hydrogen bonds. Through a combined effort, the 2D-IR experiments give a physical timescale for the solvent fluctuations, and the molecular dynamics simulations are able to describe these timescales as specific motions in the solvent, i.e. the breaking and forming of hydrogen bonds. In Chapter 4-5, the breaking and forming of dihydrogen bonds between BH_4^- and H_2O are investigated.

2D-IR experiments on HOD in H_2O directly measures the hydrogen bond fluctuations. Isotope substitution is used to make a local mode to probe the local structural changes. Without isotope substitution (neat H_2O), the vibrations will be delocalized, and one would be probing vibrational energy transport, not local structural changes of the solvent. Overall, three timescales are extracted from the FFCF of HOD in H_2O: a fast librational motion, an intermediate time, and a slow timescale related to the breaking and forming of hydrogen bonds.[6] Similar results are determined for HOD in D_2O where the intermediate time (180 fs

in this experiment) relates to the vibration between the oxygen atoms of two hydrogen bonded partners.[7] In neat H_2O, vibrations are delocalized and energy redistribution occurs on a fast timescale.[29] Other isotope substitutions of H_2O have been investigated where the linear absorption lineshape of the OT stretch of HOT in H_2O is characterized in comparison to OH and OD stretches.[30]

Temperature dependent 2D-IR studies further investigate the activation energy of the breaking and forming of hydrogen bonds. Nicodemus *et al.* perform 2D-IR in the all parallel polarization on the OH stretch of HOD in D_2O, and using an Arrhenius model, an activation energy (E_a) for the hydrogen bond breaking and forming process is determined (3.6 kcal/mol).[9] At the magic angle, the E_a (6.1 kcal/mol) is $\sim$ 4 kT higher compared to the all parallel value, and they attribute the higher value due to different contributions of rotational motions.[10] These activation energies, however, are much higher than that determined from classical molecular dynamics simulations,[31] and both 2D-IR studies reveal an unrealistically fast barrier attempt rate ($\sim$ 2 fs). In Chapter 8, the unrealistically fast barrier attempt rates will be explored in terms of the entropy of activation. It should be noted that the experimental observable may not be exactly measuring the energy to break and form hydrogen bonds, and molecular dynamics are required to elucidate insight into what the 2D-IR experiments are observing in H_2O. Another issue is that the simulations, referenced above, appear to look like two states (switching between populations). The simulations are relying on observables from the temperature dependence of an absorption band with an isosbestic point which leaves out detailed dynamical information of the local structural environment.[32]

1.3 HYDRIDE DONORS

BH_4^- is a model system for insight in terms of a molecular understanding of the solvation of hydride donors in the condensed phase. Due to the small size and low computational cost, $ab-intio$ molecular dynamics are utilized to map the reaction pathway for the hydrogen evolution reaction (HER) of BH_4^- in H_2O[33] and explore the free energies associated with the reaction pathway of CO_2 reduction in an aqueous solution with $NaBH_4$.[16] BH_4^- is a viable IR

chromophore with two IR active modes: antisymmetric BH stretch (ν_3) and bend (ν_4). The solvent dynamics of BH_4^- in various solvents can be determined with 2D-IR. By probing the antisymmetric BH stretch as a local mode, the dihydrogen bond rearrangement timescale can be determined and previously has been on par with the hydrogen bond breaking and forming timescales in H_2O.[19] A combination of molecular dynamics (a molecular snapshot of the solvation environment) and solvaton dynamics (experimental timescales for the breaking and forming of dihydrogen bonds) crafts a comprehensive picture of the solvation of BH_4^- that can ultimately be transferred to other metal hydride derivatives. Though the fundamental science for each of these hydride derivatives is diverse, their overall mechanisms involve net hydride transfers. Therefore, insights on the solvent dynamics of hydride transfers for BH_4^- could be extrapolated to assist in engineering other metal hydride derivatives.

Over the past 70 years, BH_4^- has been exhaustively studied for its high hydrogen storage capacity and strong reduction potential. In the 1950's, the HER of BH_4^- in H_2O was of interest for producing H_2(g). In H_2O, every mole of $NaBH_4$ contains the potential to generate 4 moles of H_2(g)

$$NaBH_4(aq) + (2 + x)H_2O(l) \rightarrow NaBO_2 \cdot xH_2O + 4\,H_2(g) \tag{1.3}$$

where the half-reactions are

$$BH_4^-(aq) + 4OH^-(aq) \rightarrow BO_2^-(aq) + 2H_2O(l) + 4H + 4e^- \tag{1.4}$$

$$4\,H_2O(l) + 4H + 4e^- \rightarrow 4H_2(g) + 4OH^-(aq). \tag{1.5}$$

Different studies vary the metal counterion, Al,[34] Li,[35] and Na[36,37], to see an effect on the production and rate of H_2(g) generation.

Further studies, in the late 1950's and early 1960's, investigated the effect of pH and found that the decrease of the pH leads to a faster rate for the HER. Varying the pH leads to three rate constants that contribute to the overall rate for the BH_4^- HER: one based on $[H_3O^+]$, one for $[H_2O]$, and one for the concentration of a general acid, [HA].[38,39]

$$\frac{d[BH_4^-]}{dt} = -k_{H_3O^+}[H_3O^+][BH_4^-] - k_{H_2O}[H_2O][BH_4^-] - \sum_i k_{HA_i}[HA_i][BH_4^-] \tag{1.6}$$

Overall, the first step of the BH_4^- HER under acidic conditions is proposed as first-order with respect to the reactant. In terms of the pH, $k_{H3O^+}[BH_4^-]$ ($\sim 5 \times 10^6$ $s^{-1}M^{-1}$) is 10^{18} faster than $k_{H2O}[BH_4^-]$ ($\sim 5 \times 10^{-9}$ $s^{-1}M^{-1}$).[37–42] Therefore, in the absence of HA, the rate is dependent on the slow k_{H_2O}. In all studies, the respective rate constants fall into good agreement.

Despite broad agreement on the overall rate of reaction, there is disagreement over the elementary reaction steps. Based on isotope kinetic studies from the 1960's, the initial step is proposed as a loss of a H^- [40,42]

$$BH_4^- \rightarrow BH_3 + H^- \tag{1.7}$$

or an addition of a H^+ to BH_4^-.[43]

$$BH_4^- + H^+ \rightarrow BH_5 \tag{1.8}$$

Other hydroxyborohydride intermediates are proposed, such as $BH_3(OH)^-$, $BH_2(OH)_2^-$, and $BH(OH)_3^-$.[38,39,44–50] The most probable intermediate is $BH_3(OH)^-$ determined through ^{11}B-NMR; all subsequent reaction steps are very rapid with no evidence of other intermediates.[43] A comprehensive molecular dynamic study reports that the overall HER in H_2O is exothermic involving an initial BH_5 intermediate and a metastable hydroxyborohydride intermediate, BH_3OH^-.[33] Thus, the initial addition of a H^+ to BH_4^- is indicative of the strong dependence on pH in the classic rate studies. The other rates for the other hydroxyborohydride intermediates are exothermic steps that perhaps appear on an ultrafast time scale. Perhaps, the addition of acid lowers the activation for the initial rate determining step. Thus, manipulating the pH has a drastic effect on the HER.

Another interesting research path for BH_4^- is to be a model for the facilitation of CO_2 reduction. A quintessential challenge in CO_2 reduction chemistry is understanding how to selectively reduce CO_2 instead of protons. BH_4^- facilitates CO_2 reduction to formate in various aqueous solvents, but CO_2 reduction is in direct competition with the HER.[51]

$$BH_4^-(aq) + CO_2(g) + nH_2O(l) + \longrightarrow B_{(4-n)}(OH)_{(n+1)}(aq) + HCO_2(aq) + H^+(aq) \tag{1.9}$$

To improve the efficiency of CO_2 reduction, the competing HER of a hydride donor needs to be suppressed.[51] A possible solution to minimize the HER is using a water-miscible aprotic solvent, like an IL, with the addition of BH_4^-. ILs are good candidates for CO_2 reduction due to low vapor pressures allowing high operating temperatures,[52–54] high selectivity where ILs can be designed for to capture and reduce CO_2 through myriad combinations of anions and cations,[55–57] and high CO_2 solubility with efficient facilitation of CO_2 reduction.[58–60] Understanding solvent dynamics becomes crucial as the solvent molecules play a critical role in the stabilization of the $[BH_3{-}H{-}CO_2]^-$ intermediate, a molecular species that is found to be unstable in quantum chemistry calculations with just a dielectric continuum.[16]

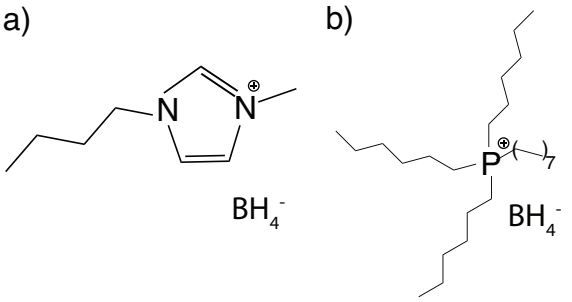

Figure 8: BH_4^- based ionic liquids are molten salts that consist of a contact pair of a BH_4^- anion and an aprotic cation, such as a) 1-butyl-3-methylimidazolium (BMIM) or b) tetradecyl(trihexyl)phosphonium ($P_{14,6,6,6}$).

A more direct approach of minimizing the HER involves using the novel BH_4^- based ionic liquids as a candidate for CO_2 reduction, where BH_4^- is the anion.[61] Currently, BH_4^- based ionic liquids are being studied for hydrogen storage applications, *i.e* jet fuel alternatives.[62,63] Two interesting subjects for CO_2 reduction involve the common 1-butyl-3-methylimidazolium (BMIM) cation and a bulky tetradecyl(trihexyl)phosphonium ($P_{14,6,6,6}$) cation (Figure 8). [BMIM][BH4] is a selective reducing agent,[64] while sterically hindered phosphonium ILs have been shown to be a good absorbent for CO_2.[65] Unfortunately, there is a current lack of molecular understanding for how the hydride behaves in these IL environments that inhibits their development as candidates for CO_2 reduction.

1.4 2D-IR OF ILS

Most ILs can be classified into two groups: aprotic and protic. Most of the current 2D-IR studies of ILs focus on aprotic ILs. The addition of a viable vibrational chromophore is a common approach at elucidating structural dynamics from aprotic ILs where the vibrational chromophore has a reasonable extinction coefficient (> 100 $M^{-1}cm^{-1}$) and its IR mode appears in a region with no strong solvent bands. 2D-IR experiments using SCN^- as a vibrational probe in imidazolium based ILs reveal that the nitrile stretch of SCN^- is a good reporter of the ion cage breaking and forming timescales.[11] and a good reporter on water-induced dynamical heterogeneity in ILs.[12] A further temperature dependent 2D-IR study extracts activation energies for motions experienced by SCN^- in a homogoulous series of imidazolium based ILs of varying alkyl chain length.[14] Other vibrational probes have also been used to probe solvation dynamics in ILs, such as methanol and CO_2. Kramer *et al.* showed that the reorientation motions of methanol in an imidazolium IL contribute to the spectral diffusion.[27] Also, the solvation dynamics of CO_2 absorbed in ILs are determined[13] and the development of a spectroscopic map to connect molecular dynamic simulations to 2D-IR experiments.[66–68] Current focus is on deep eutectic solvents that involve ILs and a hydrogen acceptor component, and the hydrogen bond breaking and forming timescales are affected by the heterogeneity of the mixture.[69,70]

1.5 PROTONATED MOLTEN SALTS

The other class of ILs, protic ionic liquids (PILs), are molten salts at room temperature composed of a Brønsted acid-base pair. The solvation dynamics of aprotic ionic liquids are well established and trend linearly with viscosity.[13,14,71] PILs have mainly been characterized by just bulk characteristics (viscosity, ion mobilities, molar volume, vapour pressure, *etc.*),[72–76] yet a more intriguing question is how a PIL facilitates proton transfer.

A PIL is formed through an acid-base neutralization reaction of a Brønsted acid (HA)

and Brønsted base (B) pair.

$$HA + B \longrightarrow HB^+ + A^- \tag{1.10}$$

The first ionic liquid synthesized was a PIL in 1914 by titrating nitric acid into a solution of ethyl-amine.[77] Typically, PILs are characterized by their ΔpK_a, which is the difference between the pK_a of the base and the pK_a of the acid.[78]

$$\Delta pK_a = pK_{a(\text{base})} - pK_{a(\text{acid})} \tag{1.11}$$

A high Δ pK_a (>10) indicates complete proton transfer, but a low ΔpK_a (<10) indicates that the acid does not fully dissociate and there is incomplete proton transfer. At lower ΔpK_as, neutral Brønsted acid (HA) and Brønsted base (B) molecules remain in solution along with their respective cation (HB^+) and anion (A^-) products.

Ethyl-ammonium nitrate (EAN) is a 'good' PIL, $\Delta pK_a = 10.93$, and an intriguing candidate to replace water as an electrolyte in hydrogen fuel cells.[79] Since EAN has a $\Delta pK_a >$ 10, it behaves as a free diffusion of ions.[72,74,75,78] There is also evidence that suggests EAN is a good CO_2 absorbent[80] (Henry's law constant for CO_2 in EAN is 20 MPa)[81] and EAN has a low vapor pressure, an advantageous characteristic of ILs.[82] In comparing EAN to H_2O, far-IR spectroscopy indicates that the hydrogen bond strength is similar to that of H_2O,[83] and IR-pump IR-probe spectroscopy reveals a possible large jump angle indicative of a proton jump mechanism.[84] Hayes *et al.* discuss that EAN forms bifurcated hydrogen bonds, a three-centered hydrogen bond, due to how the nanostructure can accommodate them.[85]

The 3-D hydrogen bonding network of EAN includes charge dense (ammonium cation and nitrate anion) and charge depleted (alkyl chain) regions that lead to structural and dynamical heterogeneity.[86] In the last 10-15 years, the structural heterogeneity of ionic liquids has been shown experimentally using X-ray diffraction and neutron scattering.[87–89] Molecular dynamics with atomistic modeling show evidence of the heterogeneity of ILs that consist of short (polar regions) and long (alkyl chain) length scales.[89–92] The structural heterogeneity in ILs leads to dynamical heterogeneity. Rotational motions of methanol in an IL correlate to motions suggestive of interactions in stiff and soft environments where these regions are

classified by diffusive timescales, i.e. timescales are slower in the frictionally stiff region.[93,94] With 2D-IR, inorganic and organic azides report different timescales of structural reorganization in imidazolium salts, so this suggests that an azide is interacting with different structures of the ILs based on its relative size and properties.[95]

In Chapters 6 and 7, SCN^- is used to probe the structural and dynamical heterogeneity in EAN through a combination of polarization- and temperature-dependent 2D-IR experiments. This analytical method can then be used as a tool to help develop other PILs as candidates for proton conducting electrolytes.

1.6 SUMMARY

The research investigations in Chapters 4-7 are inter-related through the exploration of hydrogen bonding networks. There are two sub-categories: hydride transfer in H_2O (Chapters 4 and 5) and proton transfer in a molten salt (Chapters 6 and 7). The solvent dynamics of these hydrogen bonded environments are important to understand to have a full picture of the chemistry and physics in the condensed phase. The investigations follow three main themes: vibrational mode coupling, solvent dynamics, and separating rotational and structural motions from solvent fluctuations. Using polarization- and temperature-dependent 2D-IR, three different hydrogen bonding environments are investigated: hydrides in aqueous solutions, hydride molten salts, and protonated molten salts.

First, the investigation begins with the solvation dynamics of a common hydride donor, BH_4^-. The 2D-IR spectra of BH_4^- in various media (aqueous and non-aqueous) illustrate what can be understood with 2D-IR spectroscopy through interpretation of cross-peaks that correlate to inter- and intra-molecular coupling. Furthermore, the loss of correlation in frequency space is captured by the FFCF thus resulting in a timescale of the rearrangement of dihydrogen bonds around the hydride donor. By increasing the base concentration, a change in the timescale of solvent reorganization provides insight as to how the rate of the HER is suppressed. In Chapter 5, an investigation on the novel BH_4^- based ILs reveal the reorganizational timescale of the cations around the anion where the HER is completely

suppressed, *i.e.* in the absence of H_2O.

Next, we will investigate the PIL EAN through the use of a vibrational probe, SCN^-. Polarization- and temperature-dependent 2D-IR is used to investigate two motions that contribute to spectral diffusion: rotational (RISD) and structural (SSD). On one hand, polarization-dependent 2D-IR isolates the rotational and structural components that contribute to the loss of correlation in frequency space. On the other hand, temperature-dependent 2D-IR accesses an activation energy correlated to the rearrangement of hydrogen bonds around SCN^-. Thus, the activation energy can be further separated into rotational and structural components as well. As rotations are a key component to hydrogen bond switching in a jump model,[17] rotational component of SCN^- in EAN and in H_2O will assist in comparing the 3-D hydrogen bonding networks of the two solvents.

2.0 THEORY

In this chapter, we will build off of the overview of 2D-IR spectroscopy presented in Chapter 1. The theory in this section was initially laid out in detail by Hamm and Zanni.[96]

2.1 RESPONSE PATHWAYS

In 2D-IR, the macroscopic polarization ($P^{(3)}(t)$) is detected, and it can be described as a trace of the interaction between the transition dipole moment operator ($\hat{\mu}$) and the density matrix ($\hat{\rho}^{(3)}(t)$).

$$P^{(3)}(t) = Tr(\hat{\mu}\hat{\rho}^{(3)}(t)) \tag{2.1}$$

As a function of time, the macroscopic polarization changes based on the response of the molecule. $P^{(3)}(t)$, however, does not directly equal the third order non-linear response ($R^{(3)}(t_3, t_2, t_1)$ but is convoluted with the electric field of the laser pulses: pump 1 and 2 ($E_1(t - t_3 - t_2 - t_1)$ and $E_2(t - t_3 - t_2)$, respectively) and the probe ($E_3(t - t_3)$).

$$\begin{aligned} P^{(3)}(t) \propto \int_0^\infty dt_3 \int_0^\infty dt_2 \int_0^\infty dt_1 E_3(t - t_3) E_2(t - t_3 - t_2) \\ \times E_1(t - t_3 - t_2 - t_1) R^{(3)}(t_3, t_2, t_1) \end{aligned} \tag{2.2}$$

where t_1 is the first coherence time, t_2 is the population time, and t_3 is the second coherence time.

Using time-dependent perturbation theory and the Liouville-von Neumann equation, $R^{(3)}(t_3, t_2, t_1)$ can be written as nested commutators, where ρ (density matrix) can be written

as $|\psi\rangle\langle\psi|$.

$$R^{(3)}(t_3,t_2,t_1) \propto \int_0^\infty dt_3 \int_0^\infty dt_2 \int_0^\infty dt_1 \; i\langle \mu_3(t_3+t_2+t_1)[\mu_2(t_2+t_1), [\mu_1(t_1),[\mu_0(0),\rho(-\infty)]]]\rangle \tag{2.3}$$

The $E(t)$ can act on either side of the ρ, since each $E(t)$ also has a complex conjugate ($E^*(t)$). The interactions of laser pulses on the density matrix leads to different response pathways that contribute to the 2D-IR signal. Conventionally, interactions on the left side of the density matrix will be by $E(t)$ and interactions on the right hand side will be by $E^*(t)$.

For a single local mode, there are 6 unique possible pathways along with their complex conjugates. Looking at one of the response pathways, $R_1^{(3)}(t_3,t_2,t_1)$, the macroscopic polarization shows that there is one interaction ($E_1(t-t_3-t_2-t_1)$) on the left side of the ρ and two interactions ($E_2^*(t-t_3-t_2)$ and $E_3^*(t-t_3)$) on the right side of the ρ.

$$P_1^{(3)}(t) \propto \int_0^\infty dt_3 \int_0^\infty dt_2 \int_0^\infty dt_1 E_3^*(t-t_3)E_2^*(t-t_3-t_2) \times E_1(t-t_3-t_2-t_1)R_1^{(3)}(t_3,t_2,t_1) \tag{2.4}$$

Thus, $R_1^{(3)*}(t_3,t_2,t_1)$, the complex conjugate of $R_1^{(3)}(t_3,t_2,t_1)$, has one interaction on the right hand side of the ρ and two interactions on the left side of the ρ. $R_1^{(3)}(t_3,t_2,t_1)$ and its complex conjugate can be expanded in terms of the transition dipole moment at each interaction with the laser field.

$$R_1^{(3)}(t_3,t_2,t_1) \propto i\langle \mu_3\mu_1\rho(-\infty)\mu_0\mu_2\rangle \tag{2.5}$$

$$R_1^{(3)*}(t_3,t_2,t_1) \propto i\langle \mu_2\mu_0\rho(-\infty)\mu_1\mu_3\rangle \tag{2.6}$$

Double-sided Feynman diagrams are a useful tool to represent the response pathways (Figure 9). A solid arrow represents an interaction between the density matrix and each pulse. The interactions walk up and down the vibrational energy ladder experiencing the first and second excited state manifolds. An arrow towards the ρ represents an interaction with the $E(t)$ that excites ρ, and an arrow away from the ρ represents an interaction with

the $E(t)$ that de-excites ρ. The emitted vibrational photon echo is represented as a dashed arrow away from the ρ.

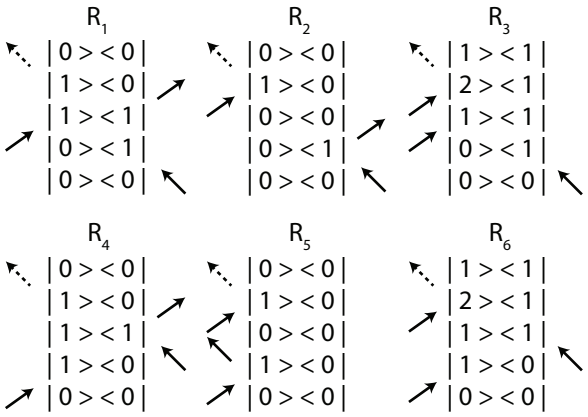

Figure 9: A total of 3 rephasing ($R_1^{(3)}$ (t_3, t_2, t_1), $R_2^{(3)}(t_3, t_2, t_1)$, and $R_3^{(3)}(t_3, t_2, t_1)$) and non-rephasing ($R_4^{(3)}(t_3, t_2, t_1)$, $R_5^{(3)}(t_3, t_2, t_1)$, and $R_6^{(3)}(t_3, t_2, t_1)$) pathways contribute to the 2D-IR spectra for a single oscillator. The Feynman diagrams help visualize the pathways showing interactions (arrow) up or down the vibrational energy ladder on both sides of the density matrix. The emitted photon echo response is represented by a dashed arrow. Each pathway has a complex conjugate.

$R_1^{(3)}(t_3, t_2, t_1)$ shows a response pathway for the stimulated emission (SE). The first pulse interacts to the right of the density matrix generating a coherence state in the first excited state ($\rho = |0\rangle\langle 1|$) at t_1. Another interaction with the density matrix (on the left side) causes a population state in the first excited state ($\rho = |1\rangle\langle 1|$). At t_3, the probe interacts to the right hand side of the density matrix generating a different coherence state as that during t_1 followed by the emitted vibrational photon echo. Overall, expanding the nested commutators in $R^{(3)}(t_3, t_2, t_1)$ reveals 4 pathways accessing the first vibrational excited state ($R_1^{(3)}(t_3, t_2, t_1)$, $R_2^{(3)}(t_3, t_2, t_1)$, $R_4^{(3)}(t_3, t_2, t_1)$, and $R_5^{(3)}(t_3, t_2, t_1)$) while two other pathways access the second vibrational excited state ($R_3^{(3)}(t_3, t_2, t_1)$, and $R_6^{(3)}(t_3, t_2, t_1)$). A similar analysis can be performed on the other 5 pathways for a single oscillator system.

Both $R_1^{(3)}(t_3, t_2, t_1)$ and $R_4^{(3)}(t_3, t_2, t_1)$ correlate to the SE, but these pathways can be further separated as rephasing and non-rephasing, respectively (Figure 9). A rephasing

pathway ($R_1^{(3)}(t_3,t_2,t_1)$, $R_2^{(3)}(t_3,t_2,t_1)$, and $R_3^{(3)}(t_3,t_2,t_1)$) has a different coherence during t_1 than t_3, and a non-rephasing pathway ($R_4^{(3)}(t_3,t_2,t_1)$,$R_5^{(3)}(t_3,t_2,t_1)$, and $R_6^{(3)}(t_3,t_2,t_1)$) has the same coherence state during t_1 and t_3. Similar to the SE, the ground state bleach ($R_2^{(3)}(t_3,t_2,t_1)$, $R_5^{(3)}(t_3,t_2,t_1)$) and the excited state absorption ($R_3^{(3)}(t_3,t_2,t_1)$, $R_6^{(3)}(t_3,t_2,t_1)$) consists of rephasing and non-rephasing pathways. The double-sided Feynman diagrams can help visualize a more complicated system where two or more vibrations are coupled.

2.2 ASSIGNING CROSSPEAKS

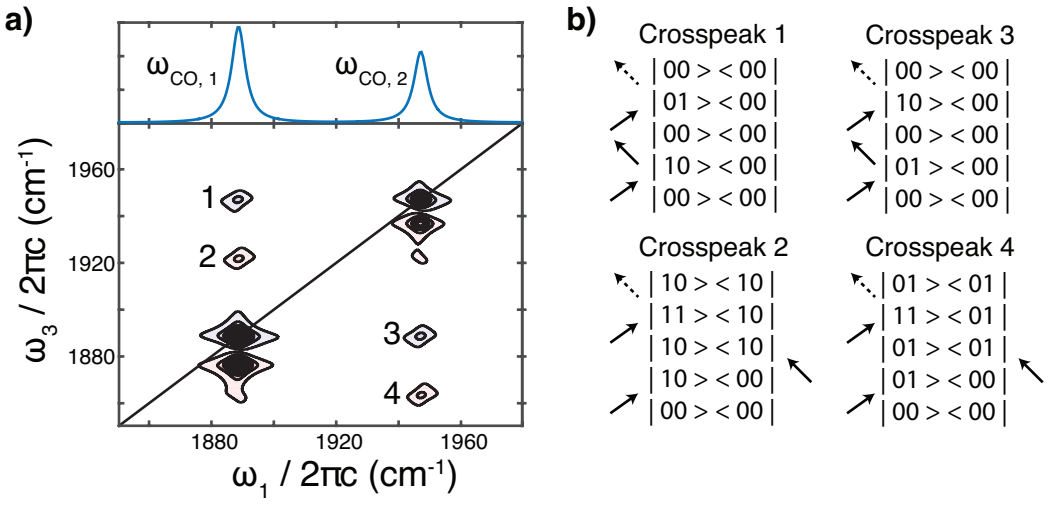

Figure 10: A simulated 2D-IR spectrum is constructed of two coupled vibrations ($\omega_{\mathrm{CO,\,1}}$ and $\omega_{\mathrm{CO,\,2}}$) through response function formalism. The coupling is reflective of two C=O modes in a Rh complex.[96] a) The linear spectrum shows two independent vibrational modes ($\omega_{\mathrm{CO,\,1}}$ and $\omega_{\mathrm{CO,\,2}}$), and the 2D-IR spectrum shows 4 crosspeaks indicating coupling between the two vibrational modes. b) Each crosspeak consists of a unique response pathway. The density matrix is written to include both vibrations ($|\omega_{\mathrm{CO,\,1}}\omega_{\mathrm{CO,\,2}}\rangle\ \langle\omega_{\mathrm{CO,\,1}}\omega_{\mathrm{CO,\,2}}|$) and shown here are the rephasing pathways where there are also non-rephasing pathways that contribute to the signal.

Where 2D-NMR shows the coupling between spins, coupled vibrations show up as crosspeaks in a 2D-IR spectrum. Crosspeaks can correlate to chemical reactions,[97] conformational changes,[98] and vibrational energy transfer.[99] For example, in the case for two C=O modes in a Rh complex, the normal modes are coupled due to π backbonding into the d-orbitals of Rh.

A new term needs to be added to the Hamiltonian to account for the coupling of two local modes (ω_a and ω_b). The Hamiltonian is expressed in terms of raising ($b^\dagger$) and lowering (b) operators. The first two terms are the time-independent Hamiltonian for each local mode. The second term includes the coupling term needed to model crosspeaks for ω_a and ω_b where β is the coupling constant. The last two terms are to account for the ESA where Δ is the local mode's anharmonic shift.

$$\begin{aligned} H =& \hbar\omega_a(b_a^\dagger b_a + \frac{1}{2}) + \hbar\omega_b(b_b^\dagger b_b + \frac{1}{2}) + \beta_{ab}(b_a^\dagger b_b + b_b^\dagger b_a) \\ & - \frac{\Delta_a}{2} b_a^\dagger b_a^\dagger b_a b_a - \frac{\Delta_b}{2} b_b^\dagger b_b^\dagger b_b b_b \end{aligned} \tag{2.7}$$

Four crosspeaks appear when simulating the 2D-IR spectrum of two coupled vibrations with response function formalism (Figure 10a). A crosspeak has a different ω_1 than ω_3. For crosspeak 1, the local mode is initially excited at $\omega_{\mathrm{CO,\,1}}$ during t_1 and excited at $\omega_{\mathrm{CO,\,2}}$ during t_3.

The response pathways show how the vibrational energy is transferred between coupled vibrations (Figure 10b). The response pathway of crosspeak 1 consists of a first coherence state of $|1\ 0\rangle\langle 0\ 0|$ ($\omega_1 \rightarrow\ \omega_{\mathrm{CO,\,1}}$) and a second coherence state of $|0\ 1\rangle\langle 0\ 0|$ ($\omega_3 \rightarrow\ \omega_{\mathrm{CO,\,2}}$). Crosspeak 1 is negative with a population state in the ground state of both $\omega_{\mathrm{CO,\,1}}$ and $\omega_{\mathrm{CO,\,2}}$. The corresponding positive peak (crosspeak 2) consists of the second probe interacting on the right side of the ρ that generates a population state in the first excited manifold for $\omega_{\mathrm{CO,\,1}}$ ($|1\ 0\rangle\langle 1\ 0|$). This analysis can be adapted to more complicated systems to assist in assigning multiple crosspeaks in a 2D-IR spectrum, like in Chapter 4 and 5 where three coupled vibrational modes of BH_4^- are investigated.

2.3 FREQUENCY FLUCTUATION CORRELATION FUNCTION

Initially used to describe the dephasing in NMR, Kubo's stochastic theory of lineshapes describes a semiclassical theory of dephasing.[100] In this limit, the solvent is treated classically and the vibrational probe is treated quantum mechanically. Solvent fluctuations compress and stretch the potential of the vibrational probe modulating the vibrational frequency. Thus, the time-dependent frequency of the vibrational probe can be expressed with two terms: a time independent average frequency (ω_{01}) and a time dependent fluctuating component ($\delta\omega(t)$).

$$\omega_{01}(t) = \omega_{01} + \delta\omega_{01}(t) \tag{2.8}$$

As time progresses, the vibrational frequency changes as the solvent environment around the molecule evolves. Over a time trajectory, the instantaneous frequency for a single molecule fluctuates around its mean value following Gaussian statistics, i.e. the distribution of frequencies is Gaussian. Thus, the oscillation period for a single molecule changes in time due to the instantaneous frequency changing. For an experiment, we will be looking at an ensemble average of the time trajectory of many molecules. At an early time, the molecules will be in phase with each other and slowly become out of phase (dephase) at longer times.

Based on this idea of dephasing, an analytical solution can describe the frequency fluctuation correlation function, FFCF. First, the time evolution of the density matrix of a single molecule can be written at the first coherence state as

$$\frac{d}{dt}\rho_{01}(t) = -i\omega_{01}(t)\rho_{01}(t). \tag{2.9}$$

For simplicity, we will initially ignore the interactions with the electric field and with the dephasing term. Therefore, we can rewrite the element of the density matrix for the coherence state as

$$\rho_{01}(t) \propto e^{-i\omega_{01}t}. \tag{2.10}$$

In our experiment, however, we have a laser focused on a large amount of molecules all in slightly different solvent environments. Therefore, we need to include Equation 2.8, where

there is a component to account for the random fluctuations in the vibrational frequency, but with a time average, this term vanishes ($\langle \delta\omega_{01} \rangle = 0$). The density matrix can now be expressed as

$$\rho_{01}(t) \propto e^{-i\omega_{01}t} \langle e^{-i\int_0^\infty \delta\omega_{01}(\tau)d\tau} \rangle \tag{2.11}$$

where the second term of this equation ($\langle e^{-i\int_0^\infty \delta\omega_{01}(\tau)d\tau} \rangle$) is the phenomenological treatment of dephasing (e^{-t/T_2}). The dephasing time (T_2) is expressed in terms of the pure dephasing time (T_2^*), the population relaxation time (T_1), and the orientational relaxation time (T_{or}).

$$\frac{1}{T_2} = \frac{1}{2T_1} + \frac{1}{T_2^*} + \frac{1}{3T_{or}} \tag{2.12}$$

Unfortunately, Equation 2.11 can be complicated to work with. If the fluctuations follow Gaussian statistics, then we can reorder the ensemble average into a more 'user-friendly' term using a cumulant expansion. First, using a more familiar mathematical series, an average of an exponential can be expressed in terms of x using a power series.

$$\langle e^{-ikx} \rangle = \sum_{n=0}^{\infty} \frac{(-ik)^n}{n!} \langle x^n \rangle \tag{2.13}$$

The same exponential average can be expanded in terms of central moments of the distribution that are identified as the cumulants.

$$\langle e^{-ikx} \rangle = \sum_{n=0}^{\infty} \frac{(-ik)^n}{n!} \langle (x - x_0)^n \rangle \tag{2.14}$$

Expanding the cumulant out to the first three terms, we see that the first cumulant is the mean,

$$c_1(x) = \langle x \rangle \tag{2.15}$$

the second cumulant is the variance,

$$c_1(x) = \langle x^2 \rangle - \langle x \rangle^2 \tag{2.16}$$

and the third cumulant is the skewness.

$$c_1(x) = \langle x^3 \rangle - \langle 3x \rangle \langle x^2 \rangle + 2\langle x \rangle^3 \tag{2.17}$$

The second term in Equation 2.11 can be expanded out in terms of $\delta\omega_{01}$. Gaussian statistics implies that higher order cumulants are zero. Thus, for a Gaussian distribution, we can truncate the cumulant expansion at the second order.

$$\langle e^{-i\int_0^t \omega_{01}(\tau)d\tau}\rangle = 1 - i\int_0^t d\tau\delta\omega_{01} - \frac{1}{2}\int_0^t\int_0^{\tau'} d\tau' d\tau''\langle\delta\omega_{01}(\tau'')\delta\omega_{01}(0)\rangle \tag{2.18}$$

Defining $\langle e^{-i\int_0^t \omega_{01}(\tau)d\tau}\rangle$ as $e^{g(t)}$, the equation can also be rewritten in an 'easier to digest' form.

$$\langle e^{-i\int_0^t \omega_{01}(\tau)d\tau}\rangle = 1 - g_1(t) - \frac{1}{2}g_2(t). \tag{2.19}$$

The second term, $g_1(t)$, vanishes due to taking the ensemble average of the random frequency fluctuations ($\langle\delta\omega_{01}\rangle = 0$). Therefore, the leading term is $g_2(t)$, and it is the lineshape function for the FFCF.

Kubo introduced an exponential ansatz to represent the FFCF

$$\langle\delta\omega_{01}(\tau)\delta\omega_{01}(0)\rangle = \Delta\omega^2 e^{-t/\tau_c} \tag{2.20}$$

where $\Delta\omega^2$ is the frequency fluctuation amplitude and τ_c is the correlation time of frequency fluctuations. The Kubo lineshape function is revealed by integrating Equation 2.20 twice.

$$g(t) = \Delta\omega^2\tau_c^2[e^{-t/\tau_c} + \frac{t}{\tau_c} - 1] \tag{2.21}$$

The linshape function can be discussed with respect to three limits: 1) slow modulation, 2) fast modulation, and 3) a convolution of 1 and 2.

In the fast modulation limit ($\Delta\omega\cdot\tau_c << 1$), frequency fluctuations are small and/or very rapid. The lineshape function can be expressed as a delta function

$$g(t) = \Delta\omega^2\tau_c t \rightarrow t/T_2^* \tag{2.22}$$

where T_2^* is the pure dephasing time ($\Delta\omega\tau_c$). The absorption lineshape in this limit is a Lorentzian

$$A(\omega) \propto \Re\int_0^\infty e^{-(\omega-\omega_{01})}e^{-g(t)} \propto \frac{1/T_2^*}{(\omega-\omega_{01})^2 + 1/T_2^{*2}} \tag{2.23}$$

where g(t) is defined in Equation 2.22. Since T_2^* is defined as $(\Delta\omega\tau_c)^{-1}$, the fast modulation limit has a fast time resulting in a linewidth that is narrower than the distribution of

frequencies. Therefore, this limit is the homogenous limit. Thus, the timescale of frequency fluctuations is in the motionally narrowing limit.

In the slow modulation limit ($\Delta\omega \cdot \tau_c >> 1$), frequency fluctuations occur on a slower timescale than the the time needed to resolve the frequency difference $\Delta\omega$ as being a different frequency. The lineshape function can be reduced to

$$g(t) = \frac{\Delta\omega^2}{2}t^2 \tag{2.24}$$

where the FFCF is approximated as the distribution of frequencies, $\Delta\omega^2$. The lineshape in this limit results in an absorption is a Gaussian.

$$A(\omega) \propto \Re \int_0^\infty e^{-(\omega-\omega_{01})} e^{-g(t)} \propto e^{-\frac{(\omega-\omega_{01})^2}{2\Delta\omega^2}} \tag{2.25}$$

This limit is in the inhomogenous limit.

There may be systems where the FFCF decays as a multi-exponential

$$g(t) = \frac{t}{T_2^*} + \frac{\Delta\omega^2}{2}t^2 \tag{2.26}$$

that consists of contributions from both the fast and slow modulation limit (Equations 2.22 and 2.24). The absorption for this lineshape function is a Voigt profile that is a convolution of a Lorentzian (fast modulation) and a Gaussian (slow modulation) lineshape. An experimentally extracted FFCF may expand beyond these three limiting cases: 1) fast modulation, 2) slow modulation, and 3) a convolution of these two limits. Equation 2.21, however, is valid along all dynamical regimes.

2.4 EXTRACTING THE FFCF

The change in shape of the 2D spectra can be quantified by various methods – ellipticities[23,24], center-line slope (CLS)[20–22], nodal-slope[25], and phase-slope[24]. In this work, CLS is used. Building off the previous discussion of the FFCF, the quantities from these various methods will be shown to be equal to the normalized FFCF in the limit of inhomogeneous broadening. The focus will be directed on two of the above methods: ellipticity and CLS.

For the pathways that contribute to the GSB+SE peak, the third order response function ($R^{(3)}_{0\to1}(\omega_1,\omega_3,t_2)$) can be described in terms of the FFCF ($C_1(t)$) as shown as the leading term in Equation 2.18.[20,23]

$$R^{(3)}_{0\to1}(\omega_1,\omega_3,t_2) = \frac{4\pi}{(C_1(0)^2 - C_1(t_2)^2)^{1/2}} \times \exp(-\frac{C_1(0)\omega_1^2 - 2C_1(t_2)\omega_1\omega_3 + C_1(0)\omega_3^2}{2(C_1(0)^2 - C_1(t_2)^2)}) \quad (2.27)$$

Equation 2.27 can be expanded in terms of 2D-diagonals that are ellipses tilted at 45°.[23] Therefore, the 2D-IR diagonal and off-diagonal peaks are approximately equal to 2D-Gaussians. A combination of two 2D-Gaussian functions can be used to fit the diagonal (GSB+SE) and off-diagonal (ESA) peaks at a given population time (t_2),

$$\begin{aligned} G(x,y) =& A(e^{-((x-x_0)+(y-y_0))^2/2\sigma_D^2} \times e^{-((y-y_0)-(x-x_0))^2/2\sigma_A^2} \\ &+ e^{-((x-x_0-\Delta)+(y-y_0-\Delta)^2/2\sigma_D^2} \times e^{-((y-y_0-\Delta)-(x-x_0-\Delta))^2/2\sigma_A^2}) \end{aligned} \quad (2.28)$$

where A is the amplitude, x_0 and y_0 are the center frequencies for x and y, respectively, Δ is the anharmonic shift, $2\sqrt{2\ln 2}\sigma_D$ is the full width at half max along x, and $2\sqrt{2\ln 2}\sigma_A$ is the full width at half max along y. Therefore, the inhomogeneous broadening of the diagonal peak is σ_D, and the homogenous broadening component of the diagonal peak is σ_A. As a function of t_2, the ellipticity value (ϵ) is then determined by the σ_D and σ_A fits.

$$\epsilon = \frac{\sigma_D^2 - \sigma_A^2}{\sigma_D^2 + \sigma_A^2} \quad (2.29)$$

Ellipticity of the 2D-IR peaks is the normalized FFCF[23,24] and is dependent on changes at the FWHM, i.e. wings of the spectra.

For this work, CLS is used and is weighted towards the center of the peak. For extracting the FFCF with CLS, pump-probe slices are taken along ω_1. For the slice where the max

signal is at $\omega_1 = \omega_3 = \omega_{\text{center}}$, the $R^{(3)}_{0\to1}(\omega_1, \omega_3, t_2)$ from Equation 2.27 simplifies to a Gaussian lineshape.

$$R^{(3)}_{0\to1}(\omega_{\text{center}}, \omega_{\text{center}}, t_2) = \frac{4\pi}{(C_1(0)^2 - C_1(t_2)^2)^{1/2}} \times \exp(-\frac{C_1(0)\omega^2_{\text{center}}}{2(C_1(0)^2 - C_1(t_2)^2)}) \tag{2.30}$$

If the maximum is not at $\omega_1 = \omega_3$, then a δ term is necessary to include that describes the ω_1 of a specific slice of the 2D spectrum for $R^{(3)}_{0\to1}(\omega_1, \omega_3, t_2)$.

$$R^{(3)}_{0\to1}(\delta, \omega_3, t_2) = \frac{4\pi}{(C_1(0)^2 - C_1(t_2)^2)^{1/2}} \times \exp(-\frac{C_1(0)\delta^2 - 2C_1(t_2)\delta\omega_3 + C_1(0)\omega^2_3}{2(C_1(0)^2 - C_1(t_2)^2)}) \tag{2.31}$$

The first derivative of the above equation can be taken to determine the frequency coordinate that has the max signal for a specific slice along ω_1.

$$\frac{dR^{(3)}_{0\to1}(\delta, \omega_3, t_2)}{d\omega_1} = \frac{C_1(t_2)}{C_1(0)} = \frac{\langle\delta\omega_{01}(\tau'')\delta\omega_{01}(0)\rangle}{\langle\delta\omega_{01}(0)\delta\omega_{01}(0)\rangle} \tag{2.32}$$

Therefore, in the inhomogeneous limit, the CLS is the normalized FFCF.

In this work, the normalized FFCF determined from the CLS analysis will be represented as $c_2(t_2)$. By taking pump-probe slices (or cuts) along ω_1, a CLS value for a specific 2D-IR spectrum is determined. For a 2D-IR spectrum with a diagonal and off-diagonal peak, the pump-probe slice is fit to a function (a Gaussian, a Lorentzian, or a Voigt profile) to account for the GSB+SE and the ESA. The frequency at the peak minimum (for the GSB+SE) is plotted against the ω_1 for the given slice. A linear fit is performed on a series of peak minimums as a function of ω_1, where the slope of the linear fit is the CLS value. Plotting the CLS values as a function of t_2, an exponential function can be used to extract out the frequency fluctuation amplitudes and correlation times of frequency fluctuations. The error in the measurements are determined by propagating the uncertainty through the peak minimum determination, the slope fit, and the correlation fitting.

3.0 EXPERIMENTAL METHODS

3.1 PROTIC IONIC LIQUID SYNTHESIS

Ethyl-ammonium nitrate (EAN) is synthesized by a Brønsted acid-base neutralization reaction.[75] For this reaction, an equimolar amount of acid (nitric acid) and base (ethylamine) concentration are needed. To ensure the reaction is complete, however, one should include a 5% excess of the base.

The reaction is extremely exothermic. Before adding acid, the temperature of the base solution needs to be equilibrated in a dry ice-acetone bath for 5 minutes. Also, the amount of base should not exceed 10-20% of the volume of the round bottom flask. This is a safety precaution to increase the surface area/sample volume ratio to assist with cooling down the exothermic reaction.

Acid is added drop-wise into the base solution that is contained in a dry ice-acetone bath inside of a chemical hood. Before adding the acid, turn on the high-powered fan in the hood. Only a few drops of acid should be added at a time. Wait a few minutes between drops until the visible vapor from the reaction dissipates. Once all the acid is added, allow the mixture to stir in the hood for 1-2 hours. The sample needs to be dried by a vacuum pump (10 μTorr) that incorporates a liquid nitrogen cooled vacuum trap.

The final product can be characterized by FTIR. For example, EAN will have a strong NH and nitrate stretch from the ammonium cation and nitrate anion, respectively. NMR and Mass Spectrometry could also be used for a complimentary characterization.

3.2 SAMPLE PREPARATION

3.2.1 Aqueous BH_4^-

As discussed in Chapter 1, BH_4^- decomposes rapidly in aqueous solutions with H_3O^+ present due to an increased rate of the hydrogen evolution reaction (HER). The stability at a specific pH should be determined before running a 2D-IR experiment. If the HER occurs during an experiment, then gas bubbles will form in the sample window and scattering of the mid-IR pulses will decrease the S/N. Time-dependent FTIR studies at different pH values can determine the stability of the sample during the 2D-IR experiment.

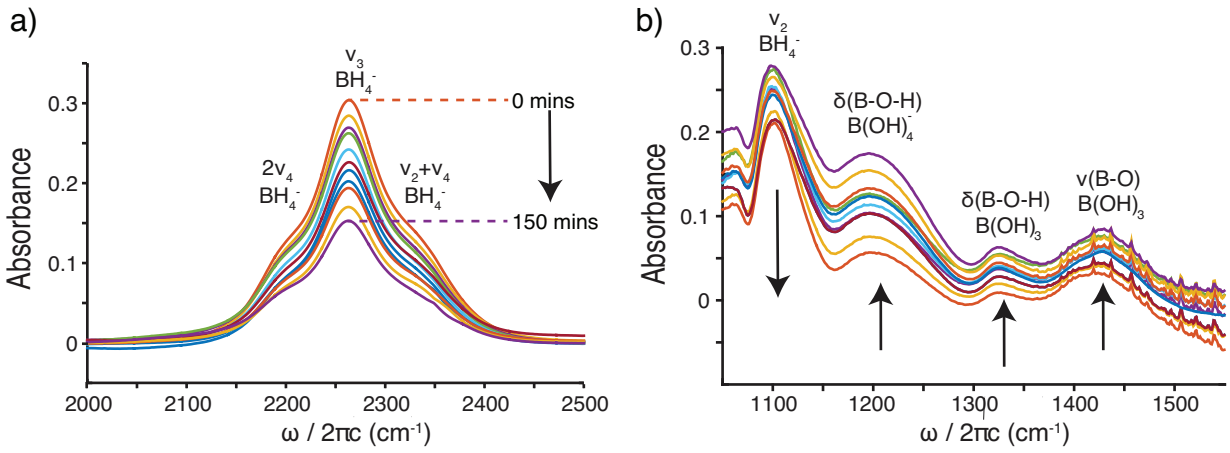

Figure 11: The BH_4^- vibrational modes can be monitored to determine the overall HER rate. a) At a pH of 9.5, the complex antisymmetric stretch (ν_3) of BH_4^- decreases as it self-hydrolyzes at room temperature. b) Deformation (δ) and stretching (ν) modes of borate appear as the HER occurs. The arrows correlate to an increase ($\uparrow$) or a decrease ($\downarrow$) in absorbance for a respective vibrational transistion.

For example, at a slightly basic solution (<0.1 M NaOH $\rightarrow \sim$ 9.5 pH), the HER occurs on a timescale of hours as the antisymmetric BH stretch (ν_3) and bend (ν_4) of BH_4^- decrease corresponding to a lower [BH_4^-]. The pH was determined by a calibrated SPR Scientific Direct basic pH meter & kit (840088). Also, vibrational modes corresponding to borate derivatives appear corresponding to products of the HER (Figure 11). At this pH, a 2D-IR

experiment may only be viable in an 1 hour time window as approximately 10% of the sample decomposes. Around the three hour time window, almost half the sample decomposes and bubbles are prevalent in the sample window. Therefore, at least 0.1 M of NaOH (> 9.5 pH) is needed for longer stability of BH_4^- during a 2D-IR experiment.

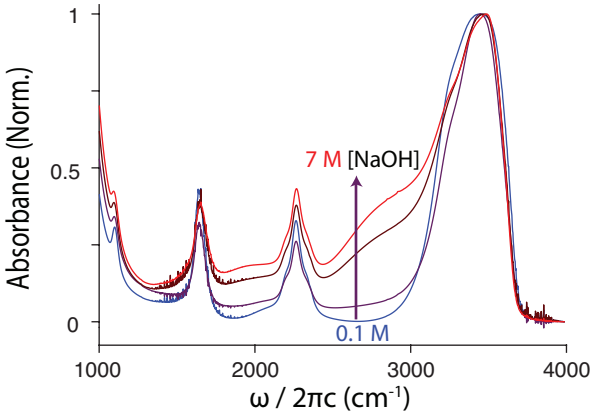

Figure 12: The absorbance of the mid-IR spectrum increases significantly with increasing [NaOH]. This is most notable in the region between 2000 and 3000 cm^{-1}. FTIR are obtained of 3 M BH_4^- in varying concentrations of NaOH with a pathlength of ∼1 μm: 0.1, 1, 5, and 7 M (blue to red).

Also, high concentrations of $NaBH_4$ (3 M) are used in the 2D-IR experiments. Different approaches are necessary to ensure the overall absorbance of the ν_3 BH stretch is below 0.4. Above 0.4, distortions will occur in a 2D-IR spectrum due to the sample reabsorption and non-linear effects with the detector. On one hand, OH^- absorbs broadly in the mid-IR (Figure 12). This effect increases as a function of the NaOH concentration. If any pathlength is used at elevated [NaOH] (> 1 M), then the solvent background saturates the detector. Therefore, no teflon spacer is used corresponding to an approximate pathlength of ∼1 μm. On the other hand, BH_4^- is a weaker chromophore (∼ 300 $M^{-1}cm^{-1}$ for the ν_3 mode) than other vibrational probes, like SCN^- or CO_2 (∼ 1000 $M^{-1}cm^{-1}$). Since the pathlength is small, a high concentration of BH_4^- (3 M) is necessary for an absorbance of ∼ 0.1 while keeping the overall absorbance (solvent background + ν_3 mode of BH_4^-) below 0.4.

3.2.2 Ionic Liquids

To ensure the ionic liquids (ILs) are kept dry, the samples are prepared in a glove bag under an inert N_2 atmosphere. All necessary materials are placed in a plastic glove bag equipped with a N_2 gas inlet: brass cell holder or Harrick cell, two CaF_2 windows, teflon spacer, and a vacuum sealed container containing the IL. The glove bag is purged with N_2 at least three times to minimize the amount of atmospheric water in the bag. Then, a few μL of the given IL is sandwiched between the two windows with the desired Teflon spacer in a spectroscopy cell (brass cell holder or Harrick cell).

3.3 FTIR

The FTIR spectra are obtained using a Nicolet 6700 FTIR (ThermoFisher Scientific). The instrument is equipped with a nitrogen purge to eliminate atmospheric bands. The spectra are baselined to zero using the region at $3950 - 4000\ \text{cm}^{-1}$. The sample FTIR spectra are normalized to the respective solvent FTIR spectra and subtracted.

The water content of each IL is determined with FTIR before the respective 2D-IR experiment. The OH stretch of H_2O at approximately $3500\ \text{cm}^{-1}$ is used to estimate the water contamination in each IL.[11] The optical density of the OH stretch is converted into a concentration assuming the molar extinction coefficient is $100\ \text{M}^{-1}\text{cm}^{-1}$.[101] Repetitive drying steps and more careful preparation may be necessary to reduce the water content.

3.4 TEMPERATURE-DEPENDENT CALIBRATION

For Chapter 7, temperature dependent 2D-IR spectra are obtained using a temperature-controlled spectroscopy cell (Harrick). The temperature is monitored for the sample by use of a thermocouple in contact with one of the CaF_2 windows. Cooling of the sample below room temperature is achieved by using a water-based chiller. A resistive heater incorporated

into a temperature-controlled spectroscopy cell is used to increase the temperature past 21 °C. At a given temperature, the sample is given ∼5 minutes to equilibrate before data collection begins.

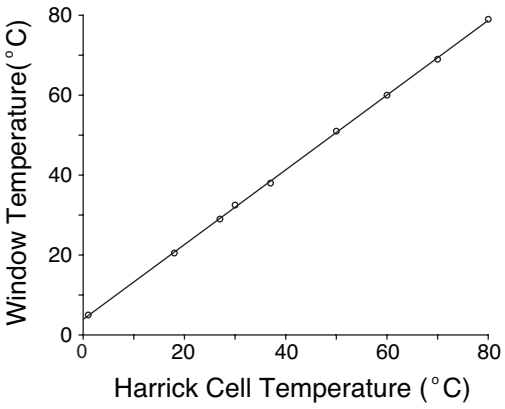

Figure 13: The temperature readout from the thermocouple of a temperature-dependent Harrick cell is calibrated to the direct temperature at the CaF_2 window.

The temperature readout from the temperature-controlled spectroscopy cell is calibrated using thermal paste and an additional external thermocouple. A CaF_2 window is placed in the temperature-controlled spectroscopy cell and is covered with a thin layer of thermal paste. The external thermal couple is placed in contact with the thin layer of thermal paste to simulate the sample temperature. For the calibration, the temperature is varied from 0 to 80 °C. A linear fit relates the temperature readout from the Harrick cell (T_{readout}) to the temperature reading of the external thermocouple on the sample window (T_{actual}).

$$T_{\text{actual}} = mT_{\text{readout}} + b \tag{3.1}$$

where the slope is 0.94 ± 0.02 and the y-intercept is 3.9 ± 0.6 °C. At temperatures above 50 °C, the difference between the two temperature readings is non-distinguishable.

3.5 2D-IR

In this manuscript, two separate 2D-IR experimental setups are used: 1) rapid scanning interferometry and 2) pulse shaping. In this section, the experimental setups are briefly described including how the set-ups differ with respect to suppressing scatter by modulating the phase of the mid-IR pulses. Scattering occurs by interference of either the pump or probe pulses to the heterodyned signal due to deficiencies in the windows (cracks or scratches) or undesirable inconsistencies in the sample (dirt, aggregates, air bubbles, etc.). This section ends with a comparison between the two methods where advantages and disadvantages for both 2D-IR set-ups are discussed.

3.5.1 Rapid Scanning

For Chapters 4 and 5, 2D-IR experiments are collected using a commercial Ti:Sapphire laser that generates a 805 nm pulse with a duration of 120 fs and a repetition rate of 5 kHz with a pulse energy of 1 mJ. A seed pulse from a Ti:Sapphire oscillator (Coherent Vitesse) is amplified by a chirped-pulse amplifier (Coherent Legend Elite).

A home-built tunable optical parametric amplifier (OPA) generates a 2.2 μJ mid-IR pulse.[102] A sapphire crystal first generates white light which mixes with the 805 nm pulse in 2 passes through a Type I beta barium borate (BBO) crystal. The resulting signal and idler difference frequency mix in a silver thiogallate (AGS) crystal to generate the mid-IR pulse ($1200 - 4000\ \text{cm}^{-1}$, $\sim 200\ \text{cm}^{-1}$ full width at half maximum).

The 2D-spectrometer uses a pump-probe geometry to collect the purely absorptive 2D spectrum.[103] The purely absorptive 2D spectrum is a sum of the rephasing and non-rephasing spectra.

Upon entering the 2D-spectrometer, the mid-IR light is separated by a wedged CaF_2 window. The majority of the mid-IR pulse passes through the CaF_2 window into a Mach-Zehnder interferometer. Here, two pump pulses with similar intensity are separated by a 50% beam splitter. One pump pulse is reflected onto a moving arm consisting of two gold mirrors on a 25 mm DC translation stage. The other pump pulse is transmitted through

the beam splitter onto two gold mirrors of a stationary arm. Part of the output from the interferometer is recorded on a single channel mercury cadmium telluride (MCT) array detector and is Fourier transformed resulting in a linear spectrum at ω_1. The other output consists of the two pump pulses focused on the sample plane with a spot size of 100 μm, and the two pump pulses are delayed by the coherence time (t_1).

To more accurately track t_1, a HeNe laser is introduced to the Mach-Zehnder interferometer and follows the same path of the two pumps. One path makes linearly polarized light, and the other path makes circularly polarized light. The HeNe is used to sort the mid-IR data by counting its fringes into bins where each bin is 2.11 fs or one period of the wavelength. A polarization cube at 45° separates the HeNe onto two different diodes that each track the change in the x- and y-directions. This gives information on the interferometer position and direction.[103,104]

The probe and reference pulses are separated from two reflections through the CaF_2 window and is focussed through a series of gold parabolic mirrors onto the sample. The third-order nonlinear signal field is heterodyned with the probe pulse, which acts as the local oscillator in this geometry. The ω_3 signal is then recorded on a 2×32 MCT array detector using a single monochromator with a 50 line/mm grating. At 2250 cm^{-1} , the resolution at this grating setting is approximately 7 cm^{-1}. For increased spectral resolution, an increased line/mm grating could be used, however, the frequency range will decrease as ω_3 is still being recorded on just 32 elements of the 2×32 MCT array detector. The reference is recorded on the other 32 array elements. A 50 mm translation stage varies the population time (t_2), the delay between the second pump pulse and the probe, from -50 ps to 200 ps.

The signal may include scattering from the two pump pulses and/or probe without modulating the phase of the pulses

$$S_{\text{scatter}}(\omega_3, t_1, t_2) \propto |E_{\text{probe}}(\omega_3) + \beta[E_{\text{pump1}}(\omega_3, t_2, t_1) + E_{\text{pump2}}(\omega_3, t_2)]|^2 \tag{3.2}$$

where $S_{\text{scatter}}(\omega_3, t_1, t_2)$ is the contributions of the scattering to the emitted photon response while $E_{\text{probe}}(\omega_3)$, $E_{\text{pump1}}(\omega_3, t_2, t_1)$, and $E_{\text{pump2}}(\omega_3, t_2)$ are contributions to the scattering signal by the probe and two pump pulses, respectively.[103] β is the fraction of the pump pulses that reach the detector.[103] The probe ($E_{\text{probe}}(\omega_3)$) is time-independent while the pumps are

time-dependent: pump 1 is dependent on both t_1 and t_2 and pump 2 is dependent on t_2. The electric field can be designated as $\cos(\omega t + \psi)$ where ω is frequency and ψ is the phase. Scattering of two pulses separated by a time delay can be described as

$$s_{scatter} = \frac{|E_{\text{probe}} + E_{\text{scatter}}|^2}{|E_{\text{probe}}|^2} = 1 + \beta'^2 + 2\beta' \cos(\omega_3 t + \psi) \tag{3.3}$$

where t is a time delay (either t_1 or t_2) and there is a time-independent $(1+\beta'^2)$ and time-dependent $2\beta' \cos(\omega_3 t + \psi)$ component that incorporates $\beta' = |E_{\text{probe}}/E_{\text{scatter}}|$.[103]

On one hand, rapid scanning back and forth of the moving arm during t_1 suppresses the scattering for the fixed arm (pump 2) as its independent of t_1. In this approach, Fourier transforming the signal with respect to t_1 sends the scattering associated with the fixed arm to a lower frequency component that is filtered out of the detected signal. On the other hand, scattering of the moving arm (pump 1) can be suppressed through quasi-phase-cycling during t_2.[103,105] This is scattering associated with pump-probe signal, and quasi-phase-cycling occurs by averaging two 2D-IR spectra by varying t_2 for half of the period of the center frequency of the laser pulse. For example, the center frequency of a BH stretch of BH_4^- is 2250 cm^{-1} and half of the period is ~7 fs. For a t_2 of 500 fs, two 2D-IR spectra would be obtained and averaged at 500 fs and 507 fs. Here, the sign of the phase of the moving arm pump flips (removing its contribution to the signal) as the 3rd order signal's phase remains constant. The quasi-phase modulation is for the central frequency, so scattering effects will increase linearly on both sides of the diagonal of the 2D spectrum.[105]

3.5.2 Pulse Shaping

In Chapters 6-7, the 2D-IR spectra are collected at the Central Laser Facility at the Rutherford Appleton Laboratory (RAL) in the United Kingdom. The 2D-IR data are collected on the Lifetime system developed by Donaldson et al. involving a 100 kHz 2D-IR spectrometer based on Yb:KGW amplifier technology[106].

The 6 W amplifier produces a ~180 fs pulse duration into the two OPAs. One OPA is for the pumps and one OPA is for the probe and reference. Pump and probe pulses are generated from Optical Parametric Amplifiers (Orpheus-1 and Orpheus-HP, Light Conversion) driven

by individual 15W and 6W Yb amplifiers (Pharos-SP and Pharos-HP, Light Conversion) operating with 300 and 180 fs pulse durations, respectively.

The 2D-IR spectrometer incorporated in the system allowes for rapid acquisitions with a few μOD of noise on 5000 laser shots.[106] Purely absorptive 2D-IR spectra are acquired in the pump-probe geometry using a collinear pair of pump pulses generated by a mid-IR pulse shaper (Phasetech Spectroscopy). The pulse shaper consists of two diffraction gratings and a germanium acousto-optic modulator (Ge-AOM). The first grating disperses the pulse into different frequencies that pass through a lens, and the Ge-AOM crystal is placed at the focal plane. The acoustic wave propagating through the Ge-AOM crystal is much slower than a sub-ps mid-IR pulse, and it can behave as a programmable grating to modulate the amplitude and phase of the dispersed frequencies. The dispersed frequencies are collimated through a second lens and the second grating compresses the pulse and reconstructs it back into the time domain. At the sample plane, the focussed pump and probe spot sizes are $\sim$60 μm FWHM. The total amount of pump and probe light incident on the sample during rapid acquisition is $\sim$12 mW and 2-3 mW, respectively. Sample heating was estimated to be 2-3 °C.[106] The instrument response time was determined to be $\sim$270 fs FWHM using Optical Kerr Effect Spectroscopy.

Shot-by-shot interferometry (time step 22 fs) with phase cycling at the repetition rate of the lasers (100 kHz) is used to collect interferograms for Fourier transform into 2D-IR spectra. The phases of the two pump pulses are shifted for each pair, but the relative phase remains at 0 ($\phi_1 - \phi_2 = 0$).[107] The phases of the pulses are programmed with the acoustic wave with an arbitrary waveform generator. With control of the phase of the pulses, the pure phase modulation leads to exact scatter suppression at all frequencies.[105]

3.5.3 Comparison of Approaches to 2D-IR Spectroscopy

Both 2D-IR experimental set-ups consist of advantages and disadvantages. The pulse shaping set-up is simpler as the delay times are programmable by the acoustic wave that propagates through the GeAOM crystal. Therefore, t_1 is well established and does not have to be traced as in the rapid scanning set-up. Also, with the pulse shaping set-up, exact scattering

suppression can be achieved as the phase can be modulated on a shot by shot basis. For the rapid scanning set up, quasi-phase modulation techniques are required, such as jittering the translation stage during t_2. By jittering the stage, exact scattering suppression occurs for the central frequency (ω_{center}), and scattering will increase along the diagonal away from ω_{center}. Also, for pulse shaping, more stability can be achieved on a single spectrum due to a higher shot by shot stability.[106]

For the pulse shaping set-up there are drawbacks as the RF amplifiers and Ge-AOM crystal can distort the waveform in a non-linear manner. As the Ge-AOM crystal operates in the Bragg regime, there is angular dispersion that can distort the temporal profile of a pulse.[108] These effects can be modulated, but it requires an additional level of complexity to the waveforms. Also, non-linear effects in the Ge-AOM crystal can distort peaks when t_1 is large. For rapid scanning, the t_1 time is solely dependent on the length of the translations stage in the Mach-Zehnder interferometer. Finally, since diffraction gratings are being used in the pulse shaping set up, the optical throughput is low (30 %)[109]. The diffraction gratings are not optimal and light is lost as it reflects off the gratings in different directions. For rapid scanning, the optical throughput is ∼50 % as a 50/50 beam splitter separates the OPA pulse into two pumps in the Mach-Zehnder interferometer.

4.0 CROWDING EFFECT ON DIHYDROGEN BONDS OF BH_4^-

The text in this chapter has been adapted from a manuscript being submitted to The Journal of Physical Chemistry B. An early version of the manuscript was submitted to a pre-print server: Johnson, C.A., Gronborg K.C., Brinzer T., Ren Z., Garrett-Roe S. ChemRxiv. 2019 (DOI: 10.26434/chemrxiv.9874694). The author's contribution includes performing all FTIR, IR-Pump-IR-Probe, and 2D-IR experiments, performing the analysis of the experimental data, and writing the manuscript except for the molecular dynamic simulations component.

4.1 CHAPTER SUMMARY

Two-dimensional infrared spectroscopy (2D-IR) probes the local solvent structure and dynamics of the ν_3 mode (BH antisymmetric stretch) of borohydride (BH_4^-) in aqueous solutions. The 2D-IR spectra of the BH stretches have broad and overlapping bands. Vibrational energy relaxation occurs on a 2 ps timescale. Energy that is initially deposited in BH stretching modes and directly in the solvent generates a long lived hot ground state. Before the hot ground state appears, some indications of intramolecular vibrational energy redistribution are observed. Within the vibrational lifetime of the BH stretching modes, the rate of structural relaxation slows proportionally to the NaOH concentration. For a molecular picture, molecular structures of borohydride in aqueous solutions varying the NaOH concentration are analyzed with Born Oppenheimer molecular dynamics (BOMD) simulations and Kohn-Sham density functional theory. We find that elevated NaOH concentrations decrease the number of dihydrogen bonds, and this slows the rate of the reorganization of the dihydrogen bond due to an ion crowding effect.

4.2 INTRODUCTION

Borohydride (BH_4^-) is a candidate material for hydrogen storage[49,110–114] and a strong reductant[36,51,115–117]. The hydrogen evolution reaction (HER) of BH_4^- has been shown to be fast enough[35,38,40,41,49,118–120] and the energy density high enough that BH_4^- has been considered for use in hydrogen fuel cells[113,121,122]. BH_4^- has been suggested as a model system to study the reduction of CO_2 to formate[16,51,123]. Improved understanding of the solvent effects of BH_4^- should help improve the optimization of BH_4^- chemistry for hydrogen storage, chemical reduction applications, and other related applications.

In H_2O, BH_4^- can protonate and then undergo a rapid self-hydrolysis to form $H_{2(g)}$ via the hydrogen evolution reaction (HER).[33–37] In CO_2 reduction applications, the HER is a side reaction and thus should be suppressed.[51] The HER can be suppressed at a high pH to limit $[H^+]$ and thus lower HER reaction rates.[37–42]

Solvent fluctuations are well known to play a key role in aqueous phase proton and hydride transfer. In H_2O, BH_4^- forms dihydrogen bonds with H_2O molecules that preferentially solvate around its tetrahedral geometry.[124] Recent Born-Oppenheimer molecular dynamics simulations (BOMD) predict that proton transfer to surrounding waters of solvation are an important ingredient in the reaction coordinate of reducing CO_2 to formate. After the hydride transfer from BH_4^- to CO_2, a water molecule stabilizes the BH_3 intermediate forming BH_3OH_2 with a ΔG of 0.2 eV at 300 K.[16] A umbrella sampling approach was used to select out different paths along the reaction coordinate.[16] If a proton is not immediately transferred away from the BH_3OH_2 through a solvent fluctuation to form BH_3OH^-, however, the reactive complex falls apart and returns to the reactants. No experiments yet provided the molecular specificity to test these dynamical predictions.

Two-dimensional infrared (2D-IR) spectroscopy measures solvent fluctuations that are important to the breaking and forming of hydrogen bonds.[6,7] Recent 2D-IR studies show that the dihydrogen bonds between BH_4^- and H_2O rearrange on the same timescale as the hydrogen bonds of water itself.[19] These experiments were performed at 1 M NaOH to suppress the HER, and these results suggest that NaOH has a minimal effect on the rearrangement of dihydrogen bonds, at least at these concentrations. Other ultrafast vibrational spectroscopy

experiments have characterized the ultrafast dynamics of BH_4^- in non-aqueous liquids and solids. IR pump-IR probe experiments on BH_4^- determined population relaxation rates of the antisymmetric stretch and bending modes in isopropylamine and solid $NaBH_4$.[125] A 2D-IR experiment examined the ν_3 antisymmetric stretch of solid $LiBH_4$ as a function of deuteration[126].

The goal of the present work is to explore the effect of solvent conditions on the structural relaxation around the BH_4^- molecules. Motivated by previous 2D-IR experiments that examined how a bulk properties of the solvent (viscosity) correlate to the local solvent dynamics in water[127] and ionic liquids[11,13], we hypothesize that the local structural dynamics of BH_4^- may scale proportionally to the viscosity of the bulk solvent. To test this, we investigate how the dynamics depend on hydroxide concentration. Molecular dynamics simulations provide first principles insights into the dihydrogen bonding that in turn will provide insight into choosing or designing the optimal solvent to control hydride transfer reactions.

In this chapter, we combine 2D-IR spectroscopy with theory for a complete picture of the dihydrogen bonding in BH_4^- as the pH increases. First, we examine the effect of NaOH concentration on the linear spectrum of the BH_4^- ν_3 mode. Next, we present a qualitative description for the structure of the 2D-IR spectra. We then discuss vibrational energy redistribution, relaxation, and thermalization of BH_4^- in aqueous solutions with IR-pump IR-probe and 2D-IR experiments. We, also, present the 2D-IR spectra as a function of NaOH concentration (0.1 to 7 M) and the dynamics of solvent reorganization around BH_4^- in water.

Following the structural solvation timescales, we present the BOMD simulations for BH_4^- in two solutions: neat H_2O and a 7 M NaOH solution. We first compare the theoretical linear IR spectrum with experiment. We, then, present the dynamical analyses that provide molecular insight into the effect of adding high concentrations of NaOH. Finally, we discuss the resulting physical picture related to the solvent reorganization timescales and how it may effect the rates of the hydrogen evolution reaction.

4.3 METHODS

BH_4^- sample preparation and FTIR analysis are described in Chapter 3. This works uses the rapid scanning 2D-IR set-up as described in Section 3.5.1.

4.3.1 IR-pump IR-probe

Similar to the 2D-IR spectrometer, a 2.2 μJ pulse from the OPA is separated into three pulses due to most of the pulse transmitting through a wedged CaF_2 window, the pump, and the other part of the light reflecting off of the wedged CaF_2 window, probe and reference. In the pump path, a mid-IR half-waveplate is set to 22.5° resulting in elliptically polarized light. To separate out different pump polarizations, a BaF_2 holographic wire grid polarizer is mechanically rotated between 0 and 90° resulting in either parallel ($I_\parallel$) or perpendicular ($I_\perp$) pump light. A chopper operating at half the repetition rate (2.5 kHz) blocks every other pump pulse. The delay between pump and probe pulses are varied with a 50 mm motorized translation stage with a delay from -50 to 200 ps. The pump and probe pulses are overlapped at the sample cell. As in the 2D-IR experiments, the signal is recorded on a 2×32 MCT array detector using a single monochromator with a 50 line/mm grating. IR-pump IR-probe spectroscopy in parallel and perpendicular polarizations gives the isotropic, $I_{\text{iso}} = I_\parallel + 2I_\perp$, and anisotropic, $I_{\text{aniso}} = (I_\parallel - I_\perp)/I_{\text{iso}}$ signals.

4.3.2 BOMD

The Born Oppenheimer molecular dynamics (BOMD) simulations have been implemented using the CP2K program.[128] One simulation was for BH_4^- in an aqueous solution, and the other simulation involved BH_4^- in a 7 M NaOH solution. For BH_4^- in an aqueous solution, the periodic boundary condition (PBC) volume was 6.2 $\mathring{A}^3$ with seven H_2O and one BH_4^- to set the density at 1.0 g/cm^3, which corresponds to the experimental condition. Due to the computational feasibility, our simulation was limited to the small cell for PBC calculation. The issue for divergence by summation of the electrostatic potential of a charged unit cell were overcome by introducing a homogenous neutralizing charge background as a counterion

as seen with the Ewald summation technique in the CP2K package.[129] We have tested the two systems with and without a counterion (BH_4^- and $NaBH_4$) in aqueous solution. The final calculated IR spectra of both systems are almost identical (Appendix A.1). For the BH_4^- in 7 M NaOH solution, the PBC volume was 6.2 $\AA^3$ with five H_2O, one OH^-, one Na^+, and one BH_4^- to keep the density at 1.0 g/cm^3. CP2K calculations used the B3LYP exchange correlation functional[130,131] with D3 dispersion correction[132] and GTH pseudo-potentials[133] with 6-31G* basis sets. The MD simulations have been implemented in a NVT ensemble at 300 K with a 0.5 fs time step. An MD integration time step of 0.5 fs approximately provided only a numerical error of 3 cm^{-1} for the antisymmetric B-H stretching mode.[134] Both systems were equilibrated for more than 200 ps and followed by production runs of 250 ps. The dipole moments at each step were calculated using a Wannier function scheme,[135] and IR spectra were calculated with the TRAVIS program.[136]

4.4 RESULTS AND DISCUSSION

4.4.1 FTIR of BH_4^- in 1 M NaOH

The lineshape of the antisymmetric stretch of BH_4^- (ν_3) consists of a complicated shape due to Fermi resonances (Figure 14a). BH_4^- is tetrahedral (T_d point group) with two Raman active modes (symmetric BH-stretch (ν_1) and the symmetric BH-bend (ν_2) with A_1 and E symmetry respectively) and two IR active modes (the antisymmetric BH-stretch (ν_3) and the antisymmetric BH-bend (ν_4) with both having T_2 symmetry). The ν_3 mode for BH_4^- in 0.1 M NaOH absorbs at 2261 cm^{-1}. Two Fermi resonances contribute to the overall lineshape: the overtone of the antisymmetric BH-bending mode ($2\nu_4$) and the combination band between the symmetric and antisymmetric BH-bending mode ($\nu_2 + \nu_4$)[137]. The $2\nu_4$ mode's center frequency is at 2204 cm^{-1}, and the $\nu_2 + \nu_4$ mode's center frequency is at 2317 cm^{-1}. The dark modes can "borrow" oscillator strength from the bright ν_3 mode because they all contain an irreducible representation with T_2 symmetry.

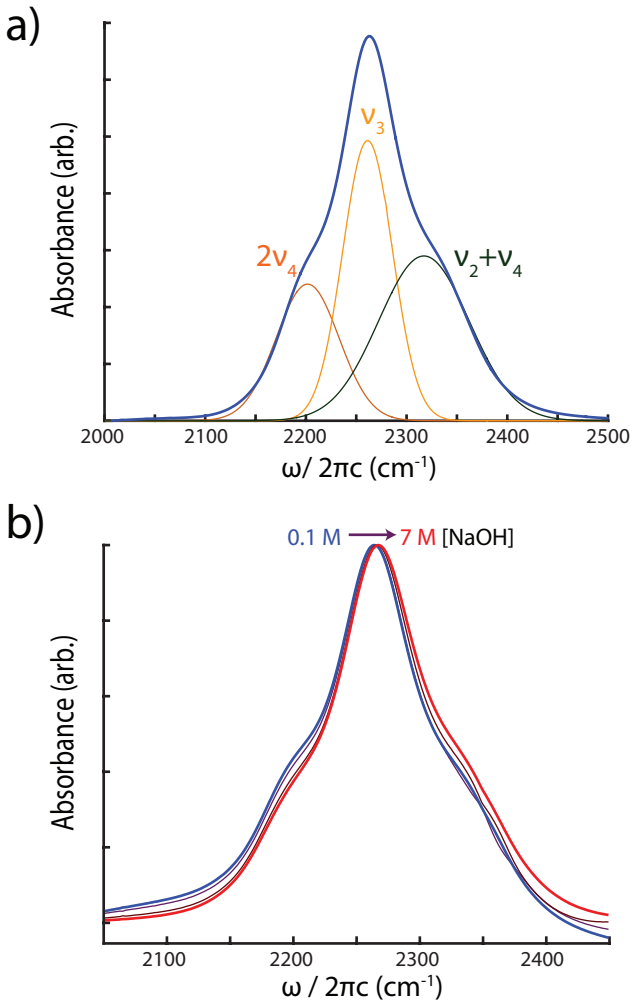

Figure 14: a) Two Fermi resonances borrow "oscillator" strength from the bright antisymmetric BH-stretch. FTIR of BH_4^- antisymmetric BH stretching mode: 1 M $NaBH_4$ in 0.1 M NaOH (blue), ν_3 (antisymmetric BH-stretch) mode centered at 2261 cm^{-1} (yellow), $2\nu_4$ (overtone of the antisymmetric BH-bend) centered at 2204 cm^{-1} (orange), and a $\nu_2+\nu_4$ (combination bend of symmetric and antisymmetric BH-bend) centered at 2317 cm^{-1} (green).[137] b) FTIR are obtained of 3 M BH_4^- while varying the $[OH^-]$: 0.1 to 7 M (blue to red). The spectrum of BH_4^- shifts slightly as a function of base concentration.

The ν_3 mode blue shifts 9 cm^{-1} when the base concentration increases from 0.1 M (2261 cm^{-1}) to 7 M (2270 cm^{-1}), likely indicating a change of the hydrogen bonding network

(Figure 14b). The molecular origin of the shift, however, is difficult to assess from FTIR alone. For the OH (OD) stretch of HOD in D2O (H2O), there is a well-established link between the vibrational frequency and the strength of hydrogen bonds. No such mapping has been established for BH_4^-, so no link between the absorption band and the local solvent environment can be drawn at the level of FTIR measurements.

2D-IR experiments and supporting BOMD simulations will reveal more about the changes in local solvation environment as the solvent condition changes.

4.4.2 Structure of the 2D-IR Spectrum

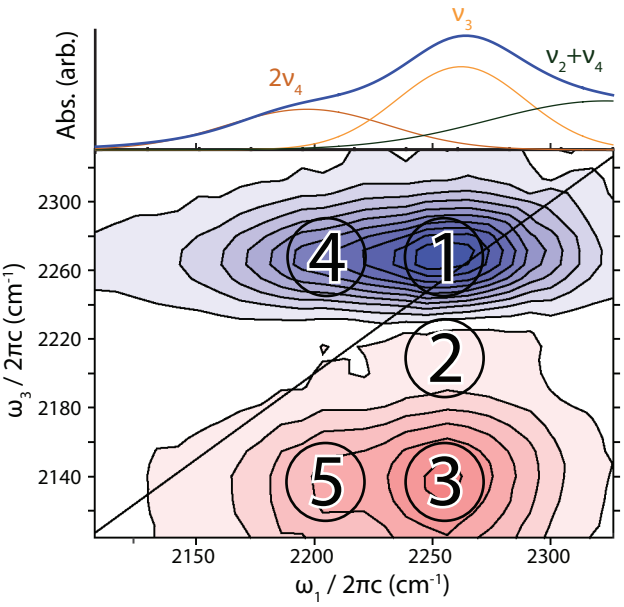

Figure 15: Coupling of the broad vibrational bands seen in the linear spectrum translates to a complicated 2D spectrum. The 2D-IR spectra of 3 M BH_4^- in 1 M NaOH at t_2 of 500 fs consists of at least 5 peaks.

The features in the 2D-IR spectrum of BH_4^- in aqueous solution are broad and unstructured (Figure 15) in agreement with previous work[19]. The breadth precludes detailed interpretation of some features in the spectrum because the broad bands overlap and cancel. The single, broad diagonal peak corresponds to the ground state bleach (GSB) and stimulated

emission of the ν_3 mode (peak 1). The band is centered at $(\omega_1, \omega_3) = (2250\,\mathrm{cm}^{-1}, 2270\,\mathrm{cm}^{-1})$, and is asymmetrical (peak 4). The unusual shape could be from a crosspeak between ν_3 and $2\nu_4$, but could also be inherent asymmetry of the diagonal band. A strong positive peak appears off of the diagonal $(2250\,\mathrm{cm}^{-1}, 2130\ \mathrm{cm}^{-1})$, which could either be an excited state absorption (ESA) of the ν_3 mode or a crosspeak with the $2\nu_4$ band (peak 3). The large positive peak (3) is also asymmetrical with a shoulder around $(2210\ \mathrm{cm}^{-1}, 2130\ \mathrm{cm}^{-1})$ (peak 5), which could be overlap of another peak (ESA of $2\nu_4$). A small positive feature (peak 2) lies between the two larger peaks at $(2250\ \mathrm{cm}^{-1}, 2210\,\mathrm{cm}^{-1})$. On the one hand, the anharmonicity of peak 3 agrees with the anharmonicity determined from IR-pump IR-probe measurements ($\sim 120\ \mathrm{cm}^{-1}$)[125]. On the other, the anharmonicty of isotope diluted BH_4^- determined from solid-state 2D-IR is much smaller ($44\ \mathrm{cm}^{-1}$)[126], more in line with the small positive feature (peak 2).

4.4.3 Vibrational Energy Redistribution, Relaxation, and Thermalization

From IR-pump IR-probe experiments, the vibrational energy relaxation and redistribution for BH_4^- can be established. First, the complex pump-probe spectra are assigned with assistance from the 2D-IR spectrum. Next, the population relaxation timescales will be discussed at each NaOH concentration. From this analysis, a heating effect as a hot ground state (HGS) is observed. Finally, a pathway for the vibrational energy relaxation and redistribution is proposed for the ν_3 mode of BH_4^-.

Signal of the GSB of the ν_3 band is still evident at 200 ps (Figure 16a). The time delay of the pump-probe experiment is varied from -2 ps to 200 ps. At early times ($\sim$ 200 fs), three vibrational bands exist: the GSB of the ν_3 and $2\nu_4$ and the ESA of the ν_3 mode. The reported population relaxation time of 1 M BH_4^- in 1 M NaOH is $\sim$ 3 ps, and the ESA of the ν_3 mode completely relaxes by a few ps. The GSB, however, does not completely relax at 200 ps. Also, the center frequency of the GSB of the ν_3 mode red shifts ($\sim 10\ \mathrm{cm}^{-1}$) at long delays. The long-lived negative absorbance of the GSB is strong evidence of a hot ground state (HGS).

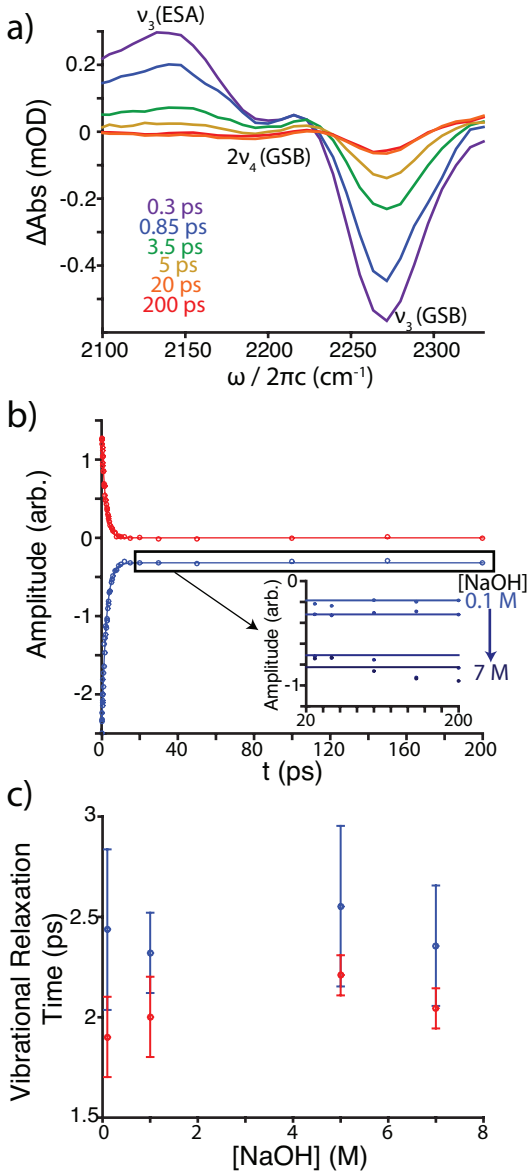

Figure 16: a) The parallel polarized IR-pump IR-probe spectra of 3 M BH_4^- in 1 M NaOH exhibits three peaks: the GSB of the ν_3 and $2\nu_4$ modes and the ESA of the ν_3 mode. The ν_3 GSB does not fully decay at 200 ps. b) The vibrational relaxation time of the isotropic signal of 3 M BH_4^- in 1 M can be resolved by plotting the max amplitude of the center frequency for the GSB (blue, $\sim 2267\ \text{cm}^{-1}$) and the ESA (red, $\sim 2241\ \text{cm}^{-1}$) of the ν_3 as a function of delay times. The GSB does not decay to zero at 200 ps. The offset from the GSB decay increases with increasing hydroxide concentrations (inset). c) The ESA and GSB result in a similar vibrational relaxation time of ~2 ps for all [NaOH].

The GSB and ESA of the ν_3 mode reveal the vibrational relaxation time for the BH stretching mode of the isotropic signal (Figure 16b). There is no significant difference between the vibrational relaxation time for the parallel, perpendicular, and the isotropic signal (Appendix A.1). The vibrational relaxation time of the ESA is $\sim$ 2 ps at all [OH^-]. The GSB amplitude of the ν_3 mode decays by a single exponential to a different constant value for each [OH^-]. The relaxation time is similar for both the GSB and ESA ($\sim$ 2 ps) (Figure 16c). As a result, the vibrational relaxation for the GSB and ESA would be a reasonable projection of the vibrational lifetime (T_1) of the ν_3 mode of BH_4^-.

From the GSB T_1 fits, the offset increases in magnitude with an increase in [OH^-] (Figure 16b inset). From the linear spectra, the mid-IR absorbance increases with an increase in the [OH^-] (Appendix A.1). Therefore, an increase in the signal at long times may correlate to an elevated heating effect where more energy is being deposited into the bath.

From the polarization-dependent pump-probe data, the anisotropy correlates to the redistribution of the triply degenerate ν_3 mode (Appendix A.1). For the ν_3 mode of BH_4^- at all [OH^-], the early ($t \sim$ 150 fs) anisotropic value is $\sim$ 0.05 and the ν_3 mode decays on a fast timescale ($\sim$ 200 fs). Our results for 3 M $NaBH_4$ in all [OH^-] compliment the results previously recorded for 1 M $NaBH_4$ in 1 M NaOH[19]. Systems with degenerate modes can have fast dynamics that reduce the initial anisotropy that are due to the scrambling of the excitation among the (nearly) degenerate states due to the fluctuating environment.[138–142] If the scrambling is fast enough, then one observes reduced anisotropy. Thus, the molecular reorientation is not dependent on the [OH^-] but correlates to the intramolecular redistribution of the triply degenerate ν_3 mode.

Furthermore, the 2D-IR spectra as a function of t_2 also show indications of vibrational energy redistribution (Figure 17). As t_2 increases from early times ($\sim$ 0.2 ps) to 1 ps, peak 4 appears to increase in amplitude. The fast rise of the crosspeak is likely due to the redistribution of vibrational energy between the ν_3 and $2\nu_4$ modes. Though the diagonal $2\nu_4$ peak is not clearly observed, if the $2\nu_4$ mode is pumped and the energy is transferred to the brighter ν_3 mode, the cross-peak can be larger than the diagonal peak. A corresponding crosspeak due to downhill energy transfer between ν_3 and $2\nu_4$ is not observed, likely due to the overlap with the ESA band (peak 5). In addition at long t_2 (200 ps), a thermalization

signal is evident in the 2D-IR spectra comparable to that from the pump-probe data. We interpret the long-lived signal of the GSB as a hot ground state, HGS.

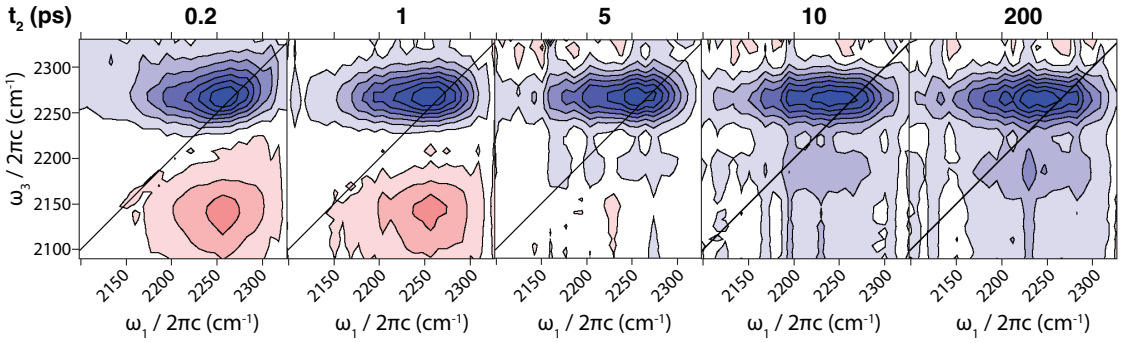

Figure 17: A hot ground state (HGS) is evident at long t_2 (200 ps) as the GSB (peak 1) remains even though the ESA (peak 3) has completely disappeared. 2D-IR spectra of 3 M $NaBH_4$ in 5 M NaOH solution are obtained at various t_2 times. The peak assignments are similar as to those described in the 2D-IR spectrum of 3 M $NaBH_4$ in 1 M NaOH (Figure 15).

Energy initially pumped into the BH-stretching modes can relax into other intra- and inter-molecular modes (Figure 18). We find the population decay of 2 ps in good agreement with both Tyborski et al.[125] and Andresen et al.'s[126] determination of the vibrational energy relaxation rates in related systems. Both assigned vibrational energy relaxation timescales occur from the ν_3 mode to the ν_4 mode on similar timescales, 3 and 1.5 ps,[19,125,126] respectively, and the ν_4 mode itself relaxes on a 3-4 ps timescale[125,126]. Energy initially deposited in the BH-stretches heats up the environment and causes a GSB that lasts until the local environment cools, a HGS. The magnitude of this HGS depends on the base concentration. Similarly, a thermalization effect has been shown to occur for HOD in water[143] and with high $[OH^-]$[127] due to the development of a large absorbance in the spectral window. Energy deposited into these water vibrations, also, contribute to the HGS that we observe. Temperature dependent FTIR support the conclusion of a HGS (Appendix A.1). The frequencies of the BH-stretches do not change, but the intensity decreases as temperature increases. This is consistent with long-lived GSBs without apparent new absorptions.

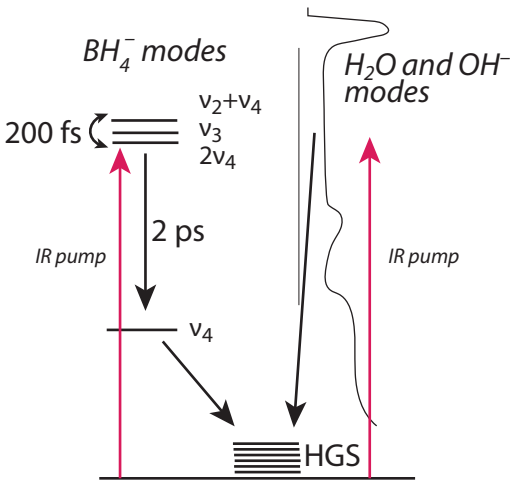

Figure 18: A possible mechanism describes vibrational energy redistribution, relaxation, and thermalization for BH_4^- in an aqueous solution. The IR pump will populate the $2\nu_4$, ν_3, or $\nu_2 + 2\nu_4$ mode, and energy may redistribute between the three modes. Also, the IR pump excites some solvent modes, directly heating the bath. Vibrational relaxation then occurs to low frequency bending modes, other intermolecular modes, and thermally populated modes (HGS) before relaxing to the ground state. Energy deposited in the solvent and BH stretches heats up the local environment generating the HGS, which cools on a timescale long compared to the experiment (200 ps).

The HGS and short T_1 ($\sim$ 2 ps) limits the t_2 range for a 2D-IR experiment on these systems. First, the T_1 of BH_4^- is faster than previously reported causing the t_2 to be more limited than previously expected, i.e the ESA absorbance (peak 3) decays to 0 by 5 ps. CLS values at times longer than $\sim$ 4 ps reflect the HGS spectrum, which is essentially a bulk effect, and not the dynamics of the initially excited molecules.

4.4.4 Spectral Diffusion of BH_4^- in Aqueous Solution Increasing [OH-]

With 2D-IR, the change in shape of the ν_3 mode's diagonal peak reports the dynamics of molecular motions (Figure 19). 2D-IR spectra for the ν_3 mode of BH_4^- are collected at various population times (t_2) while varying the concentration of NaOH: 0.1, 1, 5, and 7 M.

We limit our analysis to the first 4 ps due to a short T_1 and thermalization effect occurring past 4 ps. As the concentration of [OH^-] increases, the initial tilt of the ν_3 mode increases at early t_2 times, thus a more inhomogeneous component is present at high [OH^-] (Figure 19). At 4 ps, the ν_3 mode in 0.1 M [OH^-] loses correlation with the initial frequency (the tilt is gone), while in the 5-7 M [OH^-] a small inhomogeneous component still exists (a small tilt remains). As the [OH^-] increases, the linear spectral width of the ν_3 mode shows no apparent change confirming the correspondence to an increased inhomogeneous broadening.

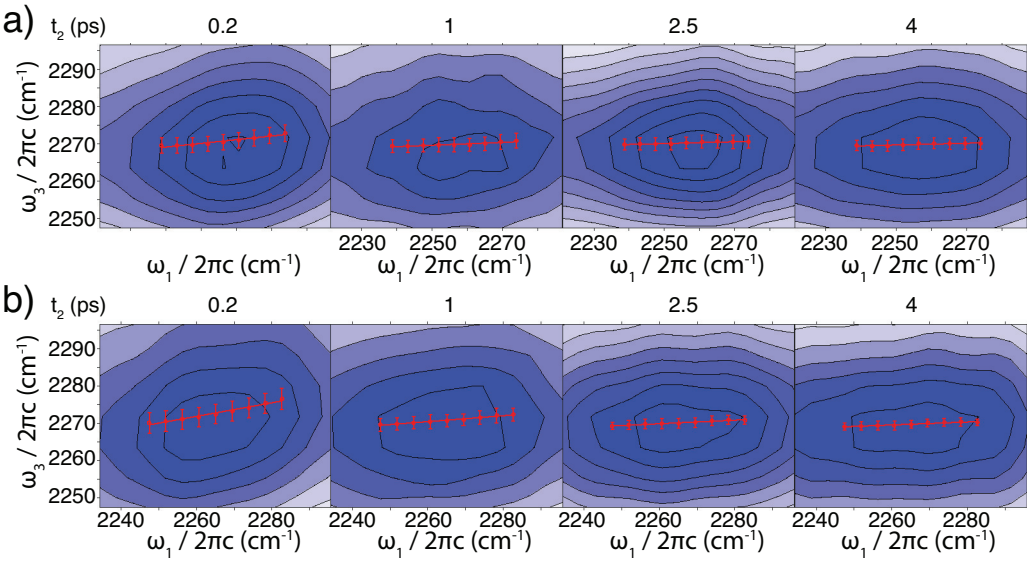

Figure 19: The tilt, or CLS values (o, red), scale with the hydroxide concentration. 2D-IR spectra of the ν_3 mode of BH_4^- at various delay times are plotted with their corresponding CLS fit: 3 M BH_4^- in a) 0.1 M NaOH and b) 5 M NaOH.

The timescales of molecular motions are quantified with the CLS of the ν_3 mode up to 4 ps (Figure 20a). The CLS results extract out the normalized frequency fluctuation correlation function (FFCF)

$$\frac{\langle \delta\omega(t)\delta\omega(0)\rangle}{\langle \delta\omega(0)\delta\omega(0)\rangle} = A_1 e^{-t/\tau_1} + c \tag{4.1}$$

where $\delta\omega(t)$ is the time-dependent frequency fluctuation. A single exponential with an offset is used to extract the timescales of frequency fluctuations where A_1 is the amplitude of the

frequency fluctuation, τ_1 is the fast timescale of frequency fluctuations, and c is an offset due to dynamics on a timescale longer than the experiment resolution.

The timescales of molecular motion of the ν_3 mode of BH_4^- slows with increasing [OH^-] (Table 1). The initial value of the CLS ($t_2 \sim 200$ fs) at 0.1 M [OH^-] is ~ 0.1. The CLS decays on a 0.5 ± 0.2 ps timescale to a small offset (0.02). As the [OH^-] increases, up to 7 M, the initial value of both the CLS and offset increase.

For the fast timescale (τ_1), we interpret these dynamics to be the equilibration of the initial excitation within the triply degenerate T_d, ν_3 modes and BH librational motions. Inelastic neutron scattering of solid BH_4^- identify librational motions at ~ 50 meV, which have an ~ 80 fs period[144]. Giammanco et al. measured an initial anisotropy of < 0.07 and interpret this as fast ($\ll$ 200 fs) vibrational energy redistribution within the T_d band.[19] From the CLS fits, the low initial CLS value (~ 0.1 to 0.22 at 200 fs) shows that the majority of the dynamics that modulate the BH-stretching frequency are in the fast modulation (homogenous) limit. The motional narrowing limit occurs when the product of the linewidth and the timescale, Γ, is $\Gamma = \Delta\tau \ll 1$. Given that the linewidth of the BH vibrations are $\Delta \sim 13$ cm^{-1}, Γ for the librations is ~ 0.17, which is well in the motional narrowing limit. The Γ for the energy redistribution with the ν_3 band should be $\ll$ 1, also in the motionally narrowed limit. Finally, the energy transfer between ν_3 and $2\nu_4$ should be $\Gamma \sim 0.4$, which is intermediate motional narrowing.

Table 1: The frequency fluctuation correlation function (FFCF) parameters are determined for the BH_4^- ν_3 mode using a single exponential with offset for BH_4^- in NaOH solutions (Equation 4.1). The parameters are extracted from CLS fits to the 2D-IR spectra at various t_2 times.

[NaOH]	A_1	τ_1 (ps)	c
0.1 M	0.12 ($\pm$0.04)	0.5 ($\pm$0.2)	0.024 ($\pm$0.007)
1 M	0.13 ($\pm$0.04)	0.4 ($\pm$0.2)	0.034 ($\pm$0.008)
5 M	0.19 ($\pm$0.04)	0.6 ($\pm$0.2)	0.047 ($\pm$0.007)
7 M	0.21 ($\pm$0.04)	0.8 ($\pm$0.4)	0.05 ($\pm$0.03)

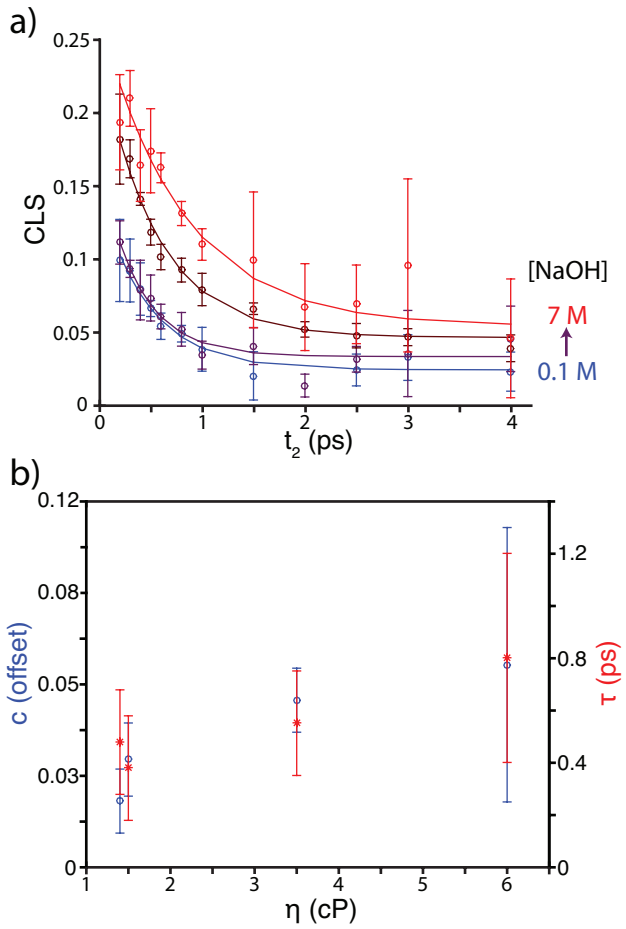

Figure 20: The timescales of molecular motion scale with increasing viscosity of the bulk solvent, i.e increasing [OH^-]. a) CLS values of the ν_3 mode of BH_4^- are determined while varying the bulk viscosity: 3 M BH_4^- in 0.1, 1, 5, and 7 M [OH^-] (blue to red). The corresponding single exponential fit with an offset extracts the frequency fluctuation correlation function (FFCF) parameters (Equation 4.1). b)The τ_1 (∗, red) and offset, c, (o, blue) FFCF parameters vary with viscosity[127] of the respective [OH^-] (0.1-7 M).

For the longer timescale, we do not resolve a clear exponential process and treat the dynamics as an offset. Giammanco et al.[19] resolves 300 fs and 1.8 ps timescales for the dynamics of BH_4^- in H_2O with 0.1 M [OH^-]; the initial value of the CLS and the fast times that we measure agree within error for low [OH]. There are several potential sources why we report an unresolved long time. First, our experiments consist of higher BH_4^- concentrations

($\sim$ 3 M compared to 1 M[19]), and we resolve slower dynamics. This is inconsistent with an energy transfer mechanism (observed in solid borohydride[125]), which would predict faster dynamics at higher concentrations of the vibrational chromophore. Also, in our measurements, there are clear heating effects after 4 ps. It is possible that the 1.8 ps timescale reported by Giammanco et al.[19] contains a component reflecting the dynamics of a HGS. We suggest that the differences are mostly due to a slowing down of the structural reorganization from the higher salt concentrations and the differences in the time window we analyze due to local heating. Despite these quantitative differences, there is broad agreement in the results and resulting physical pictures.

In summary, with the first timescale of spectral diffusion that we resolve (τ_1 time), we interpret as hindered translations of a BH_4^- in a particular local solvent shell. The slowest timescales, captured in the offset, are due to the reorganization of the local solvent shell, i.e. breaking and forming of dihydrogen bonds.

Viscosity correlates with the dynamics of structural reorganization, and higher viscosity solutions slow the spectral diffusion of BH_4^- (Figure 20b). The viscosity of < 2 M NaOH is very similar to neat H_2O ($\sim$ 1 cP)[127], and the dynamics are determined by the fluctuations of the bulk water hydrogen bonding network. As the concentration of base increases > 2 M, the viscosity of water increases to $\sim$ 6 cP[127], and we see a concomitant increase in the correlation time, which manifests as an increasing τ and offset in the FFCF. Similar effects have been seen in the dynamics of water itself as a function of $[OH^-]$[127], as well as the slowing of water dynamics at high salt concentrations[145–147]. The slowing of the reorganization time in these other salt solutions is primarily driven by a crowding effect. The first solvation shells of cations and anions overlap, which slows hydrogen bond switching. The BH_4^- seems to sense the same slow-down in both the hindered translation in the solvent shell and the reorganization of its dihydrogen bonds with H_2O. It should be noted that the experiments are performed at a high $[NaBH_4]$ (3 M) that will elevate the bulk viscosity across all samples resulting in viscosity being a minimal effect to the solvent dynamics at increasing $[OH^-]$.

4.5 BOMD OF BH_4^- IN NEAT H_2O AND 7 M NAOH

Born Oppenheimer MD simulations (BOMD) provides molecular insight into the slowing down of the solvent dynamics at increasing NaOH concentrations. The dynamical structures of BH_4^- and the free energy profiles incorporating the solvent effect were determined for two cases: BH_4^- in neat water and BH_4^- in an aqueous solution of 7 M NaOH.

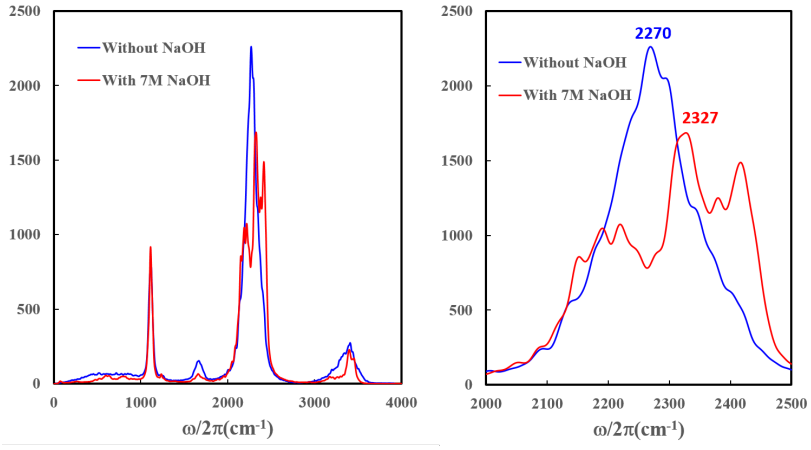

Figure 21: The simulated linear IR spectra is in good comparison to the experiment a) The linear IR spectrum is simulated with BOMD of BH_4^- in H_2O with (red) and without (blue) 7 M NaOH. b) With 7 M NaOH (red), the bright (ν_3) and dark ($2\nu_4$ and $\nu_2+\nu_4$) BH_4^- vibrational modes are evident as separate peaks in the spectrum. Without NaOH (blue), there is no clear separation between vibrational modes.

The simulated IR spectrum falls into good agreement with the experiment (Figure 21). No scaling factor is used. BOMD simulations uses an anharmonic character and allows for the calculation of overtones, combination bands, and Fermi resonances. In H_2O, the center frequency of the ν_3 mode (2270 cm^{-1}) is similar to experimentally observed frequency (2261 cm^{-1}), and both peaks are broad due to hydrogen bonding (Figure 21b). The $2\nu_4$ and $\nu_2+\nu_4$ modes become clear separate transitions in the 7 M NaOH solution spectrum as the peaks are less broad. As seen experimentally, the ν_3 mode blue shifts as the [NaOH] increases as there is a decrease in the structural hydrogen bonding network around BH_4^-.

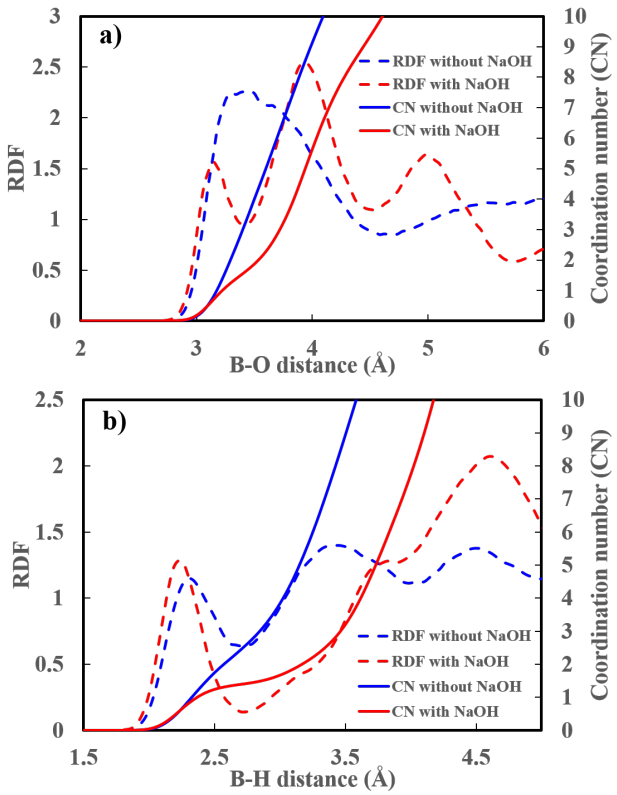

Figure 22: RDFs are determined for the BH_4^- liquid simulations in H_2O with (red,dash) and without (blue,dash) 7 M NaOH as a function of the distance between a) the boron and water oxygens ($g_{BO_w}(r)$) b) the boron and water hydrogens ($g_{BH_w}(r)$).The coordination numbers (CNs) are shown for both cases: with (red, solid) and without (blue, solid) 7 M NaOH.

In the 7 M NaOH case, the impurities of Na^+ and OH^- ions disrupt how many H_2O molecules are coordinated to BH_4^-. To quantify the solute-solvent structure, we use the radial distribution functions (RDFs) of the water oxygens ($g_{BO_w}(r)$) and the water hydrogens ($g_{BH_w}(r)$) around the B atom of borohydride, respectively, at inter-atomic distances (r) in Figure 22. The first solvation peak of the RDF in BH_4^- liquid simulation has a broad peak with a B–O distance maximum at 3.45 $\mathring{A}$. The coordination number suggests that $4-5$ solvent waters preferentially coordinate around BH_4^-. With 7 M NaOH, however, the first solvation peak is sharp at 3.14 $\mathring{A}$ with one coordinated H_2O, and the second peak is broader at 3.93 $\mathring{A}$ with approximately 5 coordinated H_2O molecules. The B–H RDFs similarly report

a less coordinated BH_4^- at higher [NaOH]. In neat H_2O, the first solvation peak is located at 2.3 $\AA$ with a coordination number of 1–2. On average, two hydrogens of the solvent H_2O and two of the four hydrogens of BH_4^- form two dihydrogen bonds. This is, perhaps, not surprising. Two dihydrogen bonds are enough to screen the negative charge on the borohydride. The partial charges on the hydrogens of water are approximately $+0.5e$, so the charge of borohydride ($-1e$) plus two water hydrogens ($2 \cdot 0.5e$) would be nearly zero. The two dihydrogen bonds cause a broadening of the antisymmetric B-H stretching mode of BH_4^-.

For the 7 M NaOH solution, the first solvation peak of the RDF is narrower with a lower coordination number than that in neat H_2O. On average, one hydrogen from the solvent H_2O and only one of the hydrogens from BH_4^- form a single dihydrogen bond. In addition to the positively charged proton, the nearby Na^+ may also serve to balance the remaining charge.

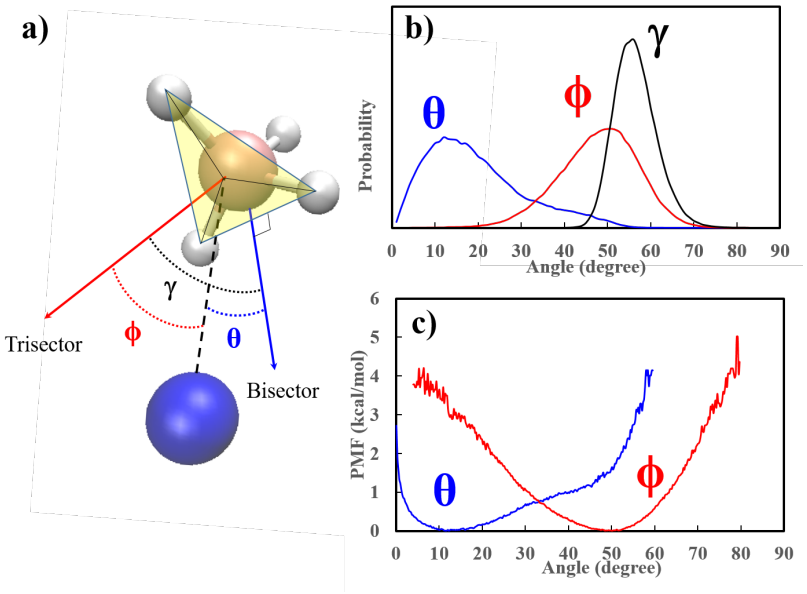

Figure 23: a) The angles between the B–Na vector and a bisector (θ) or a trisector (ϕ). The angle between the bisector and trisector (γ) is used as a reference. b) The probability distributions of the three angles and c) the potential of mean force (PMF) based on these angles are determined at 300 K.

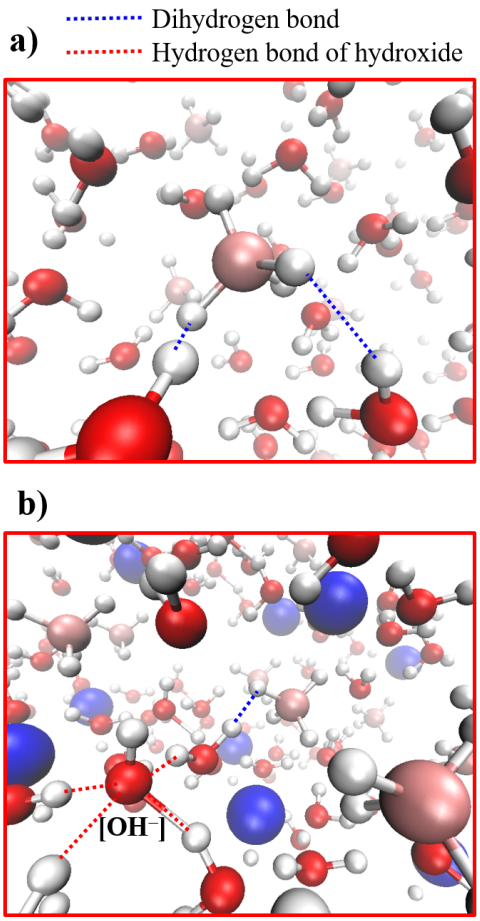

Figure 24: A snap-shot of the equilibrated structures of the BH_4^- BOMD simulations at room temperature a) without and b) with a 7 M NaOH solution.

The Na^+ cation is influential to the coordination of H_2O to BH_4^-, so the location of the Na^+ cation affects the construction of the dihydrogen bonds. An interesting question is whether Na^+ prefers to be to a bisector (-BH_2) or trisector (-BH_3) for BH_4^-. On one hand, the bisector vector is defined as the line segment which divides the H-B-H angle into two halves, where two hydrogens are selected as the closest distances from Na^+. On the other hand, the trisector denotes a spatial direction which encloses the same B–H distance of -BH_3. The most probable angles of θ and ϕ are 12° and 50°, respectively (Figure 23). These angles indicate that Na^+ is usually located near the bisector angle rather than that for a trisector. Overall, Na^+ moves around about 30° within the given energy (1.0 kcal/mol) based on the

potential of mean force (PMF) profile.

The addition of high salt concentrations inhibit the amount of H_2O that coordinates BH_4^-. In H_2O, BH_4^- is involved in two dihydrogen bonds with two H_2O molecules (Figure 24a). With the addition of 7 M NaOH, only one H_2O molecule closely coordinates BH_4^- forming a dihydrogen bond and Na^+ coordinates to BH_4^- at a bisector (Figure 24b). Also, there are 4 H_2O molecules in the second solvation shell, and 3 of them preferential coordinates the OH^-. Thus in the base solution, H_2O rearranges to coordinate the OH^- rather than the BH_4^-.

4.6 DISCUSSION

Ion pairing occurs in many polar and non-polar solvents[12,127,148–152] and water[153]. In some cases, ion pairing causes shifts in vibrational frequency. At elevated NaOH concentrations, the vibrational frequencies from 2D-IR spectroscopy on the OH stretch of an HOD molecule in H_2O shifts with pH.[127] In other cases, the changes are more subtle such as changes in the dynamics. The T_1 of a nitrile stretch for SCN^- varies with its local solvent environment.[148] With BH_4^-, the ion paring does not appear as prominent changes in the linear spectrum. Instead, ion pairing causes the vibrational frequency fluctuations to slow with an increase of the concentration of NaOH. Also, the experiments are performed at elevated [$NaBH_4$], so the frequency fluctuations timescales would not be representative to more dilute solutions. The general trend, however, of the solvent dynamics slowing down as [NaOH] increases would be transferable at lower [$NaBH_4$] solutions.

The observed changes in dynamics can be rationalized using a large-angle jump model of hydrogen bond rearrangement.[17,154] In this mechanism, the hydrogen bond breaks as a H_2O molecule rotates, undergoing a large angle jump, and forms a new hydrogen bond with an approaching H_2O molecule. The transition state is a bifurcated hydrogen bond with the initial and final hydrogen bonding partner. Experiments and theory have shown that adding hydrophobic species in solution, like trimethylamine-N-oxide (TMAO), occupy space and limits the trajectories for an approaching H_2O, i.e. formation of a new hydrogen bond.[154,155]

The excluded volume of the hydrophobe limits the number of accessible transition states thus lowering the entropy of activation. Our simulations show that the Na^+ counterion occupies space near the BH_4^-, similarly affecting the entropy of activation for the formation of a new dihydrogen bond. Also, the OH^- has a strong coordination shell which may contribute to locking its coordinated H_2O in place. A combination of the excluded volume effect of Na^+ and the high coordination of OH^- slows down the rate of the breaking and form of dihydrogen bonds between BH_4^- and H_2O.

The slower timescales of dihydrogen bond rearrangement as a function of [NaOH] and BOMD simulations shed light on the rate of the hydrogen evolution reaction. In H_2O, two rate constants contribute to the overall rate for the hydrolysis of BH_4^-: $k_{H_3O^+}$ and k_{H_2O}[37–42,156].

$$\frac{d[BH_4^-]}{dt} = -k_{H_3O^+}[H_3O^+][BH_4^-] - k_{H_2O}[H_2O][BH_4^-] \tag{4.2}$$

At a low pH, the reaction with H_3O^+ dominates the rate of BH_4^- hydrolysis, but at high pH the reaction with H_2O eventually dominates. At this limit, the rate of hydrogen evolution is solely dependent on k_{H_2O}. At high NaOH concentrations, the local solvent environment is changing as the timescale of the breaking and forming of dihydrogen bonds slow down due to an ion crowding effect. Therefore, the k_{H_2O} may be changing as a function of the salt concentration which is filling up the coordination sphere. No systematic studies have been able to detect a concentration dependence on k_{H_2O} because the rate studies[37–42,156] measured the hydrolysis reaction as a function of H_3O^+ and determined the k_{H_2O} by extrapolating to zero concentration. The prediction that k_{H_2O} decreases with occupation of the solvation shell of the BH_4^- could be tested by measuring the rate of hydrolysis as a function of ionic strength using a bystander salt such as NaCl.

Further 2D-IR spectroscopy studies complemented with a study of HER rates can further investigate the dependency of salt concentration on k_{H_2O}. A temperature-dependent 2D-IR spectroscopy will reveal an entropy of activation by applying an Eyring analysis on the temperature-dependent solvation dynamics. The entropy of activation as a function of NaOH concentration can also test the ion-crowding effecting by determining the activation entropy and comparing to the excluded volume model of Laage and Hynes[154].

4.7 CONCLUSION

As a function of NaOH concentration, solvation dynamics of BH_4^- are explored through a combined effort of 2D-IR spectroscopy and BOMD simulations.

Ultrafast infrared vibrational spectroscopy elucidates the vibrational mode coupling, relaxation, redistribution and the solvent dynamics of BH_4^- in increasing NaOH solutions. Vibrational energy relaxation from the BH stretching modes and the solvent background cause a hot ground state to dominate the spectra after $\sim$ 4 ps thus limiting the effective timeframe of the 2D-IR experiment. In the 2D-IR spectra, the breadth of the BH_4^- vibrational bands causes spectral congestion which precludes direct assignments of the peaks and crosspeaks. Rapid vibrational energy redistribution causes some crosspeaks to grow in the 2D-IR spectra. From the FFCF, the reorganization of the local structural environment around the BH_4^- slows as the NaOH concentration increases. Two different motions are determined. The fast τ_1 is reported to be a hindered rotation. A slower unresolved timescale may be related to the breaking and forming of dihydrogen bonds and is reported as an offset that increases with the NaOH concentration.

BOMD simulations support slower local structural reorganization timescales at elevated [NaOH]. In H_2O, BH_4^- is solvated by 4–5 H_2O molecules and forms two dihydrogen bonds with two of neighboring H_2O molecules in the first solvation shell. In an aqueous 7 M NaOH solution, only one dihydrogen bond forms as one H_2O molecule is in the first solvation shell. A Na^+ cation coordinates to BH_4^- at a bisector and an OH^- is preferentially solvated by 3 H_2O in the second solvation shell. The crowding effect due to high Na^+ and OH^- ions leads to a slower structural reorganization timescale, and the crowding effect gives a molecular picture for why the rate for the hydrogen evolution reaction slows down at a high pH.

5.0 VIBRATIONAL MODE COUPLING OF BH_4^- IONIC LIQUIDS

The following text in this chapter is adapted from a manuscript in preparation with plans to submit it to the Journal of Physical Chemistry B. The author's contributions include writing the manuscript, preforming DSC measurements, performing and analyzing the ultrafast vibrational spectroscopy experiments, and analyzing the peaks from a simulated 2D-IR spectrum.

5.1 CHAPTER SUMMARY

Two-dimensional infrared spectroscopy (2D-IR) probes the local solvent structure and dynamics of the ν_3 mode (BH antisymmetric stretch) of borohydride (BH_4^-) in a series of ionic liquids (ILs). The 2D-IR spectra in ILs consist of well-resolved bands with complex structure due to Fermi resonances. To assign the complicated pattern of cross-peaks, a model Hamiltonian is constructed for the three relevant modes. The vibrational energy cascade is also addressed as a thermalization effect occurs, as seen previously in aqueous solutions. Energy from the ν_3 mode is deposited into a long lived hot ground state. The solvent dynamics in the ILs ($\sim$ 30 ps) are much slower than in water ($\sim$ 2 ps), corresponding to slow reorganization of the first solvation shell. The experiments establish an initial understanding of the solvation dynamics around this model hydrogen storage material.

5.2 INTRODUCTION

Ionic liquids (ILs) show promise for many energy storage applications,[79,82,157,158] and borohydride (BH_4^-) ILs, with BH_4^- as the anion, could allow high energy density hydrogen storage in a liquid material or for use in hydrogen fuel cells.[62] Also, ILs are suggested as catalysts for CO_2 reduction,[159] and BH_4^- is a strong reducing agent that can reduce CO_2 to formate.[51,123] Characterizing the local solvent structure around BH_4^- on a sub-ps timescale for various solvents, such as ILs, can assist in optimizing the chemistry of BH_4^- for both hydrogen storage and CO_2 reduction applications.

ILs offer a myriad of useful properties ranging from their chemical tunability[55,65,160] to their low vapor pressure.[82,161] IL properties can be altered through variation of the anion or cation. Currently, BH_4^- ILs are being optimized for low vapor pressure, stability, reduced hydrogen storage costs, low toxicity and CO_2 reduction.[61,63] In aqueous solutions, $NaBH_4^-$ undergoes a rapid hydrogen evolution reaction (HER),[35,38,40,41,49,118–120] and changing the alkali cation has been demonstrated to alter the rate. $LiBH_4$ has shown a similar rate to that determined for $NaBH_4$,$Brown_{1961}$ but the slower HER for KBH_4 makes it less suitable as a candidate for hydrogen fuel cells.[112] Overall, there is minimal ability to optimize the properties of traditional alkali metal BH_4^- where developing BH_4^- ILs allows more room to adjust the selectivity for a given need, i.e. CO_2 reduction.

The BH_4^- anion can directly be probed through its infrared (IR) active stretching and bending modes. Early FTIR studies showed two IR active modes of BH_4^-: the BH antisymmetric stretching mode (ν_3) and the antisymmetric BH bending mode (ν_4).[137] The FTIR spectrum of the ν_3 mode displays a complicated shape involving three vibrational peaks. FTIR studies with isotope labeling attribute the cause of the ν_3 modes complicated lineshape arising from two Fermi resonances: the overtone of the anitsymmetric BH bending mode ($2\nu_4$) and a combination band between the symmetric BH bending mode and the anitsymmetric BH bending mode ($\nu_2+\nu_4$).[137] Anharmonic vibrational calculations of BH_4^- with various isotope combinations have confirmed the IR assignments.[162]

To better understand the vibrational coupling caused by the Fermi resonances in the linear BH_4^- infrared spectra, we use two-dimensional infrared spectroscopy (2D-IR). 2D-IR

is the vibrational analog of 2D-NMR spectroscopy, we use it to measure the coupling between vibrations. Also, direct coupling between vibrational modes generates crosspeaks shifted by the coupling energy,[163] allowing their measurement with high precision Fermi resonances have been shown to cause more complicated patterns of cross-peaks in 2D-IR spectra.[99,164] Chemical exchange spectroscopy gives rise to crosspeaks from a chemical reaction such as the switching from a complexed to an uncomplexed form and vice versa.[97] One example for chemical exchange 2D-IR is the phenol complexation to benzene where the free phenol and the complexed phenol have different center frequencies.[97] As t_2 increases, crosspeaks will grow in as the free phenol becomes complexed and vice versa.

Ultrafast IR vibrational spectroscopy can elucidate structural and dynamical information for a given system.[2–8,11–14] The ultrafast vibrational dynamics of BH_4^- have been explored in a few studies to characterize both intramolecular vibrational energy relaxation and intermolecular motion. The population relaxation times of the BH stretching and bending modes of NH_4^- have been probed through IR pump-IR probe measurements in a variety of liquid and crystal environments.[19,125,126] Two-color pump-probe experiments provide insight to the vibrational energy cascade of the ν_3 mode to the ν_4 mode and other low frequency BH_4^- modes.[125,126] 2D-IR measurements have investigated the homogeneity of solid $LiBH_4$ and various deuterated isotopomers.[126] In other 2D-IR measurements, the dynamics of the rearrangement of dihydrogen bonds between BH_4^- and H_2O correlate to the hydrogen bond dynamics of an HOD molecule in H_2O.[19] As discussed in Chapter 4, we have used 2D-IR experiments to examine the effect of hydroxide on the dynamics of BH_4^- in aqueous solutions where an elevated concentration of Na^+ and OH^- ions cause a crowding effect of the dihydrogen bonds.

The goal of this work is to establish a foundation for the nonlinear spectroscopy of BH_4^- ILs and explore how ILs can tune the rate of structural relaxation around the BH_4^- anion. The BH_4^- based ILs are classified and compared by thermophysical properties that reveal vital bulk properties, i.e. viscosity and phase transition temperatures. Using 2D-IR to developing a molecular understanding of structural relaxation around the BH_4^- anion can provide additional information and guide the future development of BH_4^- ILs for energy storage applications as the solvation dynamics can provide insight into the molecular friction of the IL.

The BH_4^- based ILs investigated in this study are 1-butyl-3-methylimidazolium borohydride ([BMIM][BH_4]) and trihexyl-(tetradecyl)phosphonium borohydride ([$P_{14,6,6,6}$][BH_4]). BMIM is a very common cation in ILs, and [BMIM][BH_4] has been shown as a selective reducing agent.[64] In an IL, the $P_{14,6,6,6}$ cation has been shown to be a "liquifier" [165,166] and a good absorbent for CO_2.[65] These properties are expected to extend to [$P_{14,6,6,6}$][BH_4]. The effects of these two cations in BH_4^- ILs have not yet been studied using ultrafast infrared vibrational spectroscopy.

In this chapter, we compare BH_4^- dissolved in an aprotic IL compared with two bulk BH_4^- ILs. First, we present the thermophysical properties (viscosity and phase transition temperatures) of the bulk BH_4^- ILs. Next, we examine the solvent effects from the linear FTIR spectra of the ν_3 mode for each BH_4^- IL. Then, we present 2D-IR spectra of the BH_4^- ILs. We assign the cross-peaks in the complicated 2D-IR spectra by simulating the spectra through the construction of a model vibrational Hamiltonian and using response function formalism. With IR pump-IR probe and 2D-IR data, we then present the vibrational energy redistribution, relaxation, and thermalization in these ILs. Finally, we present the dynamics of solvent reorganization around BH_4^- in all three IL samples, showing the solvent reorganizational timescale can be another tool in the identification/classification toolbox for BH_4^- ILs.

5.3 EXPERIMENTAL METHODS

Some of the experimental methods are described in earlier chapters. The IL drying and FTIR analysis are described in Chapter 3. This works uses the rapid scanning 2D-IR set-up as described in Section 3.5.1. The IR-Pump IR-Probe set up is described in Chapter 4.

5.3.1 BH_4^- Based IL Synthesis

Methyl imidazole (M50834-500G), 1-bromobutane (B59497-500G), sodium borohydride (Na-BH_4) (71320-100G), tetramethylammonium borohydride ($N_{1,1,1,1}BH_4^-$) (310689-10G), and

chloroform (CX1055P-4) were bought from Sigma-Aldrich, St. Louis, USA. The ionic liquid trihexyl(tetradecyl)phosphonium chloride ($[P_{14,6,6,6}][Cl]$) was brought from Cytec Industries Inc. Butyltrimethylammonium bis(trifluoromethylsulfonyl) imide ($[N_{1,1,1,4}][Tf_2N]$) was purchased from IoLiTec (258273-75-5).

Synthesis of $[P_{14,6,6,6}][BH_4]$: 10 g of $[P_{14,6,6,6}][Cl]$ was added to a round bottom flask containing 50 mL of chloroform and a stir bar. 0.796 g (1.1 eq.) of $NaBH_4$ was added to the mixture followed by addition of water. The mixture was stirred for 2 hours and the water was decanted. The chloroform layer was extracted with water three times to remove trace amounts of NaCl. Finally, the chloroform was evaporated under rotary evaporation (40 °C at 1 mbar) to yield a colorless liquid.

^{1}H NMR (600 MHz, $CDCl_3$) δ 2.347 (m, 8H), 1.486 (m, 8H), 1.301-1.244 (m, 40H), 0.874 (t, 12H), 0.234 (s, 1H), 0.071 (s, 1H), -0.092 (s, 1H), and -0.255 (s, 1H).

Synthesis of $[BMIM][BH_4]$ was performed according to a reported procedure[64].

The ionic liquids were dried by use of a vacuum pump (10 μTor) to decrease the water content and confirmed by FTIR (Appendix A.2). $[BMIM][BH_4]$ was not completely dry under vacuum after 24 hours with ∼1.6 M of H_2O present. $[P_{14,6,6,6}][BH_4]$ and the saturated $N_{1,1,1,1}BH_4$ in $[N_{1,1,1,4}][Tf_2N]$ solution had less than ∼ 0.5 M and ∼ 0.1 M $[H_2O]$, respectively.

5.3.2 Viscosity Measurements

Viscosities for $[BMIM][BH_4]$ and $[P_{14,6,6,6}][BH_4]$ were measured using a Brookfield Model HBDV-III+CP cone/plate viscometer at 5 °C intervals over the temperature range of 5-65 °C. The viscometer was calibrated against the NIST-certified viscosity standards N75 and N100 (Cannon Instruments Company). Ionic liquid samples were dried under vacuum at 50 °C overnight prior to all viscosity measurements.

The viscosity of $[N_{1,1,1,4}][Tf_2N]$ was determined with an Anton Paar Modular Compact Rheometer (MCR 302 WESP). A 25 mm diameter smooth plate was used with a gap height of 300 μm at room temperature.

5.3.3 Thermal Analysis

Phase transition temperatures were measured using a Differential Scanning Calorimeter, DSC, (PerkinElmer DSC4000) cooled by a liquid nitrogen chiller (PerkinElmer IntraCooler II). About 10 mg of the respective IL was placed in an aluminum pan. Initially, the IL samples were cooled past -80 °C and left to equilibrate for 5 minutes. Each sample was then heated at a rate of 1 °C/min up to 20-30 °C. From each thermogram, the glass transition, crystallization, and melting point temperatures were all determined, if applicable.

5.3.4 Sample Preparation

Samples were prepared on two CaF_2 windows (Crystran Ltd, UK) in a brass cell holder. About 10 μL of the given solution was sandwiched between the two windows with the desired spacer. ILs are transparent in the mid-IR region but $NaBH_4$ is only sparingly soluble. Therefore, we use a saturated solution of $N_{1,1,1,1}BH_4$ (150 mM) in $[N_{1,1,1,4}][Tf_2N]$ with a 25 μm Teflon spacer. The bulk ILs ($[P_{14,6,6,6}][BH_4]$ and $[BMIM][BH_4]$) were prepared with no spacer due to a high concentration of BH_4^- present.

5.4 RESULTS

5.4.1 Thermophysical Properties of BH_4^- Ionic Liquids

Two novel BH_4^- ILs are investigated where the cation is varied: BMIM and P_{14666}. Also, a saturated solution of $N_{1,1,1,4}$BH4 in $[N_{1,1,1,4}][Tf_2N]$ is investigated. The viscosity (η) along with the glass transition (T_g), crystallization (T_{cr}), and melting (T_m) temperatures are determined for each IL, if applicable (Table 2).

The phase-transition temperatures are obtained by analyzing thermograms collected with Differential Scanning Calorimeter (DSC) (Appendix A.2). The T_g for $[BMIM][BH_4]$ and $[N_{1,1,1,4}][Tf_2N]$ agrees to other previously reported values for imidazolium and ammonium based ILs.[167] The measured T_g for $[P_{14,6,6,6}][BH_4]]$, however, is ~10 K lower than that for

imidazolium ILs. [BMIM][BH_4] did not have a T_{cr} or T_m. The lack of a T_{cr} and T_m in [BMIM][BH_4] is similar to [BMIM][BF_4][168]. Varying the long alkyl chain of the imidazolium cation for BF_4^- based ILs shows that any chain smaller than 9 carbon atoms does not have a melting point or a crystallization point.[168] Thus, [BMIM][BF_4] and [BMIM][BH_4] are supercooled liquids past room temperature.

Table 2: Thermophysical properties are determined for the novel BH_4^- ILs and [$N_{1,1,1,4}$][Tf_2N]: viscosity (η) at room temperature, glass transition temperature (T_g), crystallization point (T_{cr}), and melting point (T_m)

	η (cP)	T_g (°C)	T_{cr} (°C)	T_m (°C)
[BMIM][BH_4]	533	-73.3	—	—
[$P_{14,6,6,6}$][BH_4]	1064	-63.2	-30.5	0.09
[$N_{1,1,1,4}$][Tf_2N]	100	-76.9	—	—

The BH_4^- ILs' viscosities vary by orders of magnitude and follow an inversely proportional trend to that of T_g.(Table 2) The viscosity for [$P_{14,6,6,6}$][BH_4] is on the same magnitude of glycerol[169]. The viscosity of the BH_4^- ILs increase by a factor of 2 as the cation is changed from BMIM to a sterically bulky $P_{14,6,6,6}^+$. The viscosity of [$N_{1,1,1,4}$][Tf_2N] is determined to be similar to previously reported values[170], and is not affected by adding $N_{1,1,1,1}BH_4$ to form a saturated solution. The viscosity of [$N_{1,1,1,4}$][Tf_2N] is, however, a factor of 5 and 10 less than that of [BMIM][BH_4] and [$P_{14,6,6,6}$][BH_4], respectively.

The temperature dependence of the viscosity for BH_4^- ILs follow a non-Arrhenius behavior as previously seen in imidazolium ILs[167] (Figure 25). Therefore, a Vogel-Fulcher-Tamman (VFT) dependence was used to represent the viscosity as a function of temperature (Appendix A.2)

$$\ln(\eta/cP) = A + \frac{B}{T - T_0} \tag{5.1}$$

where A and B are fit parameters. Similar to work from Angel et al.,[171] a high viscosity (10^{13} cP) is included at the glass transition temperature to help constrain the fitting parameters. The resulting divergence temperature, T_0, falls within $\sim 30\ ^\circ C$ for each BH_4^- IL following the previously reported trend for imidazolium ILs[167].

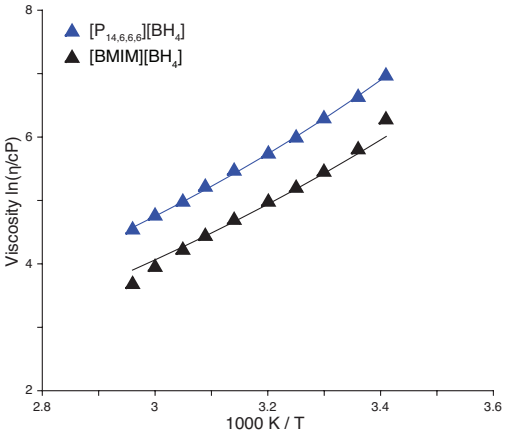

Figure 25: a) The viscosity varies as a function of temperature and follows the Vogel-Fulcher-Tamman (VFT) model. Temperature-dependent viscosity is measured for the two bulk BH_4^- based ILs: [BMIM][BH_4] (black) and [$P_{14,6,6,6}$][BH_4] (blue). The respective VFT fit is plotted with each IL (Equation 5.1).

Along with the thermophysical properties, the solvent reorganization time of the BH_4^- anion in a 2D-IR experiment can be another effective tool to provide further insight into structural and dynamical information on these novel BH_4^- ILs. Before we analyze the sub-ps solvent reorganization timescales, we will discuss the linear spectra for the ν_3 mode of BH_4^- and then address how to assign the 2D-IR spectrum.

5.4.2 FTIR of BH_4^- Ionic Liquids

In an IL, the breadth of the vibrational bands are narrow and the peaks are well defined (Figure 26a). The well documented complicated lineshape of the antisymmetric BH stretch mode (ν_3) is caused by two Fermi resonances: the overtone of the antisymmetric B-H bending mode ($2\nu_4$) and the combination band between the symmetric and antisymmetric B-H bending mode ($\nu_2 + \nu_4$).[137] The center frequency of the ν_3 mode of a saturated solution of $N_{1,1,1,1}BH_4$ in [$N_{1,1,1,4}$][Tf_2N] (2226 cm^{-1}) is red shifted from the reported center frequency in aqueous solutions (2261 cm^{-1}), as discussed in Chapter 4. The $2\nu_4$ mode and the $\nu_2 + \nu_4$

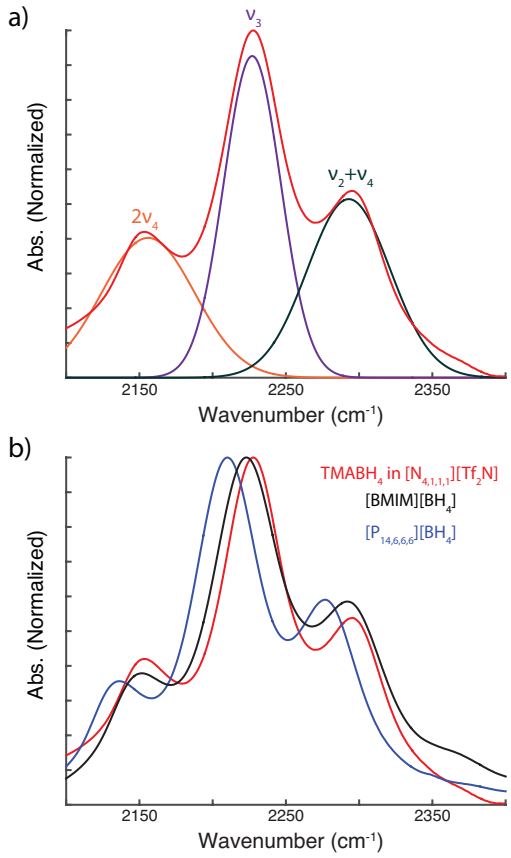

Figure 26: a) The center frequency of the ν_3 mode (B-H antisymmetric stretch) is 2226 cm^{-1} (purple) and is complicated by two Fermi resonances: $2\nu_4$ (orange), the overtone of the antisymmetric B-H bending mode, and $\nu_2 + \nu_4$ (green), the combination band between the symmetric and antisymmetric B-H bending mode. FTIR spectra are obtained of a saturated solution (150 mM) of $N_{1,1,1,1}BH_4$ in $[N_{4,1,1,1}][Tf_2N]$ (red). b) The center frequency of the ν_3 mode red shifts for the the BH_4^- ILs. FTIR spectra are obtained for the ν_3 mode of BH_4^- dissolved in an aprotic IL (red) vs two bulk BH_4^- based ILs: [BMIM][BH_4] (black) and $[P_{14,6,6,6}][BH_4^-]$ (blue).

mode of $N_{1,1,1,1}BH_4$ in $[N_{1,1,1,4}][Tf_2N]$ (2154 cm^{-1} and 2293 cm^{-1}) are also redshifted from BH_4^- in an aqueous solution (2204 cm^{-1} and 2317 cm^{-1}, respectively). The inadequate dihydrogen bonding in the aprotic IL contributes to the red shifts and narrower linewidths than those reported in aqueous solutions.

The ν_3 mode for the bulk BH_4^- ILs are red shifted from the saturated solution of $N_{1,1,1,1}BH_4$ in $[N_{1,1,1,4}][Tf_2N]$ (Figure 26b). The center frequency red shifts by 4 and 18 cm^{-1} in [BMIM][BH_4] and $[P_{14,6,6,6}][BH_4]$, respectively. In the [BMIM][BH_4] sample, dihydrogen bonding can occur between BH_4^- and the slightly acidic C-H at the 2-position of the $BMIM^+$ cation. Therefore, the bluer shift of the ν_3 mode for [BMIM][BH_4] compared to $[P_{14,6,6,6}][BH_4]$ could correlate to an effect of more dihydrogen bonding. The ratio of the absorbance for the two Fermi resonances also varies across the ILs. 2D-IR will be able to provide more insight into the vibrational coupling and local structural environment of these ILs.

5.4.3 Structure of 2D-IR Spectra of BH_4^- in $[N_{1,1,1,4}][Tf_2N]$ and BH_4^- Based Ionic Liquids

The Fermi resonances of BH_4^- complicate the 2D-IR spectra for the saturated solution of $N_{1,1,1,1}BH_4$ in $[N_{1,1,1,4}][Tf_2N]$ and the two BH_4^- ILs: [BMIM][BH_4] and $[P_{14,6,6,6}][BH_4]$ (Figure 27). Similar peaks corresponding to the vibrational modes of BH_4^- exist in each IL. A typical 2D-IR spectrum of a vibrational probe consists of two peaks: one negative peak and one positive peak. The negative peak is found on the diagonal and correlates to a combination of the ground state bleach (GSB) and stimulated emission (SE) transitions. The positive peak is anharmonically shifted off-the diagonal and correlates to the excited state absorption (ESA). Two diagonal bands are clearly evident for the ν_3 (peak 4) and $\nu_2+\nu_4$ (peak 7) modes, thus correlating to the respective GSB and SE transitions. No clear diagonal band for the $2\nu_4$ mode is evident, possibly due to overlap effects with nearby peaks of opposite signs. Two positive peaks appear anharmonically shifted from peak 4. The anharmonic shifts are comparable to that determined by solid state 2D-IR ($\sim$ 44 cm^{-1}, peak 5)[126] and by IR-pump IR-probe experiments ($\sim$ 120 cm^{-1}, peak 6).[125] Therefore, it appears that two ESA

transitions exist for the ν_3 mode of BH_4^-.

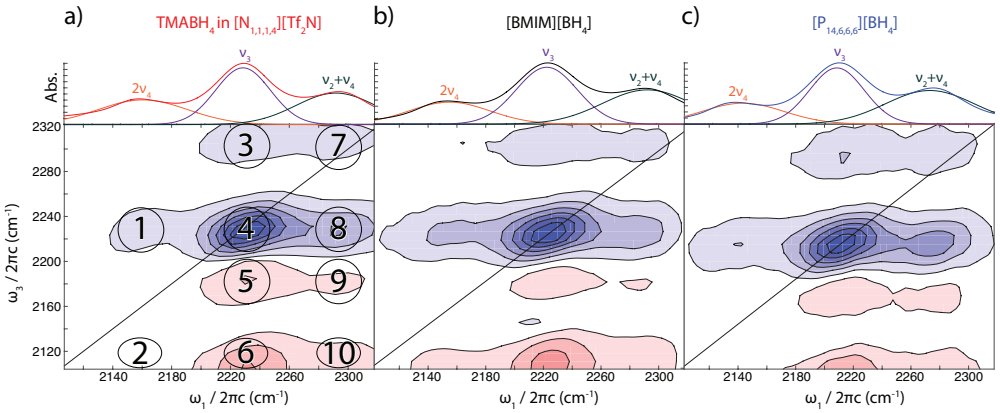

Figure 27: Several crosspeaks appear in the 2D-IR spectra of BH_4^- in ILs due to vibrational coupling between the ν_3 mode and the two Fermi resonances. 2D-IR spectra are obtained on various BH_4^- ILs at a t_2 of 0.5 ps: a) $\sim$ 150 mM $N_{1,1,1,1}BH_4$ in $[N_{1,1,1,4}][Tf_2N]$ b) [BMIM][BH_4] and c) $[P_{14,6,6,6}][BH_4]$.

In addition to multiple ESAs, several cross-peaks appear indicating vibrational energy coupling between the three vibrational modes. A crosspeak is identified as consisting of a different initial frequency (ω_1) from its final frequency (ω_3). The obtained 2D-IR spectra show crosspeaks between ν_3 and the $2\nu_4$ modes (peaks 1 and 2) and between the ν_3 and $\nu_2 + \nu_4$ modes (peaks 3, 8, and 9). A crosspeak (peak 10) between the two Fermi resonances ($2\nu_4$ and ν_2+ν_4) appears, though no complementary peak is observed.

As t_2 is varied in the experiment, intramolecular energy redistribution between modes is evident through the appearance of new crosspeaks (Figure 28). For example, the corresponding crosspeak to peak 1 (peak 14) appears either due to energy redistribution between the ν_3 and the $2\nu_4$ modes or population relaxation of peak 6 causing less overlap/cancelation effects. There are five additional positive peaks that appear in the 2D-IR spectrum as t_2 increases (peaks 11, 12, 13, 15, and 16). The positive peaks are difficult to qualitatively assign as the corresponding transitions involve a state from the second excited state manifold. A detailed approach at understanding all possible transitions is necessary to understand the complicated 2D-IR spectra of BH_4^- ILs.

5.4.4 Model Hamiltonian Analysis of the Spectrum

Quantitative modeling of the spectra allows an assignment of the complicated 2D-IR spectra of BH_4^- in $[N_{1,1,1,4}][Tf_2N]$. To model the 2D-IR spectra including the Fermi resonances, we construct a vibrational Hamiltonian with ν_2, ν_3, and ν_4 modes including cubic and quartic couplings (Equation 5.2). Building off of previous models, we extend this approach for a more complete and robust representation for three coupled vibrations.

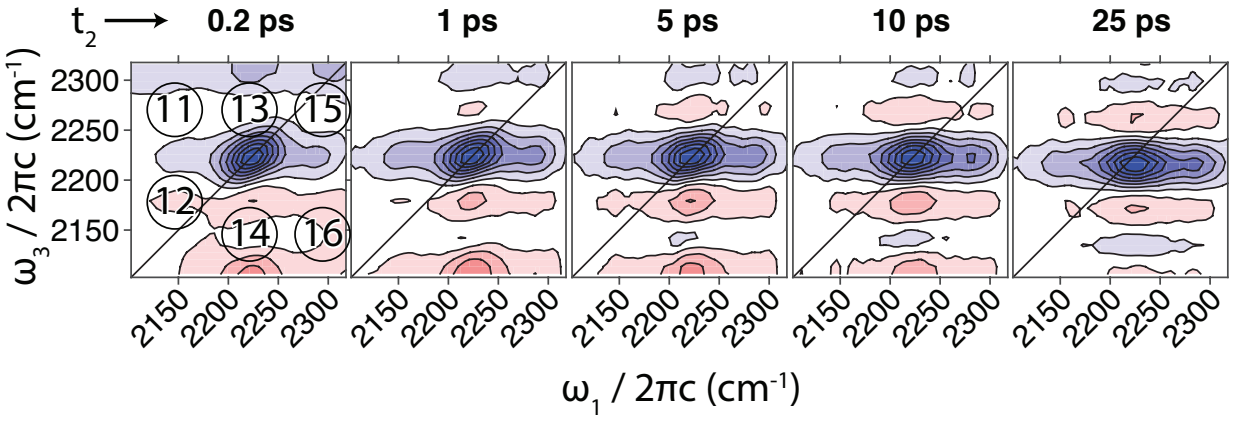

Figure 28: Crosspeaks appear over time due to vibrational energy redistribution between the vibrational modes. 2D-IR spectra of $[BMIM][BH_4]$ are obtained with varying t_2 from 0.2 to 25 ps.

The vibrational Hamiltonian consists of the creation operator ($b_i^\dagger$), the annihilation operator (b_i), the position operator ($\hat{X}_i$) of mode i, and the three and four mode coupling constants (η_{ijk} and η_{ijkl}, respectively) between modes i, j, k, and l.

$$\begin{aligned} H = &\sum_{i=2}^{4} \hbar\omega_i (b_i^\dagger b_i + 1/2) \\ &+ \sum_{i,j,k=2}^{4} \frac{\eta_{ikj}}{6} \hat{X}_i \hat{X}_j \hat{X}_k \\ &+ \sum_{i,j,k,l=2}^{4} \frac{\eta_{ikjl}}{24} \hat{X}_i \hat{X}_j \hat{X}_k \hat{X}_l \end{aligned} \tag{5.2}$$

To reduce the number of free parameters, we treat only six parameters as non-zero: the three frequencies for the primary transitions ω_i, the quartic anharmonicity of the ν_3 mode, η_{3333}, and the coupling constants η_{223} and either η_{344} or η_{234}. In this approximation, we assume that the cubic and quartic diagonal anharmonicities of the lower-frequency modes ν_2 and ν_4 (η_{222}, η_{2222}, η_{444}, and η_{4444}) are zero,[99] and we use only the quartic anharmonicity to describe the diagonal anharmonicity of the ν_3 mode. The dipole operator of the ν_3 mode is non-zero, so it is a dipole allowed transition (a bright mode). The dipole operator of the other two modes is zero (dark modes), and they only contribute to the spectrum through their mixing with the ν_3 mode.

The matrix form of this Hamiltonian is calculated in a product-mode basis of states including up to ten quanta in each mode. Diagonalization of the Hamiltonian provides the eigenvalues and eigenvectors. The ten quanta ensure that the eigenvalues and eigenvectors are converged. The physical interpretation of the eigen-energies is clear, but the eigenvectors are complicated. This type of calculation is effectively a vibrational configuration interaction treatment in the harmonic oscillator basis, truncated at a certain level. The eigenvectors are mixed configurations. This mixing is a representation of the dynamical correlation of the vibrations, which is the essential physical ingredient necessary to capture Fermi resonances. The configuration mixing is the process which allows the overtone and combination bands to mix with the bright state and become IR active.

This approach consists of strengths and weaknesses. Eq. 5.2 is an effective Hamiltonian with 6 free parameters. It should be noted that the dimensionality of the problem is reduced from nine to three, which means we are treating only one of the triply degenerate sets of modes. This vastly reduces the size of the Hamiltonian matrix, at the cost of not correctly treating the symmetry of the problem. As a result, the effective coupling constants are not directly related to the coupling constants from an anharmonic quantum chemistry calculation.

In addition, we neglect quartic couplings. In general, cubic and quartic couplings are of similar order of magnitude, and quartic terms are required to maintain a bound potential for all values of the normal mode displacement. For the current work, the fitting of the spectra do not converge with quartic couplings, so only cubic couplings are retained. The

eigenvectors and eigenvalues are checked to ensure that no spurious divergences contaminate the results by, for example, checking that the lowest energy state has very high overlap with the uncoupled vibrational ground state. Future work will extend this formalism to correctly treat the symmetry and dimensionality to connect these couplings to vibrational potential energy surfaces from quantum chemistry.

Diagonalizing this vibrational Hamiltonian generates eigenvalues and eigenstates of the coupled modes. Matrix elements of the dipole operator in the eigenvector basis provides the transition amplitudes between eigenstates. The eigen-energies and mixing coefficients are inputs to a response-function formalism which sums over all the rephasing and non-rephasing pathways and generates the 2D spectra.[96] The line-broadening is applied to the simulations based on the experimentally extracted frequency fluctuations of the diagonal ν_3 band (Section 5.4.3).

The free parameters of Equation 5.2 are adjusted to reproduce the features in the experimental spectrum (Appendix A.2). The parameters are highly coupled; they are sensitive to small changes but not unique in their ability to reproduce the spectrum. For example, spectra calculated with two different forms of coupling of the ν_4-mode to the ν_3-mode are successful at reasonably reproducing the spectra. Both $\eta_{2,3,4} \neq 0$ and $\eta_{344} \neq 0$ can produce similar features in the spectra, essentially the eigenvalues and dipole matrix-elements. As such, we suggest that this model provides a qualitative picture of the complex vibrational manifold of states and guides our assignment of the transitions.

The resulting complicated energy level diagram (Table 3) shows only the states that carry appreciable oscillator strength ($> 1\%$ of the largest transition). Each eigenstate exhibits mixed excited state character, but the largest components identify eigenstates 4, 5, and 6 as the $2\nu_4$, ν_3, and $\nu_2 + \nu_4$ modes, as expected. The mixture of the $|0, 1, 0\rangle$ configuration in eigenstates 4 and 6 is what lends oscillator strength to these otherwise dark modes, the defining characteristic of Fermi resonances. The two-exciton manifold is more complicated, including 7 mixed states (eigenstates 14 through 20) that can be reached from the one-exciton manifold.

From the eigenvalues and eigenstates of the coupled modes, the simulated spectrum reproduces key features of the experiment (Figure 29). In all, 21 pathways contribute to 18

Table 3: The energy levels are formulated by diagonalizing the anharmonic Hamiltonian (Equation 5.2). The nomenclature for a given state is $|\nu_2, \nu_3, \nu_4\rangle$. Therefore, the representation of the first excited state of the ν_3, overtone, and combination band are $|0, 1, 0\rangle$, $|0, 0, 2\rangle$, $|1, 0, 1\rangle$ respectively. The first excited state manifold contains three mixed energy levels. The second excited state manifold is more complex with 7 mixed states that contribute to transitions in the 2D-IR spectra.

Energy Levels (#)	Energy (cm^{-1})	States, $\|\nu_2, \nu_3, \nu_4\rangle$ (% contributing)
1	0	$\|0, 0, 0\rangle$ (100 %)
1^{st} Excited State Manifold		
4	2160	$\|0, 0, 2\rangle$ (86 %)
		$\|0, 1, 0\rangle$ (13 %)
5	2208	$\|0, 1, 0\rangle$ (65 %)
		$\|0, 0, 2\rangle$ (21 %)
		$\|1, 0, 1\rangle$ (14 %)
6	2272	$\|1, 0, 1\rangle$ (77 %)
		$\|0, 1, 0\rangle$ (22 %)
2^{nd} Excited State Manifold		
14	4292	$\|0, 0, 4\rangle$ (47 %)
		$\|0, 1, 2\rangle$ (33 %)
15	4342	$\|0, 2, 0\rangle$ (55 %)
		$\|0, 0, 4\rangle$ (29 %)
		$\|1, 1, 1\rangle$ (10 %)
16	4386	$\|1, 0, 3\rangle$ (35 %)
		$\|0, 2, 0\rangle$ (26 %)
		$\|0, 1, 2\rangle$ (21 %)
		$\|0, 0, 4\rangle$ (18 %)
17	4427	$\|1, 1, 1\rangle$ (36 %)
		$\|0, 1, 2\rangle$ (24 %)
		$\|2, 0, 2\rangle$ (22 %)
		$\|1, 0, 3\rangle$ (22 %)
18	4474	$\|1, 0, 3\rangle$ (40 %)
		$\|2, 0, 2\rangle$ (21 %)
		$\|0, 1, 2\rangle$ (20 %)
		$\|1, 1, 1\rangle$ (10 %)
19	4527	$\|2, 1, 0\rangle$ (58 %)
		$\|3, 0, 1\rangle$ (26 %)
		$\|1, 1, 1\rangle$ (11 %)
20	4562	$\|2, 0, 2\rangle$ (53 %)
		$\|1, 1, 1\rangle$ (30 %)

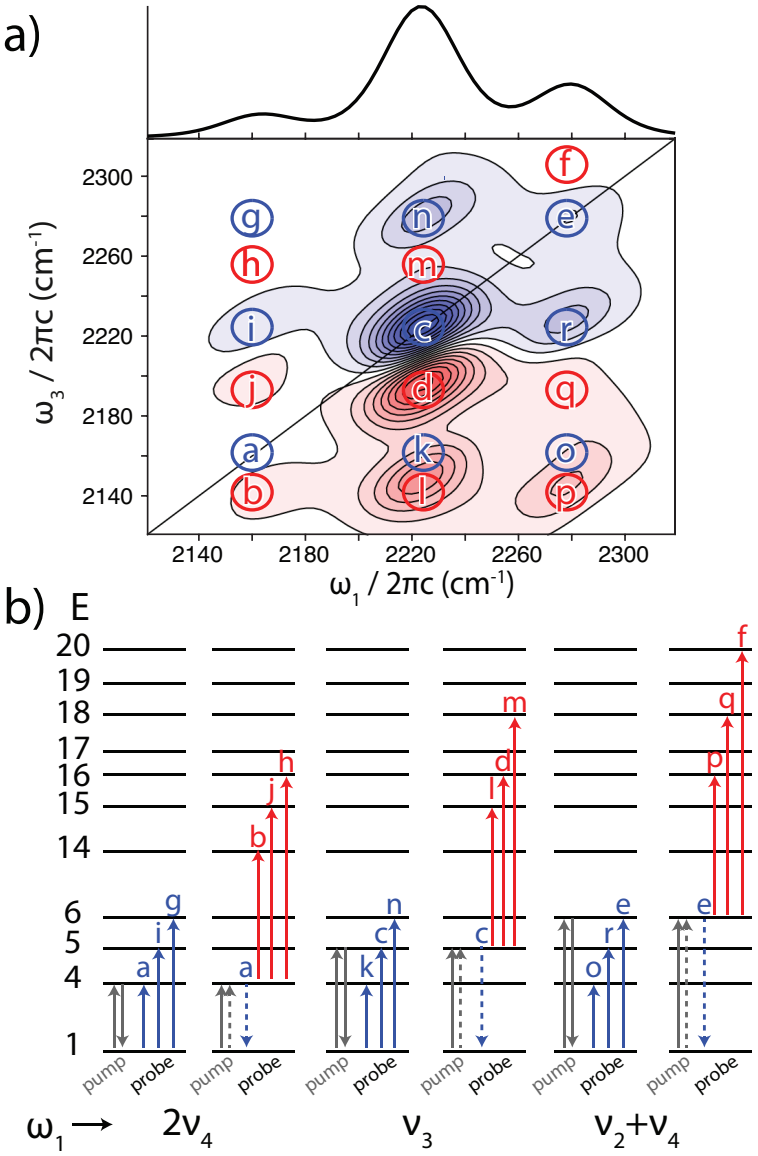

Figure 29: a) The simulated spectrum does reproduce key features of the experiment, however there are some minor differences. The results from the simulated 2D-IR spectrum reveal that there are 21 pathways that contribute to 18 peaks. The BH_4^- spectrum is simulated by response function formalism. The simulated BH_4^- 2D-IR spectrum is labeled by the most contributing pathway to a given peak. The diagonal peaks (**a**, **c**, **e**), the ESA (**b**, **c**, **f**), negative (**g**, **i**, **k**, **n**, **o**, and **r**) and positive crosspeaks (**h**, **j**, **m**, **p**, **g**) are all accounted for. b) Wave mixing diagrams represent the most contributing pathway to a given peak. The wave mixing diagrams are separated by the given population state at ω_1.

peaks in the 2D-IR spectrum of BH_4^-. Multiple Liouville pathways exist for each peak, but for simplicity, we list only the pathway with the largest contribution for each peak. Inter-state coherence pathways are included in the calculations but are not the most contributing pathway for any peak.

Many excitation pathways contribute to the 2D spectra, which we summarize in wave-mixing diagrams (Figure 29). In the wave mixing diagram, the first two electric field interactions are from the pump pulses. The third pulse generates another coherence state in the first or second excited state. There is then an emitted field, photon echo, that heterodyne mixes with the local oscillator. The third interaction can either connect the ground state and the one-exciton manifold (blue arrows), which corresponds to stimulated emission and ground state bleaches, or the one- and two-exciton manifolds (red arrows), which corresponds to excited state absorptions.

Each peak can be designated by the sequence of electric field interactions that connect the different eigenstates. For example, peak **a** comes from three electric field interactions between eigenstates 1 and 4. As another example, pumping the $\nu_2 + \nu_4$ mode (eigenstate 6) and then the $2\nu_4$ mode (state 16, $\sim 50\,\%$ $|1,0,3\rangle$) generates a crosspeak in the bottom right of the spectrum (peak **p**). In this way, each peak in the spectrum can be assigned to different pathways up and down the ladder of mixed vibrational states.

Two interesting features deal with two excited state absorptions (peaks **d** and **l**). Both originate from excitations of the ν_3 mode (eigenstate 5), ascending to eigenstates 16 and 15, respectively. Eigenstate 15 is predominantly a $2\nu_3 \equiv |0,2,0\rangle$ state which accounts for the high intensity of peak **l**. Eigenstate 16 on the other hand, is predominantly a mixture of the overtone ($|0,0,2\rangle$ and combination bands ($|1,0,1\rangle$), namely $|1,0,3\rangle$.

As much as the simulated spectrum captures many features of the experimental spectrum, there are some differences. The ordering of the intensities of the overtone and combination band is not correct in the linear and 2D spectra (diagonal peaks). In addition, the simulation gives stronger crosspeaks **g** and **h** than those observed experimentally. Given the simplicity of the model, these shortcomings are not unexpected, and more complex models may be able to better capture the features of the experimental observations. Overall, the modeling provides an initial understanding of the origin of the peaks in the 2D spectrum and sets the

stage for characterizing the dynamics.

5.4.5 Vibrational Energy Redistribution, Relaxation, and Thermalization of BH_4^- Ionic Liquids

Polarization-dependent IR pump-IR probe experiments assess the vibrational lifetime of the ν_3 mode. To isolate the vibrational lifetime from rotational effects, we measure the IR pump-IR probe spectrum from -2 to 200 ps in parallel and perpendicular polarization conditions to calculate the isotropic signal, which is equivalent to a magic angle experiment.[172] The parallel and perpendicular polarization conditions also allow us to isolate rotational dynamics by calculating the anisotropy.

The IR pump-IR probe spectra show multiple transitions which we assign to absorptions of the ν_3 and $2\nu_4$ modes (Figure 30a). The overlap of the peaks make them difficult to assign solely on the pump-probe spectra. Based on our analysis of the structure for the 2D-IR spectra, the IR pump-IR probe spectra reveal 4 transitions in the spectral window: the GSB of the ν_3 (peak 4) and $2\nu_4$ (not seen in the 2D-IR spectra) modes and the two ESA of the ν_3 mode (peak 5 and 6).

The second ESA amplitude decays to zero, whereas the GSB decays to an offset (Figure 30b). The vibrational relaxation time is measured for the isotropic signal by plotting the max/min amplitude of a single frequency as a function of delay time for the GSB and the second ESA of the ν_3 mode, respectively. Represented here by the constant (c) in the GSB fit, a significant bleach at $\sim$ 200 ps remains for the BH_4^- ILs that indicates a thermalization effect and the existence of a hot ground state (Figure 30b inset). Vibrational energy relaxation from the BH-stretch into the low-frequency bends and intermolecular motions leads to signals which relax on the timescale of thermal transport of the excited sample volume. Similar solvent heating effects are observed for BH_4^- in aqueous solutions as discussed in Chapter 4.

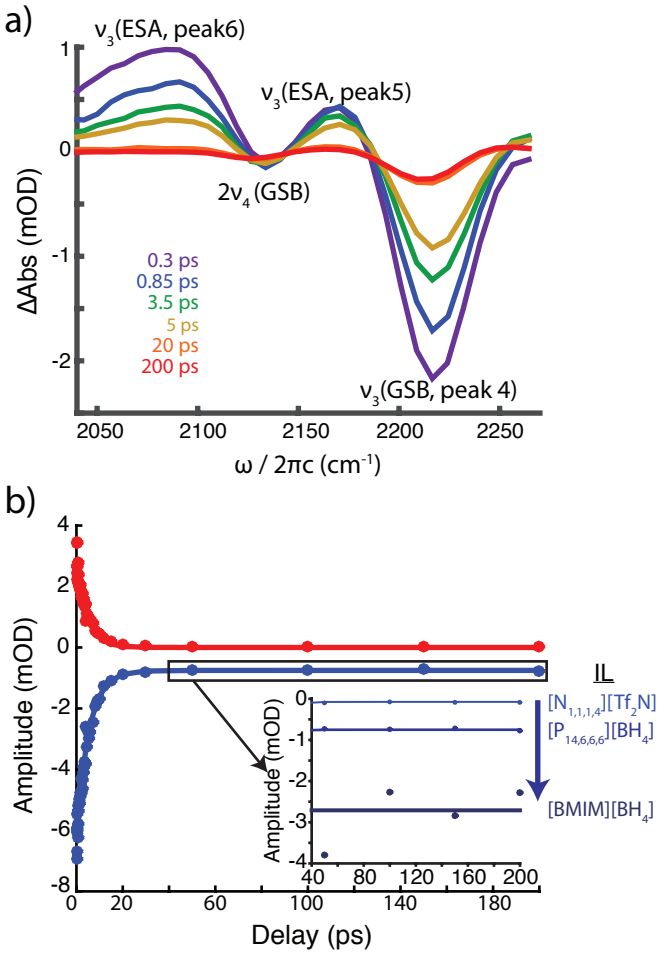

Figure 30: a) The GSB of the ν_3 mode is still evident at $\sim$ 200 ps. The IR Pump-IR Probe spectra of $[P_{14,6,6,6}][BH_4^-]$ in the all parallel direction reveals four transitions: GSB for the ν_3 and $2\nu_4$ modes and the two ESA of the ν_3 mode. b) The population relaxation time (T_1) is determined from the isotropic signal. For the isotropic signal of $[P_{14,6,6,6}]][BH_4^-]$, the amplitude at a single point of the ν_3 GSB (2216 cm^{-1}) and for the second ν_3 ESA (2084 cm^{-1}) is plotted with respect to delay time. An offset represents a long lived GSB or hot ground state (HGS) and varies in amplitude across the investigated ILs (inset).

Table 4: The population lifetime (T_1) for each IL sample is determined by plotting the max/min amplitude of the GSB and second ESA of the ν_3 mode for the isotropic signal. The ESA fits to a single exponential, and the GSB fits with a single exponential that includes an offset to account for the long-lived HGS. The amplitude of the fit is represented by A and c is the offset.

	[BMIM][BH_4]	[$P_{14,6,6,6}$][BH_4]	$N_{1,1,1,1}BH_4^-$ in [$N_{1,1,1,4}$][Tf_2N]
GSB			
A	-1.5 ± 0.2	-1.87 ± 0.09	-1.3 ± 0.05
T_1 (ps)	2.0 ± 0.5	5.3 ± 0.7	6.4 ± 0.6
c	-0.90 ± 0.09	-0.25 ± 0.08	-0.02 ± 0.04
ESA			
A	1.10 ± 0.06	0.95 ± 0.05	0.48 ± 0.01
T_1 (ps)	2.4 ± 0.3	4.6 ± 0.7	4.7 ± 0.4

The GSB and the second ESA peaks of the ν_3 mode decay on slightly different timescales between ILs (Table 4). A single exponential with an offset represents the decay of the GSB along with the long lived hot ground state, and a single exponential correlated well to the decay of the second ESA. The vibrational relaxation time calculated from the isotropic signals yields a vibrational lifetime (T_1) in the given solvent. The reported T_1 times are slower in [$P_{14,6,6,6}$]][BH_4^-] ($\sim$ 4.7 ps) and the saturated solution of $N_{1,1,1,1}BH_4$ in [$N_{1,1,1,4}$][Tf_2N] ($\sim$ 6.5 ps) than in [BMIM][BH_4] ($\sim 2-3$ ps). For [BMIM][BH_4], the faster T_1 could be attributed to a larger water content.

The measured anisotropy does not correlate to the molecular rotational dynamics of BH_4^- in different solvation environments (Appendix A.2). The anisotropic signal of the ν_3 mode of BH_4^- is $\sim$0.05 at early times (t$\sim$150 fs) and decays on a fast timescale ($\sim$200 fs) for all IL samples. The anisotropic results measured in ILs correlate to what was measured for the ν_3 mode of BH_4^- in Chapter 4. As the ILs in this study are 100-fold more viscous than H_2O, the anisotropy correlates to the intramolecular redistribution of the triply degenerate

ν_3 mode and is independent of the bath environment.

With 2D-IR, intramolecular energy redistribution between the bright mode and the Fermi resonances is determined from an amplitude change in crosspeaks. Analysis of the 2D-IR spectra (Figure 28) gives an approximately 200 fs rise and a few ps decay. We interpret the kinetics of the crosspeak as a mixture of intramolecular vibrational energy redistribution, vibrational energy relaxation, and thermalization. The fast rise (200 fs) of peak 1 is likely due to the redistribution of vibrational energy between the ν_3 and $2\nu_4$ modes. The kinetics of the corresponding crosspeak (peak 14), which is due to downhill energy transfer between ν_3 and $2\nu_4$. The kinetics, however, are not clear as peak 14 overlaps with two positive peaks that have ESA character. Other crosspeaks' amplitudes vary with t_2 and correlate energy transfer between the three coupled vibrational modes, but the kinetics are in the motionally narrowing limit.

5.4.6 Solvent Reorganizational Dynamics of BH_4^- Ionic Liquids

The solvent dynamics of BH_4^- vary with the ILs under investigation revealing different local solvent structures. 2D-IR spectra are collected up to 30 ps for each BH_4^- IL under investigation. In each IL, the vibrational lifetime of the ν_3 mode is determined to be ~3 to 6 ps depending on the respective sample. Due to the evidence of a thermalization effect, any CLS result at long t_2 ($\sim 10\ ps$) will no longer correlate to the molecule initially excited and will contain no information on the local solvent environment.

In the ILs at early t_2 ($\sim$ 0.2 ps), the 2D-IR spectrum of the ν_3 mode indicates a larger inhomogeneous component than seen previously in aqueous solutions[19,173] (Figure 28). Due to the complicated nature of the BH_4^- 2D-IR spectra, center line slope (CLS) was performed only on peak 4, which is the GSB and SE of the ν_3 mode, similar to Chapter 4 and other BH_4^- studies[19].

The FFCF parameters are extracted from the CLS results (Figure 31a). The initial CLS value ($t_2 \sim$ 200 fs) for the ν_3 mode is $\sim$ 0.35, $\sim$ 0.31, and $\sim$ 0.32 for $N_{1,1,1,1}BH_4$ in $[N_{1,1,1,4}][Tf_2N]$, $[P_{14,6,6,6}][BH_4]$, and [BMIM][BH_4] respectively. A biexponential function is used to represent the relaxation of the ν_3 mode in the ILs, where A_1 and A_2 are the amplitude

of the frequency fluctuations, τ_1 is the fast time component of the timescale of frequency fluctuations, and τ_2 is the slow time component (Table 5).

$$c_2(t) = A_1 e^{-t/\tau_1} + A_2 e^{-t/\tau_2} \tag{5.3}$$

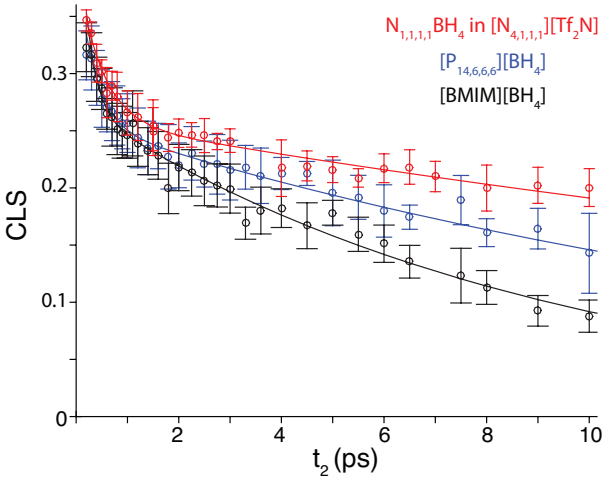

Figure 31: a) The resulting dynamics correlate to the solvent reorganization timescale in different ILs. The CLS values are calculated for all ILs and are fitted to a biexponetial $N_{1,1,1,1}BH_4$ in $[N_{1,1,1,4}][Tf_2N]$ (red), $[P_{14,6,6,6}][BH_4]$ (blue), and $[BMIM][BH_4]$ (black).

Table 5: FFCF parameters are determined for the BH_4^- ν_3 mode using a biexponential fit to the CLS values for BH_4^- in an aprotic IL and both BH_4^- ILs, respectively.

	τ_1 (ps)	τ_2 (ps)	A_1	A_2
$[BMIM][BH_4]$	0.2 ($\pm$0.2)	9.2 ($\pm$0.7)	0.2 ($\pm$0.2)	0.27 ($\pm$0.01)
$[P_{14,6,6,6}][BH_4]$	0.3 ($\pm$0.2)	17 ($\pm$2)	0.14 ($\pm$0.06)	0.257 ($\pm$0.009)
150 mM $N_{1,1,1,1}BH_4^-$ in $[N_{1,1,1,4}][Tf_2N]$	0.5 ($\pm$0.1)	33 ($\pm$7)	0.14 ($\pm$0.02)	0.259 ($\pm$0.008)

The fast and slow timescales vary in the ILs under investigation (Table 5). The fast time (τ_1) is on a sub-picosecond timescale, and the slow time (τ_2) varies on a picosecond timescale

(9.2 to 33 ps). Overall, the bulk BH_4^- ILs reorganize on a faster time scale than the saturated solution of $N_{1,1,1,1}BH_4^-$ in $[N_{1,1,1,4}][Tf_2N]$(Figure 31b). Between the two BH_4^- ILs, the more sterically hindered $[P_{14,6,6,6}][BH_4]$ reorganizes on a slower timescale than [BMIM][BH_4].

5.5 DISCUSSION

As discussed in Chapter 4, the BH_4^- 2D-IR spectrum in H_2O is broad, and the peaks are unresolved, but in an IL, the BH_4^- 2D-IR spectrum is narrow, and the peaks are resolved. The narrowed vibrational modes of BH_4^- in an IL result in less overlap of peaks with opposite signs resulting in cancelation effects. In the BH_4^- ILs 2D-IR spectra, there are a total of 16 identifiable peaks compared to only 5 possible peaks in the 2D-IR spectra of BH_4^- in H_2O. In the IL spectra, there is a well-defined overlap between peak 4 (ν_3 GSB/SE) and a crosspeak (ν_3 and $2\nu_4$). In the H_2O spectra, peak 4 is asymmetrical, and it is not clear that ν_3 GSB/SE is overlapping with a crosspeak. For another example, peak 5 (ν_3 ESA) is clearly visible in the IL spectra, but in the aqueous spectra, overlap with the broad peak 4 causes it to appear as a small positive amplitude. Overall, the resolved 2D-IR spectra allow a better understanding of vibrational coupling between the dark and bright modes BH_4^- in solution.

Using a Hamiltonian model approach, we can assign the complex 2D-IR spectra of BH_4^- in ILs. Previous ultrafast vibrational experiments on BH_4^- have identified quite different anharmonicities for the ν_3 mode: a small (44 cm^{-1}) by IR-pump IR probe spectroscopy[125] and a large (120 cm^{-1}) anharmonicity by solid state 2D-IR. In the IR pump-IR probe experiments for the BH_4^- ILs, both excited state absorbances are also evident. Our Hamiltonian model approach enables the assignment of those two ESA peaks (peak 5 and 6) with a respective pathway (**d** and **l**). Both pathways have a population state of the $|0,1,0\rangle$ (ν_3) mode, but the second coherence time populates eigenstate 15 and 16 for peaks 5 and 6, respectively. Both of these mixed eigenstates consist of a $|0,2,0\rangle$ character. Thus, the pathways correlate to a ESA peak for the ν_3 mode. In eigenstate 15, the $|0,2,0\rangle$ state contributes to over half of the character for the given state. Eigenstate 16, however, has $|1,0,3\rangle$ character as the most

contributing state, and the $|0,2,0\rangle$ state is only contributing 26%.

In addition to understanding vibrational mode coupling, we can lay out the vibrational energy cascade in an IL from the IR Pump-IR Probe data. Previously reported, a similar mechanism describes the vibrational energy redistribution, relaxation, and thermalization in aqueous solutions[174]. The IR pump populates one of the BH stretching modes or Fermi resonances: $2\nu_4$, ν_3, or $\nu_2 + 2\nu_4$. As seen by crosspeaks in the 2D-IR spectra, vibrational energy redistribution will occur between the three coupled modes on a fast timescale ($\sim$ 200 fs). Vibrational energy will then relax to low-frequency bends and intermolecular motions. As seen by an apparent bleach at long t_2 ($\sim$ 200 ps) from the IR pump-IR probe and 2D-IR, the vibrational energy will then relax into thermally populated states (HGS) before ultimately relaxing to the ground state.

Vibrational energy can relax into several low frequency modes of H_2O, resulting in a faster relaxation of the ν_3 mode. The reported T_1 for the ν_3 mode varies in each IL. The [BMIM][BH_4] sample in the IR pump-IR probe experiment has a larger water content ($\sim$1.6 M) than in the other two IL samples. While drying the sample, the sample degraded through self hydrolysis through a visual observation of $H_{2(g)}$ generation after a few hours, thus the IL could not be completely dried. As the ν_3 mode relaxes, broad water modes will accept more energy, resulting in a faster T_1 that is more on par with the T_1 in aqueous solutions, as discussed in Chapter 4.

The thermalization effect, shown by the offset in the GSB , is consistent with the trend of the T_1 of the ν_3 mode. As discussed in Chapter 4, a thermalization effect occurs in 3 M $NaBH_4$ solutions in high base concentrations. When T_1 is large, as in [$N_{1,1,1,4}$][Tf_2N], cooling of the ν_3 mode occurs instantaneously. In the bulk BH_4^- ILs, however, T_1 is faster than the cooling time. Similar T_1 effects were seen for the nitrile stretch of SCN^- in ILs, where water was introduced[12]. Thus, the rate of energy transfer to the solvent (H_2O modes) results in a faster energy jump. The thermalization effect hinders the effective t_2 range for extracting the FFCF. It should be noted that the thermalization effect is governed by the heat transfer out of the pump beam through the solvent windows and then dispersed throughout the sample.[175]

From the FFCF, timescales of frequency fluctuations are determined that correlate to

local solvent structural dynamics. The initial amplitude of the FFCF (t_2 →0.2 ps) is higher in the IL samples, so something is slower than in water. Overall, we determine a fast and slow timescale in the IL samples. The fast dynamics (τ_1) are approaching the motional narrowing limit and slightly vary with IL. In aqueous solutions, Giammanco *et al.*[19] resolve a 300 fs timescale for the dynamics of BH_4^- in H_2O, and in Chapter 4, we resolve a 200 to 800 fs fast solvent reorganizational time of BH_4^- in aqueous solutions with increasing NaOH concentrations. As the fast time is independent of the bath environment, τ_1 may correlate to the intermolecular energy redistribution of the triply degenerate ν_3 mode.

In other ionic liquids, the solvent dynamics trend linearly with viscosity. Spectral diffusion of CO_2 in a variety of ILs[13] follows a nearly linear trend with viscosity over a wide range, from 13–104 ps and 12 to 170 cP. The dynamics of SCN^-[12] and HOD[176] fall on the same trend line.[13] The τ_2 of the $N_{1,1,1,1}BH_4$ in $[N_{1,1,1,4}][Tf_2N]$ fall substantially below this trend line as it has a reported viscosity of 100 cP. The previous trendline would predict dynamics on a ∼ 60 ps timescale, while we observe a ∼ 33 ps timescale. This suggests that the local reorganization around the BH_4^- is perhaps not gated by the motion of the ions of the IL solvent in the same way.

Also, the BH_4^- ILs do not follow a correlation of viscosity with the local dynamics as seen previously in imidazolium ILs. The viscosity of $[BMIM][BH_4]$ and $[P_{14,6,6,6}][BH_4]$ (533 and 1064 cP, respectively) are 5 and 6-fold larger than the ILs studied with CO_2.[13] Therefore, it would be expected that spectral diffusion in the BH_4^- ILs would occur on a slower timescale than 104 ps, yet the spectral diffusion times are on par with CO_2 in lower viscosity solvents (12 cP). The reorganization of the ion cage around a BH_4^- anion is expected to be different from CO_2. In aqueous solutions, the slow spectral diffusion times of the ν_3 mode of BH_4^- correlate to the reorganization of dihydrogen bonds.[19] Therefore, the spectral diffusion time may be influenced by the reorganization of these dihydrogen bonds, resulting in a faster timescale. The 2-position on the BMIM cation is acidic and could dihydrogen bond with the partially negative charged hydrogens of BH_4^-. Methylating the 2-position of the cation for $[BMIM][BH_4]$ could probe the influence of dihydrogen bonds in the IL where we would expect a slower spectral diffusion time more on par with viscosity. It should also be noted that a large amount of water in the $[BMIM][BH_4]$ could indicate that dihydrogen bonding is

occuring between water and the BH_4^- anions in the first solvation shell.

Directly comparing the two BH_4^- ILs, the 2-fold less viscous [BMIM][BH_4] has a 2-fold faster spectral diffusion time than [$P_{14,6,6,6}$][BH_4]. The $P_{14,6,6,6}^+$ cation is bulkier than the BMIM cation, especially due to the long 14 carbon alkyl chain. A further 2D-IR study of varying the long alkyl chain component of a $P_{X,6,6,6}^+$ cation (where x is the long alkyl chain component) and varying the alkyl chain of the imidazolium cation could provide new insights into how sterics of the cation may influence molecular motions of these novel BH_4^- ILs. Molecular dynamic simulations can provide further insight into how the BH_4^- ILs undergo solvent reorganization compared to the well established imidazolium ILs.

5.6 CONCLUSION

In addition to bulk thermophysical properties, we identify spectroscopic characteristics for bulk BH_4^- ILs and BH_4^- dissolved in an aprotic IL. In ILs, the vibrational linewidths are narrower than water[173], which allows an analysis of the vibrational coupling between bright (ν_3) and dark ($2\nu_4$ and $\nu_2+\nu_4$) modes in the spectrum. A model Hamiltonian approach is able to capture the complicated structure of the Fermi resonances in the 2D-IR spectra. The eigenstates show that the excited state manifold consists of mixed character of three primary vibrational modes (ν_2, ν_3, and ν_4), thus revealing that two peaks in the 2D-IR spectra arise from the ESA of the ν_3 mode. The vibrational energy cascade of the ν_3 mode of BH_4^- was probed through analysis of vibrational relaxation dynamics determined from polarization-dependent IR pump-IR probe data and of crosspeaks in the 2D-IR spectra.

The timescales of frequency fluctuation give insights into how complex liquids may influence the local solvation shell around the BH_4^- and provide another tool to assist in classifying these novel ILs. Further analyzing the 2D-IR data, we extract a FFCF that reveals aspects of the local structural dynamics. In [$N_{1,1,1,4}$][Tf_2N], the slow solvent reorganizational time (τ_2) is much slower than reported for BH_4^- bulk ILs and does not correlate to previous viscosity trends,[13] indicating the structural reorganization around the BH_4^- anion is gated in a different way. Similarly for the BH_4^- ILs, [BMIM][BH_4^-] resulted in a faster τ_2 than

$[P_{14,6,6,6}][BH_4]$. This difference is likely due to a complementary effect of dihydrogen bonding in the wet [BMIM][BH_4^-] sample and steric effects with the bulky $P_{14,6,6,6}^+$. Overall, these spectroscopic characteristics, i.e. vibrational coupling, thermalization, relaxation, and spectral diffusion, can assist in classifying these novel BH_4^- ILs.

6.0 REORIENTATION-INDUCED SPECTRAL DIFFUSION OF EAN

The text in this chapter has been adapted from a manuscript being submitted to the Journal of Chemical Physics. An early version of the manuscript was submitted to a pre-print server: Johnson, C.A., Parker, A.W., Donaldson, P.M., Garrett-Roe S. ChemRxiv. 2019. DOI: 10.26434/chemrxiv.9876524. The author's contribution includes choosing the system, performing all FTIR and 2D-IR experiments, assisting in the set up of the 2D-IR experiments at the Central Laser Facility at the Rutherford Appleton Laboratory, performing the analysis of the 2D-IR data (except for the 2D-Anisotropy), and writing the manuscript.

6.1 CHAPTER SUMMARY

Using ultrafast two-dimensional infrared spectroscopy (2D-IR), a vibrational probe (thiocyanate, SCN^-) was used to investigate the hydrogen bonding network of the protic ionic liquid ethyl-ammonium nitrate (EAN). The 2D-IR experiments were performed in both parallel ($\langle ZZZZ \rangle$) and perpendicular ($\langle ZZXX \rangle$) conditions at room temperature. The non-Gaussian lineshape in the FTIR spectrum of SCN suggests two sub-ensembles. Vibrational relaxation rates provide evidence of the dynamical differences between the two sub-ensembles: charge depleted (alkyl chain) and charge dense (ammonium headgroups and nitrate ions) regions. The measured rates for spectral diffusion depend on polarization, indicating reorientation-induced spectral diffusion (RISD). A model of restricted molecular rotation (wobbling in a cone) fully describes the observed spectral diffusion in EAN. This complete characterization of the dynamics at room temperature provides the basis for the temperature-dependent measurements in Chapter 7.

6.2 INTRODUCTION

Protic ionic liquids (PILs) are room-temperature molten salts of a Brønsted acid and Brønsted base[78,177]. Their high thermal stability, low vapour pressure, high proton conductance, and "water-like" hydrogen-bonding makes them promising as proton-conducting electrolytes for next-generation fuel cells[79,82]. The exact molecular mechanism of proton transport, however, is still unclear. Proton transport, in turn, is fundamentally controlled by the hydrogen bond network – its structure and fluctuations dictate if protons move independently of the proton donor (Grotthus transport) or with the proton donor (vehicular transport). The lack of a clear mechanistic picture for hydrogen bond dynamics in PILs limits the strategic development and chemical synthesis for applications in industrial processing, and proton conducting electrolytes.

The PIL ethyl-ammonium nitrate (EAN), the first room temperature ionic liquid to be discovered[77], has been extensively studied ever since it was synthesized in 1914. EAN is a "good" PIL ($\Delta\text{pKa} = \text{pK}_{\text{a(base)}} - \text{pK}_{\text{a(acid)}} = 11.93$)[75,178], meaning the acid and base dissociate completely. In addition, EAN behaves like an ideal solution of independent ions[78] and conducts electricity by free diffusion of the ions[178].

EAN forms an extended, three-dimensional hydrogen bonding network comparable to that of $H_2O(l)$ suggesting it may have a similar proton transfer mechanism to $H_2O(l)$. EAN consists of three hydrogen bond donors on the cation and three hydrogen bond acceptors on the anion; the large hydrogen bond angles between the cation and anions result in a majority of bent hydrogen bonds.[85] Far-IR spectroscopy shows that the hydrogen bond stretching and bending modes in EAN are comparable in energy to that of $H_2O(l)$.[83] Dielectric spectroscopy[179] and combined dielectric relaxation and optical Kerr effect spectroscopies[180] provide a detailed picture of the temperature dependence of structural relaxation modes in the liquid. Classical molecular dynamics (MD) simulations find the average hydrogen bond lengths in EAN to be comparable to those of strong hydrogen bonds, and the timescales of molecular rotations of the ammonium cation (NH stretch) are faster in comparison to PILs with weakly interacting single hydrogen bonds[181]. Furthermore, ultrafast mid-IR spectroscopy suggests that the ammonium of EAN undergoes large angle jumps when switching

hydrogen bond partners.[84]

EAN displays both structural and dynamical heterogeneity.[89,182] Ionic liquids (ILs) in general have a propensity to form polar and non-polar domains with sizes on a nanometer length-scale. The polar domains are charge dense and dominated by electrostatic ordering of the cations and anions, whilst the non-polar domains are charge depleted and dominated by weaker van der Waals interactions between alkyl groups.[92,183] Neutron scattering experiments and modeling show that EAN has alternation of charge-enhanced and charge-depleted regions on a nanometer lengthscale.[89,182] In EAN and ethyl-ammonium formate, ultrafast IR-pump IR-probe experiments reveal different rotational times depending on the region under investigation; ionic sub-domains relax much more slowly than the hydrophobic sub-domains.[86] In MD simulations, increasing the alkyl chain length of a primary ammonium PIL increases the dynamical heterogeneity.[184] Solutes can effectively report the dynamical heterogeneity because the solute's vibrational and rotational dynamics can differ in the soft or stiff regions[94,185].

The nitrile stretch of SCN^-, the ν_3 mode, is sensitive to its local environment[148]. In water, neutron scattering suggests that SCN^- accepts one hydrogen bond along with two additional "hydration bonds," which are Coulombic in nature, within the first hydration shell.[186] Early MD simulations notes few linear hydrogen bonds with water[187] and many arrangements of dipolar character, while more recent MD simulations of $SeCN^-$[188] find an average of 3-4 hydrogen bonds, with one of them being an axial (linear) hydrogen bond. Ultrafast infrared spectroscopy can use the ν_3 mode of pseudo-halide anions to investigate ultrafast vibrational dynamics of water and other polar solvents[148,189–194], concentrated ion solutions[195–197], ILs[11,12,152,198,199], supported IL membranes[200], deep eutectic solvents[201], and colloid emulsions[202]. Furthermore, a combination of MD simulations and ultrafast infrared spectroscopy have developed a spectroscopic map of $SeCN^-$ in D_2O that describes the frequency dependence of the nitrile stretch on the hydrogen bonding environment[188].

2D-IR spectroscopy can report two-point correlations in vibrational frequency and orientation. The frequency fluctuation correlation function (FFCF) is revealed through a change in shape of the 2D-IR spectra. The intensities of the spectra encode the orientations of the chromophores with respect to the lab frame. Orientational relaxation can be measured

through both the orientational anisotropy from pump-probe spectra, the standard technique, and also two-dimensional anisotropy, from 2D-IR spectra[203]. When an IR chromophore's vibrational frequency depends on its instantaneous orientation (like a Stark shift), then the frequency and orientational dynamics become coupled.[26,27] The relative angle of the molecule's dipole with the local electric field determines the magnitude of the vibrational frequency shift. As a result, rotation of either the molecule with the respect to a fixed solvation cage or rotation of the solvent electric field relative to the molecule will produce fluctuations in the vibrational frequency. First described by Fourkas et al. for Vibrational Sum Frequency Generation[28] and elaborated by Fayer et al. for 2D-IR spectroscopy[26,27], the FFCF extracted from 2D spectra can be decomposed into reorientation-induced spectral diffusion (RISD) and structural spectral diffusion (SSD) when polarization information is available.

The dynamics of SCN^- in EAN at room temperature are presented in this chapter in comparison to H_2O. The 2D-IR lineshapes of SCN^- in H_2O indicate only a single ensemble and are thus a negative control for sub-ensembles in this context. In Chapter 7, we will compare the activation energies for the dynamics of SCN^- in EAN and H_2O in detail.

In this chapter, we develop an assignment of the two sub-ensembles of SCN^- in EAN. The non-Gaussian structure of the IR absorption spectrum of SCN^- in EAN hints of the presence of two hydrogen bonding environments. The two sub-ensembles are indicated by the frequency-dependent rate of vibrational relaxation in the 2D-IR measurements. The SCN^- band shifts and narrows as a function of the population time, t_2, which strongly indicates two different vibrational relaxation rates. We also observe that the rates of decay of rotational anisotropy are frequency dependent, and the frequency fluctuations also vary somewhat across the spectra. Nevertheless, the time constants for rotational motion and frequency fluctuations are the same for the two sub-ensembles, within error. Treating the frequency and rotational dynamics as representing an average of the two ensembles, a wobbling-in-a-cone RISD model shows that rotational motion suffices to account for the observed spectral diffusion on a few picosecond timescale. The slower times in the rotational anisotropy decay ($\sim$ 25 ps) are believed to represent the slower process of total orientational relaxation either through rotational diffusion or cone-jump processes. The temperature dependence and activation energies of the dynamics of SCN^- in EAN determined through this

approach are reported in Chapter 7.

6.3 EXPERIMENTAL METHODS

The synthesis of EAN, sample preparation, and FTIR methods are described in Chapter 3. This chapter uses the pulse shaping 2D-IR set-up as described in Section 3.5.2.

6.3.1 EAN Synthesis

Ammonium thiocyanate (NH_4SCN, purity $> 97.5\%$), ethyl-amine (67-70 $\%_{wt}$), and 15.7 M HNO_3 were purchased from Sigma Aldrich. EAN was synthesized by an acid-base titration. Before use, the PIL was dried using a vacuum pump (10 μTorr). Solutions were 100 mM of NH_4SCN added to dry EAN and H_2O respectively. The water content in EAN was < 40 mM after drying, confirmed by FTIR (Appendix A.3).

6.3.2 2D-IR

The 2D-IR spectra were recorded simultaneously in the parallel ($\langle ZZZZ \rangle$) and perpendicular ($\langle ZZXX \rangle$) direction for both SCN^- in EAN and H_2O. This enabled polarization dependent data sets to be collected with high signal-to-noise in a matter of minutes. For this chapter, each pair of simultaneously collected $\langle ZZZZ \rangle$ and $\langle ZZXX \rangle$ 2D-IR spectra were recorded with 10s of averaging. Thus, a total of 37 waiting times per temperature meant that 23 temperatures could be collected in under 3 hours. Before the sample, a wire grid polarizer was accurately set to polarize the probe beam at 45° to the bench. The pump pulses were kept parallel to the bench. After the sample, another wire gird polarizer was used to reflect and transmit the $\langle ZZZZ \rangle$ and $\langle ZZXX \rangle$ signals respectively, which were routed to a separate 128 element MCT array detectors. The $\langle ZZXX \rangle$ signal was corrected after collection by multiplying the amplitude of the 2D signal by a correction factor (0.89, i.e. 10 % error). The correction factor was determined by adjusting the anisotropy from a negative offset attributed to a 10 % transmission error in the wire-grid polarizer. The spectral resolution

was 4 cm^{-1} for ω_1 and 3 cm^{-1} for ω_3. The population time (t_2) was varied up to 11 ps for both samples. A thermalization effect was evident for EAN at a long t_2 (> 11 ps); the short vibrational lifetime of the CN stretch in H_2O (2 ps) limits the effective t_2 range ($\sim$ 5.5 ps).

6.4 RESULTS

6.4.1 FTIR

The linear IR spectrum of the nitrile stretching mode (ν_3) of SCN^- EAN provides the first hint that there may be multiple local environments of SCN^- in EAN (Figure 32). In H_2O, the center frequency of the ν_3 mode of SCN^- is 2065 cm^{-1} with a FWHM of $\sim$36 cm^{-1}. The center frequency of the ν_3 mode of SCN^- in EAN is 2059 cm^{-1} with a FWHM of $\sim$50 cm^{-1}; the ν_3 band is also asymmetric with a shoulder at 2070 cm^{-1}. The appearance of a shoulder suggests that SCN^- populates two different environments in EAN. We will show that via measurements of the ν_3 absorption band, 2D-IR can provide additional insight into the hydrogen bonding network of EAN using SCN^- as a vibrational probe.

6.4.2 2D-IR

The change of the shape of the 2D-IR spectra of SCN- with time is complex (Figure 33a). The inhomogeneous linewidth is $\sim$ 40 cm^{-1} at early t_2 times. The spectra remain stretched along the diagonal at 10 ps, indicating that spectral diffusion is not complete in the timeframe of the experiment. In addition, while spectral diffusion occurs, the center frequency of the nitrile band shifts from 2065 cm^{-1} at $t_2 = 0.2$ ps to $\sim$ 2075 cm^{-1} at 10 ps and simultaneously narrows.

To visualize the change in the spectrum, we fit the slices of the spectrum along the pump axis (ω_1) to two Gaussian peaks, one positive and one negative, to account for the negative ground state bleach (GSB) and stimulated emission (SE) and the anharmonically shifted, positive excited state absorption (ESA). These fits determine two parameters, the peak frequency, ω_{center}, and the peak width, σ, which are functions of the initial frequency,

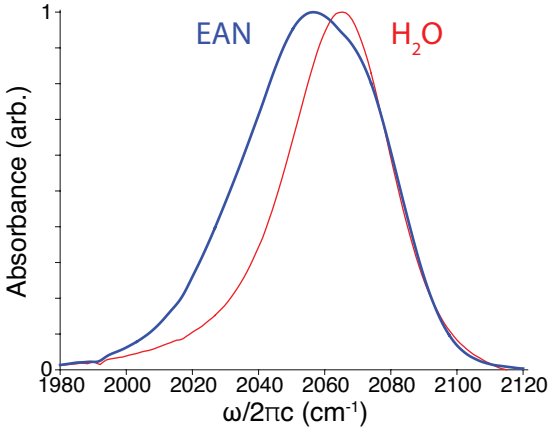

Figure 32: Solvent-subtracted FTIR spectra of the nitrile stretching mode, ν_3 , of SCN^- in EAN (blue) and H_2O (red). In EAN, the nitrile stretch of SCN^- consists of an asymmetrical shape that suggests more than one hydrogen bonding environment.

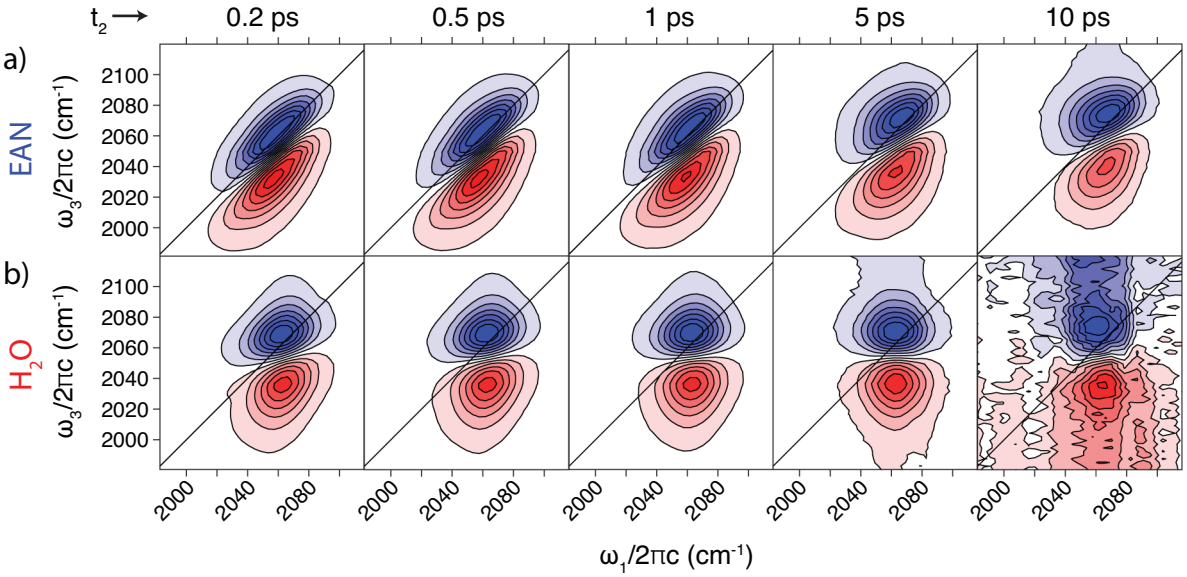

Figure 33: 2D-IR spectra are obtained on the nitrile stretch of SCN^- in a) EAN and b)H_2O at 19 °C in the $\langle ZZZZ \rangle$ polarization condition. Spectral diffusion is much faster in H_2O (< 1 ps) than in EAN (~ 10 ps).

ω_1. The anharmonic shift is constant with frequency and waiting time (~ 20 cm^{-1}).

For Markovian dynamics on a harmonic potential, one expects the centers of the peaks, ω_{center}, to relax to the center of the band (~ 2065 cm^{-1})[20,23,204]. Vibrational modes initially at both low and high frequency will, on average, move towards the average frequency as a function of time. Additionally, one expects the widths of the peaks, σ, to begin at the homogeneous linewidth and then increase together until they reach the average linewidth.

This simple expectation, however, is not what is observed here. The center frequencies (Figure 34a) initially move to toward the center (during the first 1-2 ps) and then all begin to shift to higher wavenumbers (~ 2070 cm^{-1}). The widths start near the homogeneous width, ~ 12 cm^{-1}, and they all increase with time. One side of the spectrum, however, broadens more than the other (Figure 34b).

The vibrational relaxation rate also seems to vary across the spectrum. To isolate population relaxation from orientational relaxation, we calculate the isotropic spectrum 2D-IR spectrum, $S_{\text{iso}}(\omega_1, t_2, \omega_3)$, from the $\langle ZZZZ \rangle$ and $\langle ZZXX \rangle$ measurements, $S_{ZZZZ}(\omega_1, t_2, \omega_3)$ and $S_{ZZXX}(\omega_1, t_2, \omega_3)$,

$$S_{\text{iso}}(\omega_1, t_2, \omega_3) = S_{ZZZZ}(\omega_1, t_2, \omega_3) + 2S_{ZZXX}(\omega_1, t_2, \omega_3). \tag{6.1}$$

Each slice along ω_1 is fit to positive and negative Gaussian profiles representing the ESA and GSB/SE peaks in the 2D-IR spectrum. We assume single exponential loss of the ESA and SE which refill the GSB. Fitting the integrated Gaussian representing the ESA at each ω_1 to an exponential decay we determine the vibrational relaxation time constant, T_1 (Figure 34e). At low ω_1 (2030 cm^{-1}), the apparent T_1 time is ~ 2 ps, and, at high ω_1 (2090 cm^{-1}) it is ~ 4 ps. The loss of signal on the low frequency frequency side of the spectrum relative to the high frequency side of the spectrum is due to faster vibrational relaxation. This effect causes the peak in the 2D-IR spectrum to shift as a function of t_2.

6.4.3 A Model Fitting Approach

To test the hypothesis that two overlapping subensembles with different vibrational relaxation dynamics cause the observed changes in the spectra, we simulate the spectra and

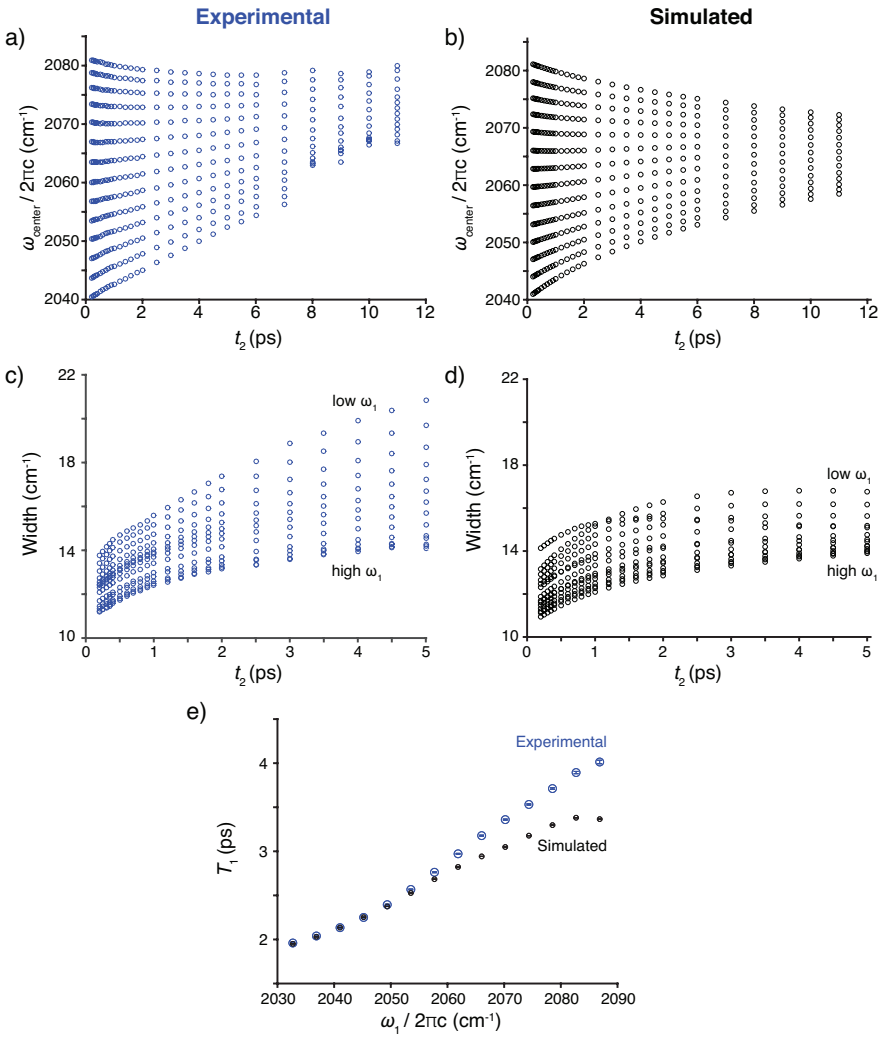

Figure 34: Summary of the analysis of the 2D-IR spectra show frequency-dependent changes in position, width, and amplitude. a) The peaks of the 0-1 band (GSB/SE) as a function of ω_1 shift as a function of t_2. In the first $\sim 2ps$, the peaks converge towards the average frequency due to spectral diffusion. Afterwards, the peak centers shift progressively higher in frequency. c) The width of the 0-1 band increases in an ω_1-dependent fashion. At 0.2 ps, all slices of the 0-1 band has a ~ 12 cm^{-1} standard deviation. Over time, the width of all slices increases, but the widths increase much more on the low frequency side of the spectrum. e) The apparent vibrational energy relaxation time, T_1, extracted from the spectra also vary across the spectrum from $2-4$ ps. b,d,e) Simulations of the 2D-IR spectra using response function formalism and assuming two sub-ensembles reproduce these measures of the spectra semi-quantitatively.

perform a global fit of the model parameters. We calculate third-order response functions based on truncating the cumulant expansion at second order (equivalent to assuming Gaussian statistics). For each subensemble, we include independent, free-fitting variables for the timescales of frequency fluctuations, orientational relaxation, and population relaxation.

To describe frequency fluctuations, we used a Kubo lineshape[96] function incorporating a fast (homogeneous) and a slow component

$$g(t) = \frac{t}{T_2} + \Delta^2 \tau^2 \left(e^{-t/\tau} - 1 + \frac{t}{\tau} \right) \tag{6.2}$$

where T_2 is the dephasing time, Δ is the range of frequencies sampled by the chromophore, and τ is the correlation time. To describe orientational relaxation, we assume single exponential decay of the orientational correlations, and the appropriate orientational averages and orientational relaxation were incorporated to reproduce parallel and perpendicular spectra.[96] Errors are estimated by bootstrapping.[205] The nonlinear least squares fitting is repeated on 100 synthetic data sets, in which random samples of the full data set are chosen, with replacement, to preserve the number of data points. The observed variation in fit parameters serves as an estimate of the error. To describe population relaxation, we assume single exponential loss of the ESA and SE, which refills the GSB and is described by a time constant, T_1. In the fitting procedure, each sub-ensemble has an independent lineshape, orientational relaxation time, and vibrational lifetime. The $\langle ZZZZ \rangle$ and $\langle ZZXX \rangle$ were fit simultaneously at each respective t_2 and temperature.

The complete set of best fit parameters is given in the Appendix A.3. The most notable results are that the spectra are best fit with two sub-ensembles separated by ~ 15 cm^{-1}. The low-frequency sub-ensemble contributes a higher initial intensity by a factor of 1.4, but decays more rapidly ($T_1 = 2.0$ ps versus 5.7 ps). The lower frequency sub-ensemble has faster dynamics, both reorientational times (22 ± 1 ps versus 34 ± 1 ps) and spectral diffusion times (3.3 ± 0.5 ps versus 11.1 ± 0.5 ps).

Overall, the two population 2D-IR simulation replicates the main features in the 2D-IR spectra of SCN^- in EAN data (Figure 35). At early t_2, the GSB peak is elongated along the diagonal. As t_2 increases, the GSB visibly shifts to the higher frequency side as the lower

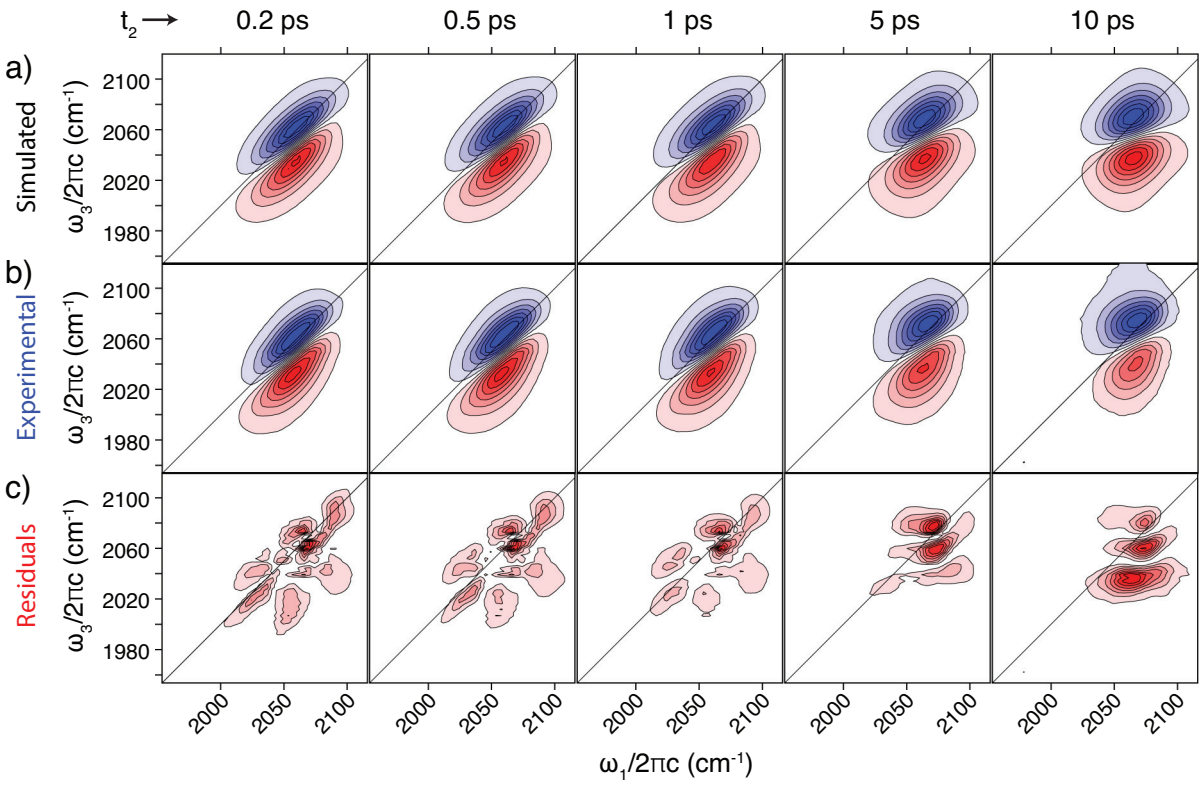

Figure 35: The simulated 2D-IR spectra involving two populations reproduce the main features of the experimental 2D-IR spectra for the nitrle stretch of SCN^- in EAN at $\langle ZZZZ \rangle$ polarization: a) simulated from two different populations at 19 °C b) experimental SCN^- in EAN. c) The residuals begins to show a systematic error at long t_2 (¿5 ps) indicating an unaccounted for HGS. At early t_2 (0.2 ps), the max residual value is $\sim$ 4 % of the max experimental signal and decreases to $\sim$ 1 % at long t_2 (10 ps).

frequency region of the GSB relaxes in a few ps. At a long t_2 (10 ps), there is a systematic error in the residuals due to a hot ground state (HGS) that is not accounted for.

Analyzing the simulated spectra in the same way as the experimental spectra (Figure 34) shows reasonable, semi-quantitative agreement. The band centers shift towards higher frequency on the same timescale as the experiment (Figure 34b). As the lower frequency population relaxes, the longer-lived population dominates and causes the spectrum and the peak centers to converge towards higher frequency, though the magnitude of the shift is somewhat less than the experiment. The widths of the bands also increase as in the experiment (Figure 34d), though the spread is less than in the experiment. Lastly, the trend of the apparent T_1 as a function of ω_1 for the simulated data is similar to the experiment (Figure 34e). The two populations overlap, and T_1 increases smoothly across ω_1. At low ω_1 (2030—2060 cm^{-1}), the trend of the apparent T_1 is concave up indicating the most contributing sub-ensemble in that frequency range. (Note that the T_1 times extracted from treating the simulated spectra like the experimental spectra are similar, but not identical to the T_1 times in the best-fit simulations (2 ps and 5.7 ps).) At high ω_1 (2060—2080 cm^{-1}), the apparent T_1 goes through an inflection point revealing a new sub-ensemble. On the high frequency side, there is a moderate difference in magnitude of the apparent T_1, which we attribute to systematic error from thermalization effects (hot ground state).

There are some limitations to the spectral modeling. At long t_2 ($>$ 5 ps), the two-population simulated model falls short of duplicating the exact experimental trends for the center frequency and width and at high frequency for T_1. The HGS shifts the experimental center frequency artificially increasing the lineshape width. Also, the long-lived HGS inflates T_1 at high frequencies. There may also be inaccuracies in the model lineshape due to several assumptions. The model assumes that 1) the FFCF is polarization independent, 2) the FFCF is single exponential, and 3) orientation and frequency factorize. There are indications that each of these assumptions is not rigorously correct, which will be highlighted in the following Sections. Despite these limitations, the model supports the hypothesis that two sub-ensembles with different vibrational relaxation rates are responsible for the apparent shift in the center position of the peaks in the 2D-IR spectra and the observed frequency-dependent variation of the spectral linewidth.

In the next section (Section 6.4.4), we show the correlation between the orientational dynamics and the initial frequency of the vibrational chromophore by examining the 2D rotational anisotropy, which motivates the subsequent RISD analysis (Section 6.4.5.2).

6.4.4 Rotational Anisotropy

Rotational anisotropy in the 2D-IR data is inconclusive regarding the two overlapping sub-ensembles in EAN. Analyzing the full two-dimensional rotational anisotropy shows that the timescale for decay of rotational anisotropy does vary across the 2D-IR spectrum, showing that rotational motion and spectral diffusion are coupled.

The two-dimensional anisotropy map directly shows how the anisotropy depends on the vibrational frequency (Figure 36a). As was first demonstrated for liquid water[203], a two-dimensional anisotropy map can be calculated from each point in a set of 2D-IR spectra

$$\alpha(\omega_1, t_2, \omega_3) = \frac{S_{ZZZZ}(\omega_1, t_2, \omega_3) - S_{ZZXX}(\omega_1, t_2, \omega_3)}{S_{ZZZZ}(\omega_1, t_2, \omega_3) + 2S_{ZZXX}(\omega_1, t_2, \omega_3)}. \tag{6.3}$$

At early times, $t_2 = 0.2$ ps, the anistropy is near 0.4 along the diagonal and decreases to below 0.3 away from the frequency diagonal. If there is no rotational anisotropy, then the value should be constant across the entire ω_1, ω_3 plane.

The 2D anisotropic signal decays at different rates for different frequencies. Timescales can be extracted by fitting each point of the 2D anisotropic signal to a biexponential function. The amplitude of the fastest motions is small (~ 0.05) for all points (data not shown) but including this term increases the quality of the fits. The weighted correlation time, $\tau_{\text{rot}}^{\text{total}}$,

$$\tau_{\text{rot}}^{\text{total}}(\omega_1, t_2, \omega_3) = \int \mathrm{d}t \; \alpha(\omega_1, t_2, \omega_3)/0.4 \tag{6.4}$$

varies from $\sim$ 25 ps near to the ω_1-ω_3 diagonal to $\sim$ 5 ps in the off-diagonal regions (Figure 36b). This is the first important indicator of the coupling of rotations and vibrational frequency fluctuations (Section 6.4.5.2). This observation suggests that molecules whose vibrational frequencies remain correlated also tend to maintain rotational correlations. Along the diagonal, there are two regions of slightly slower decay of the rotational anisotropy, which are suggestive of the two sub-ensembles, but the times for each region are similar.

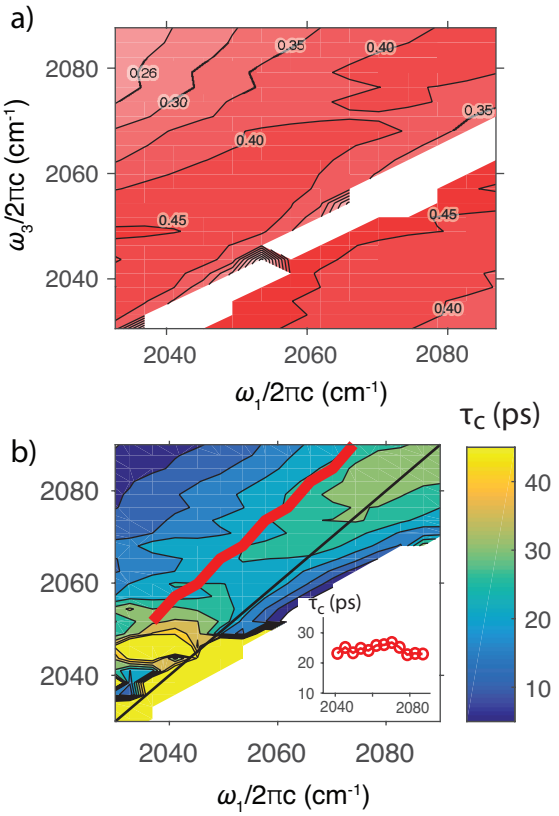

Figure 36: The 2D anisotropy of SCN^- in EAN at 19 °C is frequency dependent. a) The initial value of the anisotropy is highest (~ 0.4) near the diagonal and lower (< 0.3) away from the diagonal. b) The total rotational correlation time for each point in the 2D anisotropy spectrum, $\tau_{\text{rot}}^{\text{total}}$ (Eq. 6.4), varies across the spectrum. The times are the slowest along the frequency diagonal (~ 30 ps) and fastest off the diagonal (~ 5 ps), which indicates coupling of rotational motion and vibrational frequency fluctuations. (Inset) Rotation times near the frequency diagonal (red line) vary mildly.

Rotational anisotropy for the excited state absorption decays on longer timescales, up to ~ 100 ps in some regions. In the ideal case, the rotational anisotropy should decay identically for GSB/SE and ESA. Our calculations suggest that a combination of the spectral diffusion and frequency shifts due to the frequency-dependent vibrational relaxation rate lead to a slower decay of the rotational anisotropy. As a note of caution, the longest population times in the experiment are 12 ps so the rotational timescales > 10 ps should be treated as estimates based on the initial slope of the anisotropy decay. The reported times are thus lower bounds and slower processes could be present. Thermal signals do appear in the 2D-IR spectra beyond ~ 10 ps, though typically thermal transients are isotropic.[86,206]

In summary, the two-dimensional rotational anisotropy shows that rotational motions and vibrational frequency fluctuations of the SCN^- are correlated. The next section will treat the coupled dynamics with the theory for reorientation-induced spectral diffusion.

6.4.5 Frequency Fluctuations

The 2D-IR signal depends on the vibrational frequency of the SCN^- probe molecule, the laser polarizations, and the orientation of the molecule with respect to the laser fields. Typically, the orientation and vibrational frequency of the vibrational chromophore are assumed to be uncorrelated, in which case the third-order response function factorizes into terms that depend on orientation and vibrational frequency. In such an ideal case, the vibrational frequency fluctuation correlation function can be determined in any polarization condition. When the molecule's vibrational frequency depends on its orientation, however, one can no longer separate the frequency fluctuations from rotational motions. Thus, the measured frequency fluctuation correlation functions depend on the polarization condition employed by the experiment. To emphasize this dependence on polarization, the extracted correlation functions will be referred to as polarization-weighted frequency fluctuation correlation functions (PW-FFCFs).

The PW-FFCFs of SCN^- in H_2O and EAN depend on the laser polarization configuration, which indicates RISD. This section will describe the measured PW-FFCFs and subsequent analysis using a model of RISD and SSD.

6.4.5.1 PW-FFCFs Separating the RISD from the PW-FFCFs, $c_2(t_2)$, of SCN^- will further explore the dependence of rotational motions on the frequency fluctuations. To extract the PW-FFCF, we perform a CLS analysis over both sub-ensembles (2040 to 2082 cm^{-1}), thus the PW-FFCF consists of contributions from both low- and high-frequency sub-ensembles, which is reasonable given the broad similarity of rotational times. The CLS of both the $\langle ZZZZ \rangle$ and $\langle ZZXX \rangle$ spectra begin near ~ 0.8 (a large inhomogeneity). Spectral diffusion is not complete for either the $\langle ZZZZ \rangle$ or $\langle ZZXX \rangle$ within the timeframe of the experiment (~ 11 ps). The CLS of $\langle ZZXX \rangle$ is less than $\langle ZZZZ \rangle$, a strong indicator of RISD.

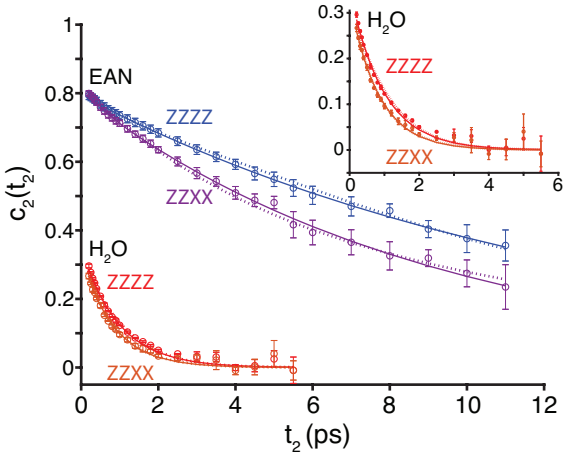

Figure 37: The PW-FFCFs ($c_2(t_2)$) are determined with a CLS analysis of SCN^- in EAN: $\langle ZZZZ \rangle$ (blue), $\langle ZZXX \rangle$ (purple) and in H_2O: $\langle ZZZZ \rangle$ (red), $\langle ZZXX \rangle$ (orange). In both cases, the $\langle ZZXX \rangle$ CLS decays faster than the $\langle ZZZZ \rangle$ CLS. The data are well described by exponential fits (solid lines) as well as the RISD models (dashed lines). In H_2O, the difference is smaller but still significant (inset).

The PW-FFCFs of SCN^- in H_2O also show RISD, but it is less pronounced (Figure 37 inset). In H_2O, the initial CLS value is much less than EAN. At an early time ($t_2 \sim 0.2$ ps), the initial CLS values for the $\langle ZZZZ \rangle$ signal (0.296 ± 0.005) are similar but systematically larger than the $\langle ZZXX \rangle$ signal (0.267 ± 0.008). For both polarization signals, spectral diffusion occurs within a few ps, and, again, the CLS of $\langle ZZXX \rangle$ signal is always lower than $\langle ZZZZ \rangle$.

Table 6: The parameters for the PW-FFCF at room temperature are extracted from the CLS values (Figure 37) using a biexponential for EAN and a single exponential for H_2O.

	a_2	τ_1 (ps)	a_2	τ_2 (ps)	τ_{total} (ps)
EAN					
$\langle ZZZZ \rangle$	0.3 ± 0.02	0.2 ± 0.1	0.795 ± 0.003	13.3 ± 0.2	10.7 ± 0.5
$\langle ZZXX \rangle$	0.05 ± 0.01	0.3 ± 0.2	0.791 ± 0.007	9.2 ± 0.3	7.3 ± 0.5
H_2O					
$\langle ZZZZ \rangle$	0.35 ± 0.01	0.96 ± 0.04	—	—	0.338 ± 0.009
$\langle ZZXX \rangle$	0.33 ± 0.01	0.83 ± 0.04	—	—	0.274 ± 0.008

The frequency fluctuation dynamics are clearly much slower in EAN than in H_2O (Table 29. Different mathematical functions are required to extract the PW-FFCF from the CLS results for SCN^- in EAN and in H_2O. In EAN, a biexponential fit captures both fast and slow frequency fluctuations; in H_2O, a single exponential is sufficient to fit the decay. Since the individual time constants and amplitudes are cross-correlated due to the linear dependence of the exponential functions, we also report an integrated correlation time, $\tau_{\text{total}}^{\text{FFCF}}$

$$\tau_{\text{total}}^{\text{FFCF}} = \sum_i a_i^{\text{FFCF}} \tau_i^{\text{FFCF}}. \tag{6.5}$$

The integrated correlation time accounts for motions in the motionally narrowing limit that decrease the amplitude as these motions are not incorporated in the timescale. The $\tau_{\text{total}}^{\text{FFCF}}$ extracted from $\langle ZZZZ \rangle$ is slower than that for $\langle ZZXX \rangle$ in both EAN and H_2O, as expected for RISD. The timescale of frequency fluctuations are slower in EAN than H_2O by ~ 10 ps. One explanation for a slower timescale is that EAN (32 cP[207]) is more viscous than H_2O by 30 times, but the individual τ_i dynamics do not differ by the same magnitude. It should

be noted, however, that the τ_{total} timescales differ roughly by the same magnitude difference between the viscosities of EAN and H_2O. We explore the assignment of the EAN dynamics further in the the Discussion (Section 7.5) and in Chapter 7.

While we fit the low and high frequency parts of the spectrum simultaneously, the CLS values and PW-FFCF fits are mildly dependent on the ω_1 range for SCN^- in EAN (data not shown). While the exponential fit constants are consistent with faster dynamics on the low frequency edge and slower dynamics on the high frequency side, the differences were limited to the first ~ 2 ps and the 2–10 ps range decayed with very similar rates. Having few data points along ω_1 also leads to uncertainty in the slope of center lines, so the error bars in the low and high windows largely overlap with the average CLS.

We also attempted to fit the two overlapping sub-ensembles with a method proposed by Yuan et al.[208]. This approach also failed to resolve separate dynamics for the two sub-ensembles (Appendix A.3). Because the two sub-ensembles overlap in frequency (much more than in the Yuan et al.[208]) and one spectral feature decays in amplitude much faster than the other, the extracted fitting parameters are strongly cross-correlated.

Neither the $\langle ZZZZ \rangle$ nor $\langle ZZXX \rangle$ PW-FFCFs alone indicate the presence of more than one sub-ensemble of SCN^- in EAN. To determine CLS requires fitting over a frequency range (2040–2082 cm^{-1}). We interpret the resulting fits as a weighted average of the two sub-ensembles. Nevertheless, the FFCFs decay in nearly exponential fashion in the observed time-window, leaving no obvious signatures of differences in dynamics. We suspect this is a result of the significant overlap of the two distributions, which makes separating the sub-ensembles in the spectrum impossible, and the differences in vibrational relaxation rates, which biases the extracted PW-FFCFs to the longer-lived species.

Analyzing the 2D-IR spectra directly provides an average characterization of the frequency fluctuation dynamics of SCN in EAN, but it was unable to capture robustly the differences in dynamics of the two sub-ensembles. Further analysis based on a model of RISD demonstrates that hindered rotational motion is sufficient to explain the observed spectral diffusion of SCN^- in EAN.

6.4.5.2 RISD Unifies Anisotropy and FFCF Measurements

One framework to understand the frequency fluctuations of a vibrational chromophore considers the coupling of the vibrator's dipole to the local electric field created by the surrounding solvent, like a Stark effect. This model naturally couples rotational motion and the vibrational frequency, which explains the observed variation of timescales and activation energies in the different polarization conditions.

The simplest qualitative picture of reorientation-induced spectral diffusion (RISD) is the Stark effect. If the vibration of a molecule is anharmonic and has a projection onto the dipole of the molecule, then vibrational frequency of that mode will depend on the angle between the local electric field and the molecular dipole. Molecules aligned with the local electric field will have frequencies shifted in one direction; molecules aligned against the field will have frequencies shifted in the other direction; and molecules perpendicular to the field will have no net shift. The constant of proportionality for this frequency shift is the Stark tuning rate. The consequence for 2D-spectroscopy is that different polarization conditions will observe different rates of spectral diffusion. In the all parallel configuration, $\langle ZZZZ \rangle$, molecules that have not rotated contribute the most to the spectrum. In the crossed-polarization configuration, $\langle ZZXX \rangle$, molecules that have rotated contribute the most to the spectrum. Molecules that do not rotate tend to keep their orientation relative to the local solvent field, so do not change their vibrational frequency as much as the molecules which do rotate and tend to move to a different angle relative to the local field and a new vibrational frequency. As a result, the FFCF measured in the $\langle ZZZZ \rangle$ polarization condition will relax to zero more slowly than the $\langle ZZXX \rangle$ polarization condition when there is RISD.

A theory for the effects of RISD on 2D-IR spectra is derived in the context of the Stark effect[26,27], but the essential physical picture is the same even when the origin of the vibrational frequency shifts is not a true Stark effect. Theoretical work has shown that both electrostatics beyond the dipole approximation and chemical interactions, like charge transfer, play important roles in determining the C≡N stretching frequency[188,209,210]. Nevertheless, if these interactions are vectorial in nature, i.e. they depend on the orientation of the molecule, then they can be incorporated into the conceptual framework of RISD. For $SeCN^-$, the electric field at the position of the C projected onto the CN bond-vector does accurately predict

the C≡N stretching frequency, but this is largely due to a cancellation of effects[188]. This phenomenological association of local electric field with vibrational frequency still strongly supports the concept that the vibrational frequency will be sensitive to molecular orientation.

The contributions of molecular rotation and structural fluctuations of the solvent can be quantitatively separated.[26–28] As a starting ansatz, we take the PW-FFCF to be a sum of two frequency fluctuation correlation functions,

$$\begin{aligned} C_p(t) &= \langle \delta\omega_v(t)\delta\omega_v(0)\rangle + \langle \delta\omega_s(t)\delta\omega_s(0)\rangle \\ &= C_p^v(t) + C_s(t) \end{aligned} \tag{6.6}$$

Here, $\delta\omega_v$ is the frequency shift due to interactions that depend on molecular orientation, so they are vectorial in nature, and $\delta\omega_s$ is the frequency shift due to orientation independent effects that are scalar in nature. The term C_p^v carries all of the polarization dependence and represents the relative orientation of the solvent cage. The scalar term, C_s, is polarization independent and relates to isotropic physical effects, such as density fluctuations. The polarization independent scalar term becomes necessary to include when the two PW-FFCFs ($\langle ZZZZ\rangle$ and $\langle ZZXX\rangle$) converge to a non-zero value (an offset) in the system[211]. We neglect this term, as in previously studied systems[26,27], because the PW-FFCFs do not converge to a offset. In this approximation, the PW-FFCF can be simplified to the product of SSD, $F(t)$, and RISD, $R_p(t)$,

$$C_p(t) = F(t)R_p(t). \tag{6.7}$$

Additionally, the time dependence of the RISD, $R_p(t)$, can be expressed solely in terms of the reorientation time for each polarization condition after the appropriate orientational averaging of the signals[26,27]. For $\langle ZZZZ\rangle$, the result is

$$R_{ZZZZ}(t) = \frac{\langle \delta\omega(t)\delta\omega(0)\rangle_{\text{para}}}{\Delta^2/3} = \frac{3}{25}\left[\frac{11L_1(t) + 4L_3(t)}{1 + 0.8L_2(t)}\right], \tag{6.8}$$

while for $\langle ZZXX\rangle$ the result is

$$R_{ZZXX}(t) = \frac{\langle \delta\omega(t)\delta\omega(0)\rangle_{\text{perp}}}{\Delta^2/3} = \frac{3}{25}\left[\frac{7L_1(t) - 2L_3(t)}{1 - 0.4L_2(t)}\right]. \tag{6.9}$$

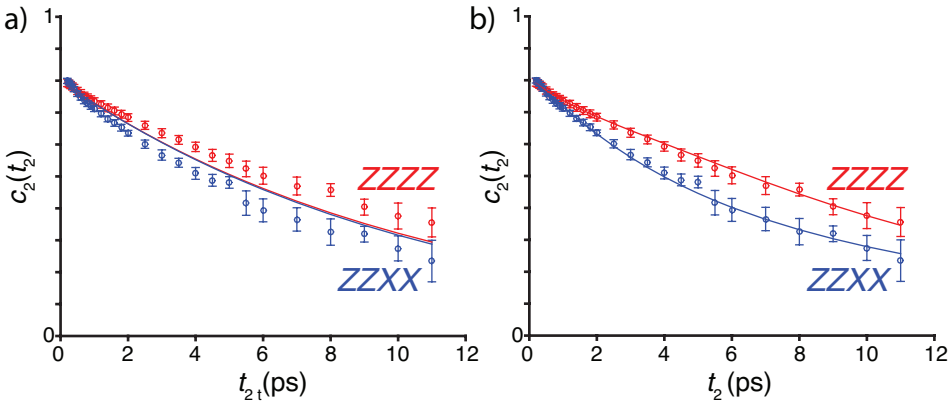

Figure 38: The PW-FFCF ($\langle ZZZZ \rangle$, red and $\langle ZZXX \rangle$, blue) of SCN^- in EAN at 19 °C are fit with a model that separates structural and rotational as independent contributions to spectral diffusion. a) A model with one rotational time and biexponential SSD fails to fit the data. b) A wobbling-in-a-cone model captures the observed dynamics.

where Δ is a normalization factor for the total frequency fluctuation amplitude. Assuming the reorientation of the dipole's motion to be diffusive, the l^{th}-order Legendre polynomial orientational correlation function is[26]

$$L_l(t) = e^{-l(l+1)D_m t}, \tag{6.10}$$

where the orientational diffusion constant, D_m, is inversely proportional to the molecular rotational timescale from an anisotropy experiment

$$D_m = 1/(6\tau^{\text{rot}}). \tag{6.11}$$

To emphasize the parametric dependence of $R_p(t)$ on the reorientation time, τ^{rot}, we will write it as $R_p(t;\tau^{\text{rot}})$.

In H_2O, a model of free rotational diffusion and a single exponential decay of SSD,

$$C_p(t_2) = a^{\text{SSD}} \exp(-t_2/\tau^{\text{SSD}}) R_p(t_2;\tau^{\text{rot}}) \tag{6.12}$$

adequately describe the data (Figure 37 inset). The total SSD timescale ($\tau^{\mathrm{SSD}}_{\mathrm{total}} = a^{\mathrm{SSD}}\tau^{\mathrm{SSD}}$) is similar to the rotational timescale (τ^{rot}), and, therefore, both rotations and local structural changes contribute to spectral diffusion of SCN^- in H_2O.

In EAN, neither a model based on a single rotational time and a single exponential SSD (Eq. 6.12) (data not shown), nor biexponential SSD

$$\begin{aligned} C_p(t_2) = &\left(a_1^{\mathrm{SSD}} \exp(-t_2/\tau_1^{\mathrm{SSD}}) + a_2^{\mathrm{SSD}} \exp(-t_2/\tau_2^{\mathrm{SSD}})\right) \\ &\times R_p(t_2; \tau^{\mathrm{rot}}) \end{aligned} \tag{6.13}$$

fit the $\langle ZZZZ \rangle$ and $\langle ZZXX \rangle$ data simultaneously (Figure 38a). The biexponential SSD fit falls between the two PW-FFCFs. The data suggest both the presence of faster rotational motion, which causes the observed separation of $\langle ZZZZ \rangle$ and $\langle ZZXX \rangle$, and also slower reorientation which maintains the offset from zero.

Models that restrict or bias reorientation naturally provide these two timescales. The wobbling-in-a-cone model provide convenient analytical forms to parameterize the PW-FFCF data. Following Kramer et al.[27], the orientational correlation function, $L_l(t)$, can be approximated in terms of an exponential decay to an offset, S_l. The term S_l is a complicated function of the order, l, and the half-cone angle, θ. The time-constant of the decay, $\tau_{l,\mathrm{eff}}$, itself depends both on the rotational diffusion constant, D_m, and the order, l,

$$L_l(t) = S_l^2 + (1 - S_l^2) \exp(-t/\tau_{l,\mathrm{eff}}). \tag{6.14}$$

This form of $L(t)$ can be inserted in Eqs. 6.8 and 6.9. We found that a constant SSD, $F(t) = a^{\mathrm{SSD}}$, was sufficient to fit the data. The constant accounts for the product of the Stark tuning rate and the variance of the electric field fluctuations due to the solvent (Ref.[27], Eq. 15). Our final fitting function for the PW-FFCFs was then

$$C_p(t_2) = a^{\mathrm{SSD}} R_p(t_2; \tau^{\mathrm{rot}}). \tag{6.15}$$

We were also able to model the data successfully as the sum of two independent rotational terms

$$C_p(t_2) = F_1(t) R_p(t_2; \tau_1^{\mathrm{rot}}) + F_2(t) R_p(t_2; \tau_2^{\mathrm{rot}}) \tag{6.16}$$

Table 7: Simultaneously fitting the $\langle ZZZZ \rangle$ and $\langle ZZXX \rangle$ CLS (19°C) provides SSD and RISD timescales in H_2O, τ^{SSD} and τ^{rot}, respectively. In EAN, it provides a RISD time, τ^{rot}, and cone half-angle, θ.

	EAN	H_2O
a^{SSD}	0.81	0.341
τ^{SSD} (ps)	—	1.9
$\tau^{\mathrm{SSD}}_{\mathrm{total}}$ (ps)	—	0.65
τ^{rot} (ps)	2.6	0.56
θ (degrees)	108	—

where τ_1^{rot} and τ_2^{rot} are two independent rotational timescales. This model fits the PW-FFCF data because it also provides two rotational times (decay to an offset), but the model is not consistent with the observed 2D-anisotropy or frequency dependent CLS (data not shown). We, therefore, disfavor this model and prefer the model of restricted reorientation, Eqs. 7.8 and 6.15.

In summary, for SCN^- in EAN, a model of restricted reorientation fits the data. Rotational motion fully accounts for the observed spectral diffusion, and no SSD time can be extracted. for SCN^- in H_2O, both SSD and RISD contribute to spectral diffusion in the timeframe of the experiment and can be characterized.

6.5 DISCUSSION

6.5.1 Molecular Interpretation of Heterogeneous Dynamics

Our experiments suggest two sub-ensembles for the SCN^- in EAN. In previous pump-probe measurements, heterogeneous dynamics were detected in ammonium based PILs[86]. Population relaxation of SCN^- shows strong indications of dynamical heterogeneity in EAN. One sub-ensemble is characterized by a lower vibrational frequency (2059 cm^{-1}) and shorter vibrational relaxation time ($\sim$ 2 ps).The other sub-ensemble has a higher vibrational frequency (2070 cm^{-1}) and longer vibrational relaxation time ($\sim$ 5 ps). Based on these features, we propose a molecular description of the solvation environment around the SCN^- in each sub-ensemble. Based on calculations of hydrogen bonding to $SeCN^-$in water,[212] the apparent vibrational frequency shifts suggest that the low frequency ensemble has more, but weaker, hydrogen bonds, while the high frequency ensemble has fewer, but stronger, hydrogen bonds. Many other experiments have used the rate of vibrational relaxation of SCN^- as a probe of the local solvation environment[12,148,149,191,193,213]. Ren et al.[12] also identified sub-ensembles of SCN^- with different vibrational relaxation rates in an aprotic ionic liquid. In that case, the lower frequency, shorter lived sub-ensemble was identified as an effect of water in the first one or two solvation shells. In the present case, the linear spectra and 2D-IR dynamics did not change significantly over the range of water content that we could access (1 M–40 mM), which suggests, but does not completely rule out, that the effect is not due to the presence of water. In a Fermi's golden rule picture,[193,213,214] the vibrational lifetime is proportional to the product of the square of a coupling constant and the vibrational density of states of accepting modes. Our experiments are not able to separate these two possible contributions, but at least one of the two quantities must be high enough to double the rate of vibrational relaxation.

Our proposed assignment is also consistent with the heterogeneous dynamics observed in molecular simulations of imidazolium ionic liquids and EAN. Molecular simulations[94,185] provide evidence that translational and rotational motion of a vibrational probe are slower when it is involved in a strong, specific hydrogen bond. In imidazolium ionic liquids, these

structures are associated with charge dense regions of the liquid, while the faster domains are associated with relatively charge depleted regions. EAN also consists of regions that are enhanced and depleted charge density[89]; the charge depleted regions are relatively concentrated in the alkyl chain length, and the charge dense regions are relatively concentrated in the ammonium headgroups and nitrate ions. Similarly, molecular simulations show that the cation-anion regions of EAN resulted in slower reorientation dynamics due to the strong interactions, while the alkyl chain region reoriented on a faster timescale due to a lack of strong Coulombic interaction[184].

In EAN, the frequency fluctuations are dominated by rotational motions, while, in H_2O, both SSD and RISD contribute. While dynamical heterogeneity is present with respect to T_1 in EAN, the 2D-ansiotropy plot reveals that there is no difference in anisotropy along ω_1. Therefore, it is reasonable to analyze the dynamics over the average of the two subensembles. In EAN, RISD fully captures the frequency fluctuations dynamics, because the SSD is unresolved. The RISD analysis in EAN, however, is not biexponential, i.e. a separate rotational timescale for each sub-ensemble. Instead, a wobbling in a cone RISD approach provides a single fast timescale ($\sim$ 2 ps). The timescale correlates to SCN^- undergoing free diffusive rotations in a constrained angular space. In previous pump-probe measurements[84], a long-lived rotation was identified by examining the ND stretch of EAN with a large angle jump (106 °) comparable to the angle extracted from the wobbling in a cone approach used here (108 °). The 2D anisotropy analysis suggests longer rotational timescales (20-40 ps), which could be large angle jumps to a new local environment where the SCN^- explores a new cone. The observed cone angles are large, which is inconsistent with a specific steric hindrance. (Considering both the S and N ends of the molecule, the SCN^- would sweep out a full sphere even at half-angles of 90 °.) The cone could also be the effect of an energetic bias in the rotational distribution, which was also observed for SCN^- in an ionic liquid colloidal dispersion.[202,211]

Overall, a two population model may be an over simplification to effectively capture all the nuances of the multiple subenembles of EAN with SCN^-, and further molecular simulations are needed to test our interpretation of how the solute SCN^- behaves in EAN. The insights on the solvation environment of EAN fueled a temperature-dependent 2D-IR

study where we explore an interpretation of the thermodynamics of the transition state of SCN^- in EAN compared with H_2O in Chapter 7.

6.6 CONCLUSION

In this chapter, we quantitatively characterize the dynamics and heterogeneity of the 3D hydrogen bonding network in the PIL EAN. The 2D-IR experimental approach used allowed the data to be gathered in a timescale of hours by collecting the $\langle ZZZZ \rangle$ and $\langle ZZXX \rangle$ simultaneously at 100 kHz.[203] Combined with the analysis approach synthesized from the work of others[26,27,203], this approach provides a powerful protocol for the further characterization of other PILs with a view to establishing 2D-IR spectroscopy as a useful tool for developing molecular models of PILs in support of tuning their properties for practical applications.

In summary, we observe dynamical heterogeneity in the 3D hydrogen bonding network of the PIL, EAN. Using SCN^- as a vibrational probe in EAN, the linear FTIR spectra reveals a high frequency shoulder on the vibrational band of the nitrile stretch. From our 2D-IR data, the molecular rotation and vibrational relaxation timescales are found to be frequency dependent leading to the hypothesis that SCN^- resides in at least two structural sub-ensembles. This is confirmed by simulating the 2D-IR spectra. Applying the RISD analysis, we determine that the frequency fluctuations are in the RISD limit, and a wobbling-in-a-cone model extracts a single fast timescale of molecular rotation. There are slower reorientations ($\sim$ 30 ps timescale) responsible for the final loss of rotational anisotropy, which may be large angle jumps. Overall, we interpret the two different sub-ensembles in EAN to be correlated to charge depleted (alkyl chain) and charge dense regions (ammonium headgroups and nitrate ions). In Chapter 7, we develop the investigation of the dynamics of hydrogen bonding of SCN^- in EAN and H_2O to obtain the temperature-dependence and activation energies of SCN^- in EAN and H_2O.

7.0 TEMPERATURE-DEPENDENT DYNAMICS OF EAN

The text in this chapter has been adapted from a manuscript being submitted to the Journal of Chemical Physics. Elements of this chapter were part of a submission to a pre-print server: Johnson, C.A., Parker, A.W., Donaldson, P.M., Garrett-Roe S. ChemRxiv. 2019. DOI: 10.26434/chemrxiv.9876524. The author's contribution includes choosing the system, performing all FTIR and 2D-IR experiments, assisting in the design of the 2D-IR experiments at the Central Laser Facility at the Rutherford Appleton Laboratory, performing all analysis, and writing the manuscript.

7.1 CHAPTER SUMMARY

Using ultrafast two-dimensional infrared spectroscopy (2D-IR), a vibrational probe (thiocyanate, SCN^-) is used to compare the hydrogen bonding network of the protic ionic liquid ethyl-ammonium nitrate (EAN) to that of H_2O. In the previous chapter, we assigned the spectral features of two subensembles for SCN^- in EAN. This chapter presents 2D-IR experiments in both parallel ($\langle ZZZZ \rangle$) and perpendicular ($\langle ZZXX \rangle$) conditions as a function of temperature for both EAN ($14 - 130$ °C) and H_2O ($5 - 89$ °C). With polarization control, the frequency fluctuation correlation function can be separated into structural and rotational components. An Arrhenius analysis leads to independent activation energies for the $\langle ZZZZ \rangle$, $\langle ZZXX \rangle$, isotropic, anisotropic signals, structural spectral diffusion, and reorientation-induced spectral diffusion. The rotational activation energies are similar for both EAN and H_2O suggesting that SCN^- follows a similar jump model, i.e. where hydrogen bond reorientation is dominated by large angular jumps stemming from molecular

rotation dynamics. The frequency prefactors are explained through the entropy of activation.

7.2 INTRODUCTION

Protic ionic liquids (PILs) are promising solvents for chemical synthesis[215,216], CO_2 absorption,[80] and hydrogen fuel cells.[79,82] Understanding PIL's hydrogen bonding network and proton transfer dynamics is crucial in further developing them as electrolytes for fuel cells. The PIL ethyl-ammonium nitrate (EAN) shows similarities in hydrogen bonding patterns and dynamics to that of water[84,86,89,182,217]. This evidence suggests that the hydrogen bonding network of EAN has similar hydrogen bond strength and thermodynamics as water. The enthalpy and entropy of activation for breaking hydrogen bonds in EAN, however, has yet to be determined.

Polarization and temperature-dependent two-dimensional infrared spectroscopy (2D-IR) can extract the activation energy for molecular processes. In these experiments, we use SCN^- as a probe of hydrogen bond dynamics in EAN. When hydrogen bonding is the dominant contribution to the frequency fluctuations, then the activation energy of hydrogen bond switching can be extracted from temperature-dependent 2D-IR. Previous temperature-dependent 2D-IR experiments of OH (OD) bands of HOD in D_2O (H_2O), for example, have found the activation energy to break water-water hydrogen bonds in H_2O to be 3.5 kcal/mol and 6.2 kcal/mol under different polarization conditions.[9,10] Also, a temperature-dependent 2D-IR study of SCN^- in various imidizolium ILs analyzed the alkyl chain-length dependence of the activation energy for structural reorganization in a series of aprotic ionic liquids.[14] Temperature-dependent 2D-IR studies are most commonly performed in one polarization condition (usually all parallel polarizations, less often the magic angle). At a single polarization condition, however, the frequency correlation function may contain contributions of both spectral diffusion from rotation of the probe molecule, reorientation-induced spectral diffusion (RISD), and structural motions of the surrounding solvent, structural spectral diffusion (SSD) to the signal.[26,27] Using both parallel ($\langle ZZZZ \rangle$) and perpendicular ($\langle ZZXX \rangle$) polarizations, a more complete picture of the independent structural and rotational activation

energies of hydrogen bond switching in EAN and H_2O can be achieved.

In Chapter 6, we provided an analysis of polarization dependent 2D-IR experiments SCN^- in EAN and H_2O at room temperature. At least two hydrogen bonding environments for SCN^- in EAN exist. The two subensembles have similar CN-stretching frequencies but they are distinct in their vibrational relaxation rates. Due to spectral overlap of the two subensembles, individual molecular rotation timescales and vibrational frequency fluctuations could not be fully resolved for each subensemble. Averaging over the two-subensembles, a RISD model based on restricted molecular rotation (wobbling in a cone) fully describes the observed spectral diffusion in EAN.

In this chapter, we separate the rotational and structural components of the activation energy for hydrogen bond switching of EAN and H_2O using SCN^- as a vibrational probe. First, we will present the temperature dependent 2D-IR data of the nitrile stretch (ν_3) of SCN^- in EAN and H_2O. Next, we discuss the temperature dependence of the polarization-weighted frequency fluctuation correlation function (PW-FFCF) dynamics. Then, we present the temperature dependence of the anisotropy from an average of both sub-ensembles in EAN. Finally, we separate the rotational and structural contributions to the PW-FFCF of SCN^- in EAN and H_2O.

7.3 EXPERIMENTAL METHODS

The synthesis of EAN, sample preparation, FTIR, and temperature calibration of the spectroscopy cell methods are described in Chapter 3 and the previous chapter. This chapter uses the pulse shaping 2D-IR set-up as described in Section 3.5.2 and polarization-dependence as described in the previous chapter.

7.3.1 Temperature-dependent 2D-IR

For EAN, the temperature ranged from just above its glass transition temperature (13 °C)[75] up to 160 °C, but degradation of the sample was apparent above 130 °C. For H_2O, the

temperature was varied from 5 to 89 °C. Cooling of the sample below room temperature was achieved by using a water-based chiller. A resistive heater incorporated into a temperature-controlled spectroscopy cell (Harrick) was used to increase the temperature from room temperature up to 160 °C. At a given temperature, the sample was given ∼5 mins to equilibrate before data collection began. The temperature was monitored by use of a thermocouple in contact with one of the CaF_2 windows.

7.4 RESULTS

7.4.1 Temperature-dependent Spectral Diffusion Dynamics

In EAN, the change of the shape of the 2D-IR spectra is complex reflecting the two hydrogen bonding subensembles as described in Chapter 6. In the linear spectra, shoulder on the ν_3 mode of SCN^- in EAN is the first suggestions of multiple ensembles. Because the two subensembles overlap, the corresponding 2D-IR spectra show only one peak for ground state bleach and stimulated emission (blue) and one anharmonically shifted excited state absorption (red). With a polarization- and temperature-dependent study, separating the SSD and RISD components of the PW-FFCF can reveal which motion dominates spectral diffusion.

Temperature-dependent 2D-IR spectra of SCN^- in EAN and H_2O are obtained for both $\langle ZZZZ \rangle$ (Figure 39a-b) and $\langle ZZXX \rangle$ polarization conditions (Appendix A.4). At a low temperature (14 °C), the ν_3 fundamental of SCN^- in EAN is stretched along the diagonal with a large inhomogenous component at early times (t_2 = 0.2 ps), and spectral diffusion is not complete within the time frame of the experiment (t_2 ∼11 ps). As the temperature increases (130 °C), the homogenous linewidth increases and spectral diffusion is nearly finished within 5 ps. In H_2O, even at a temperature close to the freezing point (5 °C), the ν_3 fundamental of SCN^- shows substantial homogeneous character, and spectral diffusion occurs within a few ps. As temperature increases, rate of spectral diffusion also increases; by 89 °C spectral diffusion is complete within 1 ps.

The CLS values at early time ($t_2 \sim 0.2$ ps) decrease with elevated temperature as the

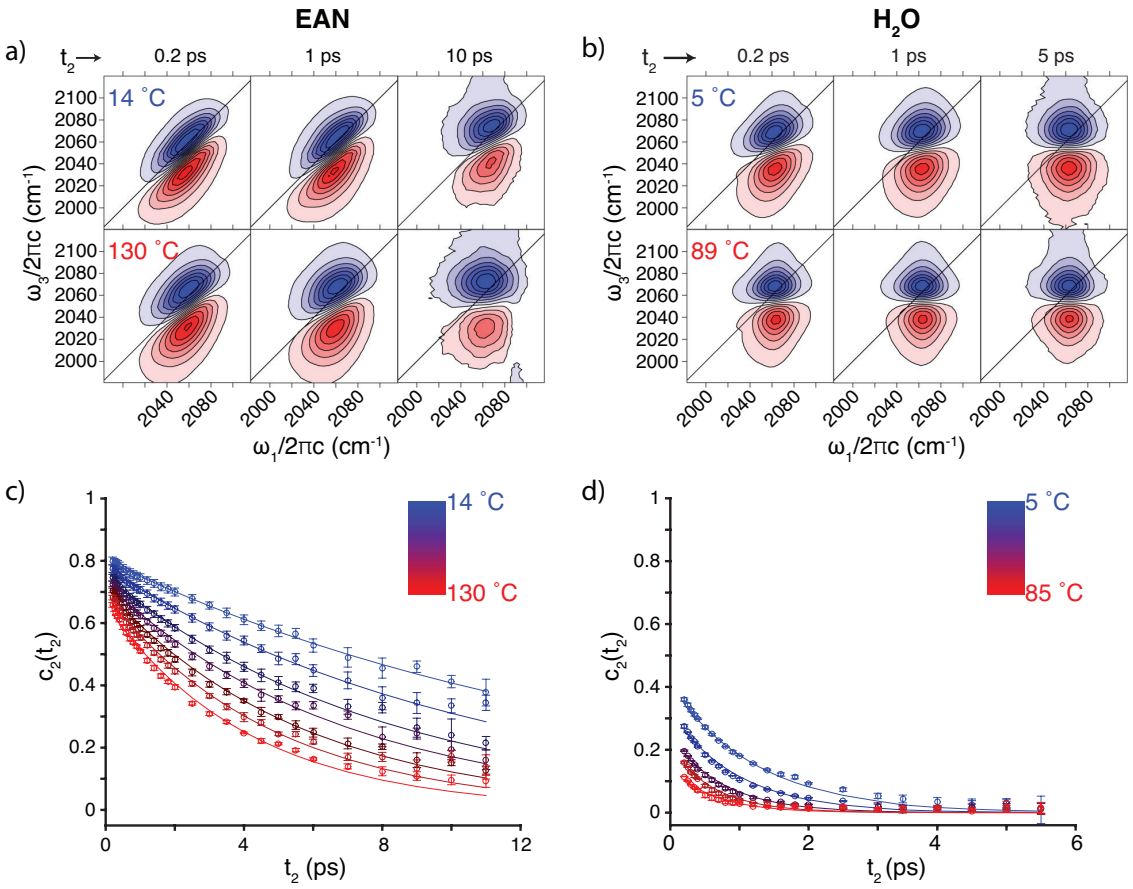

Figure 39: a) A larger inhomongeneous component is evident at low (14 °C) than high (130 °C) temperatures of the $\langle ZZZZ \rangle$ 2D-IR spectra of SCN^- in EAN. b) As seen in EAN, a similar trend is evident for the $\langle ZZZZ \rangle$ 2D-IR spectra of SCN^- in H_2O at low (5 °C) and high (85 °C) temperatures. c) As the temperature increases (14, 34, 54, 74, 94, 110, and 130 °C), the FFCF ($c_2(t_2)$ determined by CLS for SCN^- in EAN shows a faster spectral diffusion time (blue to red). d) The FFCF of SCN- in H_2O determined by CLS shows faster frequency fluctuations (blue to red) with elevated temperatures (5, 24, 44, 64, 89 °C).

motions begin to approach the motional narrowing limit (Figure 39c-d). In EAN, the low temperature (14 °C) CLS value (0.80 ± 0.01) decreases to 0.66 as the temperature increases to 130 °C. In H_2O, the low temperature (5 °C) initial CLS value (0.360 ± 0.005) decreases to 0.115 at 89 °C.

EAN and H_2O require different functional forms to accurately fit the PW-FFCF ($c_2(t_2)$). In EAN, a biexponential fit captures both a fast and slow frequency fluctuations. The integrated correlation time, $\tau_{\text{total}}^{\text{FFCF}}$, provides a more stable descriptor of the dynamics as a function of temperature

$$\tau_{\text{total}}^{\text{FFCF}} = \sum_i a_i^{\text{FFCF}} \tau_i^{\text{FFCF}}. \tag{7.1}$$

The individual time constants and amplitudes are cross-correlated due to the linear dependence of the exponential functions. The total correlation time is less sensitive to this effect and incorporates the variation in both amplitudes and time constants. In H_2O, a single exponential fits the PW-FFCF at all temperatures, and the integrated correlation is simply $\tau_{\text{total}}^{\text{FFCF}} = a_1^{\text{FFCF}} \tau_1^{\text{FFCF}}$.

Spectral diffusion is a thermally activated process in both EAN and H_2O, but it is always slower in EAN than in H_2O (Table 29). Comparing the $\langle ZZZZ \rangle$ signals at room temperature, the frequency fluctuations in EAN are 15-fold slower than H_2O. The dynamics speed up with increasing temperature until, by $\sim$ 100 °C, they are similar to H_2O at room temperature (Figure 39). As the temperature increases in EAN (14 °C to 130 °C), $\tau_{\text{total}}^{\text{ZZZZ}}$ decreases from 12.0 ± 0.6 ps to 3 ± 1 ps. As the temperature increases in H_2O (5 °C to 89 °C), $\tau_{\text{total}}^{\text{ZZZZ}}$ decreases from 0.51 ± 0.01 ps to 0.09 ± 0.006 ps. A similar trend is determined for the $\langle ZZXX \rangle$ signal (Appendix A.4).

The timescales of frequency fluctuations follow an Arrhenius behavior for both EAN and H_2O (Figure 40)

$$\ln(1/\tau) = \ln(A) - E_a/k_B T, \tag{7.2}$$

where k_B is Boltzmann's constant, E_a is the activation energy (slope of the Arrhenius plot) and A is the "frequency prefactor" (y-intercept of the Arrhenius plot), which is usually interpreted as the frequency of motion over the barrier. The Arrhenius fit parameters for each polarization condition differ in both EAN and H_2O (Table 9). In EAN, the activation

Table 8: The PW-FFCF are determined using exponential fits to the CLS results (Figure 39) for SCN^- in EAN and H_2O at various temperatures.

	a_2	τ_1 (ps)	a_2	τ_2 (ps)	τ_{total} (ps)
EAN					
14 °C					
$\langle ZZZZ \rangle$	0.03 ± 0.03	0.2 ± 0.2	0.799 ± 0.004	15.0 ± 0.3	12.0 ± 0.6
$\langle ZZXX \rangle$	0.045 ± 0.02	0.3 ± 0.2	0.803 ± 0.007	10.1 ± 0.3	8.1 ± 0.6
130 °C					
$\langle ZZZZ \rangle$	0.26 ± 0.08	1.5 ± 0.4	0.43 ± 0.08	6 ± 1	3 ± 1
$\langle ZZXX \rangle$	0.42 ± 0.07	1.3 ± 0.2	0.25 ± 0.07	7 ± 2	2 ± 2
H_2O					
5 °C					
$\langle ZZZZ \rangle$	0.40 ± 0.01	1.19 ± 0.06	—	—	0.51 ± 0.01
$\langle ZZXX \rangle$	0.383 ± 0.009	1.08 ± 0.05	—	—	0.41 ± 0.01
89 °C					
$\langle ZZZZ \rangle$	0.144 ± 0.007	0.62 ± 0.07	—	—	0.09 ± 0.006
$\langle ZZXX \rangle$	0.12 ± 0.01	0.56 ± 0.09	—	—	0.066 ± 0.007

energy for the $\langle ZZXX \rangle$ signal (2.8±0.1 kcal/mol) is slightly larger than that for the $\langle ZZZZ \rangle$ signal (2.7±0.1 kcal/mol)), both roughly $4k_BT$. The inverse of the frequency prefactor ranges from 60 to $\sim$ 100 fs for $\langle ZZZZ \rangle$ and $\langle ZZXX \rangle$, respectively. In H_2O, there is no significant difference in the energy of solvent reorganization ($\sim$ 4.3-4.5 kcal/mol). The inverse of the frequency prefactors for $\langle ZZZZ \rangle$ (0.21 $\pm$ 0.06 fs) and $\langle ZZXX \rangle$ (0.11 $\pm$ 0.03 fs) are both unrealistically fast. Both timescales are much faster than the fastest intermolecular motions in water, the librational mode ($\sim$ 40 fs). Comparing the $\langle ZZZZ \rangle$ signals, the energy values determined for the frequency fluctuations in H_2O (4.3 $\pm$ 0.2 kcal/mol) are roughly $3k_BT$ higher than in EAN (2.8 $\pm$ 0.07 kcal/mol). A similar trend emerges in the $\langle ZZXX \rangle$ signals. Adding H_2O (0.1−1 M) to EAN had little influence on the reported E_a (Appendix A.4). The spectral diffusion times are faster but the activation energies are not statistically different from the dry EAN for both $\langle ZZZZ \rangle$ and $\langle ZZXX \rangle$ signals.

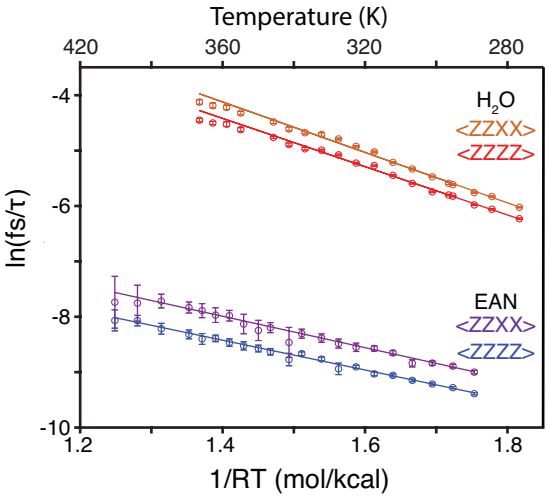

Figure 40: The activation energies for the spectral diffusion timescales at a given polarization are similar for SCN^- in EAN ($\sim$ 2.7 kcal/mol) and H_2O ($\sim$ 4.3 kcal/mol), respectively. An Arrhenius model is used to fit the polarization-temperature-dependent CLS results for SCN^- in H_2O ($\langle ZZZZ \rangle$, red and $\langle ZZXX \rangle$, orange) and EAN ($\langle ZZZZ \rangle$, blue and $\langle ZZXX \rangle$, purple).

In summary, the frequency fluctuation dynamics of SCN^- in EAN (averaging over the two subensembles) and in H_2O lead to statistically different activation energies and frequency

Table 9: The Arrhenius fit parameters are determined from the polarization/temperature dependent timescales of frequency fluctuations for SCN^- in EAN and H_2O.

	Arrhenius Fit	
	1/A (fs)	E_a (kcal/mol)
EAN		
$\langle ZZZZ \rangle$	100 ± 40	2.7 ± 0.1
$\langle ZZXX \rangle$	60 ± 10	2.8 ± 0.1
H_2O		
$\langle ZZZZ \rangle$	0.21 ± 0.06	4.3 ± 0.2
$\langle ZZXX \rangle$	0.11 ± 0.03	4.5 ± 0.2

prefactors. The frequency fluctuations themselves can contain contributions from rotations and from fluctuations of the local environment. Before we can disentangle these two contributions from the PW-FFCF, the timescales of molecular rotations need to be determined from the rotational anisotropy.

7.4.2 Temperature-dependent Rotational Anisotropy

In this section, we characterize the temperature dependence of the timescale of molecular rotation (τ^{rot}) for SCN^- in both EAN and H_2O. As with the PW-FFCF, we will now characterize the temperature dependence of the dynamics of SCN^- in both EAN and H_2O. In Chapter 6, the 2D anisotropy shows that the rotational timescale varies mildly with vibrational frequency.

To quantitatively analyze the temperature dependent rotational anisotropy, we reduce the full 2D anisotropy to the equivalent of a pump-probe spectrum. The 2D-IR spectra for

$\langle ZZZZ \rangle$ and $\langle ZZXX \rangle$ are both converted to a pump-probe spectrum by integrating across ω_1 (1960 to 2120 cm^{-1}). The GSB/SE and ESA features are fit to two overlapping Gaussians of opposite signs, and the rotational anisotropy at each t_2, $\alpha(t_2)$, is then

$$\alpha(t_2) = \frac{S_{ZZZZ}(t_2) - S_{ZZXX}(t_2)}{S_{ZZZZ}(t_2) + 2S_{ZZXX}(t_2)} \tag{7.3}$$

where S_p is the integrated area of the GSB/SE component for polarization p.

Using this measure of the rotational anisotropy, both H_2O and EAN qualitatively show thermally activated rotational dynamics (Figure 41). For EAN at 14 °C, near its freezing temperature, rotational anisotropy decreases little (from 0.4 to 0.3) over the time range accessed by the experiment. At 130 °C, the rotational dynamics are faster. The initial value of the anisotropy (0.35) is less than the ideal value (0.4) due to rotations moving into the motionally narrowed regime. The rotational anisotropy then decays to ~ 0.05 by 11 ps. For H_2O at 5 °C, near its freezing temperature, the initial anisotropy signal is ~ 0.35, and it decays to ~ 0.07 by 6 ps. At 89 °C, the anisotropy begins at ~ 0.28 and decays to zero by 4 ps.

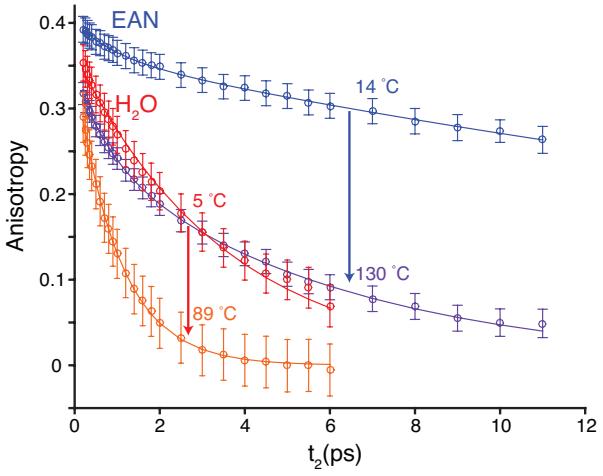

Figure 41: The timescale of molecular rotation is slower in EAN than H_2O for the ν_3 mode of SCN^-. The 2D-IR data is converted into a pump-probe spectrum for each t_2, and the anisotropy is calculated for SCN^- in EAN (14 °C, blue and 130 °C, purple) and H_2O (5 °C, red and 89 °C, orange).

The qualitative description is made quantitative by fitting the anisotropy decays as a function of temperature (Table 10). A single exponential suffices to fit the H_2O data. A biexponential is needed to fit the EAN data. To compare H_2O and EAN, we again calculate a total correlation time by integrating the normalized orientational correlation function.

$$\tau_{\text{total}}^{\text{rot}} = \int_0^\infty \alpha(t)/0.4 \; dt \tag{7.4}$$

where $\alpha(t)$ is the rotational anisotropy exponential fit, and 0.4 is the ideal initial value for the anisotropy. In principle, one can analyze the temperature dependence for each term in a multiexponential fit. As with $\tau_{\text{total}}^{\text{FFCF}}$, we find the total correlation time, $\tau_{\text{total}}^{\text{rot}}$, to be a more stable fitting parameter than the individual time constants. At all temperatures, the rotational dynamics of SCN^- in EAN, as quantified by $\tau_{\text{total}}^{\text{rot}}$, are much slower than in H_2O.

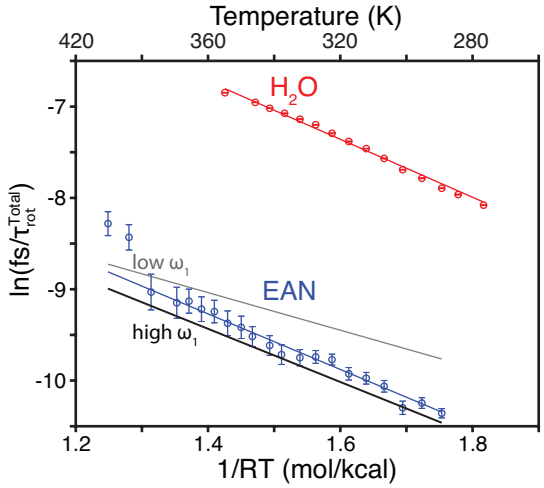

Figure 42: The temperature dependence of $\tau_{\text{total}}^{\text{rot}}$ follows an Arrhenius behavior in both EAN and H_2O. An Arrhenius model is used to fit the temperature dependent $\tau_{\text{total}}^{\text{rot}}$ for SCN^- in EAN (blue) and H_2O (red). The Arrhenius fit for the temperature dependent $\tau_{\text{total}}^{\text{rot}}$ is shown in relation to the temperature dependent Arrhenius fits at low (2046 cm^{-1}) and high (2076 cm^{-1}) ω_1

.

The rotational timescales fit to an Arrhenius model; the log of the rate varies linearly with inverse temperature (Figure 42). As discussed in Chapter 6, the anisotropy varies across ω_1

Table 10: Temperature-dependent timescales of molecular rotation are determined through exponential fits of the anisotropy of SCN^- in EAN and H_2O.

	a_1^{rot}	τ_1^{rot} (ps)	a_2^{rot}	τ_2^{rot} (ps)	$\tau_{\text{total}}^{\text{rot}}$ (ps)
EAN					
14 $°C$	0.040 ± 0.003	1.0 ± 0.2	0.361 ± 0.003	35 ± 1	31 ± 4
130 $°C$	0.090 ± 0.009	0.8 ± 0.1	0.25 ± 0.01	6.0 ± 0.3	4 ± 1
H_2O					
5 $°C$	0.364 ± 0.005	3.5 ± 0.1	—	—	3.2 ± 0.3
89 $°C$	0.348 ± 0.004	1.02 ± 0.02	—	—	0.889 ± 0.004

Table 11: The Arrhenius parameters are determined for the timescales of molecular rotation of SCN^- in EAN and H_2O.

	$1/A_{\text{rot}}$ (fs)	E_a^{rot} (kcal/mol))
EAN	150 ± 40	3.0 ± 0.2
H_2O	9 ± 2	3.2 ± 0.2

for SCN^- in EAN. As a result, the E_{a}^{rot} varies across ω_1 (Appendix A.4). Therefore, using an average across the vibrational band, the E_{a}^{rot} and A_{rot} lie in between a limit of the Arrhenius parameter for low and high ω_1.

Though the timescales for rotational motion are very different in EAN and H_2O, the activation energies are, remarkably, the same within error (Table 11). The cause for the distinctly different timescales is not the energy of activation but the frequency prefactor, A; in units of time, $1/A_{\text{rot}}$ was slower in EAN (150 ± 40 fs) than H_2O (9 ± 2 fs). We interpret the frequency prefactors for rotations below (Section 7.5).

So far, we have shown the temperature-dependent dynamics and activation energy for the PW-FFCF and anisotropy. For SCN^- in EAN, both of these analyses involve an average over both subensembles. With the temperature-dependent rotational anisotropy in hand, we will now disentangle the SSD and RISD components from the PW-FFCF.

7.4.3 Temperature-dependent RISD

Using the approach described in Chapter 6, we determined the RISD for SCN^- in EAN as a function of temperature. Briefly, in this approximation, the PW-FFCF, $C_p(t)$, can be

simplified to the product of SSD, $F(t)$, and RISD, $R_p(t)$.

$$C_p(t) = F(t)R_p(t). \tag{7.5}$$

Additionally, the time dependence of the RISD, $R_p(t)$, can be expressed solely in terms of the reorientation time for each polarization condition after the appropriate orientational averaging of the signals[26,27].

In H_2O, a single exponential was used to model the SSD component of the PW-FFCF

$$C_p(t_2) = a_1^{\mathrm{SSD}} e^{-t_2/\tau_1^{\mathrm{SSD}}} R_p(t_2; \tau_{\mathrm{total}}^{\mathrm{rot}}). \tag{7.6}$$

Here, τ_1^{SSD} represents the timescale of solvent structural reorganization.

In EAN, neither a single nor biexponential $F(t)$ was able to fit the data. To describe the average rotational motions, a restricted molecular rotation (wobbling in a cone) model is used for $R_p(t)$

$$C_p(t_2) = F(t)R_p(t; \tau^{\mathrm{rot}}) \tag{7.7}$$

where τ_1^{rot} is a molecular rotational time inside of a restricted angular space of θ. Following Kramer et al.[27], the orientational correlation functions, $L_l(t)$, are defined in terms of an exponential decay to an offset, S_l, which is a function of the Legendre polynomial order, l, and the half-cone angle, θ,

$$L_l(t) = S_l^2 + (1 - S_l^2)\exp(-t/\tau_{l,\mathrm{eff}}). \tag{7.8}$$

$R_p(t_2, \tau^{\mathrm{rot}})$ is constructed from the appropriate combination of these orientational correlation functions[27]. The simplest form for SSD that fit the data was a constant, $F(t) = a^{\mathrm{SSD}}$.

Simultaneous fitting of the $\langle ZZZZ \rangle$ and $\langle ZZXX \rangle$ CLS results separated the SSD from the RISD (Table 12). As discussed in Chapter 6, we extract from the EAN data a fast molecular rotation time (3 ps) and a large half cone angle ($\theta = 108°$). The half cone angle does not vary significantly with temperature. Overall, τ^{RISD} decreases with increasing temperature in both EAN and H_2O comparable to the trend in τ_{total}^{rot}. In addition to τ^{RISD}, a timescale for SSD (τ^{SSD}) is extracted in H_2O.

The SSD and RISD time constants follow an Arrhenius behavior (Figure 43). The inverse of the integrated SSD time ($\tau_{\mathrm{total}}^{\mathrm{SSD}} = a_1^{\mathrm{SSD}}\tau_1^{\mathrm{SSD}}$) represents the rate of structural

Table 12: The temperature-dependent PW-FFCFs are separated into their RISD and SSD components for SCN^- in EAN and H_2O.

	a^{SSD}	τ^{SSD} (ps)	τ^{RISD} (ps)	θ (degrees)
EAN				
14 °C	0.81	—	2.9	107
130 °C	0.68	—	0.70	109
H_2O				
5 °C	0.55	2.4	0.8	—
89 °C	0.14	1.4	0.3	—

solvent reorganizational dynamics, and its logarithm follows a linear trend against inverse temperature (Figure 43a). The rate of SSD in EAN is represented by an upper bound. In both EAN and H_2O the inverse of the RISD timescale (τ^{RISD}) represents the rate of SCN^- rotating in a hydrogen bonding network, and its logarithm is also linear against inverse temperature (Figure 43b).

The activation energy for the RISD component (E_a^{RISD}) in both H_2O and EAN is a few k_BT lower than the SSD component (E_a^{SSD}) in H_2O (Table 13). The E_a^{RISD} of the RISD component in EAN is statistically similar to E_a^{RISD} in H_2O.

The main difference between the various Arrhenius fits of τ^{RISD} is the frequency prefactors. First, the prefactors in EAN are much slower than in H_2O. As with the anisotropy, the large difference in observed dynamics are due to the frequency prefactors, not the activation energies. The apparent attempt time in H_2O is at least an order of magnitude lower than in EAN.

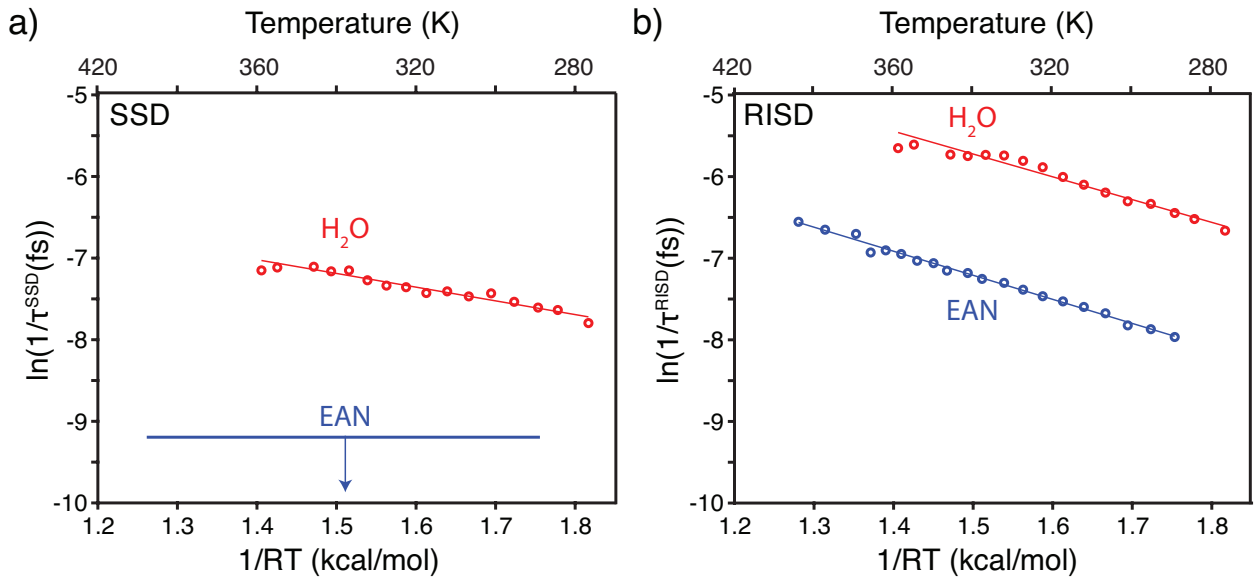

Figure 43: The activation energy for the SSD and RISD of SCN^- in H_2O and EAN are determined. a) An Arrhenius model is used to fit the temperature dependent SSD timescales in H_2O (red). Estimating the upper-limit for SSD in EAN, the timescales are expected to fall below this line if they were able to be resolved (blue). b) An Arrhenius model is also used to fit the temperature dependent RISD components in H_2O (red) and EAN (blue).

Table 13: Arrhenius fit parameters are determined for the timescales of structural fluctuations (τ^{SSD}) and molecular rotations (τ^{RISD}) for SCN^- in EAN and H_2O.

	$1/A$ (fs)	E_a (kcal/mol))
EAN		
τ^{RISD}	16 ± 4	2.9 ± 0.1
H_2O		
$\tau^{SSD}_{\mathrm{total}}$	0.7 ± 0.1	3.9 ± 0.1
τ^{RISD}_1	5 ± 3	2.8 ± 0.3

7.5 DISCUSSION

7.5.1 Separating Activation Energies for Rotations and SSD

In this work, we combine polarization and temperature dependence to extract activation energies for RISD and SSD separately. Kramer et al. extended the RISD concept developed for vibrational sum-frequency-generation spectroscopy[28] to explain that the polarization dependence of the FFCF is due to the coupling of rotational motion to spectral diffusion.[26,27] Temperature-dependent dynamics naturally access activation energies, but, without separating the RISD and SSD, we could report as many as four separate activation energies – from PW-FFCFs measured in $\langle ZZZZ \rangle$, $\langle ZZXX \rangle$, and magic-angle conditions as well as the rotational anisotropy itself. The approach developed in this chapter provides a specific way to separate the activation energies of rotations of the probe molecule and structural fluctuations of the solvent cage.

The sensitivity of apparent activation energy to the laser polarization has been noted in the literature. For example, experiments in different polarization conditions report different activation energies for spectral diffusion of the OH/D stretch in water, 3.5 kcal/mol in the $\langle ZZZZ \rangle$ configuration[9] and 6.2 kcal/mol at the magic angle.[10] In contrast, no statistical difference exists between the E_a^{FFCF} for the parallel and perpendicular signals for each SCN^- in EAN or H_2O. A model of spectral diffusion based on thermally activated rotations and frequency fluctuations reproduces the observation that the $\langle ZZZZ \rangle$ and $\langle ZZXX \rangle$ signals give similar activation energies and does not explain the discrepancy observed in water (data not shown). From extracting the SSD and RISD components (Equations 7.6 and 7.7), what the model shows very clearly is that apparent activation energies extracted from the PW-FFCF can vary from being dominated by rotations (RISD limit) to being dominated by structural fluctuations (SSD limit).

In H_2O, spectral diffusion of the PW-FFCF is dominated by SSD. The E_a^{SSD} is statistically similar to E_a^{FFCF}, while the E_a for molecular rotations (E_a^{rot} and E_a^{RISD}) are approximately 2 to $3k_BT$ lower, respectively. Our reported E_a^{FFCF} for SCN^- in water is $\sim 1k_BT$ higher than the literature value for OH spectral diffusion[9,10] in the $\langle ZZZZ \rangle$. We suspect that

the different vibrational probes (C≡N as opposed to O−D stretches) are coupled to different motions of the solvent. The literature value at the magic angle[10], however, is significantly higher than any of our reported activation energies.

In EAN, spectral diffusion of the PW-FFCF is dominated by RISD. The SSD component could not be resolved within the timeframe of the experiment ($\sim$ 11 ps). The E_a^{RISD} determined from τ^{RISD} are on par to the E_a^{FFCF} and E_a^{rot}.

The activation energy for SCN^- rotation in EAN is similar to that in H_2O. The E_a^{RISD} is statistically similar to the E_a^{RISD} in H_2O. This similarity implies that SCN^- rotating in an hydrogen bonding environment, either EAN or H_2O, undergoes similar processes of breaking and forming hydrogen bonds.

Bulk viscosity is another perspective to rationalize the observed dynamical trends. At room temperature, the viscosity of EAN is 30-fold higher than H_2O[207], and the observed dynamical timescales are all longer in EAN, though not by a factor of 30. As seen in previous IL studies[14,71], the correlation dynamics ($\tau_{\mathrm{total}}^{\mathrm{FFCF}}$) scale linearly as a function of temperature with the bulk viscosity in both EAN and H_2O (Figure 44). This relationship provides insight into intermolecular "friction" that may determine the bulk viscosities. The activation energy determined by the temperature dependent viscosity (4.9 kcal/mol)[73], however, is $\sim$4 kT higher than are reported $E_{\mathrm{a}}^{\mathrm{FFCF}}$s. This difference is not uncommon and has been previously reported when a solute is being used to probe dynamical information in the solvent underreports the E_{a} from bulk dynamics[218]. Overall, the activation energies for these dynamical properties in water and EAN do not track with the viscosity; therefore, the difference lies in the frequency prefactors.

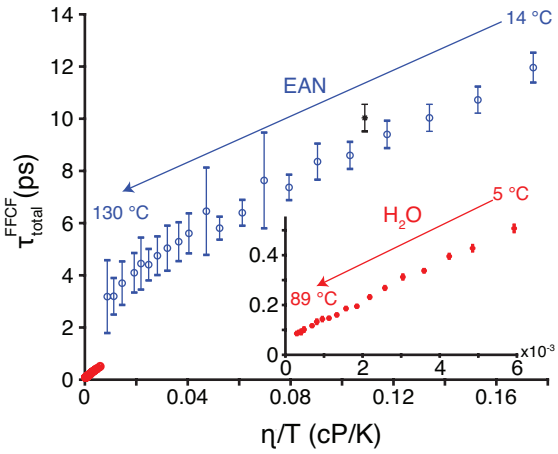

Figure 44: The timescale of solvent reorganization is linearly proportional to the bulk viscosity of the solvent. The $\tau_{\text{total}}^{\text{FFCF}}$s for $\langle ZZZZ \rangle$ is plotted against the corresponding viscosity at the respective temperature for EAN[73] (blue, o) and H_2O[219] (red, o, inset). The viscosities were extracted using a piecewise cubic Hermite polynomial method for H_2O but only an exponential function for EAN due to an insufficient temperature range. An additional data point for a different reported viscosity of EAN at room temperature is shown for comparison (black, $*$)[207].

7.5.2 Frequency Prefactors Reflect Activation Entropy

The Arrhenius prefactors can be rationalized based on analogy to the jump model proposed by Thompson and Laage[17,220]. In water, where hydrogen bond reorientation is dominated by large angular jumps, the timescale of water reorientation, τ_{rot}, can be decomposed into the time between jumps to new hydrogen bonding partners, τ_{jump}, and a time associated with the rotation of an intact hydrogen bond, τ_{frame},

$$\frac{1}{\tau_{\text{rot}}} = \frac{1}{\tau_{\text{jump}}} + \frac{1}{\tau_{\text{frame}}}. \tag{7.9}$$

In water the hydrogen bond dynamics are dominated by the large angle jumps (τ_{jump}), and the reorientation of the OH and its hydrogen bonding partner together, τ_{frame}, is a minor channel.

Thompson and Laage[221] analyzed dynamics of hydrogen bonds in a series of alcohols. As the alcohol chain lengths increase, the volume available for new hydrogen bonding partners decreases. This slows the rate of new hydrogen bond formation because molecules must wait until a new hydrogen bonding partner is nearby before a hydrogen bond switch can occur. To quantify the change in available volume, they define a volume in the transition state blocked by atoms that cannot accept a new hydrogen bond, f,[155,221] and find a direct relation to the jump times

$$\frac{1}{1-f} = \frac{\tau_{\text{jump}}^{\text{ROH}}}{\tau_{\text{jump}}^{\text{H}_2\text{O}}}. \tag{7.10}$$

They find the dynamical slowdown in ethanol, for example, is 10 ($f = 0.90$).[221]. By analogy, we calculate this quantity comparing the rotational dynamics of SCN^- in EAN and water

$$\frac{1}{1-f} = \frac{\tau_{\text{rot}}^{\text{EAN}}}{\tau_{\text{rot}}^{\text{H}_2\text{O}}}, \tag{7.11}$$

and we find $f = 0.91$. The similarity of the excluded volume factors suggests that a similar excluded volume mechanism is at play here. The dynamics of the vibrational probe in EAN, SCN^-, are probably not dictated by large angle jumps directly. If the dynamics of the nearby solvent is dictated by large angle jumps, for which there is evidence[84], it is possible that the same dependence on activation volume might apply. In the alcohols, as the alkyl chain increases, frame reorientation eventually contributes.[221] Perhaps the higher viscosity in EAN reduces this contribution to the reorientational dynamics. A chain length dependent series of ammonium nitrate PILs could test our claim that PILs undergo a similar excluded volume mechanism as H_2O. Also, our interpretation calls for molecular simulations to test this proposed model in detail.

The differences in dynamics between SCN^- in EAN and water are due not to differences in the activation energies but in the size of the accessible phase-space at the transition state. In other words, the entropy of activation, $\Delta S^\ddagger$, is the critical quantity. We interpret the observed frequency prefactors based on the Eyring equation for the rate of a process, k,

$$k = \frac{\kappa k_B T}{h} \exp(\Delta S^\ddagger / k_B) \exp(-\Delta H^\ddagger / k_B T) \tag{7.12}$$

Table 14: An Eyring analysis is performed to extract the enthalpy ($\Delta H^{\ddagger}$) and entropy ($\Delta S^{\ddagger}$) of activation for SCN^- in EAN and H_2O.

	⟨ZZZZ⟩	⟨ZZXX⟩	Anisotropy	RISD	SSD
EAN					
$\Delta H^{\ddagger}$ (kcal/mol)	2.0 ± 0.1	2.2 ± 0.1	2.4 ± 0.2	2.3 ± 0.1	—
$\Delta S^{\ddagger}$ (cal·mol^{-1}·K^{-1})	−1.4 ± 0.3	0.0 ± 0.4	−2.7 ± 0.7	2.4 ± 0.3	—
H_2O					
$\Delta H^{\ddagger}$ (kcal/mol)	3.7 ± 0.2	3.9 ± 0.2	2.4 ± 0.2	2.1 ± 0.3	3.3 ± 0.2
$\Delta S^{\ddagger}$ (cal·mol^{-1}·K^{-1})	11.1 ± 0.8	12.4 ± 0.8	3.0 ± 0.6	5 ± 1	8.5 ± 0.5

where h is Planck's constant, κ is the transmission coefficient, $\Delta H^{\ddagger}$ is the enthalpy of activation, and $\Delta S^{\ddagger}$ is the entropy of activation. Lacking other knowledge, we assume a transmission coefficient of unity, $\kappa = 1$ and temperature independent $\Delta H^{\ddagger}$ and $\Delta S^{\ddagger}$.

The difference of $\Delta S^{\ddagger}$ between EAN and H_2O assist in explaining the differences in the unrealistic barrier attempt frequency (Table 14). Fitting our data to an Eyring equation the $\Delta H^{\ddagger}$ and $\Delta S^{\ddagger}$ can be extracted from the slope and intercept, respectively. As expected, the $\Delta H^{\ddagger}$ is approximately 0.6 kcal/mol less than the respective E_a ($\Delta H^{\ddagger} = E_a - RT$). The $\Delta S^{\ddagger}$s in H_2O for both reorientation and SSD are positive. The magnitudes are similar to those reported for hydrogen bond jumps in alcohols[222] and CO_2 in an imidazolium ionic liquid[223]. A positive $\Delta S^{\ddagger}$ means that the transition state is associated with a larger phase-space volume than the reactant state. This difference is qualitatively associated with the relative increase in the number of configurations of neighboring molecules at the transition state ("disordered") compared to the reactant state ("ordered"). Because the "reaction" occurs in a high dimensional space of many solvent degrees of freedom, the assumption of a one-dimensional reaction coordinate in the Arrhenius model fails, leading to unrealistic

frequency prefactors. In EAN, however, the $\Delta S^{\ddagger}$ ranges from -2.7 to -2 cal·mol^{-1}·K^{-1} suggesting more order, or mode stiffening, in the transition state relative to the ground state. Atomistic molecular modeling of the transition state could provide a more detailed molecular picture of this intriguing observation.

7.6 CONCLUSION

Temperature-dependent 2D-IR with polarization control reveals activation energies and barrier attempt frequencies for molecular rotations and structural motions. The polarization weighted FFCF contains contributions from both structural and reorientation-induced spectral diffusion, SSD and RISD, respectively, which follow an Arrhenius behavior. The E_a^{rot} for SCN^- to rotate in the hydrogen bonding network of EAN is similar to that of H_2O, but the rates are slower in EAN. Applying an Eyring approach to understand the frequency prefactors revealed that H_2O has a positive entropy of activation while the more viscous and rigid structure of EAN produces a slightly negative entropy of activation for rotational motion. In H_2O, the activation energies from spectral diffusion are dominated by SSD. In EAN, the activation energies from spectral diffusion are dominated by RISD. As discussed in Chapter 6, the low frequency sub-ensemble correlates to SCN^- with more but weaker hydrogen bonds, and the slower rotational time in the high frequency sub-ensemble correlates to SCN^- with fewer, more directional hydrogen bonds, which may correspond to charge-depleted and charge-enhanced regions of the EAN.

This presented analytical method shows what can be accomplished in understanding the structural and rotational components of the solvent reorganization activation energies with polarization and temperature dependent 2D-IR. From our interpretations of the 2D-IR data, EAN appears to be 'water-like' in terms of the energy needed to rotate SCN^- in a hydrogen bonding network and is consistent with a jump model mechanism. These observations provide new insights into the molecular properties that make PILs promising candidates as proton conducting electrolytes over more commonly used aqueous electrolytes.

8.0 CONCLUSION

This research investigation focuses around understanding the solvent fluctuations that drive hydride and proton transfer in various hydrogen bonded networks: hydride donors, hydride molten salts, and protonated molten salts. 2D-IR is used to resolve solvent reorganization timescales that relate to the important solvent fluctuations for proton and hydride transfer, *i.e.* the breaking and forming of hydrogen bonds.

In this work, two different systems are studied with 2D-IR spectroscopy: BH_4^- and EAN. To study hydride donors, the dihydrogen bonds of BH_4^- are directly probed through the BH antisymmetric stretch in aqueous solutions of increasing OH^- concentrations. A quantitative approach is developed to assign the multiple crosspeaks as a result of vibrational coupling of bright and dark modes. To study proton transfer, the nitrile ν_3 stretch of SCN^- indirectly probes the hydrogen bonded PIL EAN. By combining polarization and temperature control, a comprehensive 2D-IR study establishes what can be understood from solvation dynamics. Overall, this research investigation focuses around vibrational mode coupling, solvent dynamics, and separating the solvent dynamics into rotational and structural motions.

8.1 VIBRATIONAL MODE COUPLING IN BH_4^-

The complex 2D-IR spectrum of the BH antisymmetric ν_3 stretch of BH_4^- is assigned. Isotope labeled FTIR studies in the 1970's assign the complicated linear spectra of the BH ν_3 stretch as mixing with two Fermi resonances.[137] The two dark modes are an overtone of the antisymmetric BH bend, $2\nu_4$, and a combination band of the symmetric and antisymmetric BH bends, $\nu_2+\nu_4$. The linear spectrum is well-established, but higher-order IR spectroscopy

results in a more complicated spectrum as states in the excited state manifold are reached. For BH_4^-, two different anharmonicities are reported in solid-state 2D-IR (44 cm^{-1})[126] and in IR-pump IR-probe spectroscopy (120 cm^{-1})[125].

For the 2D-IR spectrum of BH_4^- in an IL, two peaks contain character of the second excited state of the ν_3 mode. The 2D-IR spectrum of the ν_3 mode for BH_4^- in H_2O shows 5 peaks; while in an IL, a total of 16 peaks are resolved. Fewer dihydrogen bonds in an aprotic IL result in narrow linewidths and less cancelation effects. To identify the 2D-IR peaks, the spectra are simulated with a response function formalism and fall in good agreement with that of the experiment. In the spectral window, the simulation reveals three vibrational states in the first excited state manifold that contribute to the 2D-IR spectrum: $2\nu_4$, ν_3, and $\nu_2+\nu_4$. The second excited state manifold, however, consists of 7 states with mixed character that contribute to the 2D-IR spectrum. Two peaks shifted below the diagonal peak for the ν_3 mode have character of the excited state absorbance of ν_3 with similar anharmonicities to that determined in other ultrafast IR experiments.

8.2 SUPPRESSING THE HER OF BH_4^-

Controlling the hydrogen evolution reaction (HER) of BH_4^- is critical to improve the hydride donor's hydrogen storage and reductant potential. For use in hydrogen storage, the HER can be beneficial to release $H_{2(g)}$, but suppressing the HER is necessary for long time storage. For use as a reductant, the HER is parasitic and needs to be eliminated, so the hydride is not transferred to other protons. One avenue for suppressing the HER is by manipulating the pH. At high OH^- concentrations, the rate of the HER slows down.[38,39]

At an elevated pH, 2D-IR spectroscopy is used to monitor the solvent fluctuations of the dihydrogen bonds between BH_4 and H_2O. As the NaOH concentration increases, the dynamics of solvent fluctuations slow down. On one hand, the increase in viscosity at elevated NaOH concentrations is one explanation for the trend in dynamics. On the other hand, BOMD simulations provide support of an ion crowding effect. At elevated concentrations of hydrophopes in H_2O, a crowding effect inhibits the accessible number of transition states

for the breaking and forming of hydrogen bonds in a jump model.[154,155] With BH_4^- in elevated NaOH concentrations, the Na^+ and OH^- ions show similar behavior to that of a hydrophobes. In neat H_2O, BH_4^- forms dihydrogen bonds with 2 H_2O molecules and is solvated by an additional 2-3 H_2O molecules in the first solvation shell. Adding 7 M NaOH, the first solvation shell of BH_4^- consists of just one H_2O molecule, *i.e.* one dihydrogen bond. The decrease in the amount of solvated H_2O near BH_4^- is due to a Na^+ cation that coordinates to BH_4^- at a bisector, and a OH^- ion in the second solvent shell that preferentially coordinates to 3 H_2O molecules.

The combined effort of 2D-IR and BOMD simulations sheds light on the classic rate studies performed 60-70 years ago. In an aqueous solution, two rate constants contribute to the rate of BH_4^- hydrolysis: $k_{H_3O^+}$ and k_{H_2O}. Therefore, at a higher pH, the rate is solely dependent on k_{H_2O}. A rate constant depends on the local environment and is suggestive of restructuring of that environment. In this case, the dihydrogen bond is confined due to coordination with a counterion and the structured hydration of a OH^- ion in the second solvation shell. This molecular picture postulates that k_{H_2O} will decrease, so k_{H_2O} may be a function of the solvation shell around BH_4^-.

A compelling path forward is to provide experimental evidence of the hydroxyborohydride intermediates during the HER of BH_4^-. With *ab initio* molecular dynamics, Li *et al.* propose a comprehensive mechanism for the HER of BH_4^-.[33] The overall reaction is exothermic with two endothermic steps involving an initial BH_5 intermediate and a metastable intermediate, BH_3OH. Since the HER is pH dependent, the reaction can be catalyzed by the addition of an acid to lower the activation energy for addition of the initial proton. Therefore, an ultrafast pH jump may extract the intermediates that have low reaction barriers if they occur on an ultrafast timescale (fs to ps).

An UV Pump-IR Probe experiment can be designed to facilitate a fast proton transfer and probe the hydroxyborohydride intermediates on an ultrafast timescale. Upon UV excitation, the pK_a of a photoacid, like 2-napthol, transfers a proton within 150 fs as its pK_a decreases.[224–227] Then at various delay times, the intermediates can be probed by differences in the intermediates' vibrational frequencies for a B-O and/or B-H stretch. One key issue is to suppress the HER before the photoacid is excited. A possible solution is to include a rapid

mixing element where a solution of BH_4^- at a high pH is mixed with a solution including the photoacid. The sample will be mixed before entering the sample window, so the pH will be low enough to protonate 2-napthol but not low enough to degrade BH_4^- before the excitation of the photoacid.

8.3 EAN: ROTATION LIMITED DYNAMICS

The nitrile ν_3 stretch of SCN^- indirectly probes the three dimensional hydrogen bonding network of EAN. The population relaxation lifetime (T_1), anisotropy, and solvent dynamics are frequency dependent. Different T_1s at low and high frequency indicate that SCN^- is experiencing two subensembles, *i.e.* dynamical heterogeneity in EAN. According to MD simulations and neutron scattering experiments,[86,182,228,229] these subensembles correspond to charge dense (ammonium and nitrate ions) and charge depleted (alkyl chain) regions.

With polarization control, the FFCF can be separated into structural and rotational motions. Due to spectral overlap, the molecular rotation timescale (anisotropy) and solvent dynamics (FFCF) of each subensemble in EAN could not be separated. Thus, the respective dynamics were averaged over both subensembles. The solvent dynamics from the FFCF are due to rotations of SCN^- in EAN as the structural motions are too slow to be resolved. The rotational motions of SCN^- in EAN follow a wobbling in a cone model where rotations are restricted in an angular space, *i.e.* a cone. Coincidently, the angular space (108 °) is similar to the suggested large angle jump (106 °) from a long-lived rotation with IR Pump-IR Probe spectroscopy.[84]

8.4 EAN ~ H_2O: THERMALLY ACTIVATED DYNAMICS

After the room temperature solvent dynamics of SCN^- in EAN are established, a temperature dependent 2D-IR study explores the enthalpy and entropy of solvent reorganization. For SCN^- in EAN, the E_a from the anisotropy, PW-FFCFs, and RISD (reorientation-induced

spectral diffusion) are statistically similar, because the rotational motions are the dominating contribution to spectral diffusion. For SCN^- in H_2O, both a SSD (structural spectral diffusion) and RISD timescale are extracted from the PW-FFCFs. In H_2O, the SSD is the dominating feature of spectral diffusion as the E_a^{SSD} is statistically similar to E_a^{FFCF}.

The similar $E_{\mathrm{a}}^{\mathrm{rot}}$ of SCN^- in H_2O and in EAN suggests that the rotation mechanisms are the same. If the dynamics around SCN^- follows a jump model in EAN and in H_2O, a model for the excluded volume effect can define the transition state as being blocked by atoms which are unable to accept a new hydrogen bond

$$\frac{1}{1-f} = \frac{\tau_{\mathrm{jump}}^{\mathrm{EAN}}}{\tau_{\mathrm{jump}}^{\mathrm{H_2O}}}. \tag{8.1}$$

where f is the excluded volume factor and τ_{jump} is the jump timescale.[155,221] By comparing the timescales of molecular rotations, an excluded volume factor is determined to explain a slow down in the dynamics. Surprisingly, the value determined in comparing H_2O with EAN ($f = 0.91$) is the same for that determined for ethanol ($f = 0.90$)[221], thus providing more suggestive evidence that large angle jumps are involved in the breaking and forming of hydrogen bonds in EAN.

These investigations fueled us to revisit a classic 2D-IR experiment: HOD in H_2O or D_2O. The E_a varies with polarization in two different temperature dependent 2D-IR experiments for the all parallel condition[9] and at the magic angle[10]. From the analysis of SCN^- in EAN and SCN^- in H_2O, the E_as for the PW-FFCF are not statistically different for the parallel, perpendicular, and isotropic signals. 2D-IR experiments were performed by probing the OD stretch of HOD in H_2O at the Central Laser Facility at the Rutherford Appleton Laboratory. Our preliminary analysis suggests the E_a for the FFCF is not polarization dependent contrary to the reported values in the literature. The 2D-IR data are currently being analyzed along with complementary molecular dynamics simulations.

Another polarization- and temperature-dependent 2D-IR experiment explores the effect of chain length on a series of ammonium formate PILs. The E_a of solvent reorganization may increase as a function of chain length due to the aliphatic component slowing down rotational motions. A chain length study will also provide more evidence of the entropy of activation and the excluded volume effect compared to a series of alcohols[221]. An interesting preliminary

result is that at longer chain lengths (butyl-ammonium formate) the two subensembles are visible as separate diagonal peaks in the 2D-IR spectrum.

In summary, 2D-IR can elucidate the solvent dynamics related to solvent fluctuations which are important to understand for optimizing proton and hydride transfers. With polarization and temperature control, 2D-IR can provide a E_a for structural and rotational motions from overlapping distributions. A comprehensive study of the solvent dynamics provides new insights and more detailed descriptions to the motions that contribute to spectral diffusion. In this research investigation, the solvent dynamics provide new molecular insights into how the HER is suppressed and elucidating 'water-like' mechanisms of a protonated molten salt for promising use as a proton conducting electrolyte.

APPENDIX

A.1 BH_4^- IN [NAOH]

A.1.1 Temperature-Dependent FTIR

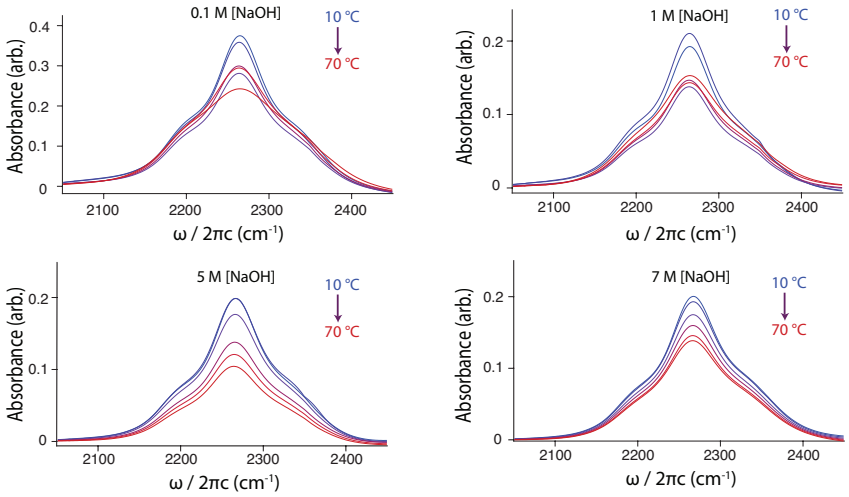

Figure 45: The overall trend of the absorbance of the BH_4^- decreases as temperature increases. FTIR are obtained of 3 M BH_4^- in 0.1, 1, 5, and 7 M NaOH at temperatures: 10, 20, 30, 40, 50, and 60 °C (blue to red).

Temperature-dependent FTIR is obtained of 3 M BH_4^- in 0.1, 1, 5, and 7 M NaOH at temperatures of 10, 20, 30, 40, 50, and 60 °C. The temperature is varied by a water based isotemp cooling/heating recirculating chiller (Fisher Scientific) and is monitored by a J-type thermocouple (National Instruments USB-TC01). The thermocouple is kept in contact with one of the CaF_2 windows in the sample cell. Once the thermocouple reaches the desired temperature, the sample is left to equilibrate for five minutes before collection. Overall the absorbance of BH_4^- tends to decrease as the temperature increases (Figure 45). The spectra also show no apparent frequency shifts with change in temperature.

A.1.2 Pump-Probe Data

Table 15: The GSB of the ν_3 of BH_4^- mode does not fully decay in 200 ps. The amplitude at 2267 cm^{-1} as a function of delay time is fit to a single exponential with an offset for the parallel, perpendicular, and isotropic signal from the IR Pump-IR probe data.

	A_1	τ_1 (ps)	c
0.1 M NaOH			
Parallel	0.63 (±0.04)	2.3 (±0.4)	0.07 (±0.03)
Isotropic	0.61 (±0.04)	2.4 (±0.5)	0.07 (±0.03)
Perpendicular	0.59 (±0.05)	2.5 (±0.5)	0.07 (±0.03)
1 M NaOH			
Parallel	0.88 (±0.05)	2.1 (±0.3)	0.14 (±0.03)
Isotropic	0.73 (±0.03)	2.3 (±0.2)	0.12 (±0.02)
Perpendicular	0.66 (±0.02)	2.4 (±0.2)	0.11 (±0.01)
5 M NaOH			
Parallel	1.2 (±0.08)	2.3 (±0.4)	0.33 (±0.05)
Isotropic	1.1 (±0.07)	2.6 (±0.4)	0.30 (±0.04)
Perpendicular	0.98(±0.07)	2.7 (±0.3)	0.29 (±0.05)
7 M NaOH			
Parallel	1.1 (±0.05)	2.2 (±0.2)	0.33 (±0.03)
Isotropic	1.0 (±0.05)	2.4 (±0.3)	0.33 (±0.03)
Perpendicular	0.96 (±0.05)	2.5 (±0.3)	0.33 (±0.03)

Table 16: The ESA decay correlates to the vibration lifetime of the ν_3 mode of BH_4^-. The amplitude at 2141 cm^{-1} as a function of delay time is fit to a single exponential fit for the parallel, perpendicular, and isotropic signal from IR Pump-IR probe data.

	A_1	T_1 (ps)
0.1 M NaOH		
Parallel	0.40 (±0.03)	1.5 (±0.2)
Isotropic	0.38 (±0.03)	1.7 (±0.2)
Perpendicular	0.38 (±0.03)	1.8 (±0.3)
1 M NaOH		
Parallel	0.53 (±0.02)	1.7 (±0.1)
Isotropic	0.45 (±0.01)	1.8 (±0.1)
Perpendicular	0.42 (±0.01)	1.9 (±0.1)
5 M NaOH		
Parallel	0.74 (±0.08)	1.6 (±0.3)
Isotropic	0.70 (±0.05)	1.7 (±0.3)
Perpendicular	0.67(±0.05)	1.8 (±0.3)
7 M NaOH		
Parallel	0.68 (±0.05)	1.5 (±0.2)
Isotropic	0.66 (±0.04)	1.6 (±0.2)
Perpendicular	0.64 (±0.04)	1.7 (±0.2)

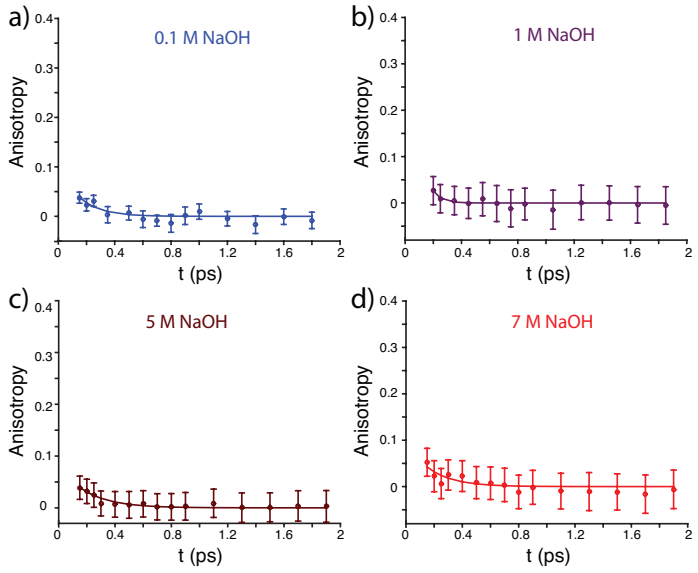

Figure 46: There is no statistical difference in the anisotropy signal for BH_4^- in all NaOH solutions: a) 0.1 M NaOH, b) 1 M NaOH, c) 5 M NaOH, d) 7 M NaOH. The anisotropy signal is reported from $\sim 150\ fs$ to 2 ps.

Table 17: The anisotropy correlates to the intramolecular redistribution of the ν_3 mode of BH_4^-. The sum of amplitudes at three frequencies (2264 cm^{-1}, 2271 cm^{-1}, 2278 cm^{-1}) for the parallel, perpendicular, and isotropic signal from the IR Pump-IR probe data are used to calculate the anisotropic signal as a function of delay time. A single exponential iss fit to reveal the timescale of molecular rotations.

	A_1	τ_{rot} (ps)
0.1 M NaOH	0.1 ($\pm$0.1)	0.1 ($\pm$0.1)
1 M NaOH	0.1 ($\pm$3)	0.06 ($\pm$0.07)
5 M NaOH	0.08 ($\pm$0.03)	0.20 ($\pm$0.06)
7 M NaOH	0.1 ($\pm$0.1)	0.2 ($\pm$0.2)

A.1.3 BOMD Simulations

Figure 47 shows the special distribution functions calculated with BOMD simulations by using the TRAVIS program. In neat H_2O, it is obvious that the oxygen distribution in the fist solvation sell constructs the spherical shape around BH_4^-. Also, hydrogen has some distributions inside of the oxygen shell, indicating that the formation of dihydrogen bonds between BH_4^- and H_2O. In 7 M NaOH, however, the oxygen distribution is not clearly forming a spherical shape which suggests a weak interaction between H_2O and BH_4^-. Also, the hydrogen distribution inside of the oxygen shell has a smaller distribution range compared to that in the BH_4^- liquid simulations. Therefore, there is a decrease in the number of dihydrogen bonds as the NaOH concentration increases.

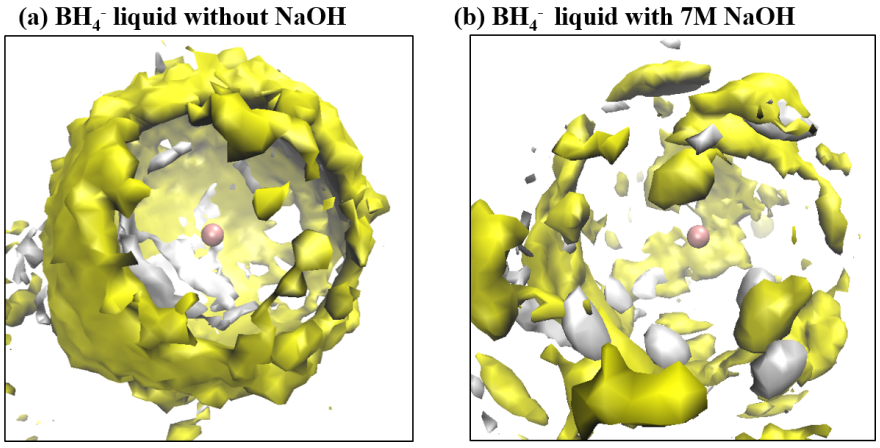

Figure 47: The three dimensional spatial distribution functions (SDFs) are determined at the isovalue, 50 nm^{-3} for the BH_4^- liquid simulations a) in neat H_2O and b) in a 7 M NaOH solution. Oxygen and hydrogen distributions are described with yellow and white colors, respectively. The pink ball indicates the boron atom.

The IR spectra is calculated by simulating BH_4^- with/without counterion, Na^+ in aqueous solution to check the divergence of the spurious Coulombic interactions between the charged unit cells. Figure 48 shows similar spectral features in the simulated IR spectra calculated for both BH_4^- and $NaBH_4$ in an aqueous solution.

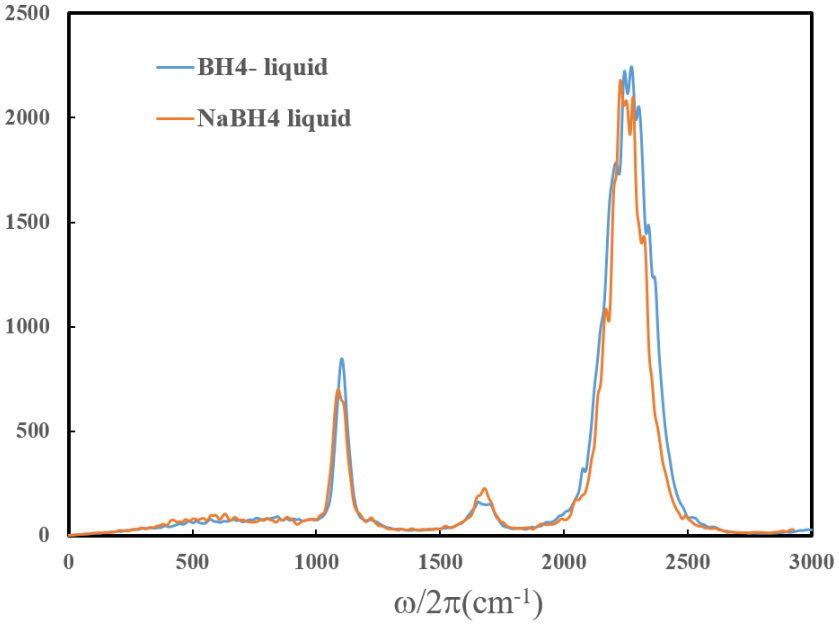

Figure 48: The simulated IR spectra is calculated for BH_4^- (blue) and $NaBH_4$ (orange) in an aqueous solution.

A.2 BH_4^- ILS

A.2.1 Water Content from FTIR

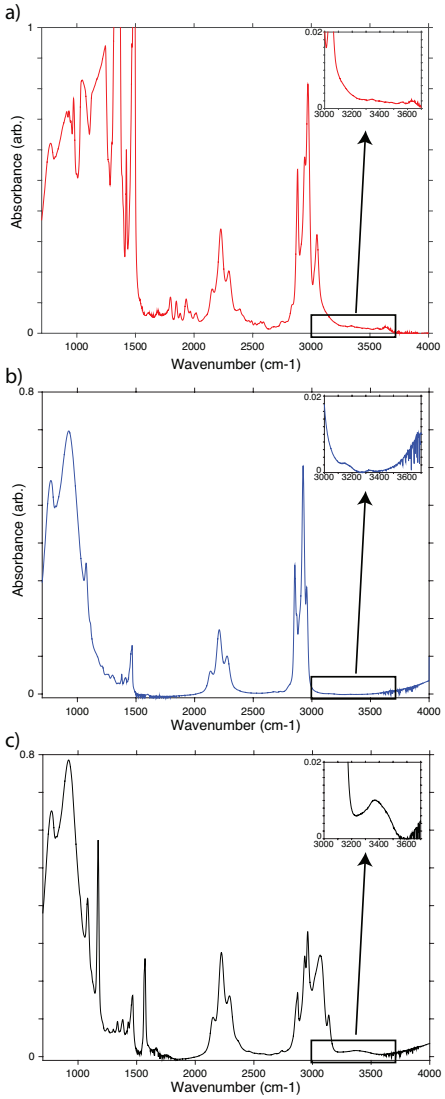

Figure 49: The water content in each IL is determined through FTIR. The FTIR spectra are obtained on a) $N_{1111}BH_4$ in $[N_{1,1,1,4}][Tf_2N]$, b) $[P_{14,6,6,6}][BH_4]$, and c) $[BMIM][BH_4]$ at room temperature. The insert in each spectrum zooms into the 3000-3700 cm^{-1} region to observe the O-H stretch of water.

The water content of each IL is determined with FTIR before the respective 2D-IR experiment as discussed in Chapter 3 (Figure 49).

The water contamination varies in each IL. In the OH stretching region, the FTIR spectra of $N_{1111}BH_4$ in $[N_{1,1,1,4}][Tf_2N]$ and $[P_{14,6,6,6}][BH_4]$ show both free and hydrogen bonded water, but the $[P_{14,6,6,6}][BH_4]$ OH stretching modes are red shifted. The $[BMIM][BH_4]$ FTIR spectrum only shows a broad OH stretching mode correlating to hydrogen bonded water. The estimated water content for the $N_{1111}BH_4$ in $[N_{1,1,1,4}][Tf_2N]$ sample (0.072 M) is lower compared to the bulk BH_4^- ILs: $[P_{14,6,6,6}][BH_4]$ (0.5 M H_2O) and $[BMIM][BH_4]$ (1 M H_2O).

The broad OH stretching peak and large water content in $[BMIM][BH_4]$ indicate that water is forming dihydrogen bonds with BH_4. While drying, the $[BMIM][BH_4]$ always has a constant stream of bubbles after hours of drying. Therefore, it is difficult to dry this sample anymore for fear of degrading the sample by observing a constant generation of H_{2g}.

A.2.2 Temperature-Dependent FTIR

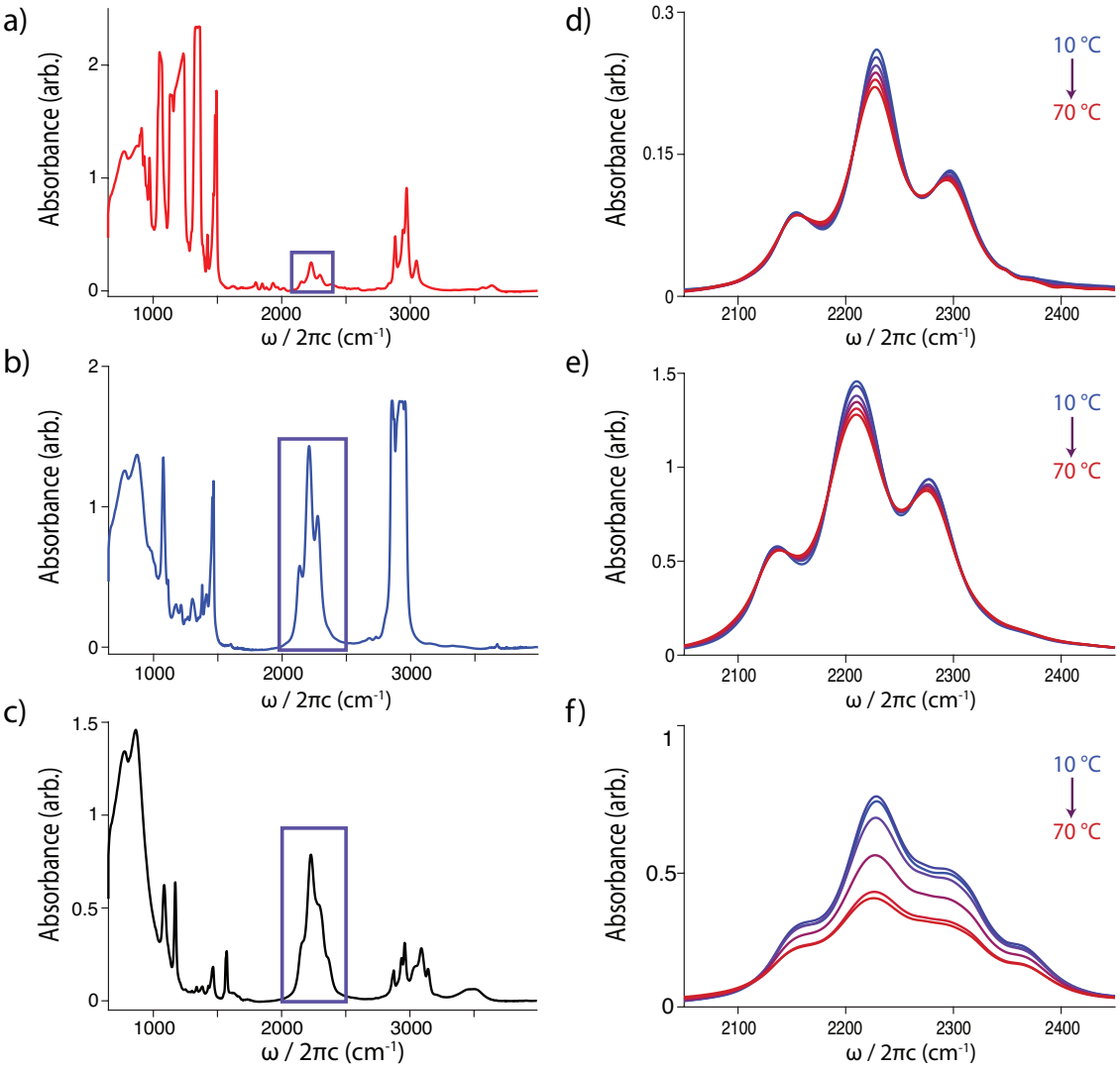

Figure 50: The FTIR spectra of a) $TMABH_4$ in $[N_{1,1,1,4}][Tf_2N]$, b) $[P_{14,6,6,6}][BH_4]$, and c) $[BMIM][BH_4]$ at room-temperature show differing characteristics. The maximum of the borohydride peak of $[P_{14,6,6,6}][BH_4]$ is red-shifted by $\sim 18\ cm^{-1}$ from those found in the other two ionic liquids. The temperature-dependent FTIR spectra of d) $TMABH_4$ in $[N_{1,1,1,4}][Tf_2N]$, e) $[P_{14,6,6,6}][BH_4]$, and f) $[BMIM][BH_4]$ show that as temperature increases the overall absorbance of the asymmetric stretch of borohydride decreases. The spectra of $[BMIM][BH_4]$ shows potential signs of degradation of the BH_4 into boric acid.

Temperature-dependent FTIR spectra are obtained of 150 mM $TMABH_4$ in $[N_{1,1,1,4}][Tf_2N]$ and of $[P_{14,6,6,6}][BH_4]$ using a CaF_2 windows separated with a 25 μm teflon spacer. The temperature-dependent FTIR spectra of $[BMIM][BH_4]$ are collected similarly without the use of a teflon spacer. The temperature is varied from 10 °C to 70 °C in ten degree intervals by a water-based isotemp cooling/heating recirculating chiller (Fisher Scientific). The temperature is monitored using a J-type thermocouple (National Instruments USB-TC01) that is kept in contact with one of the CaF_2 windows of the sample cell. Once the thermocouple indicates that the desired temperature is reached, the sample is left to equilibrate for five minutes before collection.

The full spectrum of each ionic liquid show the asymmetric stretch of borohydride, peak in the box, along with other peaks characteristic of the ionic liquid being studied (Figure 50 a-c). The asymmetric stretch of borohydride red-shifts in $[P_{14,6,6,6}][BH_4]$ by by $\sim 18\ cm^{-1}$.

The temperature-dependent FTIR spectra show a clear trend of decreased absorbance of the asymmetric borohydride stretch as the temperature is increased (Figure 50 d-f).

A.2.3 VFT Fit Parameters

Table 18: The viscosity of the BH_4^- ILs follow a non-Arrhenius behavior and are fit with a Vogel-Fulcher-Tamman as a function of temperature.

	$[BMIM][BH_4]$	$[P_{14,6,6,6}][BH_4]$
A	-2 (± 1)	-1.5 (±0.2)
B (K^{-1})	1000 (± 200)	1000 (±100)
T (K)	168 (± 6)	179 (±1)

A.2.4 DSC

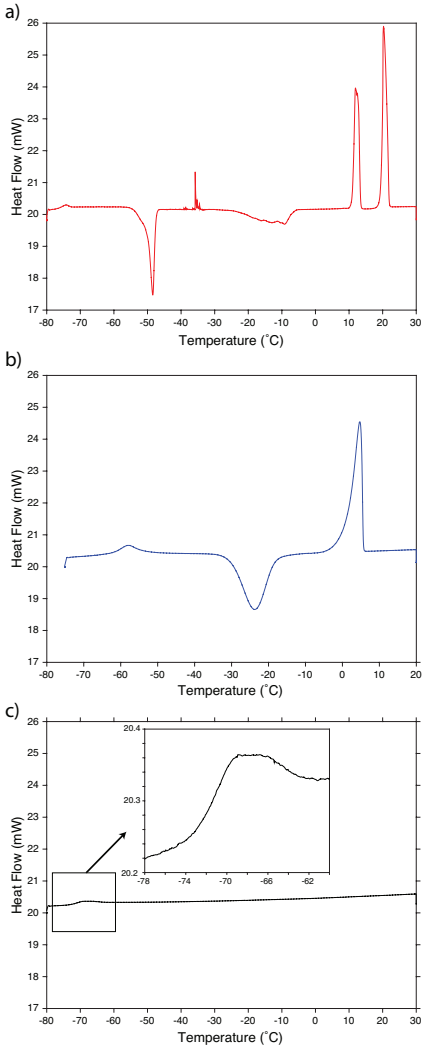

Figure 51: The DSC thermograms reveal the phase transitions for a) $TMABH_4$ in $[N_{1,1,1,4}][Tf_2N]$, b) $[P_{14,6,6,6}][BH_4]$, and c) $[BMIM][BH_4]$.

The phase transition temperatures are determined by differential scanning calorimetry (DSC) for all IL samples in this study (Figure 51). Initially, the the IL sample is cooled past -80 °C and left to equilibrate for 5 minutes. The sample is then heated at a rate of 1 °C/min up to 20-30 °C. From each thermogram, the glass transition, crystallization, and melting point temperatures are all determined if applicable. The thermogram of $[BMIM][BH_4]$ shows only a glass transition temperature by a baseline change at -73.3 °C., thus the IL is a supercooled

liquid up too room temperature. The thermogram of $[P_{14,6,6,6}][BH_4]$ reveals all three possible transitions.

A.2.5 Vibrational Relaxation Times

IR pump-IR probe experiments are performed on all IL samples in this study. The delay times are varied from -0.2 ps to 200 ps. At each delay time, the IR pump polarization are varied between parallel and perpendicular polarization.

Table 19: The vibrational relaxation times (t_{para}) for the parallel signal are not significantly different between the GSB and the ESA of the ν_3 mode of BH_4^-.

	[BMIM][BH_4]	$[P_{14,6,6,6}][BH_4]$	150 mM $N_{1,1,1,1}BH_4^-$ in [$N_{1,1,1,4}$][Tf_2N]
GSB			
A	-1.8 (±0.2)	-2.0 (± 0.1)	-1.55 (±0.07)
t_{para} (ps)	1.9 (±0.6)	4.8 (±0.8)	6.0 (±0.7)
c	-0.9 (±0.1)	-0.3 (±0.1)	-0.03 (±0.06)
ESA			
A	1.26 (±0.09)	1.02 (±0.08)	0.58 (±0.03)
t_{para} (ps)	2.2 (±0.3)	4.1 (±0.8)	4.3 (±0.5)

The vibrational relaxation times are calculated for each polarization sequence. The min amplitude of the GSB of the ν_3 mode and the max amplitude of the second ESA are plotted as a function of delay time. The amplitude as a function of time is fit to a single exponential for the ESA (Table 19). A single exponential with an offset is used for the GSB due to a long lived bleach at 200 ps (Table 20). There is no significant difference between the vibrational relaxation time due to polarization.

Table 20: The vibrational relaxation times (t_{perp}) for the perpendicular signal are not significantly different between the GSB and the ESA of the ν_3 mode of BH_4^-.

	[BMIM][BH_4]	[$P_{14,6,6,6}$][BH_4]	150 mM $N_{1,1,1,1}BH_4^-$ in [$N_{1,1,1,4}$][Tf_2N]
GSB			
A	-1.4 (±0.2)	-1.72 (± 0.08)	-1.2 (±0.05)
t_{perp} (ps)	2.1 (±0.6)	5.6 (±0.9)	6.8 (±0.6)
c	-0.89 (±0.09)	-0.24 (±0.07)	-0.02 (±0.04)
ESA			
A	1.02 (±0.05)	0.87 (±0.04)	0.440 (±0.009)
t_{perp} (ps)	2.6 (±0.3)	4.9 (±0.6)	5.2 (±0.3)

A.2.6 Anisotropy

The anisotropy is calculated from the parallel and perpendicular IR pump-IR probe data ($I_{\text{aniso}} = (I_{\parallel} - I_{\perp})/(I_{\parallel} + 2I_{\perp})$). Similar to the determination of the vibrational relaxation times, the min amplitude of the GSB of the ν_3 mode of BH_4^- is used.

The initial anisotropy values (<0.1) for all IL samples are low indicating the timescales are mostly in the motionally narrowing limit (Figure 52). The anisotropy values decay to 0 within a few 100 fs.

A single exponential is used to capture the fast molecular reorientational timescale (t_{rot}) of BH_4^- (Table 21). The timescales for all of the IL samples are in the motionally narrowing limit. The fast t_{rot} indicates a fast reorientation of the triply degenerate ν_3 mode.

Table 21: The anisotropy reveals the timescale of molecular rotations (t_{rot}). A single exponential is used to extract the t_{rot} for the ν_3 mode of BH_4^- in [BMIM][BH_4], [$P_{14,6,6,6}$][BH_4] and 150 mM $N_{1,1,1,1}BH_4^-$ in [$N_{1,1,1,4}$][Tf_2N].

	[BMIM][BH_4]	[$P_{14,6,6,6}$][BH_4]	150 mM $N_{1,1,1,1}BH_4^-$ in [$N_{1,1,1,4}$][Tf_2N]
A	0.03 (± 0.09)	0.08 (±0.07)	0.2 (±0.1)
t_{rot} (ps)	0.2 (±0.7)	0.2 (±0.2)	0.12 (±0.05)

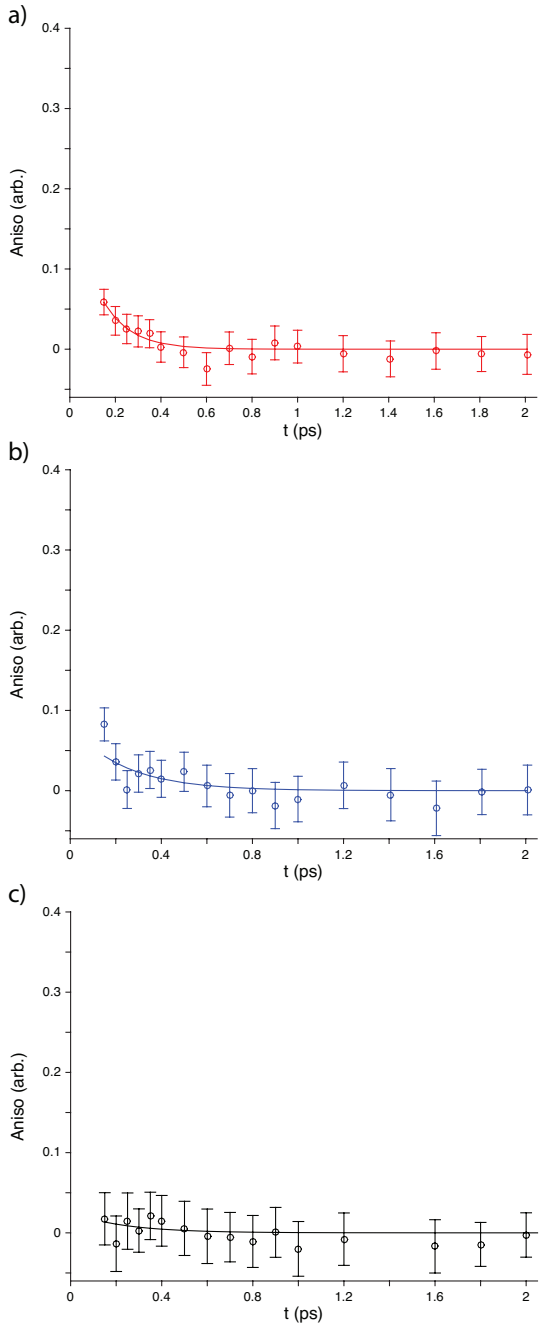

Figure 52: Anisotropy results of a) $N_{1,1,1,1}BH_4^-$ in $[N_{1,1,1,4}][Tf_2N]$, b) $[P_{14,6,6,6}][BH_4]$, and c) [BMIM][BH_4] show a fast reorientation of the triply degenerate ν_3 mode.

A.3 EAN RISD

A.3.1 Water Content from FTIR

The FTIR spectrum of EAN has two main identifiable vibrational bands (Figure 53). The NH stretch vibrational band is centered at 3093 cm^{-1} and is broad due to hydrogen bonding. The nitrate antisymmetric vibrational band appears at 1326 cm^{-1} and 1400 cm^{-1}. The peaks are saturated from using a 25 μm spacer. The EAN spectrum has a weak overtone in the region were the antisymmetric nitrile stretch (ν_3) of SCN^- appears.

The water content is estimated by the water band around 3500 cm^{-1}. This method of estimating the water content in an IL produces comparable results to a Karl-Fischer titration.[11] A clear OH vibrational band is not present. This is due to a small amount of H_2O present, along with overlap of the tail end of the NH vibrational band. We estimate the water content in EAN to be less than 40 mM.

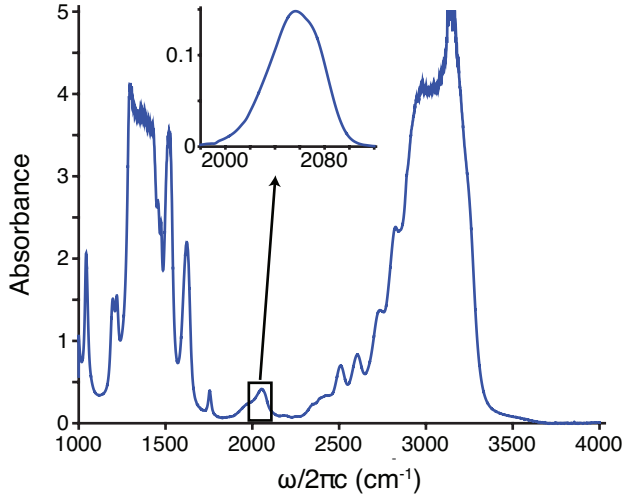

Figure 53: In EAN, the mid-IR region (1800-2200 cm^{-1}) is clear from any strong vibrational modes. The antisymmetric nitrile stretch (ν_3) of SCN^- appears on top of a weak overtone band of EAN, and subtracting off the solvent spectrum reveals EAN to have an asymmetrical shape (insert).

A.3.2 Simulated Spectra for Two Subensembles

The 2D-IR spectra are calculated in the typical approximations of Gaussian statistics. We factorize the orientational and frequency fluctuation terms. The cumulant expansion allows us to represent the frequency fluctuations in terms of the two-time frequency correlation functions. In these approximation, the total response from the two subensembles is

$$S(t_1,t_2,t_3) = \sum_{i=1}^{2} a^i Y_p^i(t_1,t_2,t_3) P^i(t_1,t_2,t_3) \left(\sum_{j=1}^{6} R_j^i(t_1,t_2,t_3) \right) \tag{.1}$$

where a^i is the intensity contributed by species i, Y_p^i is the orientational response for polarization condition p, P^i models population relaxation, and R_j^i is frequency response from Feynman diagram j, each given for subensemble component i.

Frequency fluctuations lead to the typical third-order response functions

$$\begin{aligned} R_1^i(t_1,t_2,t_3) &= \exp(-i\omega_0^i(t_1-t_3)+\phi)\exp(-g^i(t_1)+g^i(t_2)-g^i(t_3) \\ &\quad - g^i(t_1+t_2) - g^i(t_2+t_3) + g^i(t_1+t_2+t_3)) \end{aligned} \tag{.2}$$

$$R_2^i(t_1,t_2,t_3) = R_1^i \tag{.3}$$

$$R_3^i(t_1,t_2,t_3) = -(\mu_{12}^i)^2 R_1^i \exp(i\Delta_{\text{anh}} t_3) \tag{.4}$$

$$\begin{aligned} R_4^i(t_1,t_2,t_3) &= \exp(-i\omega_0^i(t_1+t_3)-\phi)\exp(-g^i(t_1)-g^i(t_2)-g^i(t_3) \\ &\quad + g^i(t_1+t_2) + g^i(t_2+t_3) - g^i(t_1+t_2+t_3)) \end{aligned} \tag{.5}$$

$$R_5^i(t_1,t_2,t_3) = R_4^i \tag{.6}$$

$$R_6^i(t_1,t_2,t_3) = -(\mu_{12}^i)^2 R_3^i \exp(-i\Delta_{\text{anh}}^i t_3) \tag{.7}$$

where ω_o^i is the center frequency of component i, Δ_{anh}^i is the anharmonicity, μ_{12}^i is the ratio of the transition dipole moment of the $v=1\rightarrow 2$ and $v=0\rightarrow 1$ transitions, ϕ accounts for residual phase error in the measurement, and g^i is the lineshape function. We use a Kubo lineshape with a fast (homogeneous) mode and an intermediate (spectral diffusion) mode

$$g^i(t) = \frac{t}{T_2^i} + (\Delta^i)^2 (\tau^i)^2 \left(e^{-t/\tau^i} - 1 + \frac{t}{\tau^i} \right) \tag{.8}$$

Orientational dynamics are accounted for with the usual orientation factors depending on the laser polarization. The parallel polarization ($\langle ZZZZ \rangle$) gives rise to a term

$$Y^i_{ZZZZ}(t_1, t_2, t_3) = \frac{1}{9} \exp\left(-\frac{t_1}{\tau^i_o}\right) \left(1 + \frac{4}{5} \exp\left(-\frac{t_2}{\tau^i_o}\right)\right) \exp\left(-\frac{t_3}{\tau^i_o}\right), \tag{.9}$$

where τ^i_o is the orientational relaxation time. Similarly, the perpendicular (crossed) polarization ($\langle ZZXX \rangle$) gives rise to

$$Y^i_{ZZXX}(t_1, t_2, t_3) = \frac{1}{9} \exp\left(-\frac{t_1}{\tau^i_o}\right) \left(1 - \frac{2}{5} \exp\left(-\frac{t_2}{\tau^i_o}\right)\right) \exp\left(-\frac{t_3}{\tau^i_o}\right). \tag{.10}$$

Population relaxation is modeled with a term

$$P^i(t_1, t_2, t_3) = \exp\left(-\frac{t_1}{2T^i_1} - \frac{t_2}{T^i_1} - \frac{t_3}{2T^i_1}\right), \tag{.11}$$

where the factor of 2 accounts for the more rapid signal decay during the coherence times.

The signal is calculated in the rotating frame; the time domain has 64 steps separated by $\mathrm{d}t = 0.05$ ps. The initial point in the time-domain is divided by 2 to reduce baseline artifacts due to the single-sided signal. The FFT is performed with zero-padding to 128 points.

We find that the nonlinear least-squares fitting converged faster when defining the frequency and amplitude of one subensemble relative to the other, in this case $\omega^{(2)}_0 = \omega^{(1)}_0 - \delta\omega$ and $a^{(2)} = ra^{(1)}$. The table below reports the resulting frequency splitting $\delta\omega$ and amplitude ratio r. Additionally, the anharmonicities and transition dipole ratios are each identical within error, so they are collapsed to a shared free parameter, $\Delta^{(1)}_{\mathrm{anh}} = \Delta^{(2)}_{\mathrm{anh}} = \Delta_{\mathrm{anh}}$ and $\mu^{(1)}_{12} = \mu^{(2)}_{12} = \mu_{12}$.

The constrained nonlinear least-squares fitting is performed in MATLAB using the active-set algorithm as implemented in `fmincon`. The reported fit values are robust to the precise values of the constraints (not reported). The error function that is minimized is the sum of the sum of the root-mean-square deviation of the experimental spectra and the simulation including both polarization conditions.

The resulting best fit parameters are summarized in Table 22.

Table 22: Best fit parameters of the spectral simulation

parameter	description	value
shared parameters		
r	intensity ratio	1.4
$\omega_0^{(1)}$	center frequency	2064 cm^{-1}
$\delta\omega$	frequency difference	15.5 cm^{-1}
Δ_{anh}	anharmonic shift	20.6 cm^{-1}
μ_{12}	1-2 dipole	$\sqrt{2.0}$
ϕ	phase error	-3°
species 1		
$\tau_o^{(1)}$	reorientation time	33.8 ps
$T_1^{(1)}$	vibrational relaxation	5.7 ps
$T_2^{(1)}$	pure dephasing	1.2 ps
$\Delta^{(1)}$	inhomogeneous width	14 cm^{-1}
$\tau^{(1)}$	spectral diffusion time	11 ps
species 2		
$\tau_o^{(2)}$	reorientation time	22.5 ps
$T_1^{(2)}$	vibrational relaxation	2.0 ps
$T_2^{(2)}$	pure dephasing	1.3 ps
$\Delta^{(2)}$	inhomogeneous width	17 cm^{-1}
$\tau^{(2)}$	spectral diffusion time	3.2 ps

A.3.3 Low and High Sub-ensemble Ellipticity Fits

In the 2D-IR spectrum, we attempt to separate the low and high frequency sub-ensembles that SCN^- experiences in EAN. This method was previously published on separating different species that $MeSCN^-$ experiences in concentrated LiCl solutions.[208]

Using similar assumptions as Yuan *et. al.*[208], we limit the amount of free fitting parameters to six. The free fitting parameters are A, σ_D, and σ_A for each sub-ensemble where A is the amplitude, σ_D is the inhomogenous broadening component, and σ_A is the homogenous broadening component. The amplitude for both the diagonal and off-diagonal peaks are treated as the same. The center frequencies are set by the linear IR spectra and are only allowed to vary by $\sim$0.5 cm^{-1}. Also, the anharmonicity is set as the same for both subensembles and is only allowed to vary by $\sim$2 cm^{-1}.

The ellipticity fits fail to capture both the high and low sub-ensembles at early t_2 (Figure 54). At early t_2 (0.2 to 2 ps), the ellipticity values appear to be random, thus the low and high frequency subensembles are unable to be separated using this method.

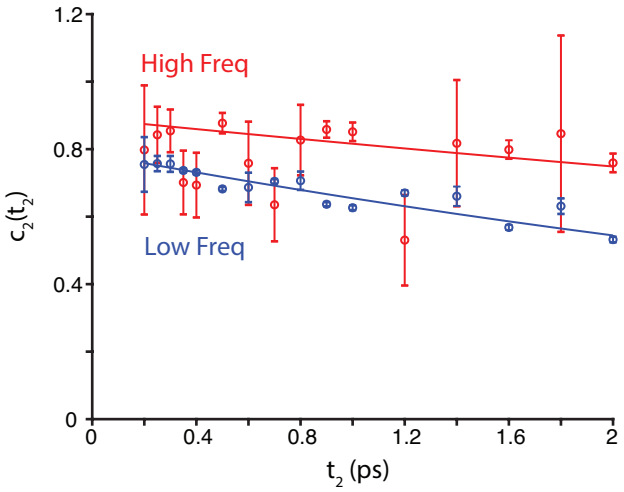

Figure 54: The ellipticity values are determined for the low and high frequency subensembles from the two 2D Gaussian fits for SCN^- in EAN.

A.4 EAN TEMPERATURE-DEPENDENT

A.4.1 Temperature-Dependent (T_1)

The vibrational lifetime (T_1) is extracted from the calculated isotropic signal, $I_{\text{iso}} = I_{\text{ZZZZ}} + 2I_{\text{ZZXX}}$ (Figure 55). The isotropic 2D-IR spectra is converted to a single pump-prob spectra by summing the areas across ω_1 (1950-2120 cm^{-1}). The single pump-probe spectra at each t_2 fits to a double Gaussian (GSB and ESA). The integrated area of the GSB is then calculated. The integrated area of the GSB peak is plotted across t_2 for each temperature and fit to a single exponential.

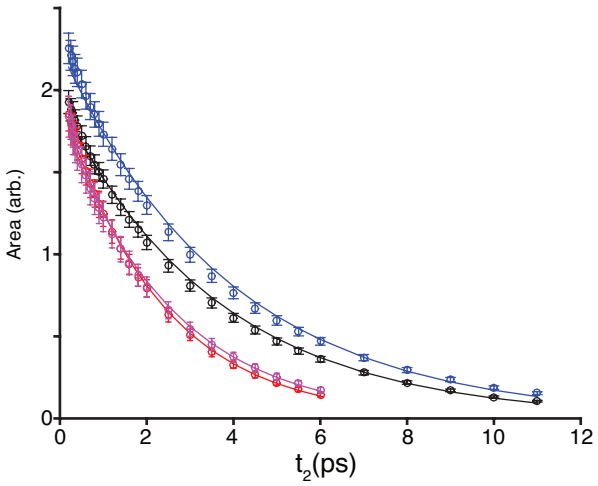

Figure 55: The vibrational lifetime (T_1) of the ν_3 mode of SCN^- varies little with temperature in both EAN (19 °C, blue and 130 °C, black) and H_2O (19 °C, red and 89 °C, purple). The T_1 is determined through an exponential fit of the area of the ground state bleach (GSB) as a function of t_2.

T_1 does not vary with temperature in both EAN and H_2O (Table 23). At room temperature, the T_1 of EAN (3.88 $\pm$ 0.09) is larger than that in H_2O (2.25 $\pm$ 0.03). Therefore, we are able to collect longer t_2 times for EAN. Increasing the temperature does not result in any statistical difference between the T_1 for EAN and H_2O respectively.

Table 23: The vibrational lifetime (T_1) of the ν_3 mode of SCN^- in EAN and H_2O are not temperature dependent. The apparent T_1 is determined from the isotropic signal.

	a_1	T_1 (ps)
EAN		
19 °C	2.25 ± 0.05	3.88 ± 0.09
130 °C	1.93 ± 0.04	3.64 ± 0.07
H_2O		
19 °C	1.96 ± 0.03	2.25 ± 0.03
89 °C	1.87 ± 0.04	2.48 ± 0.06

A.4.2 Frequency and Temperature-Dependent Anisotropy

A pump-probe projection is accomplished by taking slices of the spectrum along ω_1. For each ω_1 slice, the resulting pump-probe signal is fit to a double gaussian function and is integrated to determine an area. The anisotropic signal is then calculated from the $\langle ZZZZ \rangle$ and $\langle ZZXX \rangle$ areas as a function of t_2.

Table 24: From the calculated IR Pump-IR Probe data, the rotational molecular motion for the ν_3 mode of SCN^- in EAN is shown to be frequency dependent: Low ω_1 (2024 to 2050 cm^{-1}), High ω_1 (2054 to 2080 cm^{-1}), and Total ω_1 (1954 to 2120 cm^{-1}).

	a_1^{rot}	τ_1^{rot} (ps)	a_2^{rot}	τ_2^{rot} (ps)	τ_{total}^{rot} (ps)
EAN					
Low ω_1	0.422 ± 0.007	14.3 ± 0.8	—	—	15.1 ± 0.2
Total ω_1	0.044 ± 0.004	1.0 ± 0.2	0.353 ± 0.004	32 ± 2	28 ± 4
High ω_1	0.044 ± 0.004	1.5 ± 0.3	0.354 ± 0.005	40.2 ± 3	36 ± 5

The molecular rotation timescale in EAN is frequency dependent (Table 24). Different IR Pump-IR probe (PP) spectra are calculated varying the ω_1 range for EAN at room temperature. The anisotropy, α, is

$$\alpha = \frac{I_{\parallel} - I_{\perp}}{I_{\parallel} + 2I_{\perp}} \tag{.12}$$

where $I_{\parallel}$ is the pump-probe signal from the $\langle ZZZZ \rangle$ measurement, $I_{\perp}$ is the pump-probe signal from the $\langle ZZXX \rangle$ measurement. A biexponential fit is used to extract the timescale of molecular rotations (τ^{rot}). The low frequency PP signal produces a faster molecular rotation time than the high frequency PP.

These results support the conclusion of two overlapping subensembles with different rotational times, as concluded from the global fitting of the data.

A.4.3 Temperature-Dependent FFCF for SCN^- in EAN at $\langle ZZXX \rangle$

Similar to the ⟨ZZZZ⟩, spectral diffusion occurs faster in the ⟨ZZXX⟩ as temperature increases (Figure 56). For SCN^- in EAN at an early t_2 ($\sim$ 0.2 ps), a large inhomogeneous is present as the peak is stretched along the diagonal (Figure 56a). Spectral diffusion does not occur within the timeframe of the experiment ($\sim$ 11 ps). For SCN^- in H_2O at an early t_2 ($\sim$ 0.2 ps), mainly a homogeneous component is present (Figure 56b). Spectral diffusion occurs within a few ps.

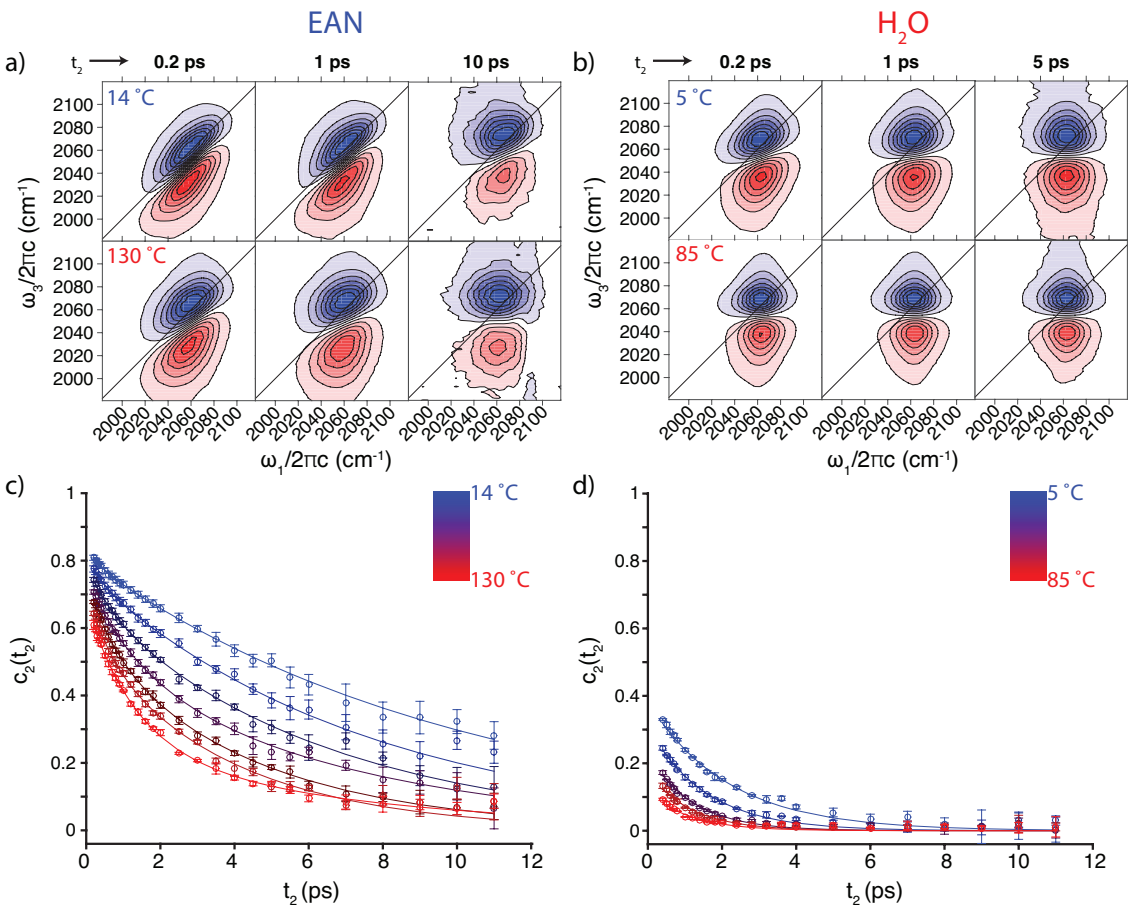

Figure 56: a) A larger inhomogeneous component is evident at low (14 °C) than high (130 °C) temperatures of the ⟨ZZXX⟩ 2D-IR spectra of SCN^- in EAN. b) A similar trend as seen in EAN is evident for the $\langle ZZXX \rangle$ 2D-IR spectra of SCN^- in H_2O at Low (5 °C) and high (85 °C) temperatures. c) As the temperature increases (blue to red), the FFCF determined by CLS for SCN^- in EAN ($\langle ZZXX \rangle$) shows a faster spectral diffusion time. d) Also, the FFCF of SCN- in H_2O ($\langle ZZXX \rangle$) is determined by CLS shows faster solvent reorganization times with elevated temperatures (blue to red).

CLS extracts the PW-FFCF for SCN^- in both EAN and H_2O at all temperatures (Figure 56c-d). At 14 °C, the initial CLS value (at $\sim$ 0.2 ps) is 0.809 ± 0.008 but decreases to 0.61 ± 0.01 at 130 °C. In H_2O, the initial CLS value decreases by $\sim$ 0.25 from 5 (0.330 ± 0.003) to 89 °C (0.093 ± 0.003).

Table 25: Temperature-dependent FFCF fit paramaters for the ⟨ZZXX⟩ signal of SCN^- in EAN and H_2O.

	a_1	τ_1 (ps)	a_2	τ_2 (ps)	τ_{total} (ps)
EAN					
14 °C	0.04 ± 0.02	0.3 ± 0.2	0.803 ± 0.007	10.1 ± 0.3	8.1 ± 0.6
130 °C	0.43 ± 0.07	1.3 ± 0.2	0.25 ± 0.07	7 ± 2	2 ± 2
H_2O					
5 °C	0.383 ± 0.009	1.08 ± 0.05	—	—	0.41 ± 0.01
85 °C	0.13 ± 0.02	0.51 ± 0.07	—	—	0.068 ± 0.006

The timescale of solvent reorganization follows an Arrhenius behavior. For SCN^- in EAN, the FFCF fits to a biexponential function, and for SCN^- in H_2O a single exponential function extracts the parameters of the FFCF (Table 25). The total correlation time ($\tau_{\text{total}}^{\text{FFCF}}$) gives the best representation for the timescale of solvent reorganization and is calculated from integrating the exponential form of the FFCF over t_2. As the temperature increases, the $\tau_{\text{total}}^{\text{FFCF}}$ decreases as solvent reorganization motions become faster.

A.4.4 EAN Spiked with H_2O

A.4.4.1 FTIR H_2O is added to EAN to understand the effect it would have on the solvent dynamics. Various concentrations of H_2O (100 mM, 500 mM, and 1000 mM) added to dry EAN show an increase in the broad OH vibrational band around 3500 cm^{-1} (Figure 57).

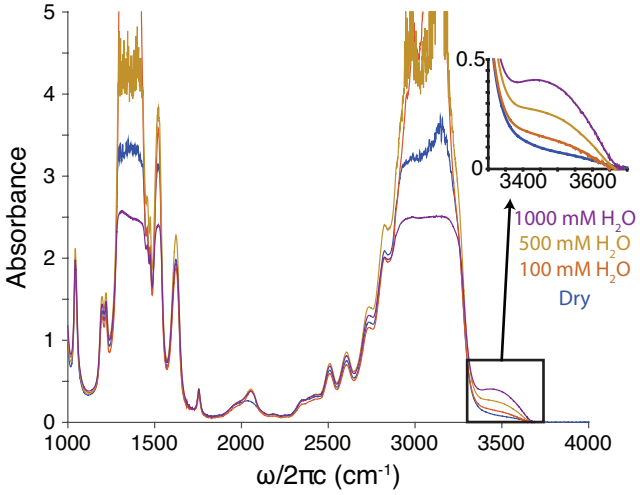

Figure 57: EAN spiked with various amounts of water shows an increase in the OH antisymmetric stretch of H_2O at 3500 cm^{-1} (insert). FTIR spectra are obtained on dry EAN (blue) and EAN spiked with 100 mM H_2O (red), 500 mM H_2O (gold), and 1000 mM H_2O (purple).

A.4.4.2 2D-IR Spectra No significant difference exists between spectral features of dry and wet EAN (Figure 58). 2D-IR spectra are obtained in both the ⟨ZZZZ⟩ and ⟨ZZXX⟩.

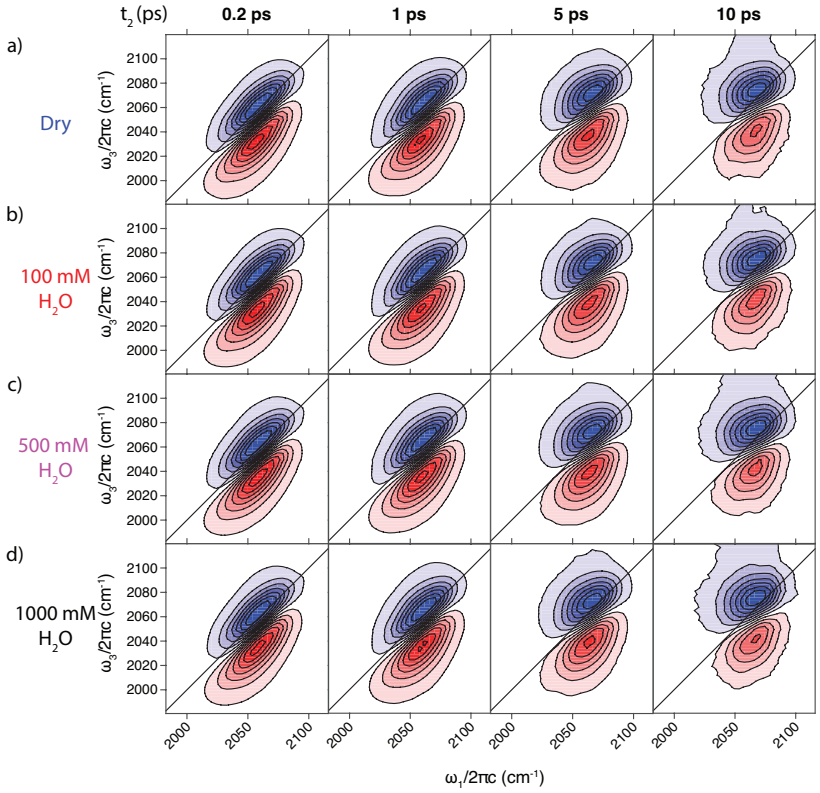

Figure 58: No significant changes in lineshape features (homogeneous and in inhomogeneous linewidths) are evident with spiking EAN with copious amounts of water. 2D-IR spectra is obtained on a) dry EAN and EAN spiked with b) 100 mM H_2O c) 500 mM H_2O and d) 1000 mM H_2O. The 2D-IR spectra are for the ⟨ZZZZ⟩ signal at room temperature.

The population time is varied from 200 fs to 11 ps, and the temperature is varied from 14 °C to 130 °C. At early t_2 ($\sim$ 200 fs), the peak is stretched along the diagonal indicating a large inhomogeneous linewidth component. As t_2 increases, the peak becomes more round, but spectral diffusion does not fully occur within the experimental time (t_2).

A.4.4.3 Vibrational Relaxation Lifetimes The vibrational lifetime (T_1) for the nitrile stretch of SCN^- in dry EAN and wet EAN are calculated from the isotropic signal (Figure

59). At early t_2, there is an initial decrease in the area from dry EAN to EAN with 1000 mM of H_2O.

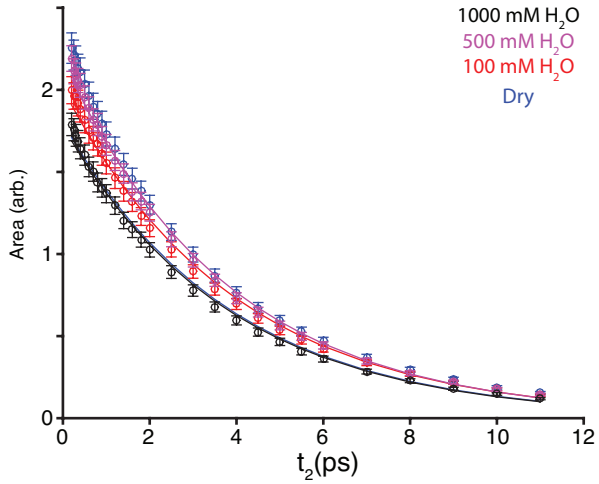

Figure 59: The area of the GSB decreases with the amount of water added, however, the apparent T_1 did not vary. The T_1 is determined through an exponential fit of the area of the GSB as a function of t_2 for dry EAN (blue) and EAN spiked with 100 mM H_2O (red), 500 mM H_2O (purple), and 1000 mM H_2O (black).

The apparent T_1 does not vary significantly in dry or wet EAN (Table 26). A single exponential is fit to the area of the calculated pump-probe spectra from the 2D-IR spectra as a function of t_2. The T_1 for EAN and wet EAN is ~ 3.85 ps.

Table 26: No difference exists in T_1 of the ν_3 mode of SCN^- in dry EAN and with various amounts of water added for the isotropic signal.

	a_1	T_1 (ps)
Dry	2.25 ± 0.05	3.88 ± 0.09
100 mM H_2O	2.01 ± 0.05	3.95 ± 0.1
500 mM H_2O	2.18 ± 0.05	3.82 ± 0.09
1000 mM H_2O	1.78 ± 0.04	3.82 ± 0.09

A.4.4.4 Anisotropy The timescale of molecular rotation of SCN^- in dry and wet EAN are determined from the anisotropic signal (Figure 60). The anisotropy is calculated by projecting the 2D-IR spectra into a single pump-probe signal. At early t_2 ($\sim$ 0.2 ps), the initial anisotropic value decreases as the H_2O concentration in EAN increases. As water is added, more motions fall into the motionally narrowing limit.

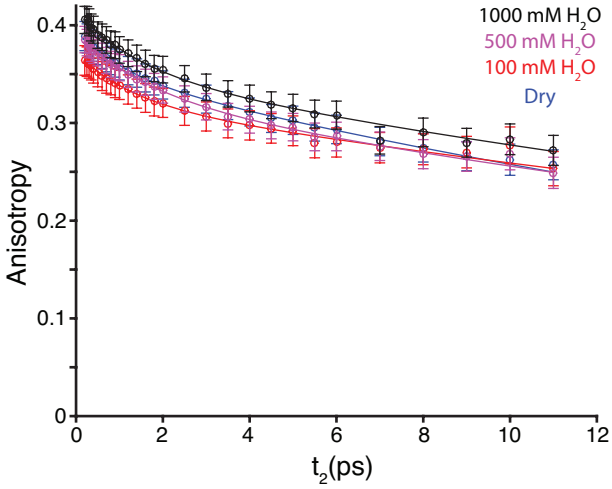

Figure 60: The timescale of molecular rotation is not significantly different between dry EAN (blue) and EAN spiked with 100 mM H_2O (red), 500 mM H_2O (purple), and 1000 mM H_2O (black). The 2D-IR data is converted into a single pump-probe spectra for each t_2 and the anisotropy is calculated from the GSB areas from the $\langle ZZZZ \rangle$ and $\langle ZZXX \rangle$ signals.

Table 27: The timescale of molecular rotation is determined through fitting the anisotropy with a biexponential fit for the the ν_3 mode of SCN^- in dry EAN and with various amounts of water added.

	a_1^{rot}	τ_1^{rot} (ps)	a_2^{rot}	τ_2^{rot} (ps)	τ_{total}^{rot} (ps)
Dry	0.044 ± 0.004	1.0 ± 0.2	0.353 ± 0.004	32 ± 2	28 ± 4
100 mM H_2O	0.050 ± 0.007	1.3 ± 0.4	0.322 ± 0.008	46 ± 7	37 ± 8
500 mM H_2O	0.063 ± 0.009	1.7 ± 0.4	0.33 ± 0.01	40 ± 6	33 ± 8
1000 mM H_2O	0.062 ± 0.009	1.5 ± 0.4	0.35 ± 0.01	42 ± 7	37 ± 9

The timescale of molecular rotations are not significantly different for SCN^- in dry and wet EAN (Table 27). A biexponential function is fit to the anisotropic signal to reveal the timescale of molecular rotations. Integrating the biexponential reveals the total timescale of molecular rotations that factors in the increase of rotations falling into the motionally narrowing limit. However, the total correlation time is not significantly different for any amount of H_2O added to EAN.

The timescale of molecular rotation follows an Arrhenius behavior in dry and wet EAN (Figure 61). Fitting the timescale of molecular rotation to an Arrhenius model reveals the activation energy needed to cause molecular rotations of SCN^- in EAN (E_a^{rot}) and the frequency prefactor (A_{rot}).

The energy needed to rotate SCN^- in EAN does not significantly differ as a function of H_2O concentration (Table 28). The E_a^{rot} increases as H_2O is added to EAN, but there is no significance between E_a^{rot}. The frequency prefactor decreases drastically as water is added to EAN as motions become faster.

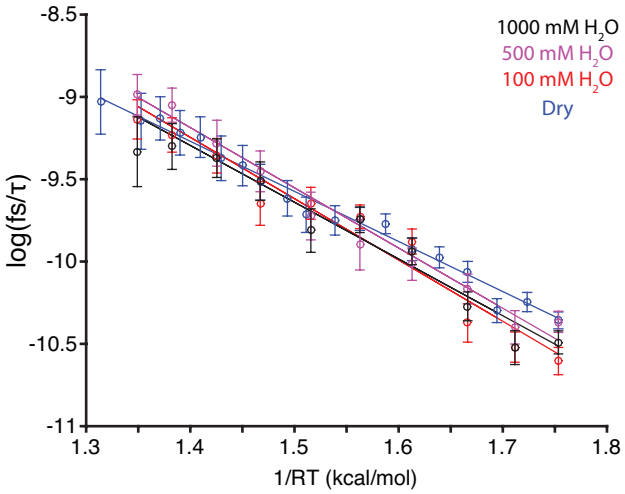

Figure 61: The anisotropy follows an Arrhenius behavior but shows no significant difference between dry EAN (blue) and EAN spiked with 100 mM H_2O (red), 500 mM H_2O (purple), and 1000 mM H_2O (black).

Table 28: From the Arrhenius fits, the energy to cause molecular rotations of SCN^- in dry EAN Are not significantly different from EAN spiked with copious amounts of water.

	$1/A_{\text{rot}}$ (fs)	E_a^{rot} (kcal/mol))
Dry	150 ± 40	3.0 ± 0.2
100 mM H_2O	60 ± 100	3.7 ± 0.7
500 mM H_2O	60 ± 60	3.7 ± 0.5
1000 mM H_2O	9 ± 50	3.5 ± 0.6

A.4.4.5 FFCF The timescale of solvent reorganization is determined from the PW-FFCF (Figure 62). For $\langle ZZZZ \rangle$, the initial CLS value ($\sim$ 0.8 at 0.2 ps) does not vary significantly between dry and wet EAN. As t_2 increases, a larger difference in the CLS values are visible between the wet and dry EAN.

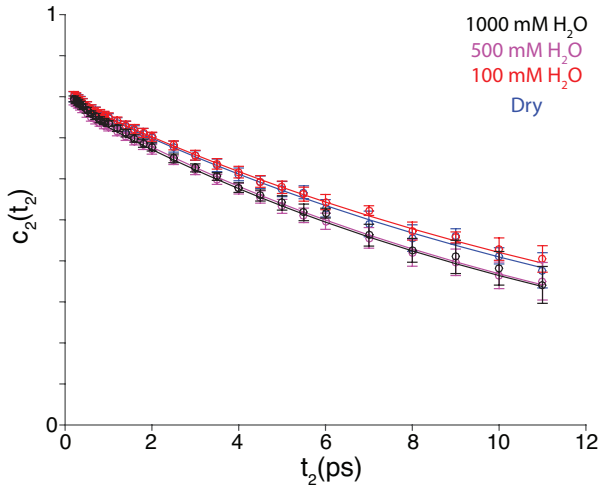

Figure 62: The timescale of solvent reorganization decreases as water is added to EAN. CLS extracts the PW-FFCF of the ν_3 mode of SCN^- in dry EAN (blue) and EAN spiked with 100 mM H_2O (red), 500 mM H_2O (purple), and 1000 mM H_2O (black) at 14 °C for the $\langle ZZZZ \rangle$.

As water is added to EAN, the timescale of solvent reorganization decreases (Table 29). The FFCF fits effectively to a biexponential timescale, and the total correlation time ($\tau_{\text{total}}^{\text{FFCF}}$) is determined through integrating the function over t_2. From dry to EAN with 1000 mM of H_2O the timescale of solvent reorganization decreases by a few ps.

Table 29: The total timescale of solvent reorganization decreases with water content in EAN. From CLS fits to the 2D-IR $\langle ZZZZ \rangle$ spectra, the extracted FFCF fits with a biexponential function.

	a_2	τ_1 (ps)	a_2	τ_2 (ps)	$\tau_{\text{total}}^{\text{FFCF}}$ (ps)
Dry	0.33 ± 0.03	0.2 ± 0.2	0.799 ± 0.004	15.0 ± 0.3	12.0 ± 0.6
100 mM H_2O	0.04 ± 0.02	0.2 ± 0.1	0.798 ± 0.003	15.6 ± 0.2	12.5 ± 0.7
500 mM H_2O	0.05 ± 0.01	0.23 ± 0.06	0.782 ± 0.002	13.1 ± 0.2	10.2 ± 0.7
1000 mM H_2O	0.033 ± 0.008	0.4 ± 0.2	0.788 ± 0.004	13.1 ± 0.3	10.4 ± 0.6

A.4.4.6 Temperature-Dependent FFCF The temperature dependence of $\tau_{\text{total}}^{\text{FFCF}}$ follows an Arrhenius behavior for both polarization conditions (Figure 63). The rate of solvent reorganization ($\ln(1/\tau_{\text{total}}^{\text{FFCF}})$) is linear in respect to inverse temperature. The Arrhenius model reveals the energy for the solvent to reorganize around SCN^- ($E_{\text{a}}^{\text{FFCF}}$).

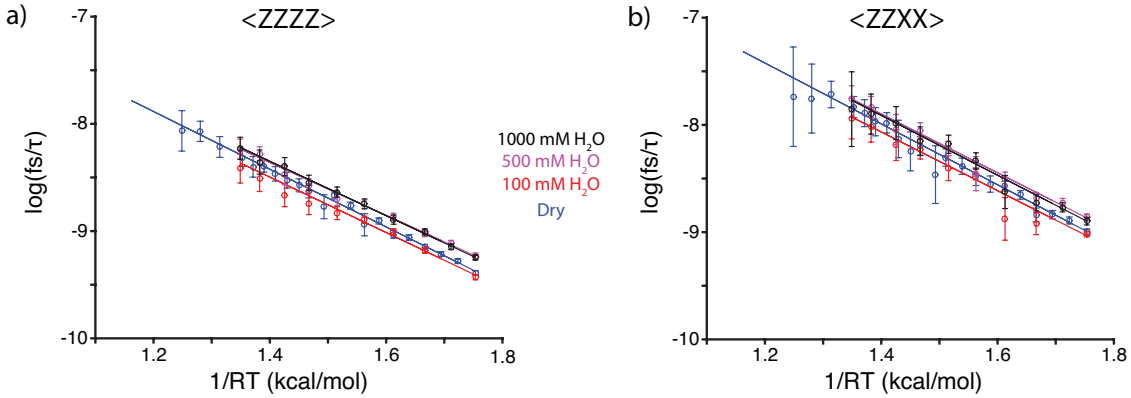

Figure 63: No significant difference in the energy for solvent reorganization exists in dry EAN (blue) and EAN spiked with 100 mM H_2O (red), 500 mM H_2O (purple), and 1000 mM H_2O (black) of a) the $\langle$ZZZZ$\rangle$ and b) the $\langle$ZZXX$\rangle$.

No difference in the energy for solvent reorganization exists for dry and wet EAN in either polarization condition (Table 30). The $E_{\text{a}}^{\text{FFCF}}$ and A_{FFCF} are not significantly different between dry and wet EAN, but the A_{FFCF} is different between $\langle$ZZZZ$\rangle$ and the $\langle$ZZXX$\rangle$.

Table 30: The timescale of solvent reorganization follows an Arrhenius behavior in dry EAN and EAN spiked with copious amounts of water. The energy to reorganize the solvent ($E_{\mathrm{a}}^{\mathrm{FFCF}}$) and the prefactor ($A_{\mathrm{FFCF}}$) are similar for dry EAN and EAN with water.

	$1/A_{\mathrm{FFCF}}$ (fs)	$E_{\mathrm{a}}^{\mathrm{FFCF}}$ (kcal/mol))
$\langle$ ZZZZ $\rangle$		
Dry	100 ± 20	2.7 ± 0.2
100 mM H_2O	130 ± 50	2.6 ± 0.3
500 mM H_2O	140 ± 30	2.5 ± 0.2
1000 mM H_2O	120 ± 20	2.6 ± 0.1
$\langle$ ZZXX $\rangle$		
Dry	56 ± 10	2.8 ± 0.1
100 mM H_2O	70 ± 30	2.7 ± 0.3
500 mM H_2O	60 ± 20	2.7 ± 0.2
1000 mM H_2O	50 ± 20	2.8 ± 0.3

BIBLIOGRAPHY

[1] King, S. *On Writing: A Memoir of the Craft*, 1st ed.; Scribner, 2000; p 288.

[2] Hochstrasser, R. M. Two-Dimensional IR-spectroscopy: Polarization Anisotropy Effects. *Chem. Phys.* **2001**, *266*, 273–284.

[3] Woutersen, S.; Hamm, P. Nonlinear two-dimensional vibrational spectroscopy of peptides. *J. Phys.-Condes. Matter* **2002**, *14*, R1035–R1062.

[4] Mukherjee, P.; Kass, I.; Arkin, I. T.; Zanni, M. T. Picosecond dynamics of a membrane protein revealed by 2D IR. *Proc. Natl. Acad. Sci. USA* **2006**, *103*, 3528–3533.

[5] Ganim, Z.; Chung, H. S.; Smith, A. W.; DeFlores, L. P.; Jones, K. C.; Tokmakoff, A. Amide I Two-Dimensional Infrared Spectroscopy of Proteins. *Acc. Chem. Res.* **2008**, *41*, 432–441.

[6] Asbury, J. B.; Steinel, T.; Kwak, K.; Corcelli, S. A.; Lawrence, C. P.; Skinner, J. L.; Fayer, M. D. Dynamics of water probed with vibrational echo correlation spectroscopy. *J. Chem. Phys.* **2004**, *121*, 12431–12446.

[7] Fecko, C. J.; Loparo, J. J.; Roberts, S. T.; Tokmakoff, A. Local Hydrogen Bonding Dynamics and Collective Reorganization in Water: Ultrafast Infrared Spectroscopy of HOD/D2O. *J. Chem. Phys.* **2005**, *122*, 54506.

[8] Roberts, S. T.; Petersen, P. B.; Ramasesha, K.; Tokmakoff, A.; Ufimtsev, I. S.; Martinez, T. J. Observation of a Zundel-like transition state during proton transfer in aqueous hydroxide solutions. *Proc. Natl. Acad. Sci.* **2009**, *106*, 15154–15159.

[9] Nicodemus, R. A.; Ramasesha, K.; Roberts, S. T.; Tokmakoff, A. Hydrogen Bond Rearrangements in Water Probed with Temperature-Dependent 2D IR. *J. Phys. Chem. Lett.* **2010**, *1*, 1068–1072.

[10] Perakis, F.; Hamm, P. Two-dimensional infrared spectroscopy of supercooled water. *J. Phys. Chem. B* **2011**, *115*, 5289–5293.

[11] Ren, Z.; Ivanova, A. S.; Couchot-Vore, D.; Garrett-Roe, S. Ultrafast Structure and Dynamics in Ionic Liquids: 2D-IR Spectroscopy Probes the Molecular Origin of Viscosity. *J. Phys. Chem. Lett.* **2014**, *5*, 1541–1546.

[12] Ren, Z.; Brinzer, T.; Dutta, S.; Garrett-Roe, S. Thiocyanate as a Local Probe of Ultrafast Structure and Dynamics in Imidazolium-Based Ionic Liquids: Water Induced Heterogeneity and Cation Induced Ion-Pairing. *J. Phys. Chem. B* **2015**, *119*, 4699–4712.

[13] Brinzer, T.; Berquist, E. J.; Ren, Z.; Dutta, S.; Johnson, C. A.; Krisher, C. S.; Lambrecht, D. S.; Garrett-Roe, S. Ultrafast Vibrational Spectroscopy (2D-IR) of CO2 in Ionic Liquids: Carbon Capture from Carbon Dioxide's Point of View. *J. Chem. Phys.* **2015**, *142*, 212425.

[14] Brinzer, T.; Garrett-Roe, S. Temperature and chain length dependence of ultrafast vibrational dynamics of thiocyanate in alkylimidazolium ionic liquids : A random walk on a rugged energy landscape. *J. Chem. Phys.* **2017**, *147*, 194501.

[15] Geissler, P. L.; Dellago, C.; Chandler, D.; Hutter, J.; Parrinello, M. Autoionization in liquid water. *Science* **2001**, *291*, 2121–2124.

[16] Groenenboom, M. C.; Keith, J. A. Quantum Chemical Analyses of BH_4 and BH3OH Hydride Transfers to CO_2 in Aqueous Solution with Potentials of Mean Force. *ChemPhysChem* **2017**, *18*, 3148–3152.

[17] Laage, D. A Molecular Jump Mechanism of Water Reorientation. *Science* **2006**, *311*, 832–835.

[18] Hassanali, A. A.; Cuny, J.; Ceriotti, M.; Pickard, C. J.; Parrinello, M. The Fuzzy Quantum Proton in the Hydrogen Chloride Hydrates. *J. Am. Chem. Soc.* **2012**, *134*, 8557–8569.

[19] Giammanco, C. H.; Kramer, P. L.; Fayer, M. D. Dynamics of Dihydrogen Bonding in Aqueous Solutions of Sodium Borohydride. *J. Phys. Chem. B* **2015**, *119*, 3546–3559.

[20] Kwak, K.; Park, S.; Finkelstein, I. J.; Fayer, M. D. Frequency-Frequency Correlation Functions and Apodization in Two-Dimensional Infrared Vibrational Echo Spectroscopy: a New Approach. *J. Chem. Phys.* **2007**, *127*, 124503.

[21] Kwak, K.; Rosenfeld, D. E.; Fayer, M. D. Taking apart the two-dimensional infrared vibrational echo spectra: More information and elimination of distortions. *J. Chem. Phys.* **2008**, *128*, 204505.

[22] Fenn, E. E.; Fayer, M. D. Extracting 2D IR Frequency-Frequency Correlation Functions from Two Component Systems. *J. Chem. Phys.* **2011**, *135*, 074502.

[23] Lazonder, K.; Pshenichnikov, M. S.; Wiersma, D. A. Easy Interpretation of Optical Two-Dimensional Correlation Spectra. *Opt. Lett.* **2006**, *31*, 3354–3356.

[24] Roberts, S. T.; Loparo, J. J.; Tokmakoff, A. Characterization of Spectral Diffusion from Two-Dimensional Line Shapes. *J. Chem. Phys.* **2006**, *125*, 84502.

[25] Eaves, J. D.; Loparo, J. J.; Fecko, C. J.; Roberts, S. T.; Tokmakoff, A.; Geissler, P. L. Hydrogen Bonds in Liquid Water are Broken Only Fleetingly. *Proc. Natl. Acad. Sci. U. S. A.* **2005**, *102*, 13019–13022.

[26] Kramer, P. L.; Nishida, J.; Giammanco, C. H.; Tamimi, A.; Fayer, M. D. Observation and Theory of Reorientation-Induced Spectral Diffusion in Polarization-Selective 2D IR Spectroscopy. *J. Chem. Phys.* **2015**, *142*, 184505.

[27] Kramer, P. L.; Nishida, J.; Fayer, M. D. Separation of Experimental 2D IR Frequency-Frequency Correlation Functions Into Structural and Reorientation-Induced Contributions. *J. Chem. Phys.* **2015**, *143*, 124505.

[28] Rivera, C. A.; Souna, A. J.; Bender, J. S.; Manfred, K.; Fourkas, J. T. Reorientation-Induced Spectral Diffusion in Vibrational Sum-Frequency-Generation Spectroscopy. *J. Phys. Chem. B* **2013**, *117*, 15875–15885.

[29] Cowan, M. L.; Bruner, B. D.; Huse, N.; Dwyer, J. R.; Chugh, B.; Nibbering, E. T. J.; Elsaesser, T.; Miller, R. J. D. Ultrafast memory loss and energy redistribution in the hydrogen bond network of liquid H2O. *Nature* **2005**, *434*, 199–202.

[30] Nicodemus, R. A.; Tokmakoff, A. Infrared spectroscopy of tritiated water. *Chem. Phys. Lett.* **2007**, *449*, 130–134.

[31] Silverstein, K. A. T.; Haymet, A. D. J.; Dill, K. A. The Strength of Hydrogen Bonds in Liquid Water and Around Nonpolar Solutes. *J. Am. Chem. Soc.* **2000**, *122*, 8037–8041.

[32] Geissler, P. L. Temperature dependence of inhomogeneous broadening: On the meaning of isosbestic points. *J. Am. Chem. Soc.* **2005**, *127*, 14930–14935.

[33] Li, P.; Henkelman, G.; Keith, J. A.; Johnson, J. K. Elucidation of Aqueous Solvent-Mediated Hydrogen-Transfer Reactions by ab Initio Molecular Dynamics and Nudged Elastic-Band Studies of $NaBH_4$ Hydrolysis. *J. Phys. Chem. C* **2014**, *118*, 21385–21399.

[34] Kilpatrick, M.; Baker, L. L.; McKinney, C. D. Studies of Fast Reactions which Evolve Gases. The Reaction of Sodium–Potassium Alloy with Water in the Presence and Absence of Oxygen. *J. Phys. Chem.* **1953**, *57*, 385–390.

[35] Kilpatrick, M.; McKinney, C. D. Kinetics of the Reaction of Lithium Borohydride in Aqueous Acid Solution. *J. Am. Chem. Soc.* **1950**, *72*, 5474–5476.

[36] Schlesinger, H. I.; Brown, H. C.; Finholt, A. E.; Gilbreath, J. R.; Hoekstra, H. R.; Hyde, E. K. Sodium Borohydride, Its Hydrolysis and its Use as a Reducing Agent and in the Generation of Hydrogen. *J. Am. Chem. Soc.* **1953**, *75*, 215–219.

[37] Pecsok, R. L. Polarographic Studies on the Oxidation and Hydrolysis of Sodium Borohydride. *J. Am. Chem. Soc.* **1953**, *75*, 2862–2864.

[38] Gardiner, J. A.; Collat, J. W. Kinetics of the Stepwise Hydrolysis of Tetrahydroborate Ion. *J. Am. Chem. Soc.* **1965**, *1964*, 1692–1700.

[39] Gardiner, J. A.; Collat, J. W. Polarography of the Tetrahydroborate Ion. The Effect of Hydrolysis on the System. *Inorg. Chem.* **1965**, *4*, 1208–1212.

[40] Davis, R. E.; Swain, C. G. General Acid Cataylsis of the Hydrolysis of Sodium Borohydride. *J. Am. Chem. Soc.* **1960**, *82*, 5949–5950.

[41] Stockmayer, W. H.; Miller, R. R.; Zeto, R. J. Kinetics of Borohydride Hydrolysis. *J. Phys. Chem.* **1961**, *65*, 1076–1077.

[42] Davis, R. Boron hydrides. IV. Concerning the geometry of the activated complex in the hydrolysis of borohydride ion by trimethylammonium ion. *J. Am. Chem. Soc.* **1962**, *81*, 5–7.

[43] Mesmer, R. E.; Jolly, W. L. The Hydrolysis of Aqueous Hydroborate. *Inorg. Chem.* **1962**, *1*, 608–612.

[44] Mikheeva, V. I.; Surs, V. Y. O Khimicheskoi Prirode Gipoborata Kaliyae. *Dokl. Akad. Nauk SSSR* **1953**, *93*, 67–69.

[45] Mikheeva, V. I.; Surs, V. Y. O Reaktsii Borida Magniya S Vodoi. *Dokl. Akad. Nauk SSSR* **1953**, *91*, 1133–1135.

[46] Mikheeva, V. I.; Fedneva, E. M. O Gidrolize Borogidrida Litiya. *Dokl. Akad. Nauk SSSR* **1955**, *101*, 99–101.

[47] Goubeau, J.; Kallfass, H. Die Reaktion Natriumborhydrid Und Wasser. *Z. Anorg. Allg. Chem.* **1959**, *299*, 160–169.

[48] Mochalov, K. N.; Gil'manshin, G. G. Polarographic Behaviour of Sodium, Potassium and Lithium Boronhydrides. *Dokl. Akad. Nauk SSSR* **1960**, *132*, 134–137.

[49] Mochalov, K. N.; Khain, V. S.; Gil'manshin, G. G. Kinetic Study of the Intermediate Hydrolysis Steps of BH_4^-. *Kinet. I Katal.* **1965**, *6*, 541–544.

[50] Mochalov, K. N.; Khain, V. S.; Gil'manshin, G. G. Generalized Scheme for the Hydrolysis of the Borohydride Ion and Diborane. *Dokl. Chem.* **1965**, *162*, 613–616.

[51] Grice, K. A.; Groenenboom, M. C.; Manuel, J. D. A.; Sovereign, M. A.; Keith, J. A. Examining the Selectivity of Borohydride for Carbon Dioxide and Bicarbonate Reduction in Protic Conditions. *Fuel* **2015**, *150*, 139–145.

[52] Earle, M. J.; Esperança, J. M. S. S.; Gilea, M. A.; Canongia Lopes, J. N.; Rebelo, L. P. N.; Magee, J. W.; Seddon, K. R.; Widegren, J. A. The distillation and volatility of ionic liquids. *Nature* **2006**, *439*, 831–834.

[53] Zaitsau, D. H.; Kabo, G. J.; Strechan, A. A.; Paulechka, Y. U.; Tschersich, A.; Verevkin, S. P.; Heintz, A. Experimental Vapor Pressures of 1-Alkyl-3-methylimidazolium Bis(trifluoromethylsulfonyl)imides and a Correlation Scheme for Estimation of Vaporization Enthalpies of Ionic Liquids. *J. Phys. Chem. A* **2006**, *110*, 7303–7306.

[54] Baltus, R. E.; Culbertson, B. H.; Dai, S.; Luo, H.; DePaoli, D. W. Low-Pressure Solubility of Carbon Dioxide in Room-Temperature Ionic Liquids Measured with a Quartz Crystal Microbalance. *J. Phys. Chem. B* **2004**, *108*, 721–727.

[55] Bates, E. D.; Mayton, R. D.; Ntai, I.; Davis, J. H. CO2 Capture by a Task-Specific Ionic Liquid. *J. Am. Chem. Soc.* **2002**, *124*, 926–927.

[56] Carlisle, T. K.; Bara, J. E.; Gabriel, C. J.; Noble, R. D.; Gin, D. L. Interpretation of CO 2 Solubility and Selectivity in Nitrile-Functionalized Room-Temperature Ionic Liquids Using a Group Contribution Approach. *Ind. Eng. Chem. Res.* **2008**, *47*, 7005–7012.

[57] Gonzalez-Miquel, M.; Palomar, J.; Omar, S.; Rodriguez, F. CO2/N-2 Selectivity Prediction in Supported Ionic Liquid Membranes (SILMs) by COSMO-RS. *Ind. Eng. Chem. Res.* **2011**, *50*, 5739–5748.

[58] Rosen, B. A.; Salehi-Khojin, A.; Thorson, M. R.; Zhu, W.; Whipple, D. T.; Kenis, P. J. A.; Masel, R. I. Ionic Liquid-Mediated Selective Conversion of CO2 to CO at Low Overpotentials. *Science* **2011**, *334*, 643–644.

[59] Brennecke, J. F.; Gurkan, B. E. Ionic Liquids for CO2 Capture and Emission Reduction. *J. Phys. Chem. Lett.* **2010**, *1*, 3459–3464.

[60] Wang, C.; Luo, X.; Luo, H.; Jiang, D.-e.; Li, H.; Dai, S. Tuning the basicity of ionic liquids for equimolar CO2 capture. *Angew. Chem. Int. Ed. Engl.* **2011**, *50*, 4918–4922.

[61] Lombardo, L.; Yang, H.; Zhao, K.; Dyson, P. J.; Züttel, A. Solvent- and Catalyst-Free Carbon Dioxide Capture and Reduction to Formate with Borohydride Ionic Liquid. *ChemSusChem* **2020**, *13*, 2025–2031.

[62] Li, S.; Gao, H.; Shreeve, J. M. Borohydride Ionic Liquids and Borane/Ionic-Liquid Solutions as Hypergolic Fuels with Superior Low Ignition-Delay Times. *Angew. Chemie Int. Ed.* **2014**, *53*, 2969–2972.

[63] Chand, D.; Zhang, J.; Shreeve, J. M. Borohydride Ionic Liquids as Hypergolic Fuels: A Quest for Improved Stability. *Chem. - A Eur. J.* **2015**, *21*, 13297–13301.

[64] Wang, J.; Song, G.; Peng, Y.; Zhu, Y. 3-Butyl-1-methylimidazolinium borohydride ([bmim][BH4])-a novel reducing agent for the selective reduction of carbon-carbon double bonds in activated conjugated alkenes. *Tetrahedron Lett.* **2008**, *49*, 6518–6520.

[65] Seo, S.; Quiroz-Guzman, M.; Desilva, M. A.; Lee, T. B.; Huang, Y.; Goodrich, B. F.; Schneider, W. F.; Brennecke, J. F. Chemically Tunable Ionic Liquids with Aprotic Heterocyclic Anion (AHA) for CO2 Capture. *J. Phys. Chem. B* **2014**, *118*, 5740–5751.

[66] Daly, Jr., C. A.; Berquist, E. J.; Brinzer, T.; Garrett-Roe, S.; Lambrecht, D. S.; Corcelli, S. A. Modeling Carbon Dioxide Vibrational Frequencies in Ionic Liquids: II. Spectroscopic Map. *J. Phys. Chem. B* **2016**, *120*, 12633–12642.

[67] Berquist, E. J.; Daly, Jr., C. A.; Brinzer, T.; Bullard, K. K.; Campbell, Z. M.; Corcelli, S. A.; Garrett-Roe, S.; Lambrecht, D. S. Modeling Carbon Dioxide Vibrational Frequencies in Ionic Liquids: I. Ab Initio Calculations. *J. Phys. Chem. B* **2017**, *121*, 208–220.

[68] Brinzer, T.; Daly, C. A.; Allison, C.; Garrett-Roe, S.; Corcelli, S. A.; Daly, Jr., C. A.; Allison, C.; Garrett-Roe, S.; Corcelli, S. A.; Daly, C. A.; Allison, C.; Garrett-Roe, S.; Corcelli, S. A. Modeling Carbon Dioxide Vibrational Frequencies in Ionic Liquids: III. Dynamics and Spectroscopy. *J. Phys. Chem. B* **2018**, *122*, 8931–8942.

[69] Cui, Y.; Kuroda, D. G. Evidence of Molecular Heterogeneities in Amide-Based Deep Eutectic Solvents. *J. Phys. Chem. A* **2018**, *122*, 1185–1193.

[70] Cui, Y.; Rushing, J. C.; Seifert, S.; Bedford, N. M.; Kuroda, D. G. Molecularly Heterogeneous Structure of a Nonionic Deep Eutectic Solvent Composed of N - Methylacetamide and Lauric Acid. *J. Phys. Chem. B* **2019**, *123*, 3984–3993.

[71] Arzhantsev, S.; Ito, N.; Heitz, M.; Maroncelli, M. Solvation dynamics of coumarin 153 in several classes of ionic liquids: cation dependence of the ultrafast component. *Chem. Phys. Lett.* **2003**, *381*, 278–286.

[72] Xu, W. Solvent-Free Electrolytes with Aqueous Solution-Like Conductivities. *Science* **2003**, *302*, 422–425.

[73] Chagnes, A.; Tougui, A.; Carre, B.; Ranganathan, N.; Lemordant, D. Abnormal Temperature Dependence of the Viscosity of Ethylammonium Nitrate–Methanol Ionic Mixtures. *J. Solution Chem.* **2004**, *33*, 247–255.

[74] Belieres, J.-P.; Gervasio, D.; Angell, C. A. Binary inorganic salt mixtures as high conductivity liquid electrolytes for $>$ 100 °C fuel cells. *Chem. Commun.* **2006**, 4799–4801.

[75] Belieres, J.-p.; Angell, C. A. Protic Ionic Liquids: Preparation, Characterization, and Proton Free Energy Level Representation †. *J. Phys. Chem. B* **2007**, *111*, 4926–4937.

[76] Greaves, T. L.; Drummond, C. J. Protic Ionic Liquids: Properties and Applications. *Chem. Rev.* **2008**, *108*, 206–237.

[77] Walden, P. Molecular Eights and Electrical Conductivity of Several Fused Salts. *Bull. Acad. Imp. Sci. St-petersbg.* **1914**, 405–422.

[78] Yoshizawa, M.; Xu, W.; Angell, C. A. Ionic Liquids by Proton Transfer: Vapor Pressure, Conductivity, and the Relevance of ΔpK_a from Aqueous Solutions. *J. Am. Chem. Soc.* **2003**, *125*, 15411–9.

[79] Rana, U. A.; Forsyth, M.; MacFarlane, D. R.; Pringle, J. M. Toward protic ionic liquid and organic ionic plastic crystal electrolytes for fuel cells. *Electrochim. Acta* **2012**, *84*, 213–222.

[80] Firaha, D. S.; Kirchner, B. CO2 absorption in the protic ionic liquid ethylammonium nitrate. *J. Chem. Eng. Data* **2014**, *59*, 3098–3104.

[81] Shiflett, M. B.; Niehaus, A. M. S.; Elliott, B. A.; Yokozeki, A. Phase Behavior of N2O and CO2 in Room-Temperature Ionic Liquids [bmim][Tf2N], [bmim][BF4], [bmim][N(CN)2], [bmim][Ac], [eam][NO3], and [bmim][SCN]. *Int. J. Thermophys.* **2012**, *33*, 412–436.

[82] Emel'yanenko, V. N.; Boeck, G.; Verevkin, S. P.; Ludwig, R. Volatile times for the very first ionic liquid: understanding the vapor pressures and enthalpies of vaporization of ethylammonium nitrate. *Chemistry* **2014**, *20*, 11640–5.

[83] Fumino, K.; Wulf, A.; Ludwig, R. Hydrogen Bonding in Protic Ionic Liquids : Reminiscent of Water. *Angew. Chem. Int. Ed.* **2009**, *48*, 3184–3186.

[84] Hunger, J.; Sonnleitner, T.; Liu, L.; Buchner, R.; Bonn, M.; Bakker, H. J. Hydrogen-Bond Dynamics in a Protic Ionic Liquid: Evidence of Large-Angle Jumps. *J. Phys. Chem. Lett.* **2012**, *3*, 3034–3038.

[85] Hayes, R.; Imberti, S.; Warr, G. G.; Atkin, R. The Nature of Hydrogen Bonding in Protic Ionic Liquids. *Angew. Chemie Int. Ed.* **2013**, *52*, 4623–4627.

[86] Zheng, Z.-P.; Fan, W.-H.; Roy, S.; Mazur, K.; Nazet, A.; Buchner, R.; Bonn, M.; Hunger, J. Ionic Liquids: Not only Structurally but also Dynamically Heterogeneous. *Angew. Chemie Int. Ed.* **2015**, *54*, 687.

[87] Bodo, E.; Gontrani, L.; Caminiti, R.; Plechkova, N. V.; Seddon, K. R.; Triolo, A. Structural Properties of 1-Alkyl-3-methylimidazolium Bis(trifluoromethyl)sulfonylamide Ionic Liquids: X-ray Diffraction Data and Molecular Dynamics Simulations. *J. Phys. Chem. B* **2010**, *114*, 16398–16407.

[88] Hardacre, C.; Holbrey, J. D.; Mullan, C. L.; Youngs, T. G. A.; Bowron, D. T. Small Angle Neutron Scattering from 1-alkyl-3-methylimidazolium Hexafluorophosphate Ionic Liquids ($[C_n mim][PF_6]$, n=4, 6, and 8). *J. Chem. Phys.* **2010**, *133*, 74510.

[89] Hayes, R.; Warr, G. G.; Atkin, R. Structure and Nanostructure in Ionic Liquids. *Chem. Rev.* **2015**, *115*, 6357–6426.

[90] Urahata, S. M.; Ribeiro, M. C. C. Structure of Ionic Liquids of 1-alkyl-3-methylimidazolium cations: A Systematic Computer Simulation Study. *J. Chem. Phys.* **2004**, *120*, 1855–1863.

[91] Wang, Y.; Voth, G. A. Unique Spatial Heterogeneity in Ionic Liquids. *J. Am. Chem. Soc.* **2005**, *127*, 12192–12193.

[92] Hu, Z.; Margulis, C. J. Heterogeneity in a Room-Temperature Ionic Liquid: Persistent Local Environments and the Red-Edge Effect. *Proc. Natl. Acad. Sci. U. S. A.* **2006**, *103*, 831–836.

[93] Araque, J. C.; Hettige, J. J.; Margulis, C. J. Ionic liquids - Conventional solvent mixtures, structurally different but dynamically similar. *J. Chem. Phys.* **2015**, *143*, 134505.

[94] Araque, J. C.; Daly, R. P.; Margulis, C. J. A link between structure, diffusion and rotations of hydrogen bonding tracers in ionic liquids. *J. Chem. Phys.* **2016**, *144*, 204504.

[95] Dutta, S.; Ren, Z.; Brinzer, T.; Garrett-Roe, S. Two-dimensional ultrafast vibrational spectroscopy of azides in ionic liquids reveals solute-specific solvation. *Phys. Chem. Chem. Phys.* **2015**, *17*, 26575–26579.

[96] Hamm, P.; Zanni, M. T. *Concepts and Methods of 2D Infrared Spectroscopy*; Cambridge University Press: New York, NY, 2011.

[97] Zheng, J. R.; Kwak, K.; Asbury, J.; Chen, X.; Piletic, I. R.; Fayer, M. D. Ultrafast dynamics of solute-solvent complexation observed at thermal equilibrium in real time. *Science* **2005**, *309*, 1338–1343.

[98] Bagchi, S.; Nebgen, B. T.; Loring, R. F.; Fayer, M. D. Dynamics of a Myoglobin Mutant Enzyme: 2D IR Vibrational Echo Experiments and Simulations. *J. Am. Chem. Soc.* **2010**, *132*, 18367–18376.

[99] Edler, J.; Hamm, P. Two-dimensional vibrational spectroscopy of the amide I band of crystalline acetanilide: Fermi resonance, conformational substates, or vibrational self-trapping? *J. Chem. Phys.* **2003**, *119*, 2709–2715.

[100] Kubo, R. In *Adv. Chem. Phys. Stoch. Process. Chem. Phys.*; Shuler, K. E., Ed.; John Wiley Sons, Inc.: Hoboken, NJ, USA, 1969; Chapter 6, pp 101–127.

[101] Venyaminov, S. Y.; Prendergast, F. G. Water (H_2O and D_2O) Molar Absorptivity in the $1000 - 4000 \sim \text{cm}^{-1}$ Range and Quantitative Infrared Spectroscopy of Aqueous Solutions. *Anal. Biochem.* **1997**, *248*, 234–245.

[102] Hamm, P.; Kaindl, R. A.; Stenger, J. Noise Suppression in Femtosecond Mid-Infrared Light Sources. *Opt. Lett.* **2000**, *25*, 1798–1800.

[103] Helbing, J.; Hamm, P. Compact Implementation of Fourier Transform Two-Dimensional IR Spectroscopy Without Phase Ambiguity. *J. Opt. Soc. Am. B* **2011**, *28*, 171.

[104] Brinzer, T. Ultrafast Dynamics of Carbon Dioxide in Imidazolium Ionic Liquids. Ph.D. thesis, University of Pittsburgh, 2018.

[105] Bloem, R.; Garrett-Roe, S.; Strzalka, H.; Hamm, P.; Donaldson, P. Enhancing signal detection and completely eliminating scattering using quasi-phase-cycling in 2D IR experiments. *Opt. Express* **2010**, *18*, 27067.

[106] Donaldson, P.; Greetham, G.; Shaw, D.; Parker, A.; Towrie, M. A 100 kHz Pulse Shaping 2D-IR Spectrometer Based on Dual Yb:KGW Amplifiers. *J. Phys. Chem. A* **2018**, *122*, 780–787.

[107] Shim, S.-H.; Strasfeld, D. B.; Ling, Y. L.; Zanni, M. T. Automated 2D IR spectroscopy using a mid-IR pulse shaper and application of this technology to the human islet amyloid polypeptide. *Proc. Natl. Acad. Sci.* **2007**, *104*, 14197–14202.

[108] Nite, J. M.; Cyran, J. D.; Krummel, A. T. Active Bragg angle compensation for shaping ultrafast mid-infrared pulses. *Opt. Express* **2012**, *20*, 23912.

[109] Shim, S.-H.; Strasfeld, D. B.; Fulmer, E. C.; Zanni, M. T. Femtosecond pulse shaping directly in the mid-IR using acousto-optic modulation. *Opt. Lett.* **2006**, *31*, 838.

[110] Zhang, J.; Fisher, T.; Gore, J.; Hazra, D.; Ramachandran, P. Heat of Reaction Measurements of Sodium Borohydride Alcoholysis and Hydrolysis. *Int. J. Hydrogen Energy* **2006**, *31*, 2292–2298.

[111] Orimo, S.-I.; Nakamori, Y.; Eliseo, J. R.; Züttel, A.; Jensen, C. M. Complex Hydrides for Hydrogen Storage. *Chem. Rev.* **2007**, *107*, 4111–4132.

[112] Liu, B.; Li, Z. A Review: Hydrogen Generation from Borohydride Hydrolysis Reaction. *J. Power Sources* **2009**, *187*, 527–534.

[113] Retnamma, R.; Novais, A. Q.; Rangel, C. Kinetics of Hydrolysis of Sodium Borohydride for Hydrogen Production in Fuel Cell Applications: A Review. *Int. J. Hydrogen Energy* **2011**, *36*, 9772–9790.

[114] Belkova, N. V.; Epstein, L. M.; Filippov, O. A.; Shubina, E. S. Hydrogen and Dihydrogen Bonds in the Reactions of Metal Hydrides. *Chem. Rev.* **2016**, *116*, 8545–8587.

[115] Satoh, T.; Suzuki, S.; Suzuki, Y.; Miyaji, Y.; Imai, Z. Reduction of Organic Compounds with Sodium Borohydride-Transition Metal Salt Systems. *Tetrahedron Lett.* **1969**, *10*, 4555–4558.

[116] Johnson, M. R.; Rickborn, B. Sodium Borohydride Reduction of Conjugated Aldehydes and Ketones. *J. Org. Chem.* **1970**, *35*, 1041–1045.

[117] Shin, H.-J.; Kim, K. K.; Benayad, A.; Yoon, S.-M.; Park, H. K.; Jung, I.-S.; Jin, M. H.; Jeong, H.-K.; Kim, J. M.; Choi, J.-Y.; Lee, Y. H. Efficient Reduction of Graphite Oxide by Sodium Borohydride and Its Effect on Electrical Conductance. *Adv. Funct. Mater.* **2009**, *19*, 1987–1992.

[118] Davis, R. E.; Kibby, C. L.; Swain, C. G. An Inverse Hydrogen Isotope Effect in the Hydrolysis of Sodium Borohydride. *J. Am. Chem. Soc.* **1960**, *82*, 5950–5951.

[119] Davis, R.; Bromels, E.; Kibby, C. Boron Hydrides. III. Hydrolysis of Sodium Borohydride in Aqueous Solution. *J. Am. Chem. Soc.* **1962**, *84*, 885–892.

[120] Wang, F. T.; Jolly, W. L. Kinetic Study of the Intermediates in the Hydrolysis of the Hydroborate Ion. *Inorg. Chem.* **1972**, *11*, 1933–1941.

[121] Amendola, S. A Safe, Portable, Hydrogen Gas Generator Using Aqueous Borohydride Solution and Ru Catalyst. *Int. J. Hydrogen Energy* **2000**, *25*, 969–975.

[122] Kojima, Y.; Kawai, Y.; Nakanishi, H.; Matsumoto, S. Compressed Hydrogen Generation Using Chemical Hydride. *J. Power Sources* **2004**, *135*, 36–41.

[123] Groenenboom, M. C.; Keith, J. A. Explicitly Unraveling the Roles of Counterions, Solvent Molecules, and Electron Correlation in Solution Phase Reaction Pathways. *J. Phys. Chem. B* **2016**, *120*, 10797–10807.

[124] Duffin, A. M.; England, A. H.; Schwartz, C. P.; Uejio, J. S.; Dallinger, G. C.; Shih, O.; Prendergast, D.; Saykally, R. J. Electronic structure of aqueous borohydride: a potential hydrogen storage medium. *Phys. Chem. Chem. Phys.* **2011**, *13*, 17077.

[125] Tyborski, T.; Costard, R.; Woerner, M.; Elsaesser, T. Ultrafast Vibrational Dynamics of BH_4^- Ions in Liquid and Crystalline Environments. *J. Chem. Phys.* **2014**, *141*, 034506.

[126] Andresen, E. R.; Gremaud, R.; Borgschulte, A.; Ramirez-Cuesta, A. J.; Züttel, A.; Hamm, P. Vibrational Dynamics of LiBH 4 by Infrared Pump-Probe and 2D Spectroscopy. *J. Phys. Chem. A* **2009**, *113*, 12838–12846.

[127] Roberts, S. T.; Ramasesha, K.; Petersen, P. B.; Mandal, A.; Tokmakoff, A. Proton Transfer in Concentrated Aqueous Hydroxide Visualized Using Ultrafast Infrared Spectroscopy. *J. Phys. Chem. A* **2011**, *115*, 3957–3972.

[128] Hutter, J.; Iannuzzi, M.; Schiffmann, F.; VandeVondele, J. cp2k: atomistic simulations of condensed matter systems. *WIREs Comp. Mol. Sci.* **2014**, *4*, 15–25.

[129] Sulpizi, M.; Sprik, M. Acidity constants from DFT-based molecular dynamics simulations. *J. Phys. Condens. Matter* **2010**, *22*, 284116.

[130] Perdew, J. P.; Burke, K.; Ernzerhof, M. Generalized Gradient Approximation Made Simple. *Phys. Rev. Lett.* **1996**, *77*, 3865–3868.

[131] Miehlich, B.; Savin, A.; Stoll, H.; Preuss, H. Results obtained with the correlation energy density functionals of becke and Lee, Yang and Parr. *Chem. Phys. Lett.* **1989**, *157*, 200 – 206.

[132] Grimme, S.; Antony, J.; Ehrlich, S.; Krieg, H. A consistent and accurate ab initio parametrization of density functional dispersion correction (DFT-D) for the 94 elements H-Pu. *J. Chem. Phys.* **2010**, *132*, 154104.

[133] Goedecker, S.; Teter, M.; Hutter, J. Separable dual-space Gaussian pseudopotentials. *Phys. Rev. B* **1996**, *54*, 1703–1710.

[134] Horníčk, J.; Kaprálová, P.; Bouř, P. Simulations of vibrational spectra from classical trajectories: Calibration with ab initio force fields. *J. Chem. Phys.* **2007**, *127*, 084502.

[135] Marzari, N.; Vanderbilt, D. Maximally localized generalized Wannier functions for composite energy bands. *Phys. Rev. B* **1997**, *56*, 12847–12865.

[136] Brehm, M.; Kirchner, B. TRAVIS - A Free Analyzer and Visualizer for Monte Carlo and Molecular Dynamics Trajectories. *J. Chem. Inf. Model* **2011**, *51*, 2007–2023, PMID: 21761915.

[137] Harvey, K. B.; McQuaker, N. R. Low Temperature Infrared and Raman Spectra of Lithium Borohydride. *Can. J. Chem.* **1971**, *49*, 3282–3286.

[138] Magde, D. Photoselection with intense laser pulses. *J. Chem. Phys.* **1978**, *68*, 3717–3733.

[139] Ansari, A.; Szabo, A. Theory of photoselection by intense light pulses. Influence of reorientational dynamics and chemical kinetics on absorbance measurements. *Biophys. J.* **1993**, *64*, 838–851.

[140] Tokmakoff, A.; Urdahl, R. S.; Zimdars, D.; Francis, R. S.; Kwok, A. S.; Fayer, M. D. Vibrational spectral diffusion and population dynamics in a glass-forming liquid: Variable bandwidth picosecond infrared spectroscopy. *J. Chem. Phys.* **1995**, *102*, 3919–3931.

[141] Bryant, J.; Bain, A. Controlled orientational photoselection via three-pulse excitation. *Chem. Phys. Lett.* **1998**, *286*, 121–130.

[142] Vorobyev, D. Y.; Kuo, C.-H.; Kuroda, D. G.; Scott, J. N.; Vanderkooi, J. M.; Hochstrasser, R. M. Water-Induced Relaxation of a Degenerate Vibration of Guanidinium Using 2D IR Echo Spectroscopy. *J. Phys. Chem. B* **2010**, *114*, 2944–2953.

[143] Yeremenko, S.; Pshenichnikov, M. S.; Wiersma, D. A. Interference Effects in IR Photon Echo Spectroscopy of Liquid Water. *Phys. Rev. A* **2006**, *73*, 21804.

[144] Borgschulte, A.; Gremaud, R.; Zuttel, A.; Martelli, P.; Remhof, A.; Ramirez-Cuesta, A. J.; Refson, K.; Bardaji, E. G.; Lohstroh, W.; Fichtner, M.; Hagemann, H.;

Ernst, M. Experimental Evidence of Librational Vibrations Determining the Stability of Calcium Borohydride. *Phys. Rev. B* **2011**, *83*, 024102.

[145] Tielrooij, K. J.; Garcia-Araez, N.; Bonn, M.; Bakker, H. J. Cooperativity in Ion Hydration. *Science* **2010**, *328*, 1006–1009.

[146] Park, S.; Fayer, M. D. Hydrogen Bond Dynamics in Aqueous NaBr Solutions. *Proc. Natl. Acad. Sci.* **2007**, *104*, 16731–16738.

[147] Stirnemann, G.; Wernersson, E.; Jungwirth, P.; Laage, D. Mechanisms of Acceleration and Retardation of Water Dynamics by Ions. *J. Am. Chem. Soc.* **2013**, *135*, 11824–11831.

[148] Lenchenkov, V.; She, C.; Lian, T. Vibrational Relaxation of CN Stretch of Pseudo-Halide Anions (OCN^-, SCN^-, and $SeCN^-$) in Polar Solvents. *J. Phys. Chem. B* **2006**, *110*, 19990–19997.

[149] Sando, G. M.; Dahl, K.; Owrutsky, J. C. Vibrational spectroscopy and dynamics of azide ion in ionic liquid and dimethyl sulfoxide water mixtures. *J. Phys. Chem. B* **2007**, *111*, 4901–9.

[150] Ji, M.; Park, S.; Gaffney, K. J. Dynamics of Ion Assembly in Solution: 2DIR Spectroscopy Study of LiNCS in Benzonitrile. *J. Phys. Chem. Lett.* **2010**, *1*, 1771–1775.

[151] Lee, K.-K.; Park, K.-H.; Kwon, D.; Choi, J.-H.; Son, H.; Park, S.; Cho, M. Ion-pairing dynamics of Li+ and SCN- in dimethylformamide solution: chemical exchange two-dimensional infrared spectroscopy. *J. Chem. Phys.* **2011**, *134*, 064506.

[152] Tamimi, A.; Fayer, M. D. Ionic Liquid Dynamics Measured with 2D IR and IR Pump-Probe Experiments on a Linear Anion and the Influence of Potassium Cations. *J. Phys. Chem. B* **2016**, *120*, 5842–5854.

[153] Park, S.; Fayer, M. D. Hydrogen Bond Dynamics in Aqueous NaBr Solutions. *Proc. Natl. Acad. Sci. U. S. A* **2007**, *104*, 16731–16738.

[154] Laage, D.; Stirnemann, G.; Sterpone, F.; Rey, R.; Hynes, J. T. Reorientation and Allied Dynamics in Water and Aqueous Solutions. *Annu. Rev. Phys. Chem.* **2011**, *62*, 395–416.

[155] Laage, D.; Stirnemann, G.; Hynes, J. T. Why Water Reorientation Slows without Iceberg Formation around Hydrophobic Solutes. *J. Phys. Chem. B* **2009**, *113*, 2428–2435.

[156] Kreevoy, M. M.; Hutchins, J. E. C. H_2BH_3 as an Intermediate in Tetrahydridoborate Hydrolysis. *J. Am. Chem. Soc.* **1972**, *94*, 6371–6376.

[157] Buzzeo, M. C.; Evans, R. G.; Compton, R. G. Non-haloaluminate room-temperature ionic liquids in electrochemistry–a review. *ChemPhysChem* **2004**, *5*, 1106–1120.

[158] Nulwala, H. B.; Tang, C. N.; Kail, B. W.; Damodaran, K.; Kaur, P.; Wickramanayake, S.; Shi, W.; Luebke, D. R. Probing the structure-property relationship of regioisomeric ionic liquids with click chemistry. *Green Chem.* **2011**, *13*, 3345.

[159] Rosen, B. A.; Haan, J. L.; Mukherjee, P.; Braunschweig, B.; Zhu, W.; Salehi-Khojin, A.; Dlott, D. D.; Masel, R. I. In Situ Spectroscopic Examination of a Low Overpotential Pathway for Carbon Dioxide Conversion to Carbon Monoxide. *J. Phys. Chem. C* **2012**, *116*, 15307–15312.

[160] Gurkan, B.; Goodrich, B. F.; Mindrup, E. M.; Ficke, L. E.; Massel, M.; Seo, S.; Senftle, T. P.; Wu, H.; Glaser, M. F.; Shah, J. K.; Maginn, E. J.; Brennecke, J. F.; Scheider, W. F. Molecular design of high capacity, low viscosity chemically tunable ionic liquids for CO2 capture. *J. Phys. Chem. Lett.* **2010**, *1*, 3494–3499.

[161] Wasserscheid, P.; Keim, W. Ionic Liquids–New "Solutions" for Transition Metal Catalysis. *Angew. Chem. Int. Ed. Engl.* **2000**, *39*, 3772–3789.

[162] Carbonnière, P.; Hagemann, H. Fermi resonances of borohydrides in a crystalline environment of alkali metals. *J. Phys. Chem. A* **2006**, *110*, 9927–9933.

[163] Khalil, M.; Demirdöven, N.; Tokmakoff, A. Coherent 2D IR Spectroscopy: Molecular Structure and Dynamics in Solution. *J. Phys. Chem. A* **2003**, *107*, 5258–5279.

[164] Nydegger, M. W.; Rock, W.; Cheatum, C. M. 2D IR Spectroscopy of the C-D stretching vibration of the deuterated formic acid dimer. *Phys. Chem. Chem. Phys.* **2011**, *13*, 6098–6104.

[165] Del Sesto, R. E.; McCleskey, T. M.; Burrell, A. K.; Baker, G. A.; Thompson, J. D.; Scott, B. L.; Wilkes, J. S.; Williams, P. Structure and magnetic behavior of transition metal based ionic liquids. *Chem. Commun.* **2008**, 447–449.

[166] Yung, K. Y.; Schadock-Hewitt, A. J.; Hunter, N. P.; Bright, F. V.; Baker, G. A. 'Liquid litmus': chemosensory pH-responsive photonic ionic liquids. *Chem. Commun.* **2011**, *47*, 4775.

[167] Jin, H.; O'Hare, B.; Dong, J.; Arzhantsev, S.; Baker, G. A.; Wishart, J. F.; Benesi, A. J.; Maroncelli, M. Physical Properties of Ionic Liquids Consisting of the 1-Butyl-3-Methylimidazolium Cation with Various Anions and the Bis(trifluoromethylsulfonyl)imide Anion with Various Cations. *J. Phys. Chem. B* **2008**, *112*, 81–92.

[168] Fredlake, C. P.; Crosthwaite, J. M.; Hert, D. G.; Aki, S. N. V. K.; Brennecke, J. F. Thermophysical Properties of Imidazolium-Based Ionic Liquids. *J. Chem. Eng. Data* **2004**, *49*, 954–964.

[169] Ferreira, A. G.; Egas, A. P.; Fonseca, I. M.; Costa, A. C.; Abreu, D. C.; Lobo, L. Q. The viscosity of glycerol. *J. Chem. Thermodyn.* **2017**, *113*, 162–182.

[170] Jacquemin, J.; Husson, P.; Padua, A. A. H.; Majer, V. Density and viscosity of several pure and water-saturated ionic liquids. *Green Chem.* **2006**, *8*, 172–180.

[171] Xu, W.; Cooper, E. I.; Angell, C. A. Ionic Liquids: Ion Mobilities, Glass Temperatures, and Fragilities. *J. Phys. Chem. B* **2003**, *107*, 6170–6178.

[172] Tokmakoff, A. Orientational Correlation Functions and Polarization Selectivity for Nonlinear Spectroscopy of Isotropic Media .1. Third Order. *J. Chem. Phys.* **1996**, *105*, 1–12.

[173] Johnson, C. A.; Gronborg, K. C.; Brinzer, T.; Ren, Z.; Garrett-Roe, S. Viscosity Dependence of the Ultrafast Vibrational Dynamics of Borohydride in NaOH Solutions: Crowding Effect on Dihydrogen Bonds. *J. Phys. Chem. B*

[174] Johnson, C. A.; Wagle, D. V.; Gronborg, K.; Brinzer, T.; Ren, Z.; Baker, G. A.; Garrett-Roe, S. Understanding Vibrational Energy Coupling and Ultrafast Vibrational Dynamics of Borohydride Based Ionic Liquids with Two-Dimensional Infrared Spectroscopy. *J. Phys. Chem. B* **2017**, *submitted*.

[175] Gavrila, G.; Godehusen, K.; Weniger, C.; Nibbering, E. T. J.; Elsaesser, T.; Eberhardt, W.; Wernet, P. Time-resolved X-ray absorption spectroscopy of infrared-laser-induced temperature jumps in liquid water. *Appl. Phys. A* **2009**, *96*, 11–18.

[176] Wong, D. B.; Giammanco, C. H.; Fenn, E. E.; Fayer, M. D. Dynamics of Isolated Water Molecules in a Sea of Ions in a Room Temperature Ionic Liquid. *J. Phys. Chem. B* **2013**, *117*, 623–635.

[177] Steele, B. C. H.; Heinzel, A. Materials for fuel-cell technologies. *Nature* **2001**, *414*, 345–352.

[178] Angell, C. A.; Byrne, N.; Belieres, J.-P. Parallel Developments in Aprotic and Protic Ionic Liquids: Physical Chemistry and Applications. *Acc. Chem. Res.* **2007**, *40*, 1228–1236.

[179] Weingartner, H.; Knocks, A.; Schrader, W.; Kaatze, U. Dielectric spectroscopy of the room temperature molten salt ethylammonium nitrate. *J. Phys. Chem. A* **2001**, *105*, 8646–8650.

[180] Sonnleitner, T.; Turton, D. A.; Hefter, G.; Ortner, A.; Waselikowski, S.; Walther, M.; Wynne, K.; Buchner, R. Ultra-Broadband Dielectric and Optical Kerr-Effect Study of the Ionic Liquids Ethyl and Propylammonium Nitrate. *J. Phys. Chem. B* **2015**, *119*, 8826–8841.

[181] Zentel, T.; Overbeck, V.; Michalik, D.; Kühn, O.; Ludwig, R. Hydrogen bonding in protic ionic liquids: structural correlations, vibrational spectroscopy, and rotational dynamics of liquid ethylammonium nitrate. *J. Phys. B At. Mol. Opt. Phys.* **2018**, *51*, 034002.

[182] Hayes, R.; Imberti, S.; Warr, G. G.; Atkin, R. Amphiphilicity determines nanostructure in protic ionic liquids. *Phys. Chem. Chem. Phys.* **2011**, *13*, 3237–3247.

[183] Araque, J. C.; Hettige, J. J.; Margulis, C. J. Modern Room Temperature Ionic Liquids, a Simple Guide to Understanding Their Structure and How It May Relate to Dynamics. *J. Phys. Chem. B* **2015**, *119*, 12727–12740.

[184] Usui, K.; Hunger, J.; Bonn, M.; Sulpizi, M. Dynamical heterogeneities of rotational motion in room temperature ionic liquids evidenced by molecular dynamics simulations. *J. Chem. Phys.* **2018**, *148*, 193811.

[185] Araque, J. C.; Margulis, C. J. In an ionic liquid, high local friction is determined by the proximity to the charge network. *J. Chem. Phys.* **2018**, *149*, 144503.

[186] Mason, P. E.; Neilson, G. W.; Dempsey, C. E.; Barnes, A. C.; Cruickshank, J. M. The hydration structure of guanidinium and thiocyanate ions: Implications for protein stability in aqueous solution. *Proc. Natl. Acad. Sci.* **2003**, *100*, 4557–4561.

[187] Sansone, R.; Ebner, C.; Probst, M. Quantum chemical and molecular dynamics study on the hydration of cyanide and thiocyanate anions. *J. Mol. Liq.* **2000**, *88*, 129–150.

[188] Yamada, S. A.; Thompson, W. H.; Fayer, M. D. Water-anion Hydrogen Bonding Dynamics: Ultrafast IR Experiments and Simulations. *J. Chem. Phys.* **2017**, *146*, 234501.

[189] Park, K. H.; Choi, S. R.; Choi, J. H.; Park, S.; Cho, M. Real-time probing of ion pairing dynamics with 2DIR spectroscopy. *ChemPhysChem* **2010**, *11*, 3632–3637.

[190] Ji, M.; Hartsock, R. W.; Sung, Z.; Gaffney, K. J. Influence of solute-solvent coordination on the orientational relaxation of ion assemblies in polar solvents. *J. Chem. Phys.* **2012**, *136*.

[191] Ohta, K.; Tayama, J.; Tominaga, K. Ultrafast vibrational dynamics of SCN^- and N_3^- in polar solvents studied by nonlinear infrared spectroscopy. *Phys. Chem. Chem. Phys.* **2012**, *14*, 10455–65.

[192] Son, H.; Jin, H.; Choi, S. R.; Jung, H. W.; Park, S. Infrared Probing of Equilibrium and Dynamics of Metal–Selenocyanate Ion Pairs in N , N -Dimethylformamide Solutions. *J. Phys. Chem. B* **2012**, *116*, 9152–9159.

[193] Czurlok, D.; Gleim, J.; Lindner, J.; Vöhringer, P. Vibrational Energy Relaxation of Thiocyanate Ions in Liquid-to-Supercritical Light and Heavy Water. A Fermi's Golden Rule Analysis. *J. Phys. Chem. Lett.* **2014**, *5*, 3373–3379.

[194] Tracy, K. M.; Barich, M. V.; Carver, C. L.; Luther, B. M.; Krummel, A. T. High-Throughput Two-Dimensional Infrared (2D IR) Spectroscopy Achieved by Interfacing Microfluidic Technology with a High Repetition Rate 2D IR Spectrometer. *J. Phys. Chem. Lett.* **2016**, *7*, 4865–4870.

[195] Park, S.; Ji, M.; Gaffney, K. J. Ligand exchange dynamics in aqueous solution studied with 2DIR spectroscopy. *J. Phys. Chem. B* **2010**, *114*, 6693–6702.

[196] Houchins, C.; Weidinger, D.; Owrutsky, J. C. Vibrational Spectroscopy and Dynamics of the Hydrazoic and Isothiocyanic Acids in Water and Methanol. *J. Phys. Chem. A* **2010**, *114*, 6569–6574.

[197] Ji, M.; Hartsock, R. W.; Sun, Z.; Gaffney, K. J. Interdependence of Conformational and Chemical Reaction Dynamics during Ion Assembly in Polar Solvents. *J. Phys. Chem. B* **2011**, *115*, 11399–11408.

[198] Kiefer, J.; Noack, K.; Penna, T. C.; Ribeiro, M. C.; Weber, H.; Kirchner, B. Vibrational signatures of anionic cyano groups in imidazolium ionic liquids. *Vib. Spectrosc.* **2017**, *91*, 141–146.

[199] Brinzer, T.; Berquist, E. J.; Dutta, S.; Johnson, C. A.; Krisher, C. S.; Lambrecht, D. S.; Garrett-Roe, S.; Ren, Z. Erratum: "Ultrafast Vibrational Spectroscopy (2D-IR) of CO2 in Ionic Liquids: Carbon Capture from Carbon Dioxide's Point of View" [J. Chem. Phys. 142, 212425 (2015)]. *J. Chem. Phys.* **2017**, *147*, 049901.

[200] Shin, J. Y.; Yamada, S. A.; Fayer, M. D. Dynamics of a Room Temperature Ionic Liquid in Supported Ionic Liquid Membranes vs the Bulk Liquid: 2D IR and Polarized IR Pump–Probe Experiments. *J. Am. Chem. Soc.* **2017**, *139*, 311–323.

[201] Cui, Y.; Fulfer, K. D.; Ma, J.; Weldeghiorghis, T. K.; Kuroda, D. G. Solvation dynamics of an ionic probe in choline chloride-based deep eutectic solvents. *Phys. Chem. Chem. Phys.* **2016**, *18*, 31471–31479.

[202] Ren, Z.; Kelly, J.; Gunathilaka, C. P.; Brinzer, T.; Dutta, S.; Johnson, C. A.; Mitra, S.; Garrett-Roe, S. Ultrafast Dynamics of Ionic Liquids in Colloidal Dispersion. *Phys. Chem. Chem. Phys.* **2017**, *19*, 32526–32535.

[203] Ramasesha, K.; Roberts, S. T.; Nicodemus, R. A.; Mandal, A.; Tokmakoff, A. Ultrafast 2D IR Anisotropy of Water Reveals Reorientation During Hydrogen-Bond Switching. *J. Chem. Phys.* **2011**, *135*, 54509.

[204] Bagchi, B.; Fleming, G. R. Dynamics of activationless reactions in solution. *J. Phys. Chem.* **1990**, *94*, 9–20.

[205] Press, W. H.; Teukolsky, S. A.; Vetterlin, W. T.; Flannery, B. P. *Numerical Recipes in C*, 2nd ed.; Cambridge University Press: New York, 1992.

[206] Stenger, J.; Madsen, D.; Hamm, P.; Nibbering, E. T. J.; Elsaesser, T. A Photon Echo Peak Shift Study of Liquid Water. *J. Phys. Chem. A* **2002**, *106*, 2341–2350.

[207] Greaves, T. L.; Weerawardena, A.; Fong, C.; Krodkiewska, I.; Drummond, C. J. Protic Ionic Liquids: Solvents with Tunable Phase Behavior and Physicochemical Properties. *J. Phys. Chem. B* **2006**, *110*, 22479–22487.

[208] Yuan, R.; Fayer, M. D. Dynamics of Water Molecules and Ions in Concentrated Lithium Chloride Solutions Probed with Ultrafast 2D IR Spectroscopy. *J. Phys. Chem. B* **2019**, *123*, 7628–7639.

[209] Lindquist, B. A.; Corcelli, S. A. Nitrile Groups as Vibrational Probes: Calculations of the CN Infrared Absorption Line Shape of Acetonitrile in Water and Tetrahydrofuran. *J. Phys. Chem. B* **2008**, *112*, 6301–6303.

[210] Lee, H.; Choi, J.-H.; Cho, M. Vibrational Solvatochromism and Electrochromism of Cyanide, Thiocyanate, and Azide Anions in Water. *Phys. Chem. Chem. Phys.* **2010**, *12*, 12658–12669.

[211] Ren, Z.; Garrett-Roe, S. Reorientation-induced spectral diffusion of non-isotropic orientation distributions. *J. Chem. Phys.* **2017**, *147*, 144504.

[212] Yamada, S. A.; Bailey, H. E.; Tamimi, A.; Li, C.; Fayer, M. D. Dynamics in a Room-Temperature Ionic Liquid from the Cation Perspective: 2D IR Vibrational Echo Spectroscopy. *J. Am. Chem. Soc.* **2017**, *139*, 2408–2420.

[213] Hamm, P.; Lim, M.; Hochstrasser, R. M. Vibrational Energy Relaxation of the Cyanide Ion in Water. *J. Chem. Phys.* **1997**, *107*, 10523–10531.

[214] Oxtoby, D. W. Vibrational Relaxation in Liquids. *Annu. Rev. Phys. Chem.* **1981**, *32*, 77–101.

[215] Dake, S. A.; Raut, D. S.; Kharat, K. R.; Mhaske, R. S.; Deshmukh, S. U.; Pawar, R. P. Ionic liquid promoted synthesis, antibacterial and in vitro antiproliferative activity of novel α-aminophosphonate derivatives. *Bioorg. Med. Chem. Lett.* **2011**, *21*, 2527–2532.

[216] Mulla, S. A. R.; Sudalai, A.; Pathan, M. Y.; Siddique, S. A.; Inamdar, S. M.; Chavan, S. S.; Reddy, R. S. Efficient, rapid synthesis of bis(indolyl)methane using ethyl ammonium nitrate as an ionic liquid. *RSC Adv.* **2012**, *2*, 3525.

[217] Fumino, K.; Wulf, A.; Ludwig, R. The potential role of hydrogen bonding in aprotic and protic ionic liquids. *Phys. Chem. Chem. Phys.* **2009**, *11*, 8790.

[218] Kaintz, A.; Baker, G.; Benesi, A.; Maroncelli, M. Solute diffusion in ionic liquids, NMR measurements and comparisons to conventional solvents. *J. Phys. Chem. B* **2013**, *117*, 11697–708.

[219] Litovitz, T. A. Temperature Dependence of the Viscosity of Associated Liquids. *J. Chem. Phys.* **1952**, *20*, 1088–1089.

[220] Laage, D.; Hynes, J. T. On the Molecular Mechanism of Water Reorientation. *J. Phys. Chem. B* **2008**, *112*, 14230–14242.

[221] Vartia, A. A.; Mitchell-Koch, K. R.; Stirnemann, G.; Laage, D.; Thompson, W. H. On the Reorientation and Hydrogen-Bond Dynamics of Alcohols. *J. Phys. Chem. B* **2011**, *115*, 12173–12178.

[222] Mesele, O. O.; Vartia, A. A.; Laage, D.; Thompson, W. H. Reorientation of Isomeric Butanols: The Multiple Effects of Steric Bulk Arrangement on Hydrogen-Bond Dynamics. *J. Phys. Chem. B* **2016**, *120*, 1546–1559.

[223] Daly, Jr., C. A.; Allison, C.; Corcelli, S. A. Modeling Carbon Dioxide Vibrational Frequencies in Ionic Liquids: IV. Temperature Dependence. *J. Phys. Chem. B* **2019**, *123*, 3797–3803.

[224] Rini, M.; Magnes, B.-Z.; Pines, E.; Nibbering, E. T. J. Real-Time Observation of Bimodal Proton Transfer in Acid-Base Pairs in Water. *Science* **2003**, *301*, 349–352.

[225] Mohammed, O. F.; Pines, D.; Dreyer, J.; Pines, E.; Nibbering, E. T. J. Sequential Proton Transfer Through Water Bridges in Acid-Base Reactions. *Science* **2005**, *310*, 83–86.

[226] Mohammed, O. F.; Pines, D.; Pines, E.; Nibbering, E. T. J. Aqueous bimolecular proton transfer in acid-base neutralization. *Chem. Phys.* **2007**, *341*, 240–257.

[227] Donten, M. L.; Hamm, P. pH-Jump Overshooting. *J. Phys. Chem. Lett.* **2011**, *2*, 1607–1611.

[228] Hayes, R.; Imberti, S.; Warr, G. G.; Atkin, R. How water dissolves in protic ionic liquids. *Angew. Chemie - Int. Ed.* **2012**, *51*, 7468–7471.

[229] Hayes, R.; Imberti, S.; Warr, G. G.; Atkin, R. Effect of cation alkyl chain length and anion type on protic ionic liquid nanostructure. *J. Phys. Chem. C* **2014**, *118*, 13998–14008.